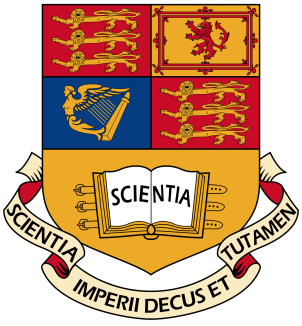
Multiphase Flow Simulation with Applications for CO_2 Storage

Aaron Lewis Goater

Department of Earth Science and Engineering
Imperial College London



A thesis submitted for the degree of Doctor of Philosophy
of Imperial College London

October 2011

Abstract

Geological storage of carbon dioxide (CO_2) has potential to significantly reduce atmospheric emissions of greenhouse gases. However, challenges exist to the successful establishment of this process. These include estimating and understanding storage capacity as well as its economic viability. A large proportion of Europe's potential storage capacity is to be found in large open aquifers. However, in times when the European carbon price is low, storage in depleted oil reservoirs may be required to make early commercial projects economically viable. Regulation will require that storage in these sites is well understood and it currently requires conformity of actual with modelled behaviour. In this thesis we consider two areas with direct implication for these issues.

Firstly, we consider the effect of top-surface structure and heterogeneity upon the storage capacity of open aquifers. It is found that top-surface structure is more likely to decrease storage efficiency in models with low average reservoir dip and/or permeability. Heterogeneity is seen to reduce injectivity and reduce capacity in low permeability models but increase lateral spread of CO_2 and storage efficiency in higher permeability cases. Both features can change storage capacity by more than a factor of two.

Secondly, we undertake investigation into 1D solutions for three-phase flow problems representative of CO_2 storage in depleted oil reservoirs. We begin by trying to determine rigorously the physical solution to three-phase flow problems that may have non-unique solutions using the third-order essentially non-oscillatory (ENO) numerical method. However, we demonstrate that ENO only produces first-order convergence in discontinuous solutions, which means rigorous analysis using our proposed methodology is not possible. We do, however, benchmark compositional three-phase, three-component ENO simulations against analytic solutions for the first time and demonstrate that ENO is still preferable to low-order numerical methods. Finally, we demonstrate the convergence of three-phase numerical solutions by comparing solutions with water-wet and oil-wet capillary pressure functions as the magnitude of the capillary pressure functions become small.

Declaration

I declare that this thesis, **Multiphase Flow Simulation with Applications for CO_2 Storage**, is entirely my own work under the supervision of Dr Tara LaForce and Prof. Martin J Blunt. The work was performed in the Department of Earth Science and Engineering at Imperial College London. All published and unpublished material used in the thesis has been given full acknowledgment. This work has not been previously submitted, in whole or in part, to any other academic institution for a degree, diploma, or any other qualification.

Aaron Lewis Goater

Department of Earth Science and Engineering

Imperial College London

October 16th 2011

Acknowledgements

I would like to begin by thanking my main PhD supervisor, Dr Tara LaForce. Her direction and encouragement and many thoughtful discussions with her were integral to this thesis. Much of what I have learnt about scientific research I have learnt from her. I would also like to thank Prof. Martin Blunt and Dr Branko Bijeljic for their help, thoughts and insight that have contributed towards this work.

I would like to thank Prof. Ann Muggeridge and Prof. Eric Mackay for agreeing to be my PhD examiners. I also would like to acknowledge the UK Engineering and Physical Sciences Research Council for funding my PhD research, and the Energy Technology Institute for funding the provision of data. I would also like to acknowledge the UK Storage Appraisal Project participants for many useful conversations and especially Jeff Masters and Eugene Balbinski for their helpful advice and Senergy Ltd for providing a geo-cellular model.

There are many other friends and colleagues around Imperial College whom it has been a great pleasure to work with, especially Lorena Lazaro Vallejo, Chris Pentland, Grace Cairns, Bilal Rashid, Lorraine Sobers, Ana Mijic, Ahmed El Sheikh, Allan Leal, Florence Bullough, Patricia Doyle, Kate Goddard and Rudolf Umla. A special mention also goes to Surinder Singh Dio, who managed to fend off many potential computer-related disasters.

Last, but by no means least, I would like to thank my parents Andrew and Christine for their love and never-ending support throughout my life; my sister Yvette and grandparents, Colin, Mary, Vernon and Gwen for always being there for me; and Kate, my partner, for her love, patience and support throughout this PhD. Without you all, I would have neither started nor finished.

List of Publications

Goater, A. L., Bijeljic, B., and Blunt, M. J. The effect of top-surface topography upon CO_2 storage capacity in open aquifers. *International Journal of Greenhouse Gas Control.* To be submitted.

Goater, A. L. and LaForce, T. Investigating the convergence of three phase simulation. *Computational Geosciences.* To be submitted.

Goater, A. L., Bijeljic, B., and Blunt, M. J. (2011). The effect of top-surface structure upon CO_2 storage capacity in open aquifers. In *1st EAGE Sustainable Earth Sciences Conference and Exhibition*, Valencia, Spain.

Goater, A. L. and LaForce, T. (2010). Multicomponent multiphase transport solutions for application to CO_2 storage. In *ECMOR XII - 12th European Conference on the Mathematics of Oil Recovery*, Oxford, UK.

Contents

Abstract **2**

Declaration **3**

Acknowledgements **4**

List of Publications **5**

Contents **5**

List of Figures **9**

List of Tables **17**

List of Notation **20**

1 Introduction **23**

1.1 Carbon Capture and Storage 24

1.2 Theory of Flow in Porous Media 27

1.3 Approaches to Modelling CO_2 Storage 29

1.3.1 1D Analytical Solutions 29

1.3.2 2D and 3D Vertical Equilibrium Solutions 31

1.3.3 3D Simulation Models 32

1.4 Thesis Overview 34

1.4.1 Aims of Thesis 34

1.4.2 Layout of Thesis 34

2 Literature Review **36**

2.1 Storage Capacity Estimation 36

2.1.1 Volumetric Storage Capacity Estimation for Aquifers 36

2.1.2 Dynamic Storage Capacity Estimation Projects and Studies for Open Aquifers 41

2.1.3 The Effect of Geological Features upon CO_2 Capacity and the Distribution of CO_2 . . . 48
2.2 Streamline Simulation and CO_2 Storage . . . 51
2.2.1 Overview/ Original Papers . . . 51
2.2.2 Improvements to the Streamline Algorithm . . . 52
2.2.3 Advantages and Limitations of Using Streamlines . . . 56
2.2.4 Streamline-based Simulation Studies of CO_2 Storage . . . 57
2.3 1D Solutions . . . 60
2.3.1 Structure of the 1D Conservation Equations . . . 60
2.3.2 Analytical Solutions of the Conservation Equations . . . 64
2.3.3 Numerical Methods and Proposed Plan to Identify Correct 3-Phase 1D Solutions . . . 67
2.3.4 Capillary Pressure Models . . . 68
2.4 Summary . . . 70

3 The Effect of Top Surface Structure and Heterogeneity upon CO_2 Storage Capacity in Open Aquifers 71
3.1 Introduction . . . 71
3.2 Modelling Methods . . . 75
3.2.1 Geocellular Model of the Base Case Forties Storage Unit . . . 75
3.2.2 Dynamic Model Setup . . . 81
3.2.3 Injection Conditions . . . 83
3.2.4 Storage Security and Trapping Assessment . . . 85
3.2.5 Sensitivity Models . . . 87
3.2.6 Methodology for Calculating Storage Capacity - Optimising Injection and Well Location . . . 89
3.2.7 Alternative Simulations using Streamlines . . . 90
3.3 Base Case Results . . . 93
3.3.1 Storage Appraisal . . . 93
3.3.2 Storage Capacity and Trapping Mechanism . . . 96
3.3.3 Model Verification . . . 98
3.3.4 Sensitivity to Reservoir Dip and Permeability . . . 107
3.4 Top-Surface Structure and Heterogeneity Sensitivity Results . . . 116
3.4.1 Effect of Top-Surface Structure upon Storage Capacity . . . 116
3.4.2 Effect of Heterogeneity upon Storage Capacity . . . 125
3.5 Discussion . . . 127
3.5.1 Limitations and Assumptions . . . 127

3.5.2 Implications of Results . . . 129
3.6 Conclusions . . . 132

4 Convergence of 1D Three Phase Solutions 134
4.1 Introduction . . . 134
4.2 Mathematical Model . . . 136
4.2.1 Advective Transport Problem . . . 136
4.2.2 Example Solution . . . 137
4.3 Numerical Model . . . 140
4.3.1 General Formulation of Finite Volume/ Finite Difference Schemes for Conservation Laws . . . 140
4.3.2 Single-Point Upstream Weighting (SPU) . . . 141
4.3.3 Total Variation Diminishing (TVD) Methods . . . 142
4.3.4 Essentially Non-Oscillatory (ENO) Scheme . . . 143
4.3.5 Modifications to ENO Algorithm and Implementation Notes . . . 147
4.3.6 Calculation of Two-Phase Saturations . . . 149
4.4 Results . . . 150
4.4.1 Immiscible Two-Phase Order of Accuracy Study . . . 150
4.4.2 Immiscible Two-Phase Code Verification . . . 153
4.4.3 Three-Phase Three-Component Benchmark Solution . . . 155
4.5 Discussion - Accuracy of ENO in Presence of Discontinuities . . . 160
4.6 Conclusions . . . 161

5 1D Three Phase Solutions in the Presence of Capillary Pressure with Varying Wettability 162
5.1 Introduction . . . 162
5.2 Mathematical Model . . . 163
5.2.1 Advective Transport Model with Capillary Pressure . . . 163
5.2.2 Capillary Pressure Models . . . 163
5.2.3 Test Models . . . 166
5.3 Numerical Model . . . 168
5.3.1 Fully Explicit Scheme . . . 168
5.3.2 Operator Splitting Scheme . . . 173
5.3.3 Calculation of Three-phase Saturations . . . 178
5.4 Results . . . 182
5.4.1 Numerical Methods Results . . . 182
5.4.2 Model A Results . . . 182
5.4.3 Model B Results . . . 183

5.4.4 Model C and D Results 183
5.5 Discussion and Conclusions 190

6 Conclusions and Future Work 191
6.1 Conclusions 191
6.2 Future Work 194
6.2.1 Storage Capacity Estimation Related Work 194
6.2.2 1D Three-Phase Solutions Related Work 195

Bibliography 197

Appendices 216

A Methodology for calculating structural closure and CO_2 migration velocity 216

B Methodology for calculating CO_2 migration velocity 219

C Simulation results - Base case injection rates 220

D Simulation results - Sensitivity study storage data 222

E Simulation results - Simulation runs used for capacity optimisation 231

F ECLIPSE input file for the base case 242

G ENO truncation error 267

H Explicit scheme capillary truncation error 268

List of Figures

1.1 An overview of geological storage options. IPCC (2005) 24
1.2 A pore-scale image demonstrating residual trapping. Trapped non-wetting phase (blue) in a sandstone (green) surrounded by wetting phase (grey). Figure from Dong (2007). 26
1.3 Importance of different trapping mechanisms over time (IPCC, 2005). . . 27
1.4 Fractional flow f_1 against saturation S_1. 30
1.5 The saturation profile of S_1 in a Buckley-Leverett solution. 31
1.6 Plume of CO_2 during the post-injection period allowing for residual trapping, from Juanes and MacMinn (2008). 32

2.1 Techno-Economic Resource-Reserve pyramid for CO_2 storage capacity in geological media within a geographic region. 1) Theoretical Storage Capacity assumes that the system's entire capacity to store CO_2 in pore space, or dissolved at maximum saturation in formation fluids is accessible and utilized. 2) Effective Storage Capacity is obtained by considering the part of the pore space that can be physically accessed and which meets a range of geological and engineering criteria. 3) Practical Storage Capacity is obtained by considering technical, legal and regulatory, infrastructural and general economic barriers. 4) Matched Storage Capacity is obtained by detailed matching of large stationary CO_2 sources with geological storage sites that are adequate in terms of capacity, injectivity and supply rate. Figure from CSLF (2008) 37
2.2 The open aquifer storage regimes after Gammer et al. (2011). 46
2.3 The composition space of a three-component system. Composition i tends from 0 to 1 as you move towards the ith corner. In the region highlighted the conservation equations are elliptic. 62

3.1 Sketch of a dipping open aquifer (left) compared to an open aquifer with a large-scale structural closure (right); it is assumed that the structure has closure in all directions. 72

3.2 Location of the Forties Sandstone member and the Forties geological model. The areal extent of the Forties geological model is identified by a black rectangle. The contours are for depth below sea level in metres. 76
3.3 Seismic interpretation of the top of the Upper Forties in depth. The location of the Forties geological model and wells are also shown.The contours are for depth. The duck points north. 77
3.4 Facies model shown for the base case at layer 38 (counted from top). The arrow points north. 78
3.5 Permeability model at top of Forties base case geological model and in a cross section. The cross section taken is shown by the black line in the top view. Ki is horizontal permeability in mD. The arrow points north. . . . 79
3.6 Porosity model at top of Forties base case geological model. The arrow points north. 80
3.7 Viking 2 relative permeability and capillary pressure from Bennion and Bachu (2008). 81
3.8 Qualitative overpressure contours for the Forties Sandstone member. The Forties base case geological model area shown in red. Map constructed using data from GeoPressure Technology Ltd. Values not shown to protect data ownership. 84
3.9 Map of cells on the top layer which are structurally closed. Due to the buoyancy of CO_2, once within these structurally closed cells it shall stay there until dissolved. 86
3.10 Permeability maps for (from left to right) the 11mD average permeability base case and two permeability sensitivities with 145mD and 1D average permeability. Figures show top layer of model viewed from above. In the key Ki is permeability in mD. 87
3.11 Porosity maps for the different dip sensitivity models. The base case has dip 0.27° and two sensitivity cases have dips 1° and 3°. Models are viewed from the west and vertically exaggerated by a factor of 15. In the key Por stands for porosity. 88
3.12 Simplification of base case model by removing heterogeneity then top-surface structure. Figures show permeability in mD, are viewed from the south and are exaggerated by a factor of 15 in the vertical direction. . . . 88
3.13 Locations of the eleven horizontal wells used for the base case and sensitivity scenarios. The model is viewed from above. 90
3.14 General methodology for calculating the capacity of each model. 92

3.15 Pressure (bars) profile at top layer at 50 years in a preliminary 6 well injection scenario. The purple 'specs' are shales that were treated as inactive cells in early simulations. Pressures around 400bars (=40MPa) and below indicate some limited pressure space, suggesting that using more wells would lead to higher storage capacities. The wells are shown in black. . . 93
3.16 The total mass of CO_2 (Mt) injected into the base case geological model per decade under our maximum injection scenario. 94
3.17 CO_2 saturation in the Forties base case model at 1000 years. The maximum gas saturation is 0.577. The model is 36km long, viewed from the south and vertically exaggerated by a factor of 15. The wells are shown in black. 96
3.18 Mechanisms trapping CO_2 in the base case model at 1000 years. Percentages show the proportion of the total amount trapped by different mechanisms. Note that trapping by precipitation is not modelled. 97
3.19 Mechanisms trapping CO_2 at 1000 years and 10,000 years. 97
3.20 Porosity distribution for 1,733,400 (left) and 450,450 (right) cell models. 98
3.21 Permeability distribution for 1,733,400 (left) and 450,450 (right) cell models 99
3.22 Permeability (mD) map for 1,733,400 (left) and 450,450 (right) cell models viewed from above. 99
3.23 Models at top show saturation profiles at 10000 years for 1,733,400 (left) and 450,450 (right) cell models. Top models show top layer viewed from above. The wells are shown in black. Bottom models show saturation distribution around injection well INJ12. 100
3.24 Pressure (in bars) profiles on top layer at 40 years for 1,733,400 (left) and 450,450 (right) cell models. Higher localised pressure is visible in the 450,450 cell model. 101
3.25 Mass (Mt) of CO_2 stored with different grid resolutions at 1000 years. . . 102
3.26 Scenario 3 - The cells at the boundary have large pore volumes to represent the volume of aquifer attached to the model. Visually these boundary cells appear with the same area as their neighbours, however their pore volume is larger. To test the effect of the resolution of these boundary cells, such as the one highlighted they were refined. This can be seen by the range of colours inside. This refinement allowed the pressure to be resolved more accurately. 103
3.27 Sensitivity of injected CO_2 volume to changes in boundary condition. . . 104
3.28 Storage efficiency results for various sensitivities 106
3.29 Sensitivity of base case storage efficiency to average permeability. 107

3.30 Figure 3.14: Top layer saturation profile at 1000 years for 145md permeability sensitivity. The injection scenario shows injected CO_2 equal to 4% of the storage unit pore volume. 0.4% of the injected left the model - meeting the 99% storage constraint; however the migration velocity constraint was failed. Wells shown in black. 108
3.31 Top layer saturation profile at 1000 years for 145md permeability sensitivity. The injection scenario shown injected CO_2 equal to 2% of the storage unit pore volume and met the storage constraints. Wells shown in black. 109
3.32 Sensitivity of base case storage efficiency to reservoir dip. 110
3.33 Sensitivity of storage efficiency due to changes in permeability in the 0.27° dip, smooth homogeneous model. 111
3.34 Saturation profile at 1000 years for the 0.27° dip, 145md permeability, smooth homogeneous model. The top layer is shown from above. 112
3.35 Cross-section of saturation profile for the 0.27° dip, 145md permeability, smooth homogeneous model at 1000 years. Estimates of change of the connected height of CO_2 and the distance over which this change occurs are shown. The connected height is estimated by CO_2 above the maximum residual gas saturation. Model exaggerated by a factor of 40 in the vertical direction. 113
3.36 Sensitivity of the stored mass (Mt) of 'low velocity CO_2' to permeability in a 0.27° dip, smooth homogeneous scenario. Low velocity CO_2 is defined in Section 3.2.4 114
3.37 Saturation profile in the top layer of a smooth, homogeneous 1 Darcy model at 1000 years. Most gas saturation is seen to be near residual. 115
3.38 Change in storage efficiency due to the introduction of top-surface structure and heterogeneity to the 11mD 0.27° smooth homogeneous case. . . 117
3.39 Saturation profile showing the top layer of a smooth homogeneous 11mD permeability model with a dip of 0.27° at 1000 years. 117
3.40 Saturation profile showing the top layer of 11mD permeability, 0.27° dip homogeneous model with top-surface structure at 1000 years. 118
3.41 Change in storage efficiency due to the introduction of top-surface structure and heterogeneity to the 145mD permeability, 0.27° dip, smooth homogeneous case. 119
3.42 Saturation of a homogeneous 145mD, 0.27° dip model with top-surface structure at 1000 years. Model viewed from south and exaggerated by factor 15 in the vertical direction. 120

3.43 Change in storage efficiency due to the introduction of top-surface structure and heterogeneity to the 1 Darcy, 0.27° dip smooth homogeneous case. 121
3.44 Change in storage efficiency due to the introduction of top-surface structure to the 145mD, 1° dip smooth homogeneous case. 123
3.45 Pressure (bars) profile around well INJ10 in heterogeneous (left) and homogeneous (right) cases at 50 years. The intersections show that localised high pressure can build up in the heterogeneous model whereas it spreads further in the homogeneous model. 125
3.46 Saturation intersections to show wider lateral migration under shales in the heterogeneous model (left) compared to the homogenous model (right) at 1000 years. Both models have 145mD permeability and 0.27° dip. . . . 126
3.47 Gas saturation intersection around well INJ2 to show structural trapping under shales at 1000 years for the 11mD heterogeneous case. 127
3.48 Range of potential general effects of the introduction of top-surface structure to intermediate and migration velocity limited storage regime models. 130

4.1 The analytic and simulated solutions in composition space for the example three-phase problem. This ternary system has water/CO_2 and water/oil two-phase regions and a large central three-phase region. The SPU simulation with 150 grid blocks is shown as red triangles and the ENO simulation with 150 grid blocks is shown as blue inverted triangles. The analytic solution is in black with solid lines denoting rarefaction curves and dashed lines indicating shocks in composition. 139
4.2 A 1D grid where the average composition of each cell is reprented by a point at the cell centre. The vertical axis represents the evolution of the cell average from time τ_n to time τ_{n+1}. The flux $\hat{F}_{k+\frac{1}{2}}$ at the boundary of the cell represent the average flux through the boundary over the timestep. 140
4.3 A grid with n_k=4 gridblocks where the colours represent the volume fraction of each phase present in each cell. 144
4.4 A grid with flux calculated at points ξ_k and the interpolations to $\hat{F}_{k+\frac{1}{2}}$. . 145
4.5 Local error at point $\xi = 0.525$ and $\tau = 1$ against grid spacing for the example with $F = \sin\frac{\pi C}{2}$, initial condition $C = \frac{2}{\pi}\cos^{-1}\frac{3\xi}{\pi}$ and boundary condition $C = 1$ so there is no initial discontinuity. The average slope of the curves shows that the local error from ENO in this problem decreases with rate $(\Delta\xi)^{3.17}$ whereas the SPU scheme's error decreases with rate$(\Delta\xi)^{1.01}$ 151

4.6 Local error at point $\xi = 0.525$ and $\tau = 1$ against grid spacing for the example with $F = \sin\frac{\pi C}{2}$, boundary condition $C = 1$ and initial condition C=0 so that there is an initial discontinuity. The average slope of the curves shows that the local error from ENO in this problem decreases with rate $(\Delta\xi)^{1.00}$ whereas the SPU schemes error decreases with rate $(\Delta\xi)^{0.84}$. There is, however, approximately a factor 10 difference between the size of the errors 153

4.7 Simulated and analytic 1D CO_2 saturation profiles after 0.5 days of injection of 95% CO_2 into a 100% water saturated aquifer. The system was assumed to be 2-phase immiscible. 154

4.8 Analytic and simulated profiles of the solution to the three-phase, three-component benchmark problem posed in Section 4.2.2. The volume fraction of the CO_2, oil and water components along the 1D reservoir is shown. ENO produces significantly less numerical diffusion than SPU at the shock fronts for the same 150 cell level of grid-refinement. The CPU times taken to reach the solutions were 2 and 5 seconds for SPU and ENO respectively. Analytic solutions provided by LaForce (2011) 157

4.9 Analytic and simulated profiles of the solution to the three-phase, three-component benchmark problem posed in Section 4.2.2. The volume fraction of the gas, oleic and aqueous phases along the 1D reservoir is shown. ENO produces significantly less numerical diffusion than SPU at the shock fronts for the same 150 cell level of grid-refinement. The CPU times taken to reach the solutions were 2 and 5 seconds for SPU and ENO respectively. Analytic solutions provided by LaForce (2011) 158

4.10 Local error at points 0.125, 1.225 and 2.275 against grid spacing $\Delta\xi$ in the three-phase, three-component benchmark problem as posed by Section 4.2.2 and shown in Figures 4.1 and 4.8. The average slope of the local error curves for SPU is 2.19, 1.05 and 0.84 for the points 0.125, 1.225 and 2.275. The average slope of the local error curves for ENO is 2.68, 1.03 and 1.08 for the points 0.125, 1.225 and 2.275. There is a factor of 3 to 20 accuracy improvement in ENO over SPU. 159

5.1 Representation of wettability using the crevice of a pore as shown in DiCarlo et al. (2000). The aqueous phase is the wetting phase, oleic phase intermediate-wet and the gas phase non-wetting. 164

5.2 The aqueous-oleic and oleic-gas capillary pressure functions in a water-wet porous medium. 165

5.3 The aqueous-oleic and aqueous-gas capillary pressure functions in an oleic-wet porous medium. 165
5.4 Flowchart of numerical method to solve three-phase, three-component transport problem with capillary pressure. 170
5.5 Cell centred and call face values used for the discretisation of the capillary pressure term. 170
5.6 General ternary phase diagram. The points demonstrate the selected mixture compositions chosen in step 1 and the compositions of the partitioned phases. Red lines indicate boundaries used in step 4. 179
5.7 The simulated solution profile with capillary pressure (in red) as outlined in Model A against the analytic (in black) and simulated(in blue) purely advective solution profile. Both solutions at $\tau = 0.25$. The simulated solution used the operator splitting scheme with 500 cells and 1250 timesteps. C_1 =CO_2, C_2 =oil, C_3 =water. 185
5.8 The simulated solution profile with capillary pressure (in red) as outlined in Model B against the analytic purely advective solution profile (in black). Both solutions at $\tau = 0.25$. The simulated solution used the explicit scheme with 1000 cells and 2500 timesteps. C_1 =CO_2, C_2 =oil, C_3 =water. 186
5.9 The simulated solution profiles with aqueous-wet capillary pressure (in red) as outlined in Model C and oleic-wet capillary pressure (in blue) as outlined in Model D against the analytic purely advective solution profile (in black). Both solutions at $\tau = 0.25$. The simulated solutions used the explicit scheme with 1500 cells and 15000 timesteps. C_1 =CO_2, C_2 =oil, C_3 =water. 187
5.10 The simulated solution profiles with aqueous-wet capillary pressure (in red) as outlined in Model C and oleic-wet capillary pressure (in blue) as outlined in Model D against the analytic purely advective solution profile (in black) and simulated purely advective solution profile (in green). Both solutions at $\tau = 0.25$. The simulated capillary pressure solutions used the explicit scheme with 1500 cells and 15000 timesteps and the simulated advection solution used 100 cells and 1000 timesteps. C_1 =CO_2, C_2 =oil, C_3 =water. 188

5.11 The simulated solution profiles with reduced aqueous-wet capillary pressure (in red) given by $u_t = 0.005$ and otherwise as outlined in Model C and reduced oleic-wet capillary pressure (in blue) given by $u_t = 0.002$ and otherwise as outlined in Model D against the analytic purely advective solution profile (in black). Both solutions at $\tau = 0.25$. The simulated solutions used the explicit scheme with 1500 cells and 10000 timesteps. C_1 =CO_2, C_2 =oil, C_3 =water. 189

A.1 Vertical cross-section through an example geocellular model. 217

List of Tables

1.1 Operational CO_2 Storage Projects (MIT, 2011) 25
1.2 Common Simulation Models 33

3.1 Initial conditions and parameters for the base case simulation. 82
3.2 Storage efficiency results for various sensitivities 105

4.1 Example parameters, after Valenti et al. (2004) 137
4.2 Constants c_{rw} for $p = 3$ 146
4.3 2 phase immiscible parameters 154
4.4 The CPU time taken to simulate the benchmark solution posed in Section 4.2.2 using ENO and SPU. The number of timesteps was fixed at 20000. 156

5.1 Capillary pressure term parameters 164
5.2 Parameters for model A 166
5.3 Parameters for model B 166
5.4 Parameters for model C and D 167

C.1 Base case injection rates 221

D.1 Setup of optimised models 223
D.2 Setup of optimised models 223
D.3 Setup of optimised models 224
D.4 Results from optimised models 225
D.5 Results from optimised models 226
D.6 Results from optimised models 227
D.7 Results from optimised models 228
D.8 Results from optimised models 229
D.9 Results from optimised models 229
D.10 Results from optimised models 230

E.1 Setup of models tested during optimisation 232
E.2 Setup of models tested during optimisation 233
E.3 Setup of models tested during optimisation 234

E.4 Notes on models tested during optimisation 235
E.5 Notes on models tested during optimisation 236
E.6 Notes on models tested during optimisation 237
E.7 Notes on models tested during optimisation 238
E.8 Results of models tested during optimisation 239
E.9 Results of models tested during optimisation 240
E.10 Results of models tested during optimisation 241

Notation

A Area of region or structural trap, [m^2] 38
$\bar{a}$ Roe's method constant, [-] 146
B Stencil, [-] 145
C_i Overall volume fraction of component i, [-] 52
$C_{k,i}^n$ Overall volume fraction of component i at gridblock k at timestep n, [-] .. 141
$C_{k,i}^{(r)}$ Overall volume fraction of component i at gridblock k at Runge Kutta timestep r, [-] 147
c_{ij} Volume fraction of component i in the jth phase, [-] 52
$c_{ij,3p}$ Volume fraction of component i in the jth phase in the 3-phase region, [-] 181
c_{rm} Constants used for polynomial interpolation in ENO method, [-] 146
C_c Capacity coefficient used under the CSLF method, [-] 38
d_w wth degree divided difference, [-] 145
d_{ij} Dispersion tensor for component i in phase j, [-] 27
E Storage efficiency factor under USDOE methodology, [-] 38
F_i Overall fractional flow of component i, [-] 52
$F_{k+\frac{1}{2},i}^n$ Overall fractional flow of component i at gridblock boundary $k+\frac{1}{2}$ at timestep n, [-] 141
f_j Fractional flow of the jth phase, [-] 29
g Gravitational constant, [ms^{-2}] 47
G function, [-] 174
h_{region} Average thickness of storage unit, [m] 38
h Connected vertical height of CO_2, [m] 111
i Component, [-] 27
j Phase, [-] 27
K Permeability, [m^2] 27
K_v/K_h Relative permeability anisotropy, [-] 45
K_i^1 K-value for partitioning of component, [-] 61
K_i^2 K-value for partitioning of component, [-] 61
k Cell number, [-] 141
k_{rj} Relative permeability of phase j, [-] 27
$k_{rj}^{(2)}$ Relative permeability of phase j in the two-phase region, [-] 138
$k_{rj}^{(3)}$ Relative permeability of phase j in the three-phase region, [-] 138
L Length of the porous medium, [m] 29
$L()$ Linear operator, [-] 147
l Counter, [-] 145

m	Iterative timestep, [-]	174
n	Timestep, [-]	51
n_c	Number of components, [-]	28
n_p	Number of phases, [-]	27
n_k	Number of gridblocks, [-]	142
NG	Net to gross ratio of the regional trap, [-]	38
p	Order of errors, [-]	142
P_{cjq}	Capillary pressure between phase q and phase j, [Pa]	28
P_j	Pressure of phase j, [Pa]	27
q	Phase counter, [-]	28
r	Left shift in ENO algorithm, [-]	145
S_{eff}	Storage efficiency parameter under EU GeoCapacity method, [-]	38
S_j	Saturation of the jth phase, [-]	27
S_{rj}	Residual saturation of the jth phase, [-]	137
$S_{r2(j)}$	Residual saturation of the oleic phase in the presence of phase j, [-]	137
S_{wc}	Connate water saturation, [-]	47
S_{wirr}	Irreducible water saturation, [-]	38
t	Time, [s]	27
t^n	Time at the nth timestep, [s]	51
T	Temperature, [°C]	28
u_t	Combined injection velocity of all phases, [ms^{-1}]	61
u_j	Darcy flow velocity of phase j, [ms^{-1}]	27
V_{CO_2}	Estimated volume of CO_2 storage, [m^3]	38
w	Degree of divided difference, [-]	144
x	Distance in the x direction, [m]	29
x_{ij}	Mole fraction of component i in phase j, [-]	27
z	Vertical distance, [m]	52
η	Space-time parameter, [-]	30
θ	Average reservoir dip, [-]	47
λ_j	Mobility of phase j, [Pa^{-1}s^{-1}]	47
μ_j	Viscosity of phase j, [Pa.s]	27
μ_{ij}	Chemical potential of component i in phase j, [joules/mole]	28
ξ	Dimensionless distance as a fraction of the system length, [Pore volumes]	29
$\Delta\xi$	Spatial discretisation size, [-]	135
ρ_j	Mass density of phase j, [kg/m^3]	27
ρ_{mj}	Molar density of phase j, [moles/m^3]	27
σ_{jq}	Interfacial tension between phase j and phase q, [N/m]	164

τ Dimensionless time in pore volumes injected, [Pore volumes injected] 29
τ_f Time of flight, [-] 51
ϕ Porosity, [-] 27

Chapter 1

Introduction

The overall cost of climate change is estimated to be equivalent to losing 5-20% of global GDP, now and forever (Stern, 2007) - far more damaging than experienced during the recent banking crisis and recession of 2008. This is in contrast to the cost of action to avoid the worst impacts of climate change, by reducing our emissions of greenhouse gases (GHG), which can be limited to 1% of GDP (Stern, 2007).

The largest contributor to GHG emissions is the energy sector, producing 25% of global emissions and 40% of the EU's emissions (IPCC, 2007; EU, 2011). Geological storage of carbon dioxide (CO_2) as part of Carbon Capture and Storage (CCS) has the potential to significantly reduce GHG emissions from the energy sector. The International Energy Agency (IEA) estimates that in future energy production scenarios without CCS, the cost of decarbonising the energy sector would be 70% more than in those with CCS (IEA, 2008). This provides a compelling argument for the geological storage of CO_2 and CCS.

However, challenges exist to the successful establishment of this industry. These include estimating and understanding storage capacity as well as its economic viability. Current regulation also poses the challenge that the monitored behaviour of injected CO_2 in the subsurface conforms with modelled behaviour. In this thesis we consider two areas with direct implication for these issues.

Firstly, we consider the effect of top-surface structure and heterogeneity upon the storage capacity and efficiency of open saline aquifers. Secondly, we undertake investigation into 1D solutions for three-phase flow problems representative of CO_2 storage in depleted oil reservoirs.

1.1 Carbon Capture and Storage

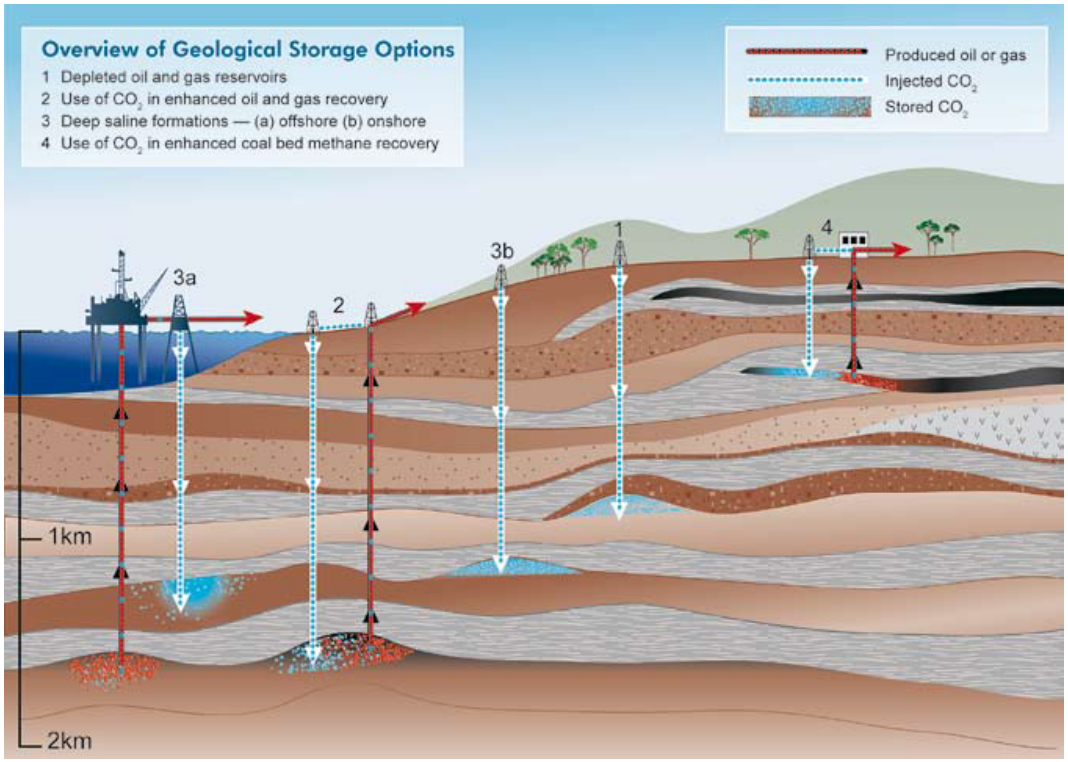


Figure 1.1: An overview of geological storage options. IPCC (2005)

Carbon Capture and Storage (CCS) - the collection of CO_2 from industrial sources and its injection underground - could contribute significantly to the reduction of atmospheric emissions of greenhouse gases (IPCC, 2005). Possible sites for injection include coalbeds, deep saline aquifers, and depleted oil and gas reservoirs as shown in Figure 1.1. Pilot projects to pioneer the storage technology are in progress across the world, as described in Table 1.1, including larger projects at Sleipner (Torp and Gale, 2004), Snohvit (Maldal and Tappel, 2004), Weyburn (Preston et al., 2005) and In Salah (Riddiford et al., 2005). In addition CO_2 Enhanced Oil Recovery (EOR) is a long established technique and dozens of CCS projects are planned including larger scale projects such as Gorgon (Flett et al., 2008) where it is planned that 3.3Mt of CO_2 will be stored each year from 2014.

Governments and industry have shown broad support for CCS but whether it becomes a significant technology to help reduce GHG emissions will ultimately depend on whether we can satisfactorily answer the following simple questions:

- Can we store CO_2 safely over geological time scales?
- Is there enough capacity to store our CO_2?

Table 1.1: Operational CO_2 Storage Projects (MIT, 2011)

Project name	Country	Started	CO_2 sink	Size (Mt/year)
Sleipner	Norway	1996	Saline	1
Weyburn	Canada	2000	EOR	1
In Salah	Algeria	2004	Depleted Gas	1.2
K12-B	Netherlands	2004	Depleted Gas	0.2
Ketzin	Germany	2008	Saline	0.06
Snohvit	Norway	2008	Depleted Gas	0.7
Otway	Australia	2008	Depleted Gas	0.1
Schwarze Pump	Germany	2008	Depleted Gas	0.1
AEP Mountaineer	USA	2009	Saline	0.1
Lacq	France	2010	Depleted Gas	0.06

- Will it be economical to capture and store CO_2?
- Will there be public support for CCS?

Each question is important but within this work we shall restrict ourselves to answering the first two questions - those that concern the physics of CO_2 storage. To answer these we need to understand, describe and predict CO_2 trapping mechanisms and the subsurface flow of CO_2 during and after injection.

There are four 'types' of trapping mechanisms that can help ensure CO_2 remains in the subsurface:

Structural and Stratigraphic Trapping

This is traditionally the primary trapping mechanism. It occurs where an impermeable layer of rock, known as the cap rock overlies the storage site and stops the vertical migration of buoyant CO_2. Oil and gas has been trapped for geological time in hydrocarbon reservoirs by this mechanism. However, the top seal could leak, fracture or be penetrated by wells through which CO_2 could migrate to the surface.

Capillary/Residual Trapping

Capillary trapping - or residual non-wetting phase trapping - seen in Figure 1.2, occurs as the CO_2 phase disconnects into an immobile fraction. It is recognized as a rapid method to immobilize CO_2 with significant trapping occuring over time scales of the order of years to decades in many injection scenarios (Ennis-King and Paterson, 2002; Juanes, 2006; Obi and Blunt, 2006; Taku Ide et al., 2007).

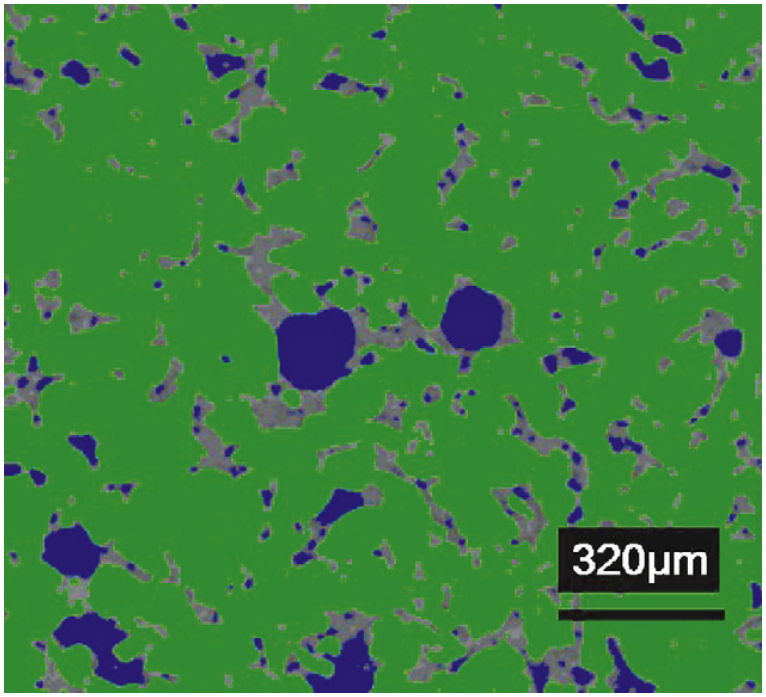


Figure 1.2: A pore-scale image demonstrating residual trapping. Trapped non-wetting phase (blue) in a sandstone (green) surrounded by wetting phase (grey). Figure from Dong (2007).

Solubility Trapping

Solubility trapping occurs when CO_2 dissolves into the reservoir brine. When brine is fully saturated with CO_2 it is denser than unsaturated brine, causing the CO_2-saturated brine to sink. The estimated time for this mechanism to be effective, when we include the effect of convective mixing, is of the order of tens to hundreds of years (Ennis-King and Paterson, 2005).

Mineral Trapping

Carbon dioxide when dissolved in water forms a weak acid which can react with the host rock and precipitate carbonate minerals. This process is called mineral trapping as the CO_2 is trapped in mineral form. This is the slowest but most secure mechanism and immobilizes the CO_2 for geological time.

These mechanisms become effective over different time scales as shown in Figure 1.3, so security progressively improves with the increasing impact of each mechanism in the sequence.

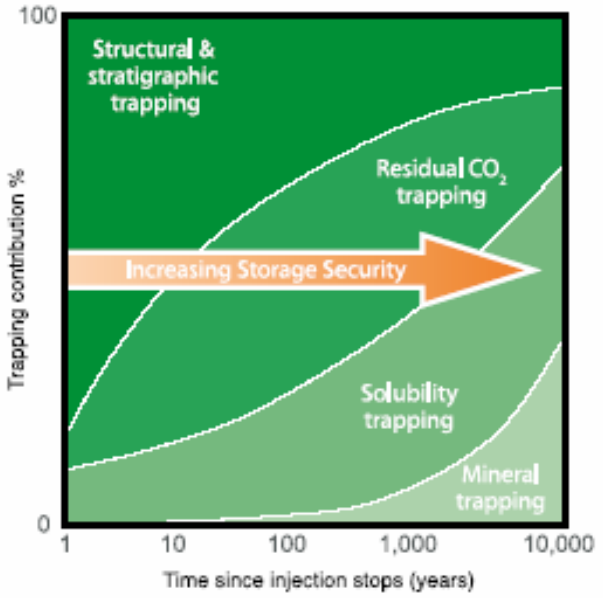


Figure 1.3: Importance of different trapping mechanisms over time (IPCC, 2005).

1.2 Theory of Flow in Porous Media

To represent the mechanisms described in Section 1.1 we use the theory of flow in porous media. This predicts and explains flow by applying a series of physical and chemical laws.

The following equations mathematically represent those physical and chemical laws from Orr (2007). The first is the continuity equation or molar balance (equivalently we could present mass balance):

$$\frac{\partial}{\partial t}\phi\sum_{j=1}^{n_p} x_{ij}\rho_j S_j + \nabla\cdot\sum_{j=1}^{n_p} x_{ij}\rho_j u_j - \nabla\cdot\phi\sum_{j=1}^{n_p} d_{ij}\cdot\nabla\rho_{mj}x_{ij} = 0 \qquad i = 1, n_c \quad (1.1)$$

where d_{ij} is the dispersion tensor for component i in phase j, ρ_{mj} is the molar density of phase j, S_j is the saturation (volume fraction) of phase j, x_{ij} is the mole fraction of component i in phase j, u_j is the Darcy flow velocity of phase j and ϕ is porosity.

Darcy's law gives the phase velocities:

$$u_j = -\frac{Kk_{rj}}{\mu_j}(\nabla P_j + \rho_j g) \quad (1.2)$$

where K is permeability and k_{rj}, μ_j, ρ_j and P_j are the relative permeability, viscosity, mass density and pressure of phase j.

Capillary equilibrium gives:

$$P_q - P_j = P_{cjq} \qquad j = 1, ..., n_p, \quad q = 1, ..., n_p, \quad q \neq j \tag{1.3}$$

where P_{cjq} is capillary pressure between phase j and phase q. Chemical equilibrium gives:

$$\mu_{ij} = \mu_{iq} \qquad j = 1, ..., n_p, \quad q = 1, ..., n_p, \quad q \neq j \tag{1.4}$$

where μ_{ij} is chemical potential of component i in phase j.

In addition, the following auxiliary relations must hold:

$$\sum_{j=1}^{n_p} S_j = 1 \tag{1.5}$$

$$\sum_{i=1}^{n_c} x_{ij} = 1 \qquad j = 1, ..., n_p \tag{1.6}$$

And finally the functions that describe the properties of each phase and its relative permeability must be given by

$$\rho_j = \rho_j(x_{1j}, x_{2j}, ..., x_{nc-1,j}, P_j, T) \tag{1.7}$$

$$\mu_j = \mu_j(x_{1j}, x_{2j}, ..., x_{nc-1,j}, P_j, T) \tag{1.8}$$

$$k_{rj} = k_{rj}(S_1, S_2, ..., S_{np-1}) \tag{1.9}$$

along with appropriate initial and boundary conditions for Equation 1.1. These equations provide enough information to determine the solution to a flow problem that models the effect of convection and dispersion and include phase equilibrium.

1.3 Approaches to Modelling CO_2 Storage

In order to determine the reservoir flow in the subsurface we must produce solutions to the physical and chemical equations shown in Section 1.2. Finding these depends upon further modelling assumptions to simplify the equations. These different modelling assumptions can lead to different styles of model. Notably, three styles of modelling are apparent, each with their own benefits:

1.3.1 1D Analytical Solutions

The first are 1D analytical solutions often using the method of characteristics. These models assume constant porosity and that change in pressure over the displacement length has no effect on phase behaviour but in any particular solution further assumptions are made such as in the Buckley-Leverett solution and Section 4.2. The advantage of this type of solution is that they produce clear, reliable, exact solutions. From this, fundamental physical mechanisms can be clearly described and their effects reliably tested. Mechanisms that may be investigated include advection, multicomponent displacements, miscibility as well as the effect of relative permeability, viscosity and volume change on mixing. Since these analytical solutions are exact they can also act as benchmarks for numerical simulation which may model more complicated systems, which is essential for testing numerical methods. The classic and simplest 1D analytic solution is the Buckley-Leverett solution, which we shall briefly describe:

Buckley-Leverett Solution

The Buckley-Leverett solution (Buckley and Leverett, 1942) is based upon solving a simplified version of Equations 1.1 that assumes constant density, immiscibility of fluid phases, no dispersion and two-phase flow. It is also assumed that the injection saturation and initial saturation in the reservoir are constant. In the solution variables are changed to the dimensionless parameters $\xi = \frac{x}{L}$ and $\tau = \frac{t\sum_j u_j}{\phi L}$ to give

$$\frac{\partial S_j}{\partial \tau} + \frac{\partial f_j}{\partial \xi} = 0 \qquad j = 1, 2 \tag{1.10}$$

where f_j is the fractional flow of phase j defined as

$$f_j = \frac{u_j}{\sum_j u_j} \tag{1.11}$$

The equation for the first phase $j = 1$ can be written

$$\frac{\partial S_1}{\partial \tau} + \frac{df_1}{dS_1}\frac{\partial S_1}{\partial \xi} = 0 \tag{1.12}$$

and to solve this a space-time parameter η is considered with which S_1 is constant with respect to, so that $\frac{\partial S_1}{\partial \eta} = 0$. Then by comparing terms in Equation 1.12 with the definition 1.13

$$\frac{\partial S_1}{\partial \tau}\frac{d\tau}{d\eta} + \frac{\partial S_1}{\partial \xi}\frac{d\xi}{d\eta} \equiv \frac{\partial S_1(\xi, \tau)}{\partial \eta} = 0 \tag{1.13}$$

and rearranging the outcomes it is found that S_1 is constant in (η, τ) space when

$$\frac{\partial \xi}{\partial \tau} = \frac{df_1}{dS_1} \tag{1.14}$$

Therefore in the solution to Equation 1.12 S_1 is constant on lines given by $\xi = \frac{df_1}{dS_1}\tau + \xi_0$. Based upon this we can almost produce the final solution at $\tau = 1$ based upon

$$\xi(S_1, \tau = 1) = \frac{df_1}{dS_1}(S_1) \tag{1.15}$$

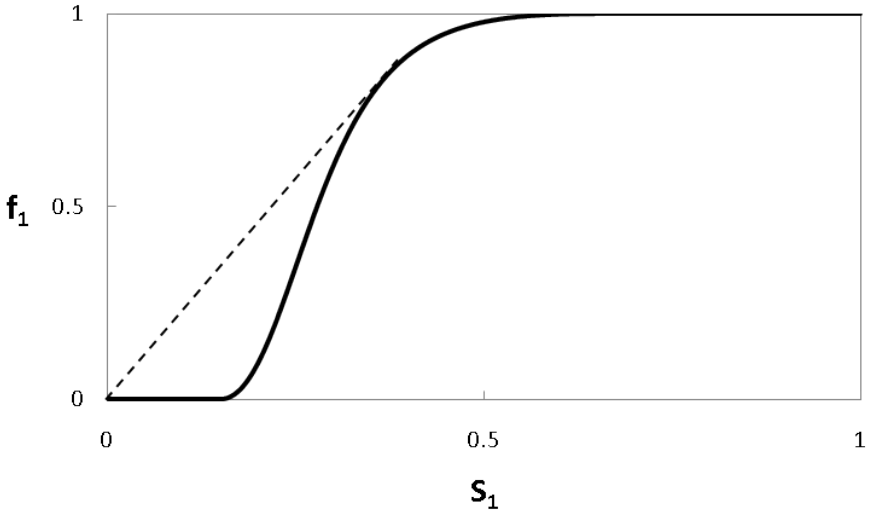


Figure 1.4: Fractional flow f_1 against saturation S_1.

However by considering the gradient in Figure 1.4 it can be seen that $\frac{df_1}{dS_1}$ is not unique with respect to S_1 and we must satisfy velocity and entropy conditions (Orr, 2007) which requires that the characteristic velocity of saturations is monotonically decreasing from downstream to upstream compositions. Using the initial condition of $S_1(\xi = 0) = 1$ and $S_1(\xi > 0) = 0$ this leads to the use of the dotted line in Figure 1.4 as the characteristic

velocity for the region of S_1 where the monotonicity condition is not satisfied by $\frac{df_1}{dS_1}$. Then using equation 1.15 we can plot saturation against distance to reach the classic Buckley-Leverett solution shown in Figure 1.5.

1D analytical solutions can also be found for more complex systems as described in Section 2.3.2. Many of these processes cannot be captured analytically in 2D and 3D. Therefore these solutions provide a good test for numerical solutions which can be checked to ensure that they correctly and accurately capture flow solutions. Once benchmarked against analytical solutions it is possible to model solutions that rely on the same physics but may be too complex to solve analytically. These analytic solutions can also be useful for testing in streamline simulation, which we talk about in Section 2.2.



Figure 1.5: The saturation profile of S_1 in a Buckley-Leverett solution.

1.3.2 2D and 3D Vertical Equilibrium Solutions

The second type of solution is also analytic but concentrates more on capturing the effect of gravity segregation due to the buoyancy of CO_2 rather than displacement profiles due to multiphase flow. Under this setup, solutions to 2D or 3D models are produced. There are two key assumptions in these models. The first is vertical hydrostatic equilibrium as described by Yortsos (1995) and Coats et al. (1971). Vertical equilibrium leads to the Dupuit approximation - that fluid flow is horizontal, with negligible vertical flow - or alternatively in the x - y direction of the frame of reference. The second key assumption is that gravity segregates all of the CO_2 phase above the denser brine phase. Thus these solutions model the development of a plume of less dense CO_2 at the top of the reservoir. These models also commonly assume that there is a sharp interface between the two phases and that the reservoir is homogeneous.

Vertical equilibrium models have been studied and applied for equivalent problems in the petroleum literature before, for example by Dietz (1953), Crane et al. (1963) and

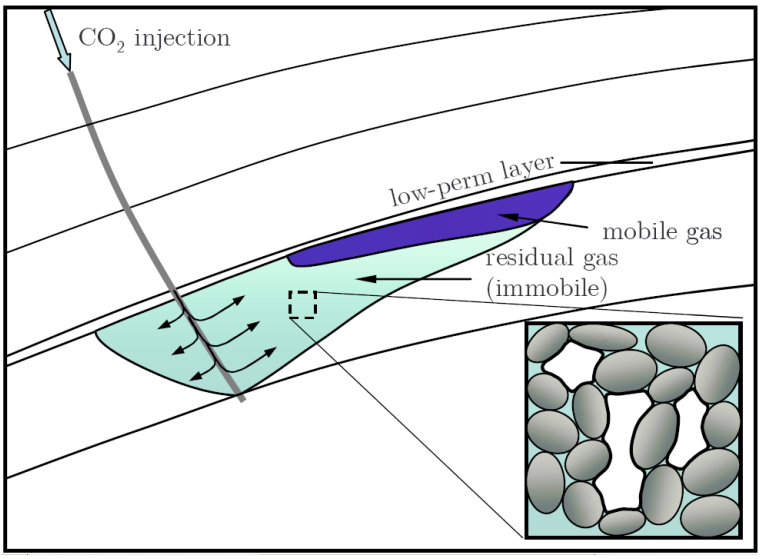


Figure 1.6: Plume of CO_2 during the post-injection period allowing for residual trapping, from Juanes and MacMinn (2008).

Fayers and Muggeridge (1990). Recently these models have been revisited and in some cases extended in the CO_2 storage literature. Lyle et al. (2005) and Nordbotten et al. (2005) produced similarity solutions that demonstrate that the effect of buoyancy upon the CO_2 plume is to cause it to spread with rate proportional to $t^{\frac{1}{2}}$ during injection and after injection proportional to $t^{\frac{1}{4}}$. Vella and Huppert (2006) then looked at spreading on a slope and showed this causes CO_2 to move faster, proportional to $t^{\frac{1}{3}}$ upslope post-injection. Hesse et al. (2008) and Juanes et al. (2010) have also worked on similar solutions capturing the effect of residual trapping upon the smooth interface flow as shown in Figure 1.6. These models utilise the method of characteristics described in Section 1.3.1.

Finally some mathematical solutions have also been produced by Nordbotten et al. (2004) to model possible leakage through an abandoned well.

1.3.3 3D Simulation Models

Finally there are 3D simulation models where all calculations are done computationally on a discretized geological model. The advantage of these models is that they are able to represent many physical features. There are numerous commercial simulation models in use, some of those used in recent CO_2 storage studies include those shown in Table 1.2. We describe in detail the general methodology used in a streamline-based simulator in Section 2.2. This differs from a grid-based simulator in that transport takes place on 1D streamlines as opposed to on a 3D grid.

Although these models are able to include a wide variety of physical features, care

Table 1.2: Common Simulation Models

Simulator	Organisation
Eclipse 100	Schlumberger
Eclipse 300	Schlumberger
Frontsim	Schlumberger
GEM	Computer Modelling Group
STARS	Computer Modelling Group
3DSL	Streamsim Technologies
TOUGH2	Lawrence Berkeley National Laboratory
Nexus	Halliburton

must be taken in their creation and use. The quality of results still depends upon the assumptions made and may also be limited by coarse discretisations. This can particularly be the case if trying to model CO_2 storage on the largest scales, such as 100km $\times$ 100km. This can make the use of simplified models desirable, such as streamline methods, which handle fluid transport in 1D - see Section 2.2 - or vertical equilibrium methods (Nilsen et al., 2011) which simplify models by removing vertical discretization.

1.4 Thesis Overview

In this introduction we have introduced CO_2 storage, the mechanisms it relies upon and the modelling techniques that can be used to capture these and model flow in porous media. These tools can help to answer questions relevant to CO_2 storage. In this thesis we shall work with models and study modelling issues with direct relevance for issues surrounding CO_2 storage.

1.4.1 Aims of Thesis

Using these modelling methods the overall aims of the work of the thesis shall be to:

- improve understanding of storage capacity in saline aquifers so that capacity can be more accurately estimated.
- improve modelling of three-phase flow for application to CO_2 storage in depleted oil reservoirs, through investigating the non-uniqueness of some mathematical solutions and developing high-order numerical methods.

Together these aim to improve understanding of CO_2 storage in two of its main targets, saline aquifers and depleted oil reservoirs.

1.4.2 Layout of Thesis

With these aims we begin in Chapter 2 with a literature review in the areas of storage capacity estimation, one-dimensional (1D) transport solutions and streamline simulation. Streamline simulation provides a clear link between the modelling work of this thesis, with both 1D work and the often 3D work of storage capacity estimation.

In Chapter 3 we consider storage capacity estimation of saline aquifers. An essential constituent of this area is estimating the efficiency with which the pore volume of potential storage sites is used, which can vary significantly depending upon a number of parameters. One effect that has received no real systematic analysis is the effect of top-surface structure upon the storage capacity and efficiency. Therefore we study, analyse and explain its effect in addition to that of heterogeneity, permeability and reservoir dip. This provides understanding of some of the key factors affecting the efficiency with which open saline aquifers can store CO_2.

In Chapters 4 and 5 we consider 1D solutions for three-phase flow problems representative of CO_2 storage in depleted oil reservoirs. In times when the European carbon price is low, storage in depleted oil reservoirs may be required to make early projects

commercially viable. Since regulation requires conformity of actual with modelled behaviour we investigate the issue of uniqueness of solutions to three-phase advective flow models. In Chapter 4 use of the Essentially Non-Oscillatory (ENO) numerical method is considered to help identify the physical solution to a 1D three-phase, three-component transport problem. This results in a new benchmark solution. In Chapter 5 we present both an explicit scheme and an operator splitting scheme to solve the problem in the presence of capillary pressure. Capillary pressure is used to demonstrate the divergence of solutions to the three-phase problem. Divergent solutions are found when including different wettability capillary pressures.

Finally in Chapter 6 the conclusions of the work are summarised and suggestions made for future work.

Chapter 2

Literature Review

We now review the literature that provides background understanding and motivation for the work of Chapters 3-5. This covers a variety of areas that have application to CO_2 storage. In Section 2.1 we survey the literature of CO_2 storage capacity estimation of saline aquifers which provides motivation for considering the effect of top-surface structure and heterogeneity upon storage capacity. In Section 2.2 we then review literature on streamline simulation, which although not used in our final results has been actively studied and provides a logical link to work on 1D solutions. In Section 2.3 we review work on 1D solutions and capillary models to motivate Chapters 4 and 5. This includes a review of three-phase literature which has application to CO_2 storage in depleted oil reservoirs.

2.1 Storage Capacity Estimation

The estimation of CO_2 storage capacity in potential storage sites is undertaken on a variety of scales from field and basin scale, to regional and national scale in order to assess the geological and economic viability of CO_2 storage. This provides a guide to policy and technical direction.

Calculating storage capacity on these large scales is challenging as significant numbers of potential storage sites, each with different characteristics, require storage appraisal. Thorough appraisal of each of these unique sites using reservoir simulation is time-consuming. So at the largest scales a fast method is needed to appraise their capacity, so that by replicating the method the capacity of large numbers of storage sites can be estimated.

2.1.1 Volumetric Storage Capacity Estimation for Aquifers

In recent years a simple type of volumetric equation, of which there are variations (CSLF, 2008; USDOE, 2010; Vangkilde-Pedersen et al., 2009, see), has been used across a wide range of national capacity studies to form the framework for capacity estimation in

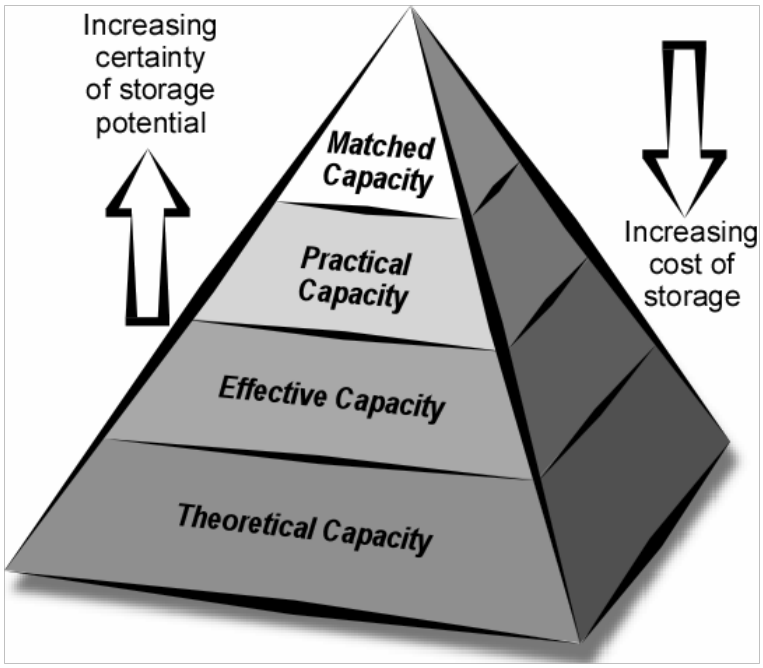


Figure 2.1: Techno-Economic Resource-Reserve pyramid for CO_2 storage capacity in geological media within a geographic region. 1) Theoretical Storage Capacity assumes that the system's entire capacity to store CO_2 in pore space, or dissolved at maximum saturation in formation fluids is accessible and utilized. 2) Effective Storage Capacity is obtained by considering the part of the pore space that can be physically accessed and which meets a range of geological and engineering criteria. 3) Practical Storage Capacity is obtained by considering technical, legal and regulatory, infrastructural and general economic barriers. 4) Matched Storage Capacity is obtained by detailed matching of large stationary CO_2 sources with geological storage sites that are adequate in terms of capacity, injectivity and supply rate. Figure from CSLF (2008)

aquifers. In particular this type of equation is used to estimate the 'Effective Storage Capacity' as defined by Bachu et al. (2007) and shown in Figure 2.1. This represents the capacity of potential storage sites to store CO_2 when a range of geological and engineering effects are taken into account. Such effects may include the quality of the reservoir and seal, pressure regimes and size of the pore volume of the reservoir or trap. However, the effective capacity does not consider all technical, legal, regulatory and general economical barriers to CO_2 storage.

Volumetric Estimation Methods

There are three main variations of this form of volumetric equation (2.1-2.3), each evaluating how much of the pore volume can be occupied by CO_2. These are also sometimes multiplied by ρ_{CO_2}, the average density of CO_2 at reservoir conditions, to give the total mass of CO_2 that can be stored.

Firstly, Vangkilde-Pedersen et al. (2009) present the equation used in the EU GeoCapacity project for calculating capacity in saline aquifers.

$$V_{CO_2} = S_{eff}(NG)Ah_{region}\phi \tag{2.1}$$

A and h_{region} are the regional or trap area and average formation thickness, respectively, ϕ is average porosity, NG is the net to gross ratio of the regional trap and S_{eff} is the EU GeoCapacity 'storage efficiency factor'.

The U.S. Department of Energy (USDOE) present their methodology (USDOE, 2010) for calculating CO_2 storage capacity:

$$V_{CO_2} = EAh_{region}\phi \tag{2.2}$$

E is the USDOE 'storage efficiency factor' of utilisation of the pore volume and all other variables are defined above.

The Carbon Sequestration Leadership Forum (CSLF) presented (CSLF, 2008) a number of formulae to estimate the volume of CO_2 stored through the different mechanisms of structural, residual, solubility and mineral trapping. At the national scale and for estimating effective capacity the structural trapping equation is to be used:

$$V_{CO_2} = C_c(1 - S_{wirr})A_{struc}h_{struc}\phi \tag{2.3}$$

A_{struc} and h_{struc} are the structural trap area and average structural trap thickness, respectively, S_{wirr} is average irreducible water saturation and C_c is the 'capacity coefficient'. The capacity coefficient is meant to take into account heterogeneity, CO_2 buoyancy and sweep efficiency. The CSLF methodology also proposes a range for the CO_2 density to be used for calculating total mass. This range is between the density of CO_2 at the initial formation pressure and the maximum allowable formation pressure, since the formation pressure is not known until injection finishes. A key difference between this and the other equations is the CSLF method is defined for estimating storage capacity within structural closures. Bachu et al. (2007) define hydrodynamic trapping as a combination of all the storage mechanisms occurring while a plume of injected CO_2 migrates within an unconfined aquifer. CO_2 stored through this hydrodynamic trapping definition may best compare to the CO_2 evaluated through the USDOE (2010) and EU GeoCapacity (Vangkilde-Pedersen et al., 2009) methodologies.

Each of the equations 2.1-2.3 represent approximately the same approach with a parameter that measures the efficiency of pore volume utilisation within a storage unit. The differences are that the CSLF method takes account of the irreducible water saturation

explicitly in a separate parameter as does the EU GeoCapacity method with the net to gross ratio. Further the CSLF method is meant for estimating storage in structural closures. Apart from this final difference, estimates using the different methods that carefully account for the different storage efficiency definitions and use of net-to-gross can produce the same numbers.

These equations provide a framework for capacity estimation. It is either possible to use the equations with fixed storage efficiency parameter values, or if further analysis suggests, vary these values for different regions, basins or storage units. I is also possible to account for uncertainty in the parameters by a Monte Carlo simulation. In the next section we look at what values of these storage efficiency parameters have been applied in previous studies where one value was applied universally to all open aquifers.

Volumetric Storage Capacity Estimation Projects and Studies

Over the past 10 years there have been numerous capacity studies at the national scale using different estimation methodologies, with varying clarity over the methodology used to reach these. A number of studies applied the above equations with fixed efficiency parameters:

Vangkilde-Pedersen et al. (2009) presented the EU GeoCapacity preliminary estimate for European CO_2 storage capacity in all open and closed aquifers as 325Gt. Within this work a number of countries produced estimates using the EU GeoCapacity formula. To determine the storage efficiency factor of the equation they chose to distinguish between storage capacity estimates for regional aquifers and estimates for individual structures and stratigraphic traps. For regional open aquifers they suggest use of a uniform storage efficiency factor of 2% based upon the work of USDOE. For individual structural or stratigraphic traps they suggest values from 3% to 40% for semi-closed low quality and open high quality reservoirs, respectively. Within this study Radoslaw et al. (2009) calculated the CO_2 storage capacity for a mixture of open aquifers, geological structures and hydrocarbon fields in Poland. They calculate Poland's total aquifer capacity is 78 Gt, selected structures 3.5Gt and hydrocarbon fields 0.8Gt. The constant storage efficiency factor of 2% was used in the regional aquifers and 20% in the structural traps.

Lewis et al. (2009) presented an application of the CSLF methodology to estimate storage capacity in onshore and offshore Ireland. Under this methodology they estimate theoretical, effective or practical storage capacities based upon data available. Keeping consistency with the CSLF methodology they only estimate the capacity of structures within the reservoirs. For the aquifers where sufficient data were available they calculated the capacity in structures as 3.5Gt using the CSLF method with $C_c(1-S_{wirr}) = 0.4$. This figure was based upon a numerical simulation filling a structure within a closed reservoir.

Ogawa et al. (2011) presented work on the Japanese national CO_2 storage capacity assessment. The assessment was split into two missions, with the first estimating an effective CO_2 storage capacity for the country. In this the saline aquifers were first classified into two categories for storage capacity assessment in terms of the type of geological structure present. Aquifers or hydrocarbon fields with structural traps were found to have 30Gt storage capacity and aquifers without geological structural closure 116Gt, providing a total storage capacity of 146Gt in Japan. They calculate the CO_2 capacity by mass using a formula broadly similar to those presented above with parameters to account for heterogeneity and CO_2 saturation. For the open units without structural traps their storage efficiency factor under the USDOE method was in the range 0.025-0.05 dependent upon the sand/clay ratio present within a reservoir. Under the GeoCapacity formula, which includes a net/gross ratio, this is equivalent to a storage efficiency factor S_{eff} of 0.125 with net to gross values from 0.2 to 0.4. For the structural closures the equivalent storage efficiency factor under the GeoCapacity formula was 0.25. In the second stage aquifers located closer to existing emissions sources are to be investigated more closely and uncertainty in parameters used in the capacity estimation methodology is to be estimated.

Bradshaw et al. (2011) evaluated the effective storage capacity in thirty six basins including aquifers, oil and gas fields and coal seams in Queensland, Australia. These came from the results of the Queensland CO_2 Geological Storage Atlas. Under their methodology they introduced a point system to rank the suitability of sites in addition to calculating storage capacities of a mixture of open and closed units. The factors taken into account in measuring suitability were bulk seal effectiveness, faults through seal, porosity, permeability and depth at base of seal.

Other studies have run preliminary assessments for national storage capacity, but require further work to produce national capacities such as work on the Indian subcontinent by Holloway et al. (2009). Li et al. (2009) and Dahowski et al. (2009) both present work on Chinese theoretical capacity estimation based on a volumetric formula $V_{CO_2} = sAh\phi$ to calculate the capacity of each basin, where s is the solubility of CO_2 in deep saline formations. Using this calculation and summing together all of the aquifers they found 3066Gt of storage, representing over 99% of China's total potential capacity, however since this represents a theoretical estimate of capacity in the capacity scale of Bachu et al. (2007) we would expect the effective capacity estimate to be lower.

In the UK Holloway (2009) reviews CO_2 storage capacity estimates up to 2008 for oil and gas fields. The total CO_2 storage capacity in UK oil fields, as estimated by the old Department for Trade and Industry, is approximated to be 1.2Gt. These estimates are considered to fit into the matched capacity in the capacity scale of Bachu et al. (2007)

due to the level of technical detail from industry put into these. The total CO_2 storage capacity of the southern North Sea gas fields is estimated as 3.9Gt CO_2 and gas fields in the East Irish Sea Basin 1Gt CO_2. Studies into the capacity of saline aquifers in the southern North Sea basin indicate several GT CO_2 storage capacities; however it was felt that none of these studies take into account all the major factors and that aquifers needed to be revisited.

The methods and studies presented so far provide important data on the pore volume available for storage and often provide information on the safety and security of seals. There are however some clear weaknesses. First, they do not take account of how the dynamics of flow affect storage efficiency at different sites, which can significantly affect storage estimation as is seen in the next section. The storage efficiencies that are used are often only taken from the literature where the cases studied may not necessarily provide suitable storage efficiencies. Finally, within the literature presented so far, there has been no accounting for uncertainty in parameters as we may expect when estimating STOIPP in the oil industry.

2.1.2 Dynamic Storage Capacity Estimation Projects and Studies for Open Aquifers

All the estimates in the last section assume universal storage efficiency and do not take into account the dynamics of CO_2 flow. In reality though, the dynamic multiphase flow and build-up of pressure within a storage unit also influences the storage efficiency. A number of projects and studies have developed methodologies that try to more explicitly account for the dynamics of flow within open storage units. Within these the storage efficiency parameters defined in Equations 2.1-2.3 are usually still used or calculated but are not always fixed and can be given different values depending upon the each basin's characteristics.

Analytical Models

A potentially useful approach for fast calculation of storage efficiencies for large numbers of storage sites are analytical models of CO_2 flow.

Szulczewski and Juanes (2009) and Juanes et al. (2010) present an analytical approach for calculating CO_2 storage capacity in open aquifers at the basin scale. The model uses simplifying assumptions to take account of dynamic phenomena such as gravity override and residual trapping in open aquifers that have a horizontal top-surface without structure. The outcome is a simple equation to calculate storage capacity or the storage

efficiency factor under the US-DOE definition using constant values for mobility, reservoir volume, CO_2 density, and water and CO_2 residual saturations. In an example basin they find storage efficiency factors from 0.8% to 1.6% depending upon the amount of residual trapping. These factors are calculated at the time when all CO_2 is residually trapped. This work has been extended in MacMinn et al. (2010) to account for dip analytically, although rather than a single form a set of closed forms and approximations are now provided. Further MacMinn et al. (2011) account for dissolution and in this case the problem is solved numerically.

A potential weakness of such analytical solutions is their inability to account for restrictions due to pressure build-up. However, the use of other analytic solutions designed to analyse the effect of pressure such as Mathias et al. (2011) can be used to supplement this information. These models often assume a closed system, which under some setups may behave differently to the open systems considered here.

Simulation Models and Studies

Alternatively, simulation models are commonly used to calculate the storage efficiency of units with particular characteristics. These efficiencies are then generally used in some way to characterise the storage efficiency of other unmodelled storage units. Three key studies (Gammer et al., 2011; Gorecki et al., 2009; Kopp et al., 2009a) have considered the effect of various parameters upon storage efficiency, however the methods of Gorecki et al. (2009) and Kopp et al. (2009a) may be best suited to estimating efficiencies within structural closures with only Gammer et al. (2011) suited to dipping open aquifers. We now consider these as well as Van der Meer and Yavuz (2009) and Goodman et al. (2011).

Van der Meer and Yavuz (2009) estimated the capacity in the Dutch subsurface using a mixture of fixed parameter analyses and a more dynamic approach. First they use the EU GeoCapacity formula with the 2% storage efficiency factor, finding a total capacity of 438Mt, although they apply this to the volume of structures rather than full open volumes. They then take into account the effect of limited injectivity into these formations after which the capacity is found to be 104Mt. The injectivity analysis takes into account the homogeneous porosity and permeability and thickness of 5 large zones that make up the total capacity. In their analysis they represent zones by connected aquifer portions and within these zones consider the number of traps and their spill points.

Kopp et al. (2009a) proposed using the Doughty et al. (2001) framework in their model, which under the CSLF capacity equation constructs the capacity coefficient C_c from three

factors:

$$C_c = C_{intrinsic} C_{geometric} C_{heterogeneity} \tag{2.4}$$

where $C_{intrinsic}$ is the intrinsic capacity coefficient, which accounts for the 1D displacement efficiency. $C_{geometric}$ is the geometric capacity coefficient, which accounts for partially penetrating well, gravity segregation and dipping aquifers and $C_{heterogeneity}$ is the heterogeneity capacity coefficient.

They ran sensitivities to various parameters to investigate their effect on the capacity coefficients in two open models without structure. The two cases were a 1D idealised gravity-free reservoir and a 3D radially symmetric domain and the parameters investigated were reservoir depth, geothermal gradient, relative permeability, permeability, capillary entry pressure, injection rate. In both the 1D and 3D case injection continued until CO_2 reached a spill-point a set distance from the well. In the 3D case this is set 1km from the well - equivalent to the field scale.

In the 1D case, their median reservoir had $C_{intrinsic} = 0.323$, their lowest value was 0.245 for a shallow reservoir and highest value was 0.505 for a basal relative permeability with low CO_2 residual. Since these efficiencies were calculated during injection it seems this analysis is best suited to injection in a structural trap. This is because post-injection the CO_2 will keep travelling and assuming all trailing CO_2 is at residual then the lowest residual saturation will lead to the furthest travel distance and poorest storage efficiency. Alternatively during injection it is feasible that CO_2 with a low residual saturation could displace water more efficiently.

In the 3D case they find values for $C_{intrinsic}$ ranging from 0.215 to 0.487 for the same sensitivities as the 1D test and values of $C_{geometric}$ ranging from 0.198 to 0.633 for the slow rate and the low permeability case respectively. In conclusion they find that deep cold and/or low permeability reservoirs are more favourable for efficient utilisation of the available storage volume. Their results provide CSLF type capacity coefficients in the range 7.1% - 18%. Their study did not include heterogeneity, structure, dip, dissolution of CO_2 into brine or the effects of relative permeability hysteresis. They comment that their horizontal cap and one injection well and lack of dissolution may lead to conservative results but that lacking heterogeneity may lead to optimistic results.

It is worth noting that the approach of Equation 2.4 is similar to one approach for estimating the recovery factor in the oil industry. For example, (Smalley et al., 2007, p4) produce a similar equation where the same effects are measured for water injected into oil, rather than CO_2 into brine. The main difference is that the time-scale at which the efficiency matters is different. Recovery factor is determined during or at the end of recovery, whereas storage efficiency factor is often calculated when CO_2 is stabilising, perhaps hundreds of thousands of years after injection.

Goodman et al. (2011) present a description of the USDOE methodology for estimating CO_2 storage capacity, which expands the USDOE definition of storage efficiency given in equation 2.2. In their calculation of the storage efficiency factor E for saline aquifers they propose the formula

$$E = E_{An/At} E_{hn/hg} E_{\phi e/\phi_{tot}} E_A E_L E_g E_d \tag{2.5}$$

where the net-to-total area ratio $E_{An/At}$ is the fraction of the total basin or region area that is suitable for CO_2 storage. The net-to-gross thickness $E_{hn/hg}$ ratio is the fraction of the geologic unit that meets their minimum porosity and permeability requirements for injection. The effective-to-total porosity $E_{\phi e/\phi_{tot}}$ ratio is the fraction of total interconnected porosity. The areal displacement efficiency E_A is the fraction of planar area surrounding the injection well that CO_2 can contact. The vertical displacement efficiency E_L is the fraction of vertical cross section that can be contacted by the CO_2 plume from a single well. The gravity displacement E_g efficiency is the fraction of net thickness that is contacted by CO_2 as a result of CO_2 buoyancy. The microscopic displacement efficiency E_d is the fraction of the CO_2 contacted, water-filled pore-volume that can be replaced by CO_2.

In their calculations Goodman et al. (2011) treat systems as open at the boundaries and mention that closed systems could in theory have their pressure remediated. Structural and hydrodynamic trapping are the focus of their methodology for estimating aquifer capacity at the basin scale, although it is not clear at what timescale the parameters are estimated. Within their analysis they do not take into account injection rate or pressure, the number of wells drilled, type of well and other economic and regulatory considerations. They use Monte Carlo simulation to account for uncertainty in a variety of parameters and find the 10th to 90th percentile of storage efficiency factors are 0.4% and 5.5% respectively when a range of values for each of the different parameters is considered. In particular they produce distributions for each of the above parameters for three geological settings - clastics, dolomite and limestone.

Gorecki et al. (2009) who present work from IEAGHG (2009) set out to use both numerical simulations and available field-data to build upon the storage coefficients built by USDOE. For basin-scale open aquifers, efficiencies were evaluated and presented with the storage efficiency factor E and the volumetric and microscopic displacement efficiencies from the USDOE work, where the volumetric efficiency is the product of the areal, vertical and gravity displacement efficiency defined by Goodman et al. (2011).

They produced a homogeneous base case model which had permeability 230mD, salinities of 53,000 ppm, pressures of 23.9MPa, depths of 2338m, temperatures of 75°C, thickness of 26m, K_v/K_h =0.1 and a halfdome structure. To determine which key parameters most strongly affect the storage efficiency factor they ran sensitivities to structure, depth, temperature, permeability anisotropy (K_v/K_h), relative permeability, and injection rate in a homogeneous model. The structures compared included domes, anticlines and flat models. In all sensitivity cases they injected 0.91Mt for 1 year so that all cases obeyed a bottom-hole pressure constraint. The storage coefficient was then calculated at the end of injection using a minimal volume block enclosing the free phase CO_2 saturation plume to measure the total pore volume.

In general, tightly closed structures, increased depth and lower temperatures, low ratios of vertical-to-horizontal permeability, and high injection rates all increased the storage efficiency. The type of top-surface structure had the strongest effect, promoting higher volumetric and macroscopic displacement efficiency and storage efficiencies between rising from 0.15 and 0.25 in the most curved formations. Variation of rate, depth and permeability anisotropy (K_v/K_h) and temperature lead to storage efficiency sensitivity of 0.07, 0.06, 0.05 and 0.03 respectively, while relative permeability had a smaller effect. As in other studies we note that calculating storage efficiency at the end of injection is best suited to the structurally secure models, and may give high values to basins without significant structure.

They also studied 195 heterogeneous models using three lithologies, five structural settings and ten depositional environments. Each lithology was assigned specific parameter distributions for K_v/K_h, relative permeability, porosity and permeability and the injection rate for all cases was reduced to 0.18Mt/yr. Based upon this they found that that lithology had an effect on storage coefficient with P90/P50/P10 ranges at the formation scale of 1.86/2.70/6.00, 2.58/3.26/5.54 and 1.41/2.04/3.27 percent for clastics, dolomites and limestone respectively.

Finally they demonstrated the effect of boundary conditions on the storage efficiency. Comparing a closed system against the open systems they found storage efficiency reduced by a factor of 25 for the closed system, demonstrating it as the key factor and signifying that if boundary conditions are known, a suitable open or closed methodology should be used.

Gammer et al. (2011) present progress from the UK Storage Appraisal Project (UKSAP). Within UKSAP storage units are either classified as closed or open. Within the open units those with potential structural traps that are known to be large and therefore important in terms of overall UK storage capacity are separated out. The remaining

open aquifer area is assumed to have smooth structural topography. Storage efficiency values under the USDOE definition are then calculated at the storage unit scale 1000 years after injection. To estimate these efficiency values, structurally smooth, homogeneous simulation models were constructed and used to investigate the effect of various parameters including horizontal and vertical permeability, porosity, thickness, dip, brine salinity and trapped gas saturation. This work showed that reservoir top-surface dip and permeability had the strongest influences on storage efficiency because they determine the velocity at which CO_2 flows and the injectivity of a model. From this conclusion three storage regimes were identified as shown in Figure 2.2 with different distributions of storage efficiency for each storage regime. These distributions accounted for the variation of storage capacities within each regime. Distributions of storage capacities were then created using a Monte Carlo framework which also accounted for uncertainty in the permeability and average reservoir top-surface dip.

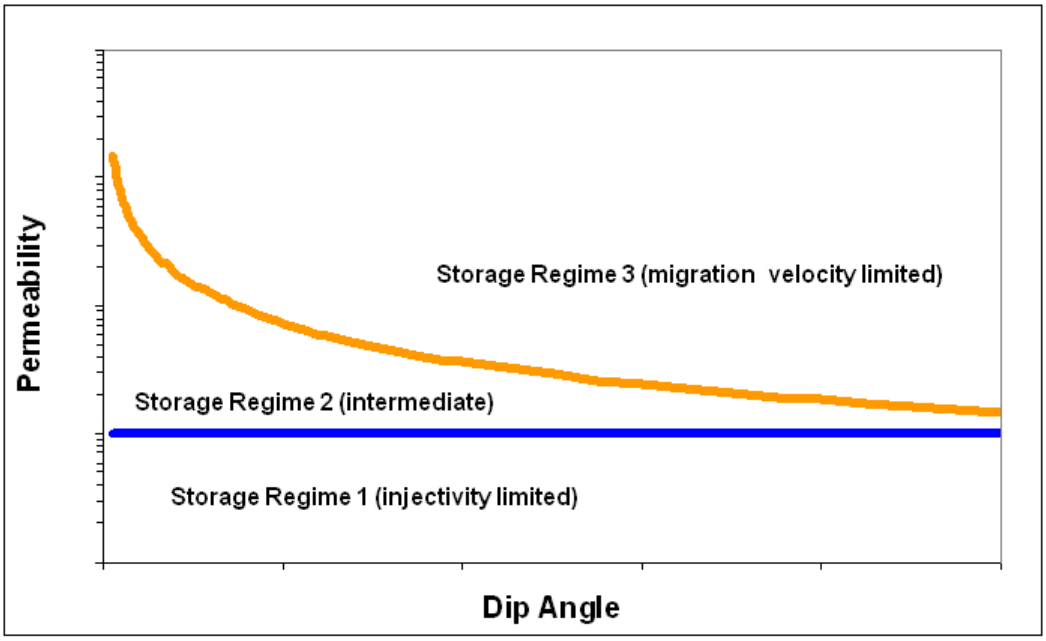


Figure 2.2: The open aquifer storage regimes after Gammer et al. (2011).

The storage regimes are described with the following within UKSAP (2011a):

- The injectivity limited regime (Regime 1 in Figure 2.2) has poor well injectivity but good storage security and is characterised by a low representative permeability.
- The intermediate regime (Regime 2 in Figure 2.2) is characterised by both good CO_2 injectivity and good storage security and therefore typically has higher storage capacities.

- The migration velocity limited regime (Regime 3 in Figure 2.2) has good CO_2 injectivity, but storage capacities are strongly constrained by the tendency of CO_2 to migrate updip due to buoyancy forces. Such stores are characterised by either a high representative permeability or significant mean dip, or both.

The migration velocity limited and intermediate storage regimes are separated by a boundary that estimates the characteristic migration velocity associated with a field. The characteristic migration velocity used to differentiate between the migration velocity limited and intermediate storage regimes was calculated using the analytic estimate as shown in Equation 2.6:

$$v = \frac{K\lambda_{CO_2}\Delta\rho g \sin\theta}{(1 - S_{wc})\phi} \tag{2.6}$$

K is permeability, λ_{CO_2} the mobility of the CO_2-rich gas phase, $\Delta\rho$ the density difference between brine and CO_2, θ the average reservoir dip, ϕ porosity and S_{wc} the connate water saturation. The injectivity limited and intermediate storage regimes 1 and 2 were separated notionally by a 10mD cut-off.

This methodology is attractive because it accounts for changes in storage efficiency due to the two key sensitivities in dipping open aquifers. However, with just three regimes the distributions used for each regime would ideally require a representative sample of fields to produce an accurate distribution of storage efficiencies. In reality a reasonable estimate for the distribution must be made based upon a smaller set of data. This problem is similar to providing a distribution of storage efficiencies for all combinations of permeability and reservoir dip. The improvement achieved by using the three storage regime distributions is that they characterise permeability-dip combinations with similar dominant behaviour.

The storage capacity work of this thesis contributed towards the UK Storage Appraisal Project and we shall consider the storage regimes further in Sections 3.3 and 3.4.

The methods and studies reviewed within this section have shown ways to account for characteristics that affect the dynamics of flow in the estimation of storage efficiency. In two cases they have also accounted for uncertainty by producing probabilistic distributions of storage capacity. The methodologies described have considered analytical or simple numerical models to estimate storage efficiency within a model. However, it offers a limited investigation into the effect of top-surface structure and heterogeneity. Therefore we discuss studies more focused on these issues and less on storage efficiency in the next section.

2.1.3 The Effect of Geological Features upon CO_2 Capacity and the Distribution of CO_2

In addition to this broad set of studies designed to use or improve the storage efficiency estimates there has also been a large amount of simulation work at the field or storage site scales concentrating upon the effect of geological features upon either storage capacity or the distribution of CO_2 that can affect the storage capacity.

Doughty et al. (2001) assessed the capacity of the saline heterogeneous Frio formation in Texas using Equation 2.4 to define a capacity coefficient. They used TOUGH2 to model 20 years injection and 40 years after in an open 1km ×1km×100m aquifer model. The formation heterogeneity was described by transition probability geostatistics and the top-surface structure was smooth and flat. They then considered a homogeneous model and finally a model with no gravity, to examine the effect of heterogeneity and gravity respectively. During injection they allowed fluid to leave the boundaries freely and considered the storage efficiency at 20 years and 60 years. In their models they found heterogeneity enhanced capacity by counteracting gravity. Doughty et al. (2001) acknowledged that the volumes over which capacity coefficients are evaluated and time at which they are evaluated are important.

Obi and Blunt (2006) used a one million cell model of CO_2 storage into an open heterogeneous 5km×9km×200m North Sea aquifer with a smooth top-surface. They found that advective transport of CO_2 was dominated by high-permeability channels and that this led to a storage efficiency around 2% evaluated at 200 years using the smallest box volume that contained the CO_2 plume. Qi et al. (2009) considered a similar heterogeneous setup, but explored the injection of water with CO_2 to enhance residual trapping. They found that storage efficiency could be increased from 3% to 9% by optimizing the injection strategy. This storage efficiency was assessed at the end of 20 years injection, when due to extra residual trapping over 90% of the CO_2 was either residually trapped or dissolved.

Flett et al. (2007) considered the impact of heterogeneity on containment and trapping. They used an open 5km×10km×120m model with a smooth dipping top-surface and notional yet realistic geological heterogeneity and compared against a homogeneous model. Flow was modelled for 1000 years with injection for the first 50. They found that with decreasing net-to-gross ratio vertical flow was progressively inhibited, promoting lateral flow. This resulted in increased tortuosity of the CO_2 pathway and improved reservoir contact and increased dissolution. They also found that the increase in the tortuosity of the CO_2 pathway delayed residual gas trapping. In reaching this result they calculated their total residual trapping by summing only CO_2 within cells where

$k_{rg} < 0.0001$.

Kuuskraa et al. (2009) considered how reservoir architecture could be used to maximise storage capacity. They created an open radial base case model with a flat topography using layering from field data containing multiple shale breaks. To investigate the effects of reservoir architecture and properties on plume dynamics they simulated a number of scenarios. These included the base case shale model, a homogeneous model and a model with 'leaky' 1mD shales each having 4 years injection and modelled for 100 years after. A final scenario with 40 years injection was also modelled. They found that when impermeable layers - which extended across the model - were included the reservoir contact was increased and they expected a plume of less than half the extent of that in the homogeneous model.

Jin et al. (2010) considered two geological models of aquifers with dimensions of the order 10km×10km×300m, one with a simpler tilted geology and the other a more complex structure including an anticline and two deep synclines. They considered open and closed forms of these models and for the first model found USDOE storage efficiency values at the end of injection varying from 0.5% to 1% depending upon whether the system was open or closed at the boundaries. The end of injection was determined in each case by reaching a pressure limit, but they also modelled storage for a further 5000 years. In the second more complex model they found storage efficiencies up to 2.75% at the end of injection. They comment that results of both geological systems show that the migration of CO_2 is strongly influenced by the local topography of the upper surface although there is not an analysis of the effect. Pickup et al. (2011) looked at the second model considered by Jin et al. (2010) comparing its results against the results a simplified smooth top version of the model. They saw that the CO_2 migration was influenced strongly by topography.

Ukaegbu et al. (2009) modelled a 5km×5km×80m heterogeneous model with dip. They comment that the highest amount of dissolved CO_2 is seen in models with the highest permeability anisotropy.

Lengler et al. (2010) investigated the impact of spatial variability of the petrophysical properties using a stochastic approach. Their model concentrated upon a 50m long, 6m deep, 2D section that had a smooth horizontal top-surface and was open at the boundaries. The permeability heterogeneity for a number of models was created geo-statistically with different correlation lengths, anisotropy ratios, upscaling, and variances of the permeability distribution. Each of these sensitivities had 29 different realizations. In the heterogeneous cases CO_2 was seen to arrive at the boundary 50m from the injection well later than in the homogeneous case more often than earlier. This is a similar result to what one may expect in a gravity-dominated oil-field displacement (Araktingi and Orr Jr, 1990). The result of this is that storage capacity is underestimated by the ho-

mogeneous model. It is also observed that generally injectivity decreases with increasing heterogeneity.

Finally, Hayek et al. (2009) provide some analytic insight into vertical flow of CO_2 where high and low permeability layers exist in a model. They solved the 1D vertical Riemann problems and proposed semi-analytical solutions describing the CO_2 evolution and why saturation discontinuities arise under low permeability layers.

Although much of this work does not directly apply its conclusions to considering storage efficiency, the understanding it provides is valuable. The effect of heterogeneity has been considered in a number of ways including its affect of dissolution, residual trapping, reservoir contact, breakthrough time and capacity. A number of studies have concluded that heterogeneity increases reservoir contact and leads to better storage efficiencies by suppressing gravity over-ride, an important finding that we shall consider later. Work considering the presence of top-surface in open aquifers has been sparser. Some studies (Jin et al., 2010; Pickup et al., 2011) have mentioned that topography strongly influences CO_2 migration, and there has been some consideration of various simple structures (Gorecki et al., 2009); however mainly those with total structural closure. In the UKSAP (Gammer et al., 2011) it has been seen that dip, which represents a form of structure can have a significant role upon storage efficiency, allowing fast migration. Elsewhere there seems to be little further evaluation or consideration of the affect of real top-surface structure, which is not entirely structurally closed. In Section 3.1 we propose work to look at this issue, which we then study in the rest of Chapter 3.

2.2 Streamline Simulation and CO_2 Storage

The emergence of streamline-based methods for reservoir simulation as an alternative to traditional grid-based finite difference began in the 1990s with 3D simulation models being published that form the base of current streamline models (Batycky et al., 1997; Peddibhotla et al., 1996, 1997).

2.2.1 Overview/ Original Papers

Batycky et al. (1997) outlined the following streamline algorithm to move a 3D reservoir flow solution forward in time globally by Δt from timestep t^n to $t^{n+1} = t^n + \Delta t$. The simulator was 3D, first-contact miscible, incompressible, allowed for changing well conditions, heterogeneity, mobility effects and gravity, but ignored capillary and dispersion effects. The algorithm is as follows:

1. Solve

$$\sum_{j=1}^{n_p} \nabla \cdot \frac{k_{rj} k}{\mu_j} (\nabla P - \rho_j g) = 0 \tag{2.7}$$

for the pressure using a standard seven-point finite-difference scheme with no-flow boundary conditions over the surface of the domain and specified pressure/rate at the wells. The resulting linear set of equations is solved with a multigrid method.
2. Apply Darcy's law to determine the total velocity at gridblock faces.
3. Trace streamlines from injectors to producers using the tracing method from Pollock (1988) and map saturations from grid to streamlines.
4. Move the saturations forward Δt by solving

$$\frac{\partial S_j}{\partial t} + \frac{\partial f_j}{\partial \tau_f} = 0 \tag{2.8}$$

numerically in one dimension, where $\tau_f = \int_0^d \frac{\phi}{|u_t(\sigma)|} d\sigma$ is the time of flight or time it takes to reach a point d on the streamline based on the total velocity $u_t(\sigma)$ along a streamline. This involves several timesteps within the numerical solver, we explain the method in detail in Section 4.3.
5. Map saturations back to the grid
6. Include a gravity step that traces gravity lines from the top of the domain to the bottom. Then move saturations forward by Δt using

$$\frac{\partial S_j}{\partial t} + \frac{1}{\phi} \frac{\partial G_j}{\partial z} = 0 \tag{2.9}$$

where G_j is the phase velocity resulting from gravity effects.
7. Return to step 1.

Peddibhotla et al. outlined a similar method in Peddibhotla et al. (1996) using analytic solutions along the streamlines which was extended in Peddibhotla et al. (1997) to solve transport numerically using a Total Variation Diminishing (TVD) Scheme. Batycky et al. (1997) noted that there is no difference between using a Single Point Upstream (SPU) scheme and TVD scheme in 2-phase immiscible flow when the front speeds are easily found and a regularly spaced grid is used. However for more complex 1D systems TVD can offer improved accuracy.

2.2.2 Improvements to the Streamline Algorithm

Streamline methods have generated a great deal of interest in the literature due to their capability to simulate reservoir fluid flow with large million-cell geological models. Most areas of the method have been looked at, either in order to improve the physics or numerical methods. These have been looked at using a number of different streamline codes. Extensions and improvements have been proposed to include the following:

Compositional Models

Thiele et al. (1997) - using a Stanford research code - presented the first extension to the streamline approach to allow for a compositional model where components can transfer between phases and are moved along streamlines as opposed to phases. As a result the phase conservation equations solved in step 4 of Section 2.2.1 are replaced by the component conservation equations:

$$\frac{\partial C_i}{\partial t} + \frac{\partial F_i}{\partial \tau_f} = 0 \tag{2.10}$$

where $F_i = \sum_{j=1}^{n_p} c_{ij} f_j$ is the fractional flow of component i and c_{ij} volume fraction of component i in the jth phase. In addition a set of thermodynamic equations for each component are added. Phase saturations, required to calculate f_j, are determined from an equilibrium calculation using the Peng-Robinson equation of state, an accelerated successive substitution algorithm, and a negative flash algorithm. Using streamlines in the compositional case actually becomes even more advantageous relative to traditional grid simulation. This is because strong nonlinearities introduced in compositional displacements by the thermodynamic equilibrium calculations exaggerate problems already encountered in immiscible displacements such as numerical diffusion and upscaling of

absolute and relative permeabilities; and streamlines have an advantage reducing these problems due to their 1D resolution of transport.

Compressibility

Cheng et al. (2006) present the first rigorous formulation for compressible streamline simulation. The key features of the formualtion are (i) introduction and tracing of an effective density along the streamlines to account for fluid expansion/compression, (ii) use of the effective density during mapping from streamlines to grid-blocks and vice-versa, and (iii) a source/sink term in the saturation equation along streamlines to account for compressibility effect. Compressibility was also previously considered by Ingebrigtsen and Bradvedt (1999). Beraldo et al. (2009) used a similar approach to Cheng et al. (2006) but used cumulative volume in the streamline formulation instead of time of flight, to reduce mass balance errors. They found the streamline-simulation could reproduce theresults of a finite-difference simulator even when typical liquid compressibilities are considered and for finely resolved models can be substantially faster.

Three-Phase Flow

Ingebrigtsen and Bradvedt (1999) presented work using three immiscible phases. The first presentation of a fully compositional three phase simulator was by Crane et al. (2000) and later on by Yan et al. (2004).

Capillary Effects

Berenblyum et al. (2003) presented an extension to the original immiscible simulator (Batycky et al., 1997) to allow for capillary effects. They achieved this by modifying the pressure equation to

$$\sum_{j=1}^{n_p} \nabla \cdot \frac{k_{rj}k}{\mu_j}(\nabla P_q - \rho_j g) + \sum_{j \neq q} \nabla \cdot \frac{k_{rj}k}{\mu_j}(\nabla P_{cjq}) = 0 \tag{2.11}$$

which changes the location of streamlines. The phase conservation equation was also changed to

$$\phi \frac{\partial S_j}{\partial t} + u_t \nabla f_j + \nabla \sum_{q \neq j} k f_j \lambda_q \nabla (P_{cjq}) = 0 \tag{2.12}$$

They dealt with the new P_{cjq} term through an extra operator splitting step which was performed back on the grid to allow for the description of 3D crossflow affects. Both the advective and capillary operator splitting schemes were explicit.

Dispersion and Diffusion

Obi and Blunt (2004) - using an Imperial research code - extended the streamline method to model diffusion and dispersion in solute transport problems using an operator splitting technique. Fluid is moved along the streamlines ignoring dispersion, then dispersion is included by solving the dispersive portion of the conservation equation on the grid. The streamline method has the same advantages as particle tracking.

Improved Gravity Segregation

Jessen and Orr (2004) presented an approach for accurate and consistent implementation of gravity effects in compositional streamline simulation. They highlighted that for small timesteps the operator splitting approximation is fairly accurate whereas large timesteps may lead to significant operator splitting errors. The problem is shown to be greater when we move to compositional and three-phase systems because there is a greater likelihood that the density contrast imposed on a fluid particle before and after it is advected may have changed, hence giving a less accurate result. The approach they took to improve the way density contrast is captured was based on the operator splitting technique developed in immiscible models and only introduces a marginal increase in CPU requirement.

Dual Porosity

Di Donato et al. (2003a) and Di Donato and Blunt (2004) - using an Imperial research code - implemented a dual porosity model in a streamline simulator. The reservoir was split into a flowing fraction, representing the fracture network and high permeability matrix, in communication with relatively stagnant regions. Streamlines captured the movement through the flowing fraction while the transfer of fluid from flowing to stagnant regions was modelled as a source/sink term in the 1D transport equation. Thiele et al. (2004) then extended this method to complex geological grids containing both single and dual porosity gridblocks. Finally, Kozlova et al. (2006) extended these two-phase immiscible models to run three-phase compressible flow.

Streamline Tracing

The accuracy of the streamline solution depends on the quality of the pressure solve, the numerical scheme used for transport, the mappings between streamlines and pressure grid and the streamline tracing algorithm. Matringe and Gerritsen (2004) compared streamline patterns against an analytic solution to show tracing errors. They then presented two methods to improve streamline tracing within grid cells, the first was an adaptive-mesh-refinement-inspired method which provides more accurate tracing where required.

The second was a higher-order variation on Pollock's tracing that used a second-order interpolation of the velocity field.

Matringe et al. (2005) concentrated further on the distribution of streamlines. They explained that the classic algorithm provides too high a density of streamlines in some places and too few around composition fronts resulting in unnecessarily high CPU cost for the given accuracy.Therefore they developed a new streamline coverage algorithm which they combine with adaptive mesh refinement along the streamlines.

Finally, Matringe et al. (2006, 2007) proposed further extensions to their work to include high-order streamline tracing on unstructured quadrilateral and triangular grids, based on the use of the stream function.

Streamline Mappings

Mallison et al. (2006) developed improved mappings to and from streamlines and the grid. The mappings used a piecewise linear representation of saturations on the background grid in order to minimize numerical smearing. The strategy for mapping saturations from streamlines to the grid was based on kriging. Gerritsen et al. (2005) included a similar method in a paper that presented a fully adaptive streamline framework.

Parallelisation

Gerritsen et al. (2009) discussed various strategies for parallelizing streamline simulators and present a single-phase shared memory implementation. The work demonstrated that streamlines are easily parallelisable due to the natural decomposition into independent 1D transport problems.

CO_2 Relevant Physics

Qi et al. (2008b) - using an Imperial research code - made a number of physical improvements to the model, with particular relevance to CO_2 storage. They added the Todd and Longstaff (1972) model to represent sub-gridblock viscous fingering which is applied via the fractional flow function along the streamline. They also accounted for two cycles of relative permeability hysteresis by applying two different trapping models. This was applied during the transport step. Finally they extended the model to allow for salt precipitation and consequently changing porosity and permeabilities.

API Tracking and Thermal Recovery

Beraldo et al. (2007) - using an Imperial research code - extended the streamline method to use API tracking. This option, which is usually used in the oil-industry, allows one to

define a three-dimensional oil density distribution at the beginning of the simulation and track its variations due to movement of oil in the reservoir.

Zhu et al. (2009) extended their model to include temperature dependent viscosity and account for thermal expansion.

2.2.3 Advantages and Limitations of Using Streamlines

Streamlines have emerged as a viable alternative to traditional grid-based models. From comparisons in the literature such as mentioned in the following comparison studies we see the following advantages and limitations of streamlines:

Advantages

- Using streamlines eliminates the grid CFL conditions by not solving fluid transport on the grid, allowing global timesteps that are independant of grid constraints, which can reduce the number of pressure solves.
- Fluid transport is now resolved in 1D, reducing its requirement for CPU time.
- Modelling transport along streamlines reduces the amount of numerical diffusion perpendicular to flow.
- Streamlines reduce the effect of grid orientation due to cartesian cells on the transport of fluid although there are still effects on the pressure solve.
- Also reduces numerical fissusion along streamlines if an analytical solution is used.

Disadvantages

- Much of the speed advantage comes in simulation models where the fluids are considered incompressible. In problems where fluids involved are highly compressible or where capillary effects or transverse dispersion are dominant, streamlines are unlikely to offer a significant speed advantage over conventional grid-based simulation.
- In an incompressible fluid formulation, a constant pressure boundary condition will impose grid orientation effects upon the pressure field if a rectangular model boundary is used. This results in fastest flow towards the nearest boundaries to the injection point.
- Mass conservation is lost.

Streamline vs Grid-Based Simulation – Comparison Studies

Numerous authors (Batycky et al., 1997; Crane et al., 2000; Di Donato et al., 2003a,b; Jessen and Orr, 2002, 2004; Maschio and Schiozer, 2002; Peddibhotla et al., 1997; Seto et al., 2007; Thiele et al., 1997; Yan et al., 2004) have compared the efficiency of the streamline algorithm against traditional reservoir simulators such as Eclipse, here we list a few.

- Batycky et al. (1997) found 2-phase streamline models run on between 20000 and 200000 gridblocks to be between 3 and 875 times faster than Eclipse. Typically a speed-up factor of 1 or 2 orders of magnitude was achieved with greater relative benefit for larger models. The outcome of this is that 3DSL does not need to ignore fine-scale heterogeneity. They compared oil production results of 21000 cell models using both a streamline and finite difference simulator. There is some deviation of around 20% after 20 years, but it is not clear how this reduces with an increased cell count.

- Thiele et al. (1997) ran a comparison with compositional displacements and showed that for their case the streamline CPU time scaled near-linearly with the number of gridblocks whereas Eclipse 300 was closer to a cubic power law.

- Crane et al. (2000) ran an extensive comparison on the SPE-9 test case again demonstrating significant CPU savings and also the requirement for far less memory.

- Seto et al. (2007) tested the effect of simplifications made by streamlines regarding gravity and capillary crossflow. In a heterogeneity-dominated system they found these were reasonable approximations when compared against finite difference simulator results.

Although these studies clarify the efficiency of modelling a certain number of cells, it is not clear how accuracy of the two approaches compares for these a set number of cells. In general streamlines will maintain comparable accuracy strongly advection-dominated problems but in more diffuse problems they may not without the addition of extra physics on the grid.

2.2.4 Streamline-based Simulation Studies of CO_2 Storage

Since streamlines are ideally suited to reservoir simulation problems where advection is dominant, simulating CO_2 storage lends itself nicely to this methodology. Many studies have also been carried out with grid based simulators, simulating varying lengths of time, different physical processes and different geology, see e.g. Ennis-King and Paterson

(2005); Kumar et al. (2004); Mo and Akervoll (2005); Nghiem et al. (2004); Oldenburg et al. (2001); Ozah et al. (2005); Pruess et al. (2003); Xu et al. (2003). Here we concentrate on the streamline based simulations.

Kovscek and Wang (2005), Jessen et al. (2005) and Qi et al. (2008a) used streamlines to study issues concerning storage of CO_2 in oil reservoirs and Enhanced Oil Recovery (EOR). Oilfields offer a significant volume of well-described reservoir space and these papers investigated different strategies to maximise the use of this storage capacity. Jessen et al. (2005) concentrated upon co-optimizing oil production and CO_2 storage and after their simulation analysis suggested five approaches. These were

- adjusting the injection gas composition to maximise CO_2 concentration;
- designing well completions to reduce the adverse affects of preferential flow of injected CO_2;
- optimizing water injection to minimise gas cycling and maximise gas storage;
- considering aquifer injection below the oil in order to store CO_2 that would otherwise rapidly break through ;
- considering reservoir repressurisation.

Kovscek and Wang (2005) looked at a similar problem but concentrated more upon gauging uncertainty of reservoir behaviour through using many different equi-probable geological models.

Qi et al. (2008a) ran a streamline simulator accounting for dissolution, dispersion, gravity, rate limited reactions, sub-grid scale viscous fingering and an advanced trapping model that allows for relative permeability hysteresis. The paper also aimed to design an injection strategy for optimal CO_2 storage by comparing simulated injections of different CO_2/water mixtures. This was also followed up with short periods of injection of brine or 'chase brine' in order to residually trap more CO_2. They demonstrated that residual/capillary trapping is effective, was able to render 79% of the injected CO_2 immobile and found optimal injection compositions.

Obi and Blunt (2006) and Qi et al. (2009) looked at simulating storage in saline aquifers using streamlines. Obi and Blunt (2006) studied a deep North Sea aquifer using a one million cell model. They allowed for gravity, dispersion, dissolution and fixed rate precipitation reaction including porosity change. They found low sequestration efficiencies(volume injected/volume reservoir) around 2%. Trapping of residual CO_2 was shown to be the most rapid and effective mechanism of rendering injected gas immobile. The study also demonstrated the need to model accurately flow in a heterogeneous aquifer.

Qi et al. (2009) ran a similar storage model to that in the oilfield case, here finding that injecting with a fractional flow of 75% was optimal for storage. A sensitivity study of the trapping model revealed that the proposed strategy is very sensitive to the estimated residual CO_2 phase saturation and trapping model.

2.3 1D Solutions

In Section 2.2.1 we saw that the original streamline method reduced the transport problem to a one dimensional problem, Equations 2.8 and in the compositional case Equations 2.10 coupled with thermodynamic conditions. We shall concentrate solely on the 1D problem in this section, reviewing work around its broader mathematics and our ability to find its solutions for the case of general flow in porous media. This shall include reviewing a variety of work on three-phase flow, which has application to CO_2 storage in depleted oil reservoirs.

For all 1D work from here on we shall use the component conservation laws 2.13. Rather than conserving saturation as in Equation 1.10, these allow for phase behaviour by conserving composition.

2.3.1 Structure of the 1D Conservation Equations

The system of component conservation equations for a constant-density, non-dispersive system

$$\frac{\partial C_i}{\partial \tau} + \frac{\partial F_i}{\partial \xi} = 0 \qquad i = 1, ..., n_c - 1 \tag{2.13}$$

as can be derived from Equation 1.1 under these assumptions. Here ξ is the dimensionless distance as a fraction of the system length and τ is the dimensionless time in pore volumes injected (PVI) as shown in Section 1.3.1. C_i and F_i are related to S_j and f_j, by

$$C_i = \sum_{j=1}^{n_p} S_j c_{ij} \tag{2.14}$$

and

$$F_i = \sum_{j=1}^{n_p} f_j c_{ij} \tag{2.15}$$

where n_p is the number of phases present and c_{ij} is the volume fraction of component i in the jth phase. The sum of C_i, S_j, F_i and f_j over their indices, along with the equilibrium volume fractions c_{ij} over the j phases are all unity.

$$\sum_{i=1}^{n_c} C_i = \sum_{j=1}^{n_p} S_j = \sum_{i=1}^{n_c} F_i = \sum_{j=1}^{n_p} f_j = \sum_{j=1}^{n_p} c_{ij} = 1 \tag{2.16}$$

The partitioning of components between phases as given by the c_{ij} may either be calculated using an equation of state or assumed to be independent of composition. In

this case the K-values

$$K_i^1 = c_{i1}/c_{i2} \tag{2.17}$$

and

$$K_i^2 = c_{i2}/c_{i3} \tag{2.18}$$

are constant. This assumption substantially simplifies the conservation law, while only causing a small change in the phase behaviour of the system for systems at low enough pressure where there is no critical point or compositions are not too close to the critical point (Orr, 2007, p.55). It is also assumed that the injection rate and initial injection composition are constant.

The form of system of Equations 2.13 has received much attention in the literature due to its occurrence in many fields and its interesting behaviour. The literature investigates when the conservation equations remain hyperbolic and the impacts of loss of hyperbolicity. We shall now review this and note which regime, hyperbolic or other, the conservation equations of particular reservoir flows fall into, as determined by their relative permeabilities.

Hyperbolicity and Loss of Hyperbolicity in the Conservation Equations

Rewriting the conservation equations as

$$\frac{\partial C_i}{\partial \tau} + M_{ji}\frac{\partial C_i}{\partial \xi} = 0 \tag{2.19}$$

where $M_{ij}(\xi, \tau, C)$ is an $n \times n$ Jacobian matrix $\frac{\partial F_j}{\partial C_i}$, are a system of first-order quasilinear partial differential equations. The classification of the system depends on the eigenvalues of the matrix M. If for each ξ, τ and C the $n \times n$ matrix M has real and distinct eigenvalues and there are n linearly independent eigenvectors, the system is said to be strictly hyperbolic. If M has real but non-distinct eigenvalues then the system is non-strictly hyperbolic and if M has any complex eigenvalues then the system is mixed hyperbolic and elliptic.

Historically the system of conservation equations were presumed to be a strictly hyperbolic system. However, Bell et al. (1986) discovered that for some three-phase immiscible systems, the equations were elliptic in regions of composition-space. For example, Figure 2.3 illustrates an elliptic region in composition space, which is equivalent to phase-space if the phases are immiscible. This inspired more investigation into the equation-type, the literature of which we shall now review.

For completeness we reviewed two-phase flow first where theory exists in many cases to prove that there are no elliptic regions and no example of an elliptic region has been

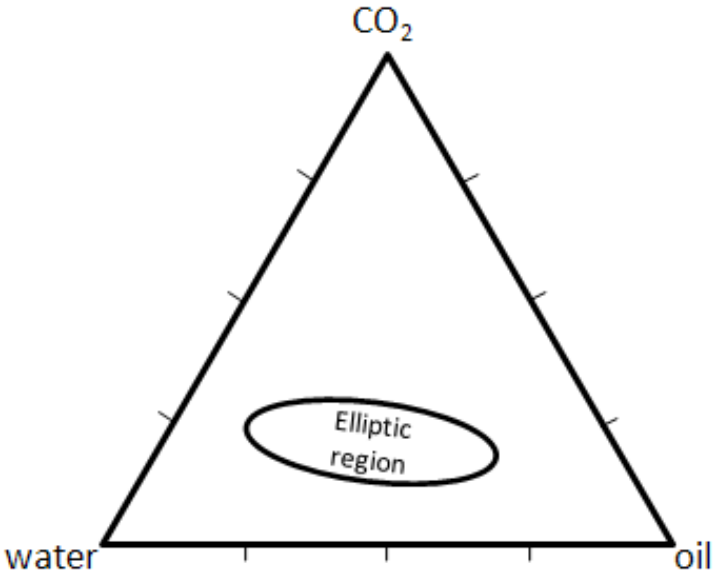


Figure 2.3: The composition space of a three-component system. Composition i tends from 0 to 1 as you move towards the ith corner. In the region highlighted the conservation equations are elliptic.

identified in the remaining cases. For the two-phase two-component problem and the two-phase three-component problem Johns (1992) showed that the eigenvalues of the Jacobian matrix A are always real. In the two-phase three-component case however there may exist non-strictly hyperbolic points where the eigenvalues are real but the same. Johansen et al. (2005) have shown that the structure of the 2-phase 4-component problem can be reduced to two two-phase three-component problems under the thermodynamic modelling assumption of constant K-values and therefore the non-existence of elliptic regions can be extended to this case.

In three-phase systems Bell et al. (1986) and Fayers (1989) found that the conservation equations are not generally strictly hyperbolic. They constructed examples for incompressible flow in the absence of diffusive effects using the Stone relative permeability models, which demonstrated the existence of elliptic regions in phase space.

These were not unique examples, as Shearer and Trangenstein (1989) showed by considering the same physical problem but with various relative permeability systems. They determined conditions for the relative permeability models which would guarantee that at least one point in the saturation triangle, called an umbilic point, has coincident characteristic speeds. Through numerical examples they found that all practically important models such as Stone, Corey, Baker and Pope satisfied these conditions. This showed that many of the important models for three-phase flow exhibit some loss of strict hyperbolicity. They also observed that when gravity was added to the problem, this often made

the elliptic region larger and commented on a separate note that there is no reason to believe the elliptic regions are physical; rather, they believe that they are an unintended consequence of the form of three-phase flow models.

Although the Stone model was found to produce regions with complex eigenvalues, Marchesin and Medeiros (1989) showed that Corey relative permeabilities always leads to real characteristic speeds, but with at least an umbilic point as Shearer and Trangenstein (1989) demonstrated before. Trangenstein (1989) extended the Corey model research to show that when gravity is included in the model the Corey relative permeabilities are the only relative permeabilities that always avoid elliptic regions. The proof in this paper was based upon a result that any relative permeability model that always lead to hyperbolic flow equations must necessarily take all relative permeabilities to be functions of their individual saturations only.

Finally, after the discovery and some investigation of elliptic regions, work was produced on removing them. Holden (1990b) presented a method to modify relative permeability models so that the 'non-removable elliptic regions' that exist in many models can be reduced to an umbilic point to prevent complex wavespeeds. This was achieved by continuously deforming the relative permeability in the three phase region.

Behaviour of Solutions in Non-Hyperbolic Systems

Having considered the hyperbolicity of the conservation equations under the main relative permeability models, the natural question to ask is what happens if a composition enters the non-hyperbolic regions of composition space?

Bell et al.'s original paper (Bell et al., 1986) made the first attempt to investigate this. They performed a linearized analysis to show that in nonhyperbolic regions solutions should grow exponentially. However, they noted that the nonhyperbolic region, if present, will be of limited extent which inherently limits the exponential growth. To examine these linear instability effects they ran numerical simulations with a dissipative numerical method. These experiments indicated that the solutions of Riemann problems remain well behaved in spite of the presence of an elliptic region in composition space that according to the linear analysis should cause instability. The simulated solutions also formed shocks linking compositions inside and outside of the non-hyperbolic region.

Bell et al. (1986) also observed that when initial compositions were outside the elliptic region the Riemann problem solution appeared to stay outside the region. Holden (1990b) later proved that when initial and injection compositions are outside the elliptic region all points in the solution stay outside. As a result producing exact analytic solutions to the Riemann problem with states outside the elliptic region can be treated in a similar way to those that have only umbilic points as their non-hyperbolicities.

Although Bell's simulation showed success and avoidance of elliptic regions, Shearer and Trangenstein (1989) commented that the elliptic regions could have some minor consequences because numerical methods can be inaccurate and could cause saturations to erroneously enter the elliptic region when they are around the edges of the region or when shocks form that cross the region. The impact of this would be particularly felt by numerical methods that require information from the characteristics since they would not be able to cope with the complex eigenvalues. It has also been shown (Azevedo et al., 2002) recently that in a system with capillarity included, the region of linear instability becomes larger than the elliptic region and can therefore be reached.

Bell et al. (1986) and Shearer and Trangenstein (1989) both took the approach of using numerical simulation as, at the time, analytic solutions were not available to analyse this complicated problem. This meant they did not know whether, even in the absence of detectable instability, the well behaved nature of simulation viewed was the correct or physical solution. To further the investigation analytic work was required into how non-hyperbolic regions might affect the mathematical solution, which simulation tends towards, or perhaps whether they affect the physical solution. In Section 2.3.2 we review literature that shows that the nonhyperbolic regions affect the uniqueness of mathematical solutions to the conservation equations. Therefore, even if Bell's simulations were 'well behaved', some undetectable instability or numerical diffusion may have forced a mathematically acceptable but non-physical solution to be simulated. Section 2.3.3 will consider this idea further. First we shall review the literature on analytic solutions that may allow us to consider these ideas.

2.3.2 Analytical Solutions of the Conservation Equations

Thus far we have considered the nature and behaviour of the conservation equations. For the best understanding of the behaviour that these equations model it is often possible to calculate the exact analytic solutions to the 1D problem, which may be viewed as a set of 1D profiles or as a single composition path in composition space. By considering 1D analytic solutions, we also gain understanding of the behaviour of the equivalent 3D problem. It is unlikely that we would gain the same understanding if we were to consider the full 3D problem directly since analytic solutions to such problems rarely exist, so 1D results also offer one of the best insights into the 3D problems. In this section we shall review work on 1D analytic solutions, how issues such as loss of hyperbolicity affect these and how we can use these solutions.

Work in the literature has studied the existence and uniqueness of solutions to these equations coupled with the thermodynamic equations and produced analytic solutions for problems with different numbers of components and phases, which we now review.

Existence and Uniqueness of Two-Phase Analytic Solutions

Work on two-phase solutions to flow in poros media is now very mature. The standard theory for problems with a single conservation law is due to Oleinik (1959), Lax (1957) and Liu (1974). However a nice proof was given later on by Holden and Risebro (2002) which proves the existence and uniqueness of a solution to the Riemann problem for a scalar conservation law.

Two Phase Solutions

Analytic solutions to a large number of two-phase multicomponent problems have been documented. The book by Orr (2007) presents an in depth analysis of solutions to Equations 2.13 for two phase systems with two, three and four components and constant initial and injection compositions. The solutions of the book are presented under the assumption that phase equilibrium is achieved through time and space constant K-values. An extension of the four-component system to include volume change on mixing was provided by Dindoruk et al. (1992) who also produced solutions for five components with constant K-values. Johns (1992) then obtained solutions with variable K-values for five and six-component systems, both for injection of a pure component. Finally a systematic procedure for calculating solutions for multicomponent systems with any number of components in the injection gas was reported by Jessen et al. (2001). In this paper Jessen et al. also allow for more complicated thermodynamics, modelled by an Soave-Redlich-Kwong equation of state.

Existence and Uniqueness of Three Phase Analytic Solutions

Proving the existence and uniqueness of a solution to the three-phase conservation equations is more complicated than for the two-phase case due to the loss of hyperbolicity raised in Section 2.3.1. To consider it, we look first at a paper which considers the existence and uniqueness of solutions to the immiscible three-phase equations. The paper by Juanes and Patzek (2004a) found that if the equations are strictly hyperbolic, then using the standard entropy condition due to Liu (1974) produces a unique solution. However, from Shearer and Trangenstein (1989) we know that realistic three-phase flow models lose strict hyperbolicity. Therefore Juanes and Patsek accompanied this with a paper (Juanes and Patzek, 2004b) which identified necessary conditions that must be satisfied by the relative permeability function so that the system of equations describing three-phase flow is strictly hyperbolic everywhere in the saturation triangle.

Beyond this idealised system, the literature shows that for systems showing loss of hyperbolicity, regions of the composition space are not covered by the classical construc-

tion of Riemann solution which obey the Liu entropy condition (Isaacson et al., 1992). This motivated the need to use a nonclassical form of solution to the equations when they are not strictly hyperbolic across all of state space. This nonclassical solution is known as a transitional wave and may be a rarefaction, shock or both (Isaacson et al., 1990). Azevedo et al. (2009) has demonstrated that analytic solutions for many of the boundary conditions of interest in enhanced oil recovery (EOR) by gas injection exhibit transitional shocks.

It has been shown (Isaacson et al., 1992) that for models with isolated umbilic points the solution for the Riemann problem with a transitional wave is unique. However, in general solutions with a transitional wave are not always unique (Azevedo and Marchesin, 1995; Azevedo et al., 1996) and non-unique solutions are found (Azevedo and Marchesin, 1995, p.3071) To obtain the physically correct solution to Equation 2.13 an additional constraint is required. This constraint is known as the viscous profile entropy condition, as documented by many authors - (Isaacson et al., 1992; Schecter et al., 1996, see). The viscous profile entropy condition states that solutions to the equation

$$C_\tau + F(C)_\xi = \epsilon[D(C)C_\xi]_\xi \tag{2.20}$$

with the dispersive term $D(C)$ will converge to the correct physical solution to Eq. 2.13 in the limit ($\epsilon \to 0$). Determining which is the correct limiting solution is not simple though as the non-unique solutions can often be close together and choosing the correct second-order dispersion tensor is not trivial. We shall review this difficulty in Section 2.3.3 after considering solutions that have attempted to achieve this.

Three-Phase Solutions

The first solutions to the Riemann problem that included transitional waves were solutions for simple analogs of three-phase flow that exhibit umbilic points (usually with quadratic flux functions f). These were presented by a number of authors (Holden, 1990a; Isaacson et al., 1988; Isaacson and Temple, 1986; Schaeffer, 1987; Shearer, 1989; Shearer et al., 1987; Temple, 1982) with the main focus on developing the mathematical theory for the solution of non-strictly hyperbolic Riemann problems. Solutions for more realistic three-phase flow problems that assume Corey type relative permeabilities were presented by Falls and Schulte (1992a,b). Guzman (1995); Guzman and Fayers (1997) presented the general theory for producing analytical solutions to the three-phase immiscible Riemann problem using different classical relative permeability models, with and without gravity. For relative permeability models with elliptic regions the viscous profile entropy condition is needed. Juanes and Patzek (2004a) then presented a catalogue of all possible

solutions to the simplified immiscible problem, describing the waves that may arise and concluding that only nine combinations of rarefactions, shocks and rarefaction shocks are possible. However this was only for the case where relative permeabilities were made strictly hyperbolic.

The compositional problem coupled with thermodynamical equilibrium were dealt with by LaForce (2005). LaForce and Johns (2005a) produced three-phase three-component solutions for more general relative permeability models and used equilibrium phase compositional data and a quadratic approximation to find the phase boundaries for their thermodynamic model. Most recently LaForce et al. made solutions for the three-phase four-component problem firstly with constant K-values (LaForce et al., 2008a,b) and then with a Peng-Robinson Equation of State (LaForce et al., 2010).

2.3.3 Numerical Methods and Proposed Plan to Identify Correct 3-Phase 1D Solutions

We have seen that determining the solution to the 3-phase conservation equations can be difficult when hyperbolicity is lost. Analytic solutions to the purely advective problem can be non-unique and to determine the physically correct solution from these an extra physical constraint must be considered. However finding the zero dispersion limit of the equation requires the use of simulation which introduces a new problem, numerical diffusion. When we are trying to determine the physically correct solution, numerical diffusion and linear instability (Azevedo et al., 2002) in and around the elliptic region may tend us towards the wrong non-unique solution. Potentially we could tend towards the numerical diffusion-limited solution since this still influences the solution when the dispersion tensor is reduced. Work has yet to be done to reduce the numerical diffusion to smaller than the physical dispersion in order to find the analytic solutions.

However, recent work has been done to compare the accuracy of a variety of high-order finite-difference schemes applied to multicomponent problems. Mallison et al. (2005) presented 1D, two-phase multicomponent results using Single Point Upstream Weighting (SPU), Total Variation Diminishing (TVD), third-order Essentially Non-Oscillatory (ENO-3), third order Weighted Essentially Non-Oscillatory (WENO-3) and fifth order Weighted Essentially Non-Oscillatory (WENO-5) methods and compared them to analytical and semi-analytical solutions. Their results suggested a third order, ENO scheme achieves accurate results more efficiently than first-order methods, produces a better treatment of phase behaviour, and is more robust than traditional TVD schemes. The high-order schemes achieved accurate results with much coarser grids than SPU and hence required fewer computationally-expensive flash solves. This time-saving outweighed the

cost due to high-order discretisations. Mallison et al. (2005) also found that the strong non-linear coupling between Equations 2.13, introduced through the phase behaviour, increased the sensitivity of numerical solutions to discretization errors and further aided the relative success of the high order methods. ENO was preferred to WENO as it maintained better accuracy where the solution was weakly hyperbolic.

Valenti et al. (2004) extended the work of Mallison et al. (2005) to include three-phase models. They presented 1D, three-phase, multicomponent results using SPU, TVD and ENO-3 to show that the high order schemes produced much sharper profiles. Valenti only compared the solutions against high resolution simulation results though rather than analytic solutions. Also the paper did not explicitly consider whether the equations they were modelling lose hyperbolicity anywhere in the phase space.

In Chapter 4 we propose to reduce numerical diffusion to smaller than physical diffusion by using the ENO-3 scheme proposed by Mallison et al. (2005) so that we can find three-phase solutions satisfying the viscous profile entropy condition. We propose the dominant second order tensor is the capillary pressure tensor as represented by the last term in Equation 5.1.

2.3.4 Capillary Pressure Models

In Section 2.3.2 we discussed the use of a second order term in three-phase models to help satisfy the viscous profile entropy condition and in Section 2.3.3 proposed the use of capillary pressure as the second order term. To do this we must find a three-phase capillary pressure model to use. We shall briefly review available capillary pressure models.

Within the petroleum literature there has been significant effort to try to provide consistent three-phase relative permeability and capillary pressure models that match experiment and have a physical explanation. Although much progress has been made a comprehensive understanding is still not available.

We are interested in using capillary pressure models that have been developed. Towards this, experimental work to describe three-phase relative permeabilites has been done e.g. Oak et al. (1990); Kalaydjian (1992); Nordtvedt et al. (1997); DiCarlo et al. (2000), sometimes including data for 2-phase capillary pressures (DiCarlo et al., 2000; Nordtvedt et al., 1997) and sometimes data for mixed wet systems (DiCarlo et al., 2000; Oak et al., 1990). In one case there is three-phase capillary pressure data (Kalaydjian, 1992), however covering the full phase space with these experiments is difficult and therefore a number of attempts have been made to combine two-phase data to form empirical three-phase relations for capillary pressure (Aziz and Settari, 1979; Lenhard and Parker, 1988; Sheffield, 1968) and relative permeability e.g. (Baker, 1988; Blunt, 2000; Fayers, 1989; Stone, 1970, 1973). However, hardly any true three-phase capillary models exist

(Holm et al., 2010) and it is not clear that these empirical models are able to produce mixed wet capillary pressure functions. To produce three-phase mixed-wet capillary pressure functions the remaining options are to use network models e.g.Blunt et al. (2002); Mani and Mohanty (1998); Holm et al. (2009), which is a very intensive approach or to use capillary bundle models (Helland and Skjaveland, 2006; van Dijke et al., 2001).

2.4 Summary

A range of literature has been reviewed to motivate the work of this thesis. This includes mathematical and numerical literature that are relevant for modelling CO_2 storage in depleted oil reservoirs and CO_2 storage capacity estimation literature relevant for CO_2 storage in saline aquifers. In particular three topics of interest arise that shall be studied.

A number of methods for estimating storage capacity in saline aquifers have been reviewed. In open aquifer we have seen that permeability and reservoir top-surface dip are key sensitivities. There has also been a number of studies using models with top-surface structure and heterogeneity. However there has been no study of the effect of top-surface structure and heterogeneity upon storage efficiency. Therefore in Chapter 3 this topic shall be considered.

Mathematical literature has shown that models of 1D three-phase flow do not always yield unique mathematical solutions. This may be concerning because current regulation on CO_2 storage requires us to be able to model fluid flow, and three-phase EOR is likely to be involved in many early CO_2 storage projects. Further literature identified that the use of a viscous profile entropy condition is required to identify the unique physical solution to these problems. In previous work where this has been implemented significant numerical diffusion has been present. Therefore in Chapter 4 high-order numerical methods are used reduce numerical diffusion with the aim of ensuring the correct solution is identified. Then in Chapter 5 capillary pressure is included in models to investigate whether non-unique mathematical solutions can be identified.

Chapter 3

The Effect of Top Surface Structure and Heterogeneity upon CO_2 Storage Capacity in Open Aquifers

3.1 Introduction

A large proportion of Europe's potential CO_2 storage capacity is to be found in large open aquifers.In this chapter a detailed analysis of storage capacity in dipping open aquifer models is performed. The implications of our results for large-scale regional storage capacity estimates are then discussed. A thorough review of the literature on storage capacity in open aquifers in Section 2.1 motivate and facilitate this work.

This survey of the literature shows us that influences on the dynamics of storage can affect storage efficiency considerably, with estimates ranging from much less than 1% to over 10% of the available pore volume. These estimates vary dependent upon the reservoir fluid and rock properties, structure and injection design. The dynamics are especially important when assessing the capacity of open as opposed to closed aquifers since in these aquifers the dynamics control when CO_2 reaches a storage boundary, which represents a potential constraint on capacity, whereas in closed aquifers the less dynamically-dependent pressure build-up generally constrains capacity.

A number of the above studies (Gammer et al., 2011; Goodman et al., 2011; Gorecki et al., 2009; Kopp et al., 2009b) have started to account for the differing dynamics of flow in different fields or basins and consequently applied different storage efficiencies for these. In this work we would like to concentrate further on developing an understanding of how the dynamics of flow can affect storage capacity and efficiency in open aquifers.

In particular we shall consider the affect of dynamics upon flow in open aquifers that do not have significant large-scale structural closure like domes or fault sealing traps (herein called dipping open aquifers). Figure 3.1 shows a simple sketch of a dipping open aquifer as opposed to an open aquifer with a large-scale structural closure. Dipping open aquifers

represent a significant proportion of storage capacity in the UK and worldwide (Holloway, 2009; Ogawa et al., 2011). In addition to this, a number of national scale storage capacity estimation studies (Gammer et al., 2011; Ogawa et al., 2011) have found it useful to implement separate capacity estimation methodologies for dipping open aquifers and large-scale open structural closures. Without these separate methodologies a potential difficulty is accounting for the significant difference in storage efficiency between the units with large-scale structural closures, which tend to be significantly more efficient at storing CO_2 but generally have less volume at the regional scale, and dipping open aquifers with possibly lower storage efficiencies but much larger pore volumes. In addition the sensitivity of storage efficiency to certain characteristics in the two cases may be quite different making the design of a universal method difficult. Thus a separate understanding of each is important; our focus will be on dipping open structures.

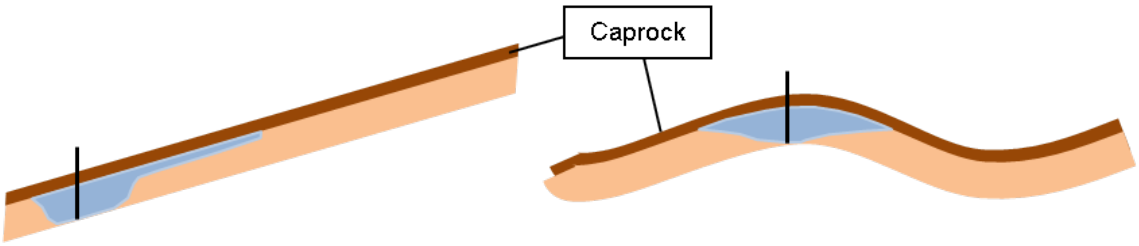


Figure 3.1: Sketch of a dipping open aquifer (left) compared to an open aquifer with a large-scale structural closure (right); it is assumed that the structure has closure in all directions.

Developing an understanding that allows us to produce methodologies to estimate the storage capacity of these dipping open aquifers requires us to understand which mechanisms are important for storage and whether storage efficiency is sensitive to variations in different characteristics. There has been numerous dynamic studies modelling how these dipping open aquifers store CO_2 (Doughty et al., 2001; Flett et al., 2007; Gammer et al., 2011; Goodman et al., 2011; Gorecki et al., 2009; Jin et al., 2010; Juanes et al., 2010; Kopp et al., 2009b; Kuuskraa et al., 2009; Lengler et al., 2010; Obi and Blunt, 2006), however fewer have looked into their sensitivity to parameter changes and of those results have often been more applicable to large-scale structural closures. For example, either a half dome has been assumed as the base case structure (Goodman et al., 2011; Gorecki et al., 2009) or results were assessed during injection thus not considering total migration (Kopp et al., 2009b), an important feature when considering dipping open aquifers. More recently however UKSAP (2011a) has considered sensitivity of dipping open aquifers to various characteristics that influence dynamics producing three storage regimes that summarise storage efficiency based on two key parameters - average dip and

permeability. In addition to this other studies (Flett et al., 2007; Kuuskraa et al., 2009) have considered the sensitivity to heterogeneity.

These sensitivity studies offer important understanding. Of particular interest we see that average dip and permeability - simplified versions of top-surface structure and heterogeneity - are key sensitivities for dipping open aquifers UKSAP (2011a). Within these sensitivity studies, though, the effect of top-surface structure was not considered and the top-surface has been considered smooth. In the rare studies where top-surface structure has been introduced (Jin et al., 2010; Pickup et al., 2011) they have commented that the characteristics of the CO_2 plume can be significantly affected by the topography of the top surface of a reservoir, but without further study or analysis.

Therefore in this work we shall:

- Look at how top-surface structure can affect storage efficiency in a dipping open aquifer in Section 3.4.
- Investigate in Section 3.3.4 whether the storage regimes shown in Figure 2.2 from Gammer et al. (2011) are still good approximations when top-surface structure and heterogeneity are present.
- Consider the effect of heterogeneity upon storage efficiency in a dipping open aquifer in Section 3.4.

To investigate the effect of top-surface structure and heterogeneity in this work we shall:

- Calculate the effective storage capacity as defined by Bradshaw et al. (2007). We shall not consider issues such as lack of data.
- Use the Vangkilde-Pedersen et al. (2009) definition (Equation 2.1) of their 'storage efficiency factor' as our storage efficiency parameter. This is a volume ratio with unit $\frac{\text{reservoir m}^3}{\text{reservoir m}^3}$. We shall however omit the use of 'factor' and refer to the *storage efficiency*.
- Measure CO_2 storage efficiency at 1000 years as opposed to at the end of injection or when CO_2 is all residually trapped. This follows the approach of Gammer et al. (2011).
- Investigate a model at the scale of a potential 'storage unit'. We consider this to be between basin scale $\sim$ 100km $\times$ 100km and field scale $\sim$1km $\times$ 1km. We shall refer to this as the '*storage unit scale*' $\sim$10km $\times$ 10km.

This investigation uncovers some surprising general results. We show that open aquifers of modest permeability can prove to be favourable storage sites with reasonable

storage capacities. These aquifers limit the speed with which the CO_2 migrates while the extensive open pore volume can help dissipate pressure, avoiding pressure problems associated with other types of storage site.

3.2 Modelling Methods

To investigate the effect of structure and heterogeneity a storage unit is modelled using the best available data from a North Sea aquifer.

3.2.1 Geocellular Model of the Base Case Forties Storage Unit

A section of the Forties sandstone member of the Sele Formation was chosen as a suitable dipping open aquifer for our base case geological model. This area of interest was selected for modelling that avoided hydrocarbon fields, significant structural closures, known faulting and communication with overlying formations. The area of interest - shown by the black box overlaying Figure 3.2 - was 21.4km $\times$ 36km and a geo-cellular model of this section of the Forties Sandstone Member was provided by Senergy Ltd. through the UK Storage Appraisal Project. The model was orientated northwest to southeast and spans several blocks in Quadrant 22 of the Central North Sea with an average thickness of 170m.

The grid dimensions of the model provided were 107 $\times$ 180 $\times$ 90 giving a total of 1,733,400 grid cells. The structural framework of the model was based on a seismic interpretation of the top of the Upper Forties shown in Figure 3.3 and well tops from the Andrew Sandstone Unit that lies below the Forties. To capture thin CO_2 tongues occurring towards the top of the storage unit, the vertical resolution is between 0.5m to 1m towards the top of the Forties interval increasing to 3m at the base. This also allowed the intra-reservoir shales to be captured in the geological model provided, thus preserving enough meaningful vertical heterogeneity.

The porosity and permeability models were built upon a simple facies model describing cells as either channel or background (Figure 3.4) that was derived using data from the 10 wells located in the Forties Sandstone member and shown in Figure 3.3. Permeability and porosity distributions for the channel facies were created using published data and local core analysis data and these distributions were used to assign permeability and porosity values within the channel facies. These values were assigned so that the centre of the channels had highest permeability and porosity, decreasing towards the edges. The background shales were modelled with near-zero porosity and permeability. These models of the channels and background created the porosity and permeability models shown in Figures 3.5 and 3.6.

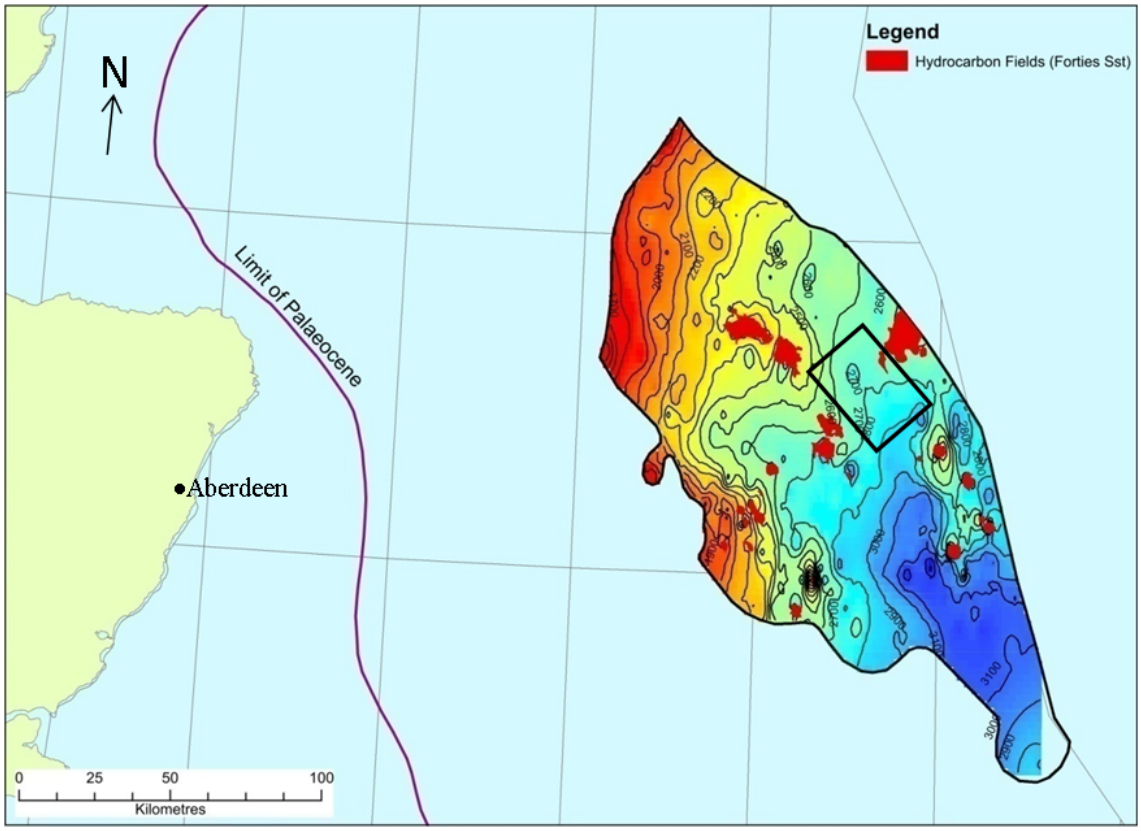


Figure 3.2: Location of the Forties Sandstone member and the Forties geological model. The areal extent of the Forties geological model is identified by a black rectangle. The contours are for depth below sea level in metres.

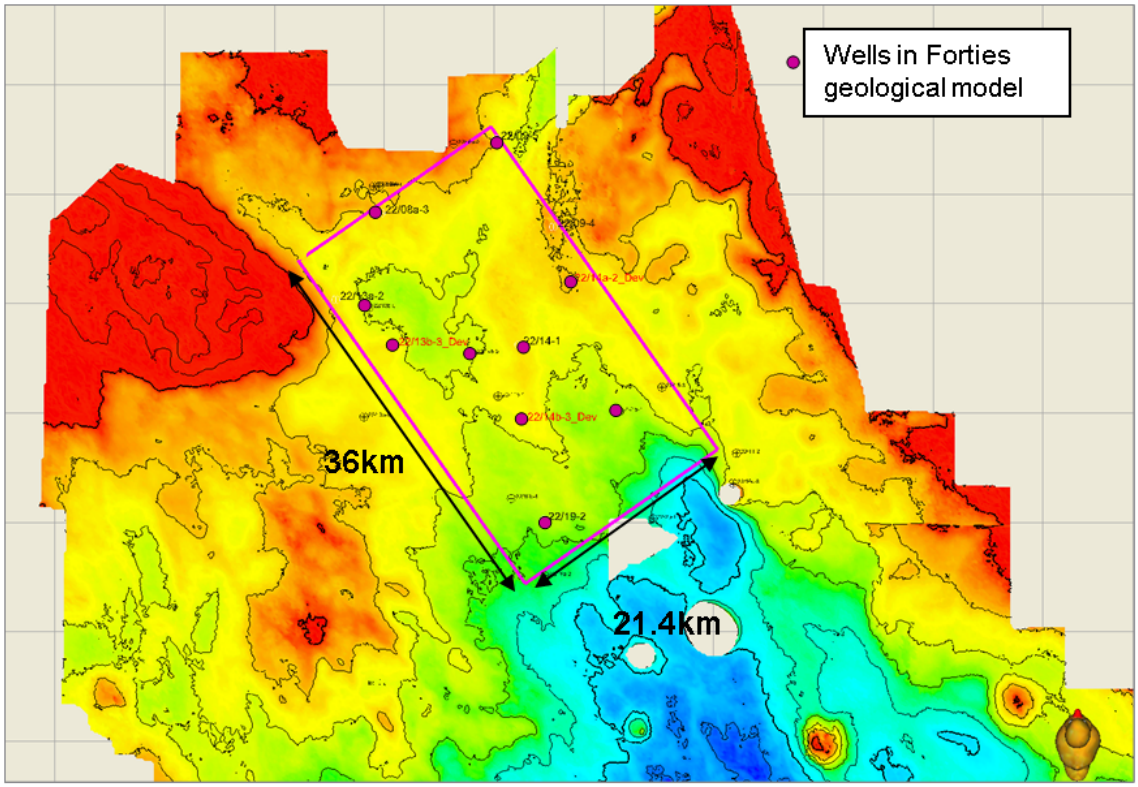


Figure 3.3: Seismic interpretation of the top of the Upper Forties in depth. The location of the Forties geological model and wells are also shown.The contours are for depth. The duck points north.

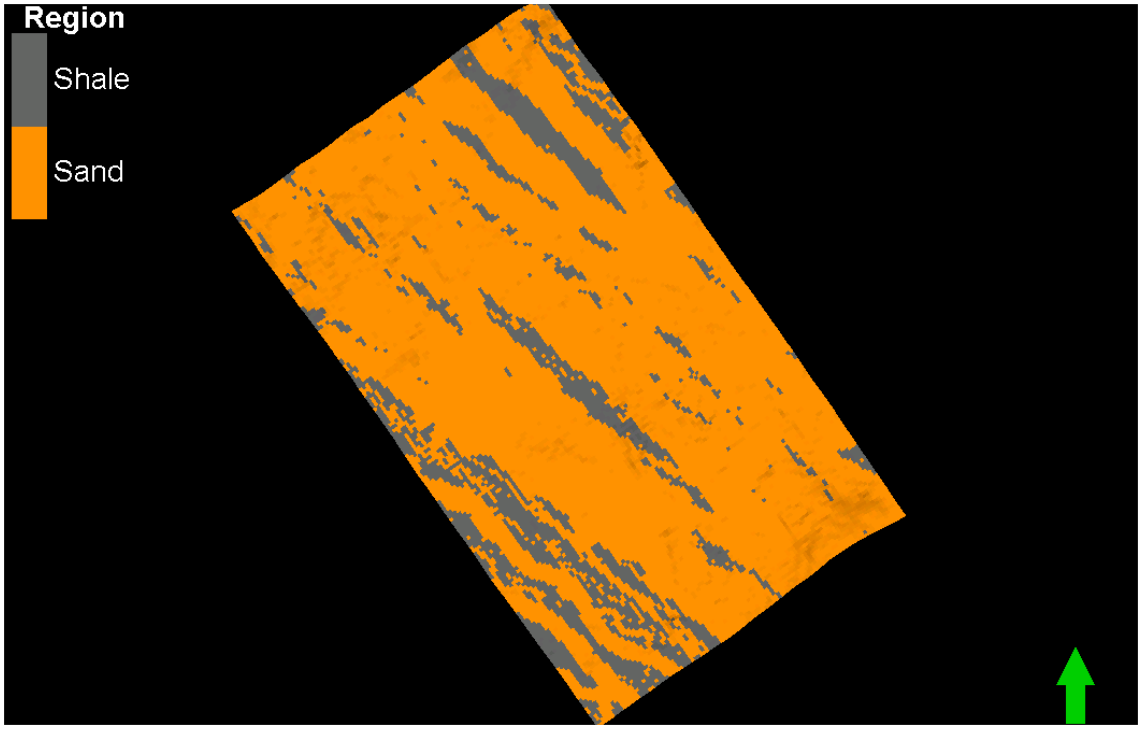


Figure 3.4: Facies model shown for the base case at layer 38 (counted from top). The arrow points north.

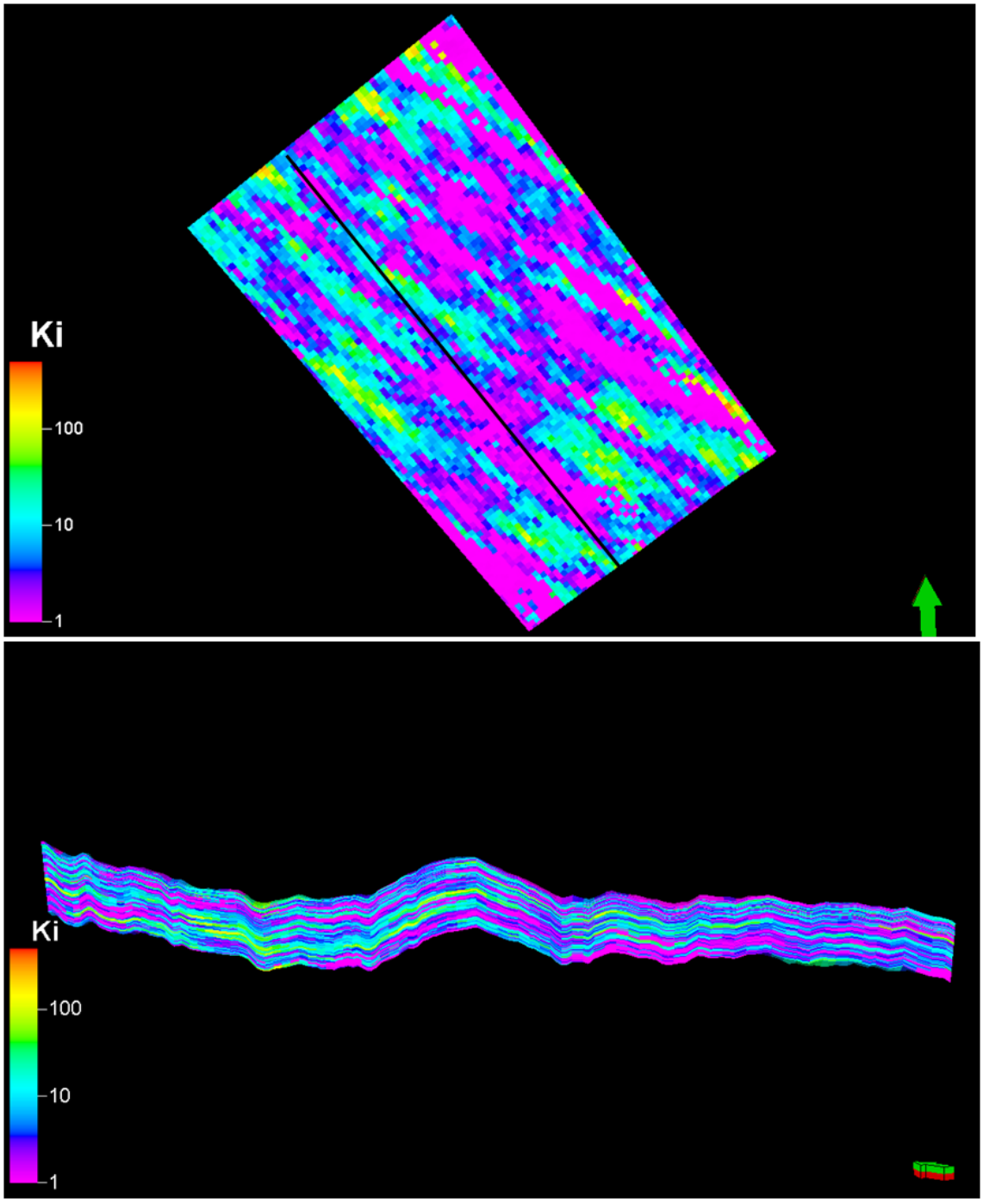


Figure 3.5: Permeability model at top of Forties base case geological model and in a cross section. The cross section taken is shown by the black line in the top view. Ki is horizontal permeability in mD. The arrow points north.

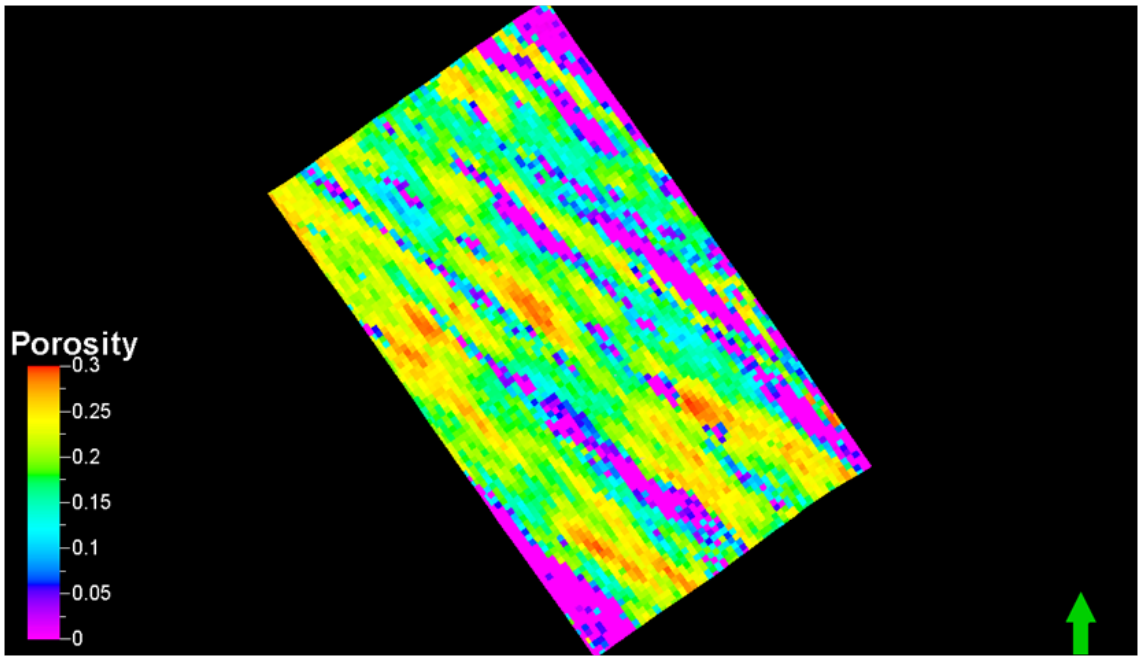


Figure 3.6: Porosity model at top of Forties base case geological model. The arrow points north.

3.2.2 Dynamic Model Setup

The dynamic model was constructed in ECLIPSE 100^{TM}. This allowed comparison against previous UKSAP work (UKSAP, 2011a). Rock properties from the geological model described in Section 3.2.1 were used. Drainage and imbibition relative permeability data as well as the capillary pressure data from the Viking 2 dataset (Bennion and Bachu, 2008), were used - see Figure 3.7. Relative permeability hysteresis was modelled using a Carlson model (Carlson, 1981).

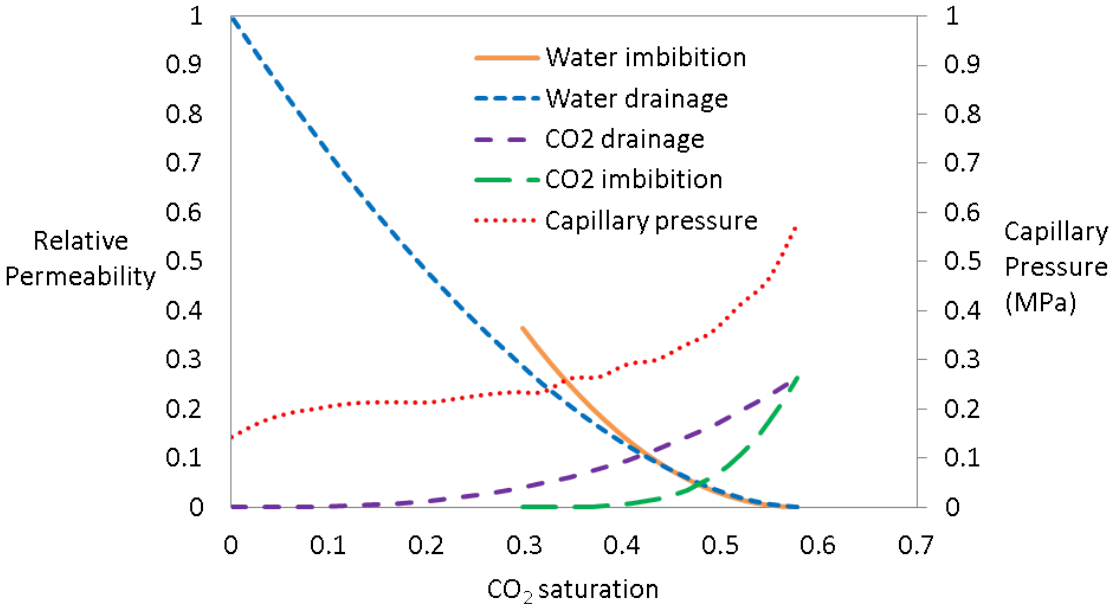


Figure 3.7: Viking 2 relative permeability and capillary pressure from Bennion and Bachu (2008).

The 1,733,400 million cell geo-cellular model grid was upscaled to a 450,450 cell model to reduce simulation runtimes. Using the 450,450 cell model 1000 year simulation runtimes varied from 7 hours to 13 days using a fast workstation PC. Upscaling of the porosity and permeability fields was applied using a factor of 2 in the two horizontal directions. This was applied to the central 104×178×90 cells leaving 1-2 layers finely resolved at the sides. A cell volume weighted arithmetic average and a pore volume weighted arithmetic average were used to calculate the coarse cell porosity and permeability values respectively. The results of sensitivity to grid resolution are shown in Section 3.3.3.

A summary of initial fluid and rock properties is given in Table 3.1. The initial pressures in the reservoir were calculated assuming hydrostatic equilibrium and a datum pressure and temperature was calculated using a geothermal gradient of 35°C /km and surface temperature of 8°C, with rounding to the nearest 5°C to coincide with the

availability of PVT data. Brine salinity estimated as 89,000ppm salinity was rounded to 100,000ppm for the same reason.

Table 3.1: Initial conditions and parameters for the base case simulation.

Parameter	Value	Source
Reservoir datum depth (below sea level)	2800m	Geological model
Brine salinity	100,000ppm	Gluyas and Hichens (2002)
Temperature	105°C	Evans et al. (2003)
Pressure at datum	32MPa	Calculated using brine density
CO_2 density at datum	660kg/m^3	TOUGH2^{TM} PVT data
CO_2 viscosity at datum	0.0000546Pa.s	TOUGH2^{TM} PVT data
Brine density at datum	1006kg/m^3	TOUGH2^{TM} PVT data
Brine viscosity at datum	0.000345Pa.s	TOUGH2^{TM} PVT data
Rock compressibility	0.0000489MPa^{-1}	CarbonStore (2011)
Porosity (arithmetic average)	0.16	Geological model
Permeability (arithmetic average)	11mD	Geological model
Volume of storage unit	2×10^{10} m^3	Geological model
Volume of Forties sandstone member	3×10^{11} m^3	CarbonStore (2011)
Fracture pressure gradient	0.0181MPa/m	UKSAP (2011a)

Dissolution of CO_2 into the brine phase and vaporisation of water into the gas phase were both modelled. All density, viscosity and phase partitioning values used during simulation were calculated using black oil PVT tables generated using the TOUGH-2^{TM} ECO_2N module (Pruess, 2005). Temperature was assumed constant in space and time in the simulations.

To represent the pressure response from the volume of the Forties sandstone connected to the Forties geological model but outside the model, significant additional pore volume was added around the boundaries of the model to make the total pore volume match the 3×10^{11}m^3 volume of the Forties sandstone member. The aquifer is believed to be open to flow beyond some of these boundaries; however this was not accounted for. Increases in the pore volume, shown in Section 3.3.3, showed that adding more pore volume to account for this would make relatively little difference to the overall volume of CO_2 injected.

The inclusion of a groundwater flow was considered and for this purpose the local change in overpressure across the field found from Figure 3.8. Based on this 1.4MPa change in overpressure over the 36km length of the model, an analytical estimate of groundwater flow velocities through the unit using Darcy's law with permeability and viscosity values from Table 3.1 was 0.04m/year. Over 1000 years this results in a migration distance of a tenth of one cell in our model and further flow through the higher permeability (∼100mD) channels would only migrate around one cell over 1000 years; so groundwater flow was neglected. We note that groundwater flows may not always be this weak.

3.2.3 Injection Conditions

Injection was simulated for 50 years and the post injection period for a further 1050 years in order to calculate the capacity of the section of the Forties sandstone member. Injection and the calculated capacity of models were constrained by the following three conditions as set out by Gammer et al. (2011), which interprets current EU regulation and IPCC suggestions:

- 99% of injected CO_2 must remain within the storage boundary after 1000 years - to be referred to as the '99% storage constraint';
- CO_2 migration velocities at 1000 years must be less than 10 metres/year and declining - the 'migration velocity constraint';
- Pressures must remain less than 90% of the estimated fracture pressure limit - the 'BHP constraint'.

In addition a minimum well injection rate of 0.1Mt/year was also applied.

A small adaptation was made to the second condition to allow for features of flow in a heterogeneous media that do not represent an increase in the risk of leakage. This was introduced to allow for cases where either a single cell or a few cells situated significantly behind the maximum extent of the CO_2 plume, but with a locally high permeability and dip, produce mobile CO_2 velocity above 10m/year. As a result an extra practical allowance was used where up to 10 visually uncorrelated cells, generally away from the furthest extent of the CO_2 plume, were allowed velocities above 10m/year. This was useful for reducing the number of computationally intensive optimisation simulations used for very minimal changes in storage efficiency. The results are insensitive to the precise number of fast-moving cells allowed.

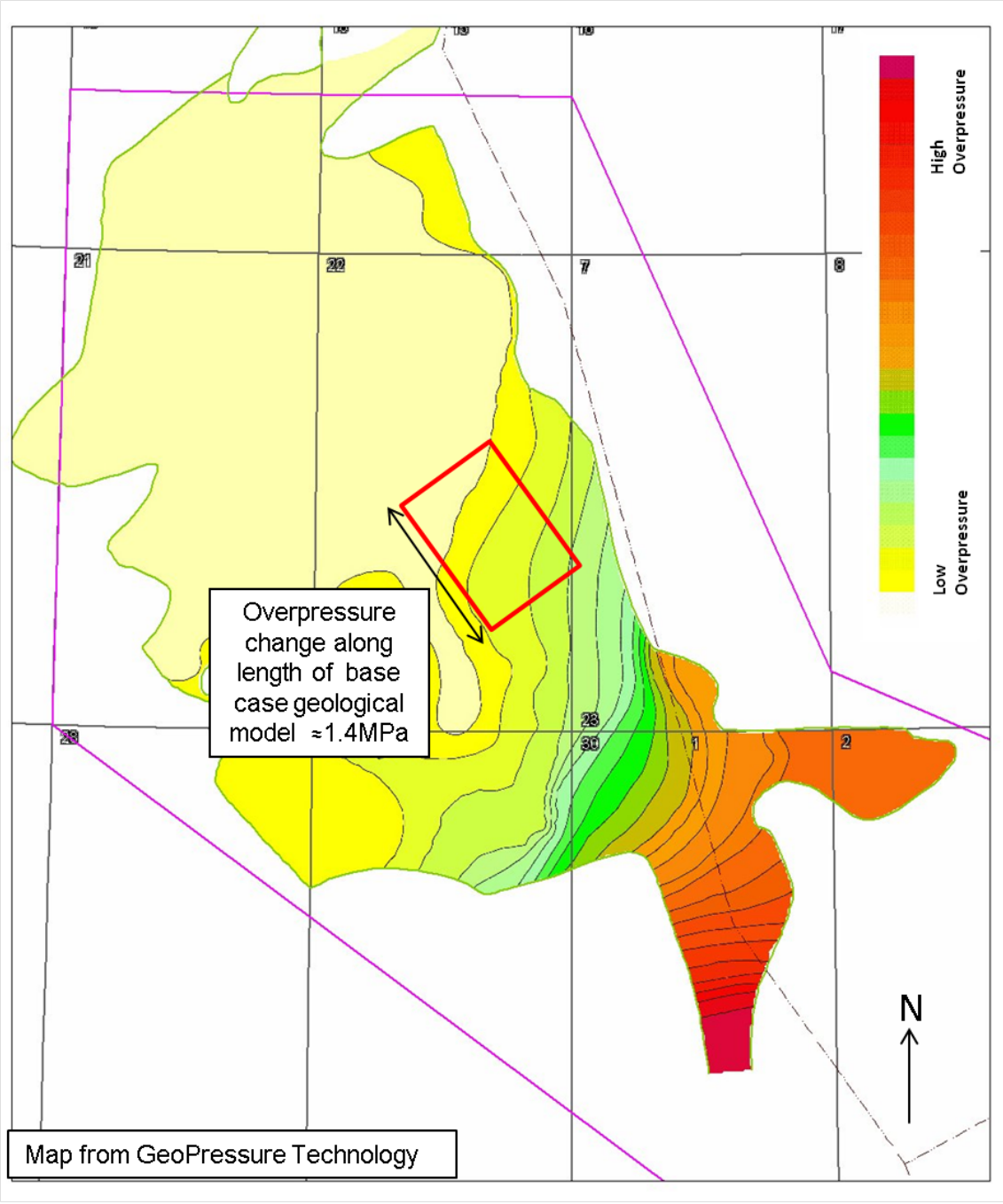


Figure 3.8: Qualitative overpressure contours for the Forties Sandstone member. The Forties base case geological model area shown in red. Map constructed using data from GeoPressure Technology Ltd. Values not shown to protect data ownership.

3.2.4 Storage Security and Trapping Assessment

Using the simulation setup described, residual, dissolution and structural trapping were all modelled. The key measures of storage security and trapping were defined and calculated for analysis as follows.

Escaped CO_2

CO_2 that reached the outer-most layers of cells at the side boundaries was regarded as outside the storage area and summed together. Any CO_2 dissolved or in its own phase in these cells was counted as 'escaped'.

Dissolved CO_2

The total dissolved CO_2 was measured as all dissolved CO_2 within the boundaries of the model, but not within the outer-most layer of 'boundary' cells.

Structural Trapping

The total amount of structurally trapped CO_2 was measured as the total free phase (not dissolved) CO_2 within structural closures. An algorithm - described in Appendix A - was written to calculate which cells were structurally closed. It calculated this using the definition that a cell 'A' is structurally closed if there is a closed loop of top layer cells surrounding the cell of which all cells have depth deeper than cell 'A'. Figure 3.9 shows the structurally closed cells in the base case model.

Residual Trapping

For the purposes of analysis residual trapping was estimated using the Land (1968) trapping model. This calculates the residual trapping in each cell using the equation

$$S^*_{gr} = \frac{S^*_{gi}}{1 + S^*_{gi}(\frac{1}{(S^*_{gi})_{max}} - 1)} \tag{3.1}$$

where $S^* = \frac{S}{(1-S_{wc})}$, S^*_{gi} is the maximum historical gas saturation on a cell, and S^*_{gr} are potential residual saturations. Using this method an example cell with saturation 0.6 would have saturation 0.3 counted as residual since it can never be displaced. Under this method all the CO_2 that is not counted as residual will eventually leave the cell unless it becomes dissolved or is structurally trapped. CO_2 within structurally enclosed cells was not counted to avoid double counting.

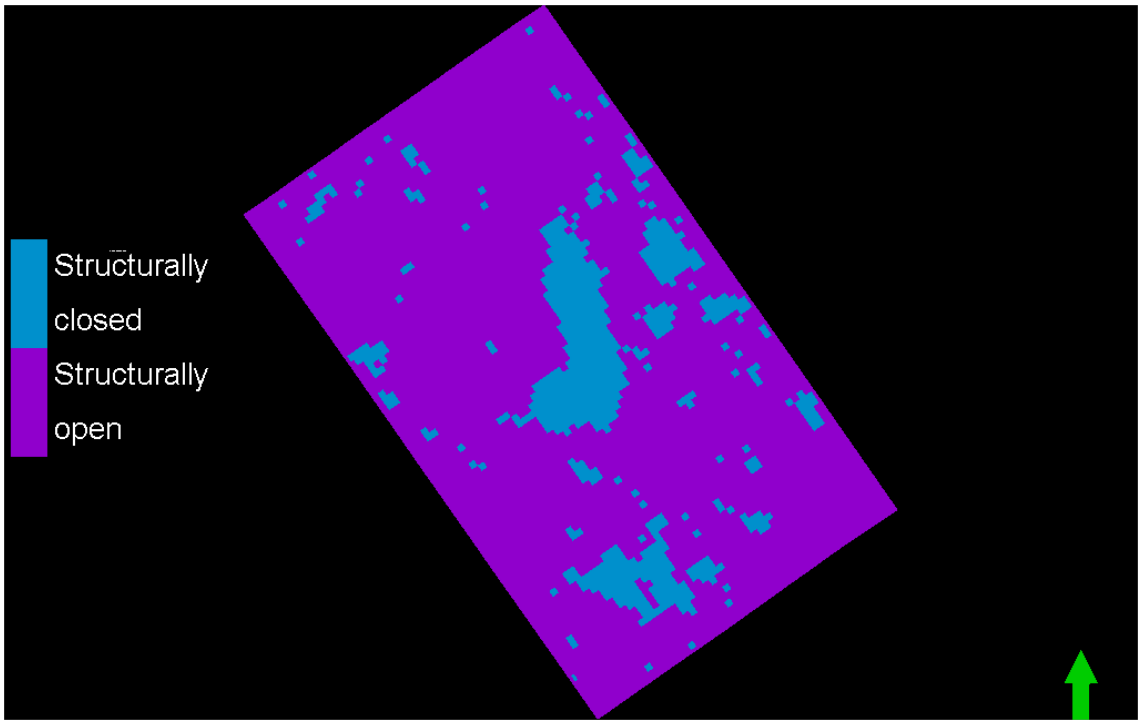


Figure 3.9: Map of cells on the top layer which are structurally closed. Due to the buoyancy of CO_2, once within these structurally closed cells it shall stay there until dissolved.

An alternative approach considered was to measure residual as the volume of CO_2 present in cells where the gas phase relative permeability $K_{r,CO_2} < 0.0001$ and the cells are not structurally closed. Although this measure provides interesting information it was found to underestimate the amount of CO_2 that was unable to leave the model due to residual trapping, since it does not include any residual in cells where $K_{r,CO_2} > 0.0001$.

Low Migration Velocity Storage

Any CO_2 that is still within the boundaries of the model and satisfying the velocity constraint at 1000 years and not trapped structurally, residually or by dissolution, we shall refer to as low velocity CO_2 and refer to the storage mechanism as low migration velocity storage. Over time the low velocity CO_2 must eventually become either structurally or residually trapped, dissolved or escape the model boundaries.

CO_2 Velocity

ECLIPSE 100^{TM} provides CO_2 flux in the perpedicular horizontal x and y directions for each cell in surface m^3/day. We converted this to estimate the CO_2 migration velocity in m/year.

3.2.5 Sensitivity Models

The sensitivities to be studied were the presence of heterogeneity and top-surface structure reservoir dip and permeability. The aim of these was to ascertain the impact the top-surface structure and heterogeneity upon storage capacity and to substantiate the storage regime results from Gammer et al. (2011).

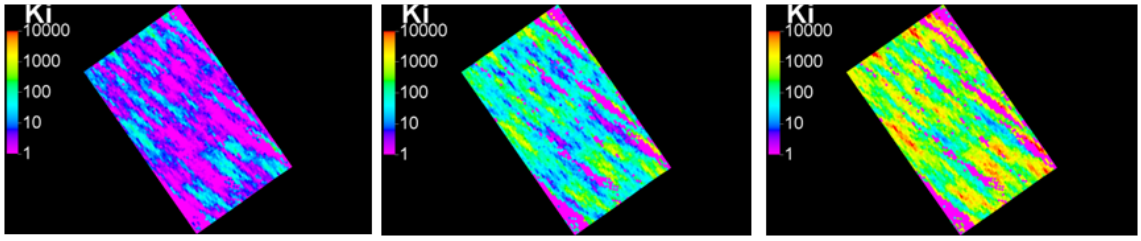


Figure 3.10: Permeability maps for (from left to right) the 11mD average permeability base case and two permeability sensitivities with 145mD and 1D average permeability. Figures show top layer of model viewed from above. In the key Ki is permeability in mD.

Firstly, to determine whether the storage regime results still applied when top-surface structure and heterogeneity were present, dip and permeability sensitivities were applied to the base case geological model. The base case model had average dip 0.27° in the SE to NW direction and pore volume weighted arithmetic average permeability 11mD. The sensitivity values used for dip were 1° and 3° and for permeability 145mD and 1D. The permeability and dip sensitivities applied to the 11mD 0.27° base case are shown in Figure 3.10 and Figure 3.11 respectively. These sensitivities allowed us to look at results representative of each of the three storage regimes and cases were categorized as shown in Table 3.2 using the characteristic migration velocity from Equation 2.6 and the 10mD cut-off. The cut-off characteristic migration velocity between the migration velocity limited and intermediate storage regimes was 10m/year due to the migration velocity constraint of Section 3.2.3.

To investigate the effect of the Forties geological model heterogeneity and top-surface structure, the same sensitivity study was run with geological models without heterogeneity and then with the top-surface structure removed recreating homogeneous smooth-topped models. Figure 3.12 shows the three different models with average horizontal permeability 11mD and dip 0.27°. In the homogeneous models the vertical to horizontal permeability ratio was set to a generic value of 0.1. Porosities and permeabilities for the homogenous models were set to the arithmetic average of the heterogeneous model. In the homogeneous models with and without top-surface structure the dip sensitivities were applied to the 145mD case to provide migration velocity limited storage regime dip scenarios. Using the results from the three dip-permeability sensitivity studies, the effect

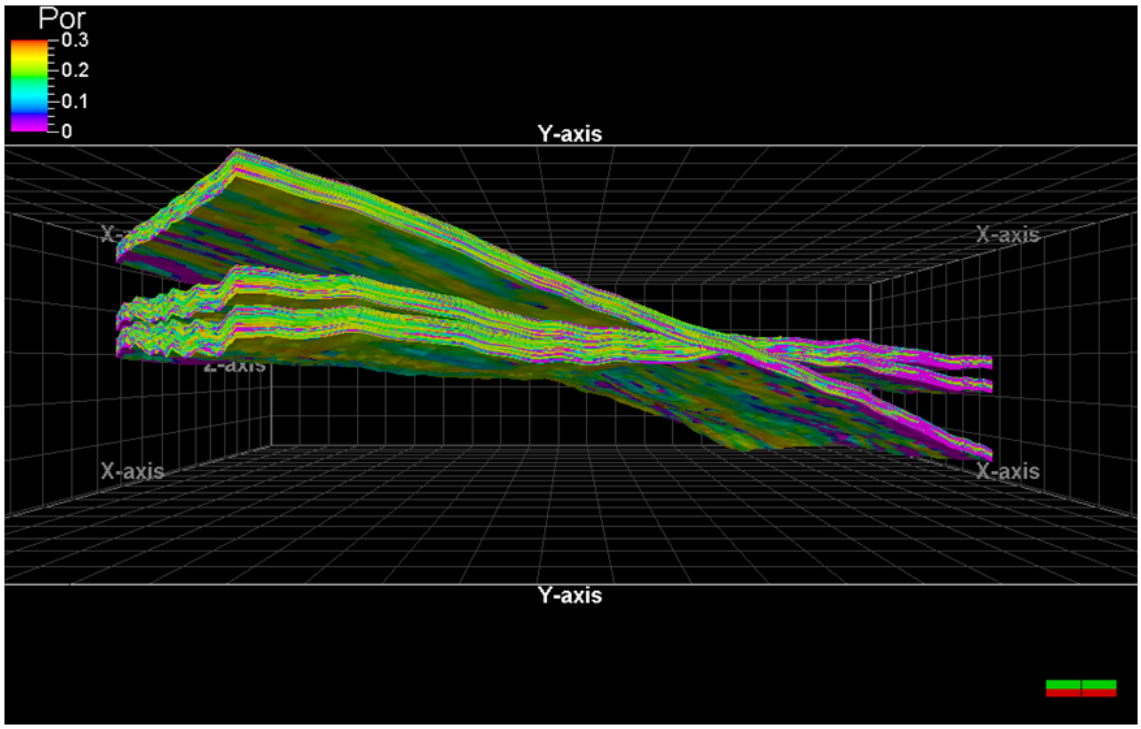


Figure 3.11: Porosity maps for the different dip sensitivity models. The base case has dip 0.27° and two sensitivity cases have dips 1° and 3°. Models are viewed from the west and vertically exaggerated by a factor of 15. In the key Por stands for porosity.

of adding and removing heterogeneity and top-surface structure could be observed.

In addition, the application of dip and permeability sensitivities to the cases without heterogeneity and/or top-surface structure was used for further substantiation of the storage regime results.

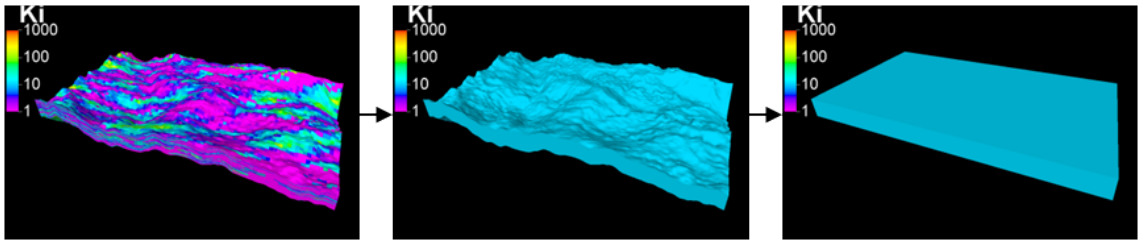


Figure 3.12: Simplification of base case model by removing heterogeneity then top-surface structure. Figures show permeability in mD, are viewed from the south and are exaggerated by a factor of 15 in the vertical direction.

3.2.6 Methodology for Calculating Storage Capacity - Optimising Injection and Well Location

In both the base case and sensitivity models the storage capacity of units was estimated, while meeting the storage constraints introduced in Section 3.2.4. To estimate these capacities a set of well placements and injection rates was required for each scenario.

It was decided that a single set of well placements would be used to keep the optimisation process feasible. However, these well placements were required to provide adequate well options to optimise storage capacity in a variety of different models with different flow behaviours. To achieve this, well locations would be designed to:

- have a reasonably even distribution,
- where possible be located preferentially down-dip,
- be located to avoid injection into shales in heterogeneous models,
- be given high enough well density for cases with lowest injectivity to be able to maximise injection under the constraints given.

It was possible to satisfy these aims with a well placement setup used for the base case model, mainly because a large number of wells were required in this case, offering flexibility for the use of different numbers of wells in different locations in other scenarios. The exact placement of these wells was chosen by eye aided by detailed visualisation of the permeability field and the local dip. The locations were optimised by gradually increasing or relocating wells in order to optimise injection into the base case. As explained further in Section 3.3.1 the optimisation of the base case scenario involved particular effort to increase the number of wells so that any additional well increased total injection by at least 0.1Mt/yr.

The final well pattern from this process to be used for the base case and all sensitivities is shown in Figure 3.13. Through the optimisation process each of the points listed above were taken into consideration, although through its manual nature the process was not strictly rigorous. In the final setup we note that 2km long horizontal wells were used to help avoid injection near shale layers and also to assist with an improved areal spread of the CO_2 plume.

With the well placement established the storage capacity in each sensitivity model was estimated by running dynamic simulations and then increasing or reducing injection rates to meet the storage constraints. For each model setup this was achieved through an iterative process described by Figure 3.14. In this process the escaped CO_2 and CO_2 velocity at 1000 years were measured as explained in Section 3.2.4 so that potential

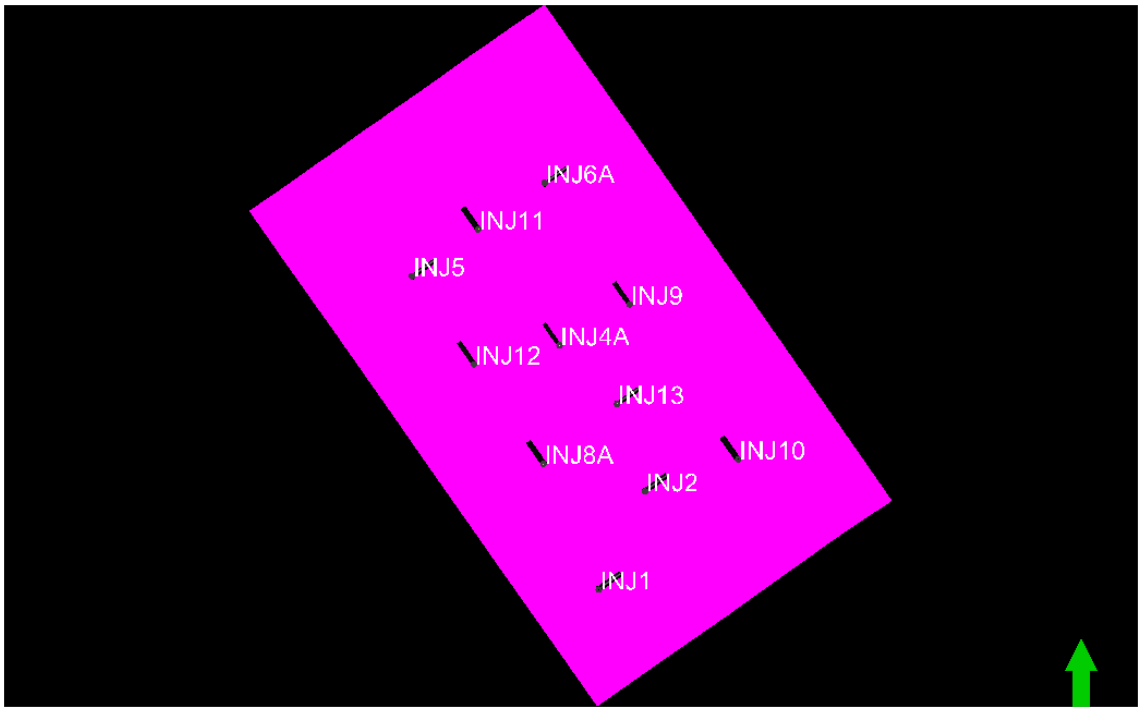


Figure 3.13: Locations of the eleven horizontal wells used for the base case and sensitivity scenarios. The model is viewed from above.

injection rate scenarios could be accepted or rejected under the 99% storage constraint or velocity constraint. The Bottom-Hole Pressure (BHP) constraint was applied directly through the simulation model setup.

3.2.7 Alternative Simulations using Streamlines

Simulations using streamline simulation were undertaken initially to make use of their superior speed. Streamline simulation is an efficient method for modelling advection-dominated, incompressible flow in a porous medium and makes higher resolution simulation of reservoir flow computationally feasible and as a result it is particularly beneficial when finer-scale geological heterogeneity is to be investigated. Preliminary simulations were undertaken using two streamline-based reservoir simulators, a research streamline code from Imperial College and 3DSL^{TM}. Both codes were able to handle the 1,733,400 cell model with runtimes all under a day; however they each had issues.

The in-house research code was unable to handle corner point geometries. Further, due to the dip that would be investigated in some models, it was unable to produce an equivalent structure using a Cartesian grid without increasing the number of cells in the model to such an extent that simulation would be computationally unfeasible. Since one aim was to investigate the effect of structure this ruled out the Imperial College research

code. 3DSL^{TM} was able to handle corner-point geometries and also simulate compressible flow with runtimes still less than a day. However, it was not able to model relative permeability hysteresis and demonstrated significantly different results when using either the drainage or imbibition relative permeabilities, thus ruling out 3DSL^{TM}. In both cases, time constraints meant upgrading the simulators was not possible, leading to the final decision to use Eclipse 100^{TM}, even though this code is slower and required the use of an upscaled model.

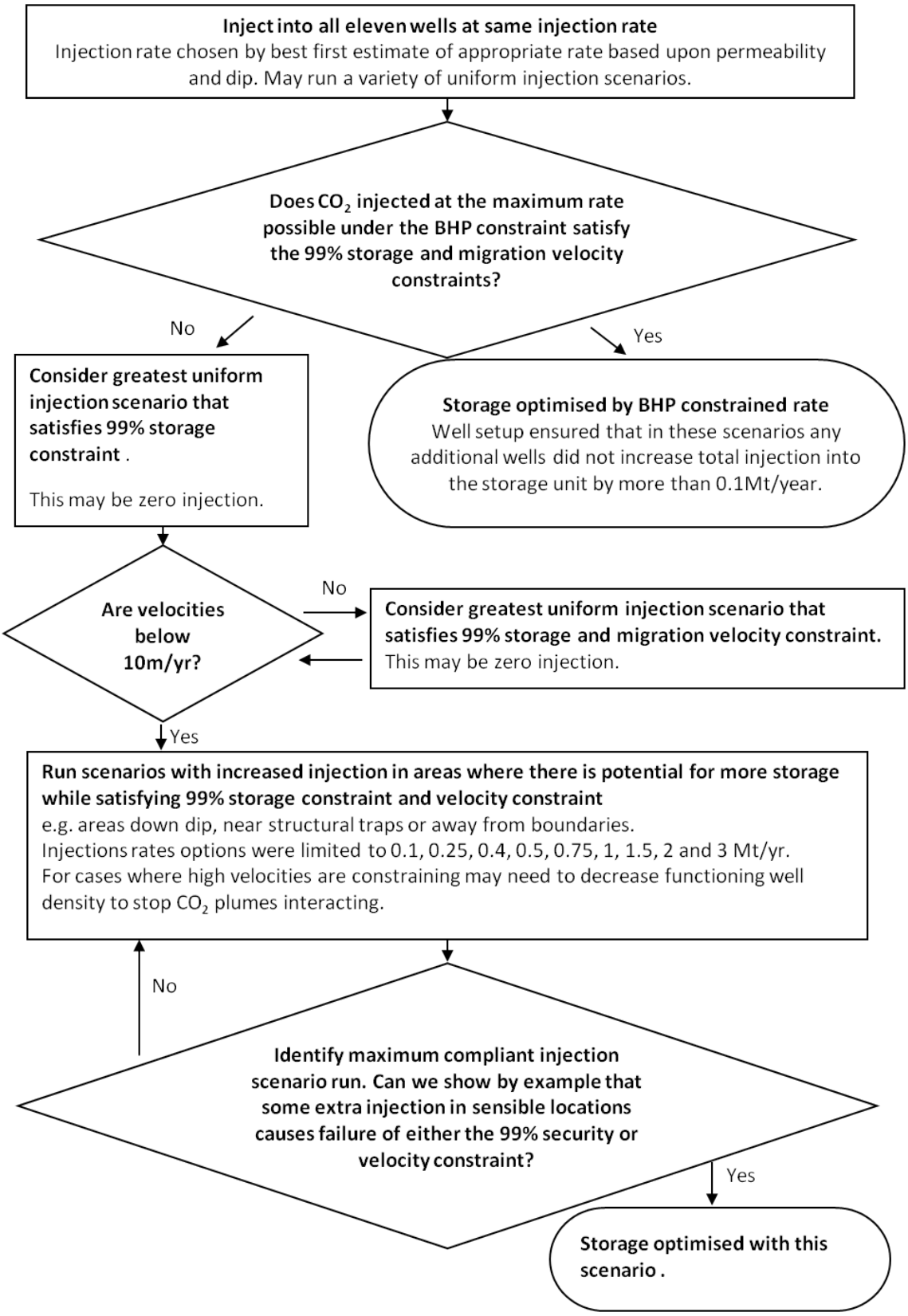


Figure 3.14: General methodology for calculating the capacity of each model.

3.3 Base Case Results

3.3.1 Storage Appraisal

The base case was first modelled in order to appraise the storage of a particular section of the Forties sandstone member. To appraise its storage the location, number and injection rate of wells had to be optimised.

At the start of the optimisation of well location and injection rate just six injection wells were operated with target injection rates of 2Mt/year. However this rate was not achieved in each well as injection was limited by the bottom hole pressure (BHP) constraint that constrains the BHP to below 90% of the fracture pressure. Despite this limitation on rate through each well Figure 3.15 demonstrates some areas where the pressure was lower than in the near well regions and actually below the fracture pressure. As a result extra injectors were added until the increase in injection rate through all wells when an extra well was added fell to 0.1Mt/yr. This determined an appropriate well density for near maximum injection.

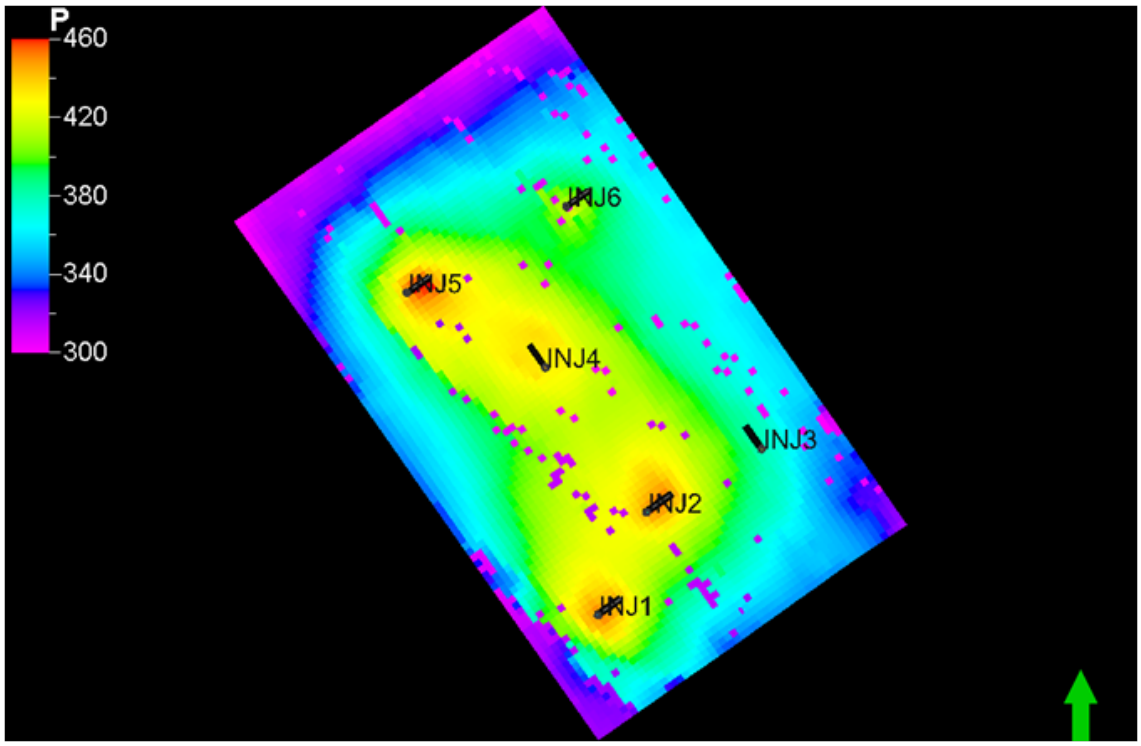


Figure 3.15: Pressure (bars) profile at top layer at 50 years in a preliminary 6 well injection scenario. The purple 'specs' are shales that were treated as inactive cells in early simulations. Pressures around 400bars (=40MPa) and below indicate some limited pressure space, suggesting that using more wells would lead to higher storage capacities. The wells are shown in black.

The limitation on well density experienced was due to the pressure interference between wells. Although pressure was seen to be relieved by the open flow boundaries of the model, pressure interference between wells increased with further injection over time. The effect of this is shown in Figure 3.16 where increased interference led to decreased injection over time. In a realistic storage case constant injection over the time period would be more likely. For the assessment of storage capacity though, we assume that capacity is not affected by the time or rate of injection, and observe this decay in rate.

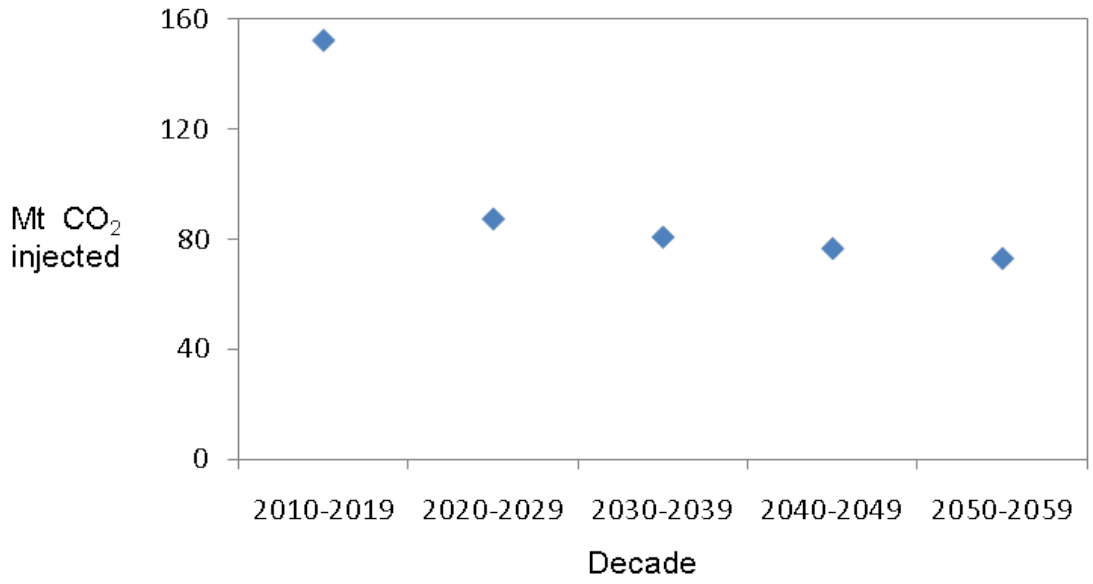


Figure 3.16: The total mass of CO_2 (Mt) injected into the base case geological model per decade under our maximum injection scenario.

While increasing the well density as explained above it was simultaneously necessary to try to satisfy the 99% storage constraint and velocity constraint with our well placements and injection rates. Due to the low average permeability of the aquifer, the extent of the CO_2 plume that could be injected under the BHP constraint was only around 5km and had velocities less than 10m/year. This meant that wells could be located fairly close to the boundary. With the ability to place wells fairly freely under the two migration constraints, they had little impact upon injection and rather capacity was constrained by how much it was possible to inject due to BHP and well density.

The final injection setup for the model is shown in Section 3.2.6 where it is noted that horizontal wells were used to avoid injection into shale layers. To summarise, storage was constrained by a combination of the BHP constraint, which broadly determined the well density, and to a lesser extent the 99% storage constraint, which determined how

near to the boundary we could inject. This combination of the two factors is behaviour typical of open aquifers from the injectivity limited or intermediate storage regimes. Good injectivity that could be achieved through any one well alone, as well as the permeability of 11mD being slightly greater than the notional 10mD boundary, would tend to categorise it as in the intermediate storage regime.

3.3.2 Storage Capacity and Trapping Mechanism

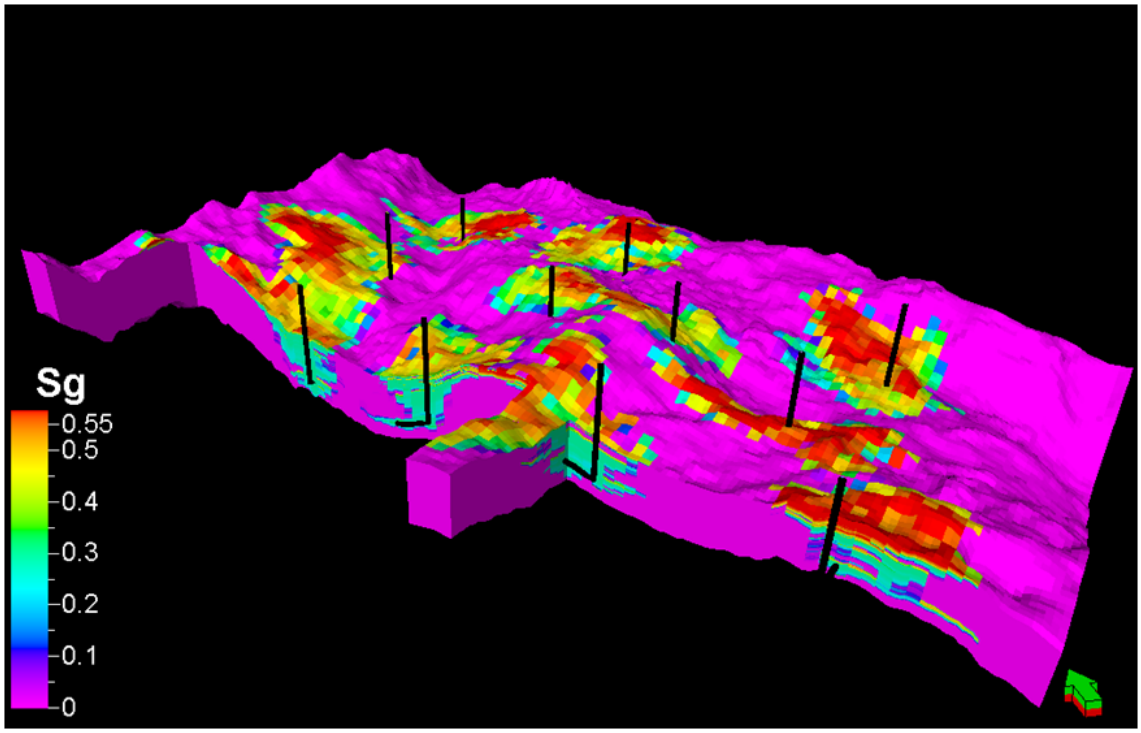


Figure 3.17: CO_2 saturation in the Forties base case model at 1000 years. The maximum gas saturation is 0.577. The model is 36km long, viewed from the south and vertically exaggerated by a factor of 15. The wells are shown in black.

Having determined well locations and rates into the section of the Forties sandstone member, as outlined in Section 3.3.1, its capacity was estimated as 471Mt representing a storage efficiency of 3.5%. The final distribution of saturations at 1000 years is shown in Figure 3.17 and Figure 3.18 shows which mechanisms trapped this CO_2, using the method explained in Section 3.2.4.

In this case residual trapping is most significant. However, due to the low migration rates, we were able to store 18% of our injected CO_2 without residual, structural trapping or dissolution which are more permanent trapping mechanisms, since low velocity CO_2 was still mobile and unconfined. The low permeability of this model explains this high amount of low migration velocity storage as it leads to low migration velocities such that this CO_2 is migrating less than 10m/year.

In Figure 3.19 we see that over time this low velocity CO_2 becomes increasingly trapped by the other mechanisms; however even at 10,000 years 7% of CO_2 is still mobile.

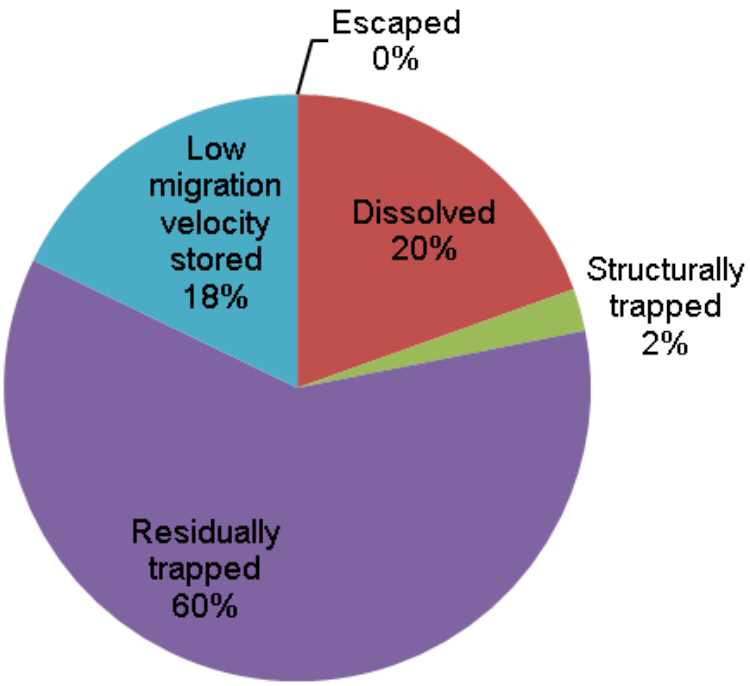


Figure 3.18: Mechanisms trapping CO_2 in the base case model at 1000 years. Percentages show the proportion of the total amount trapped by different mechanisms. Note that trapping by precipitation is not modelled.

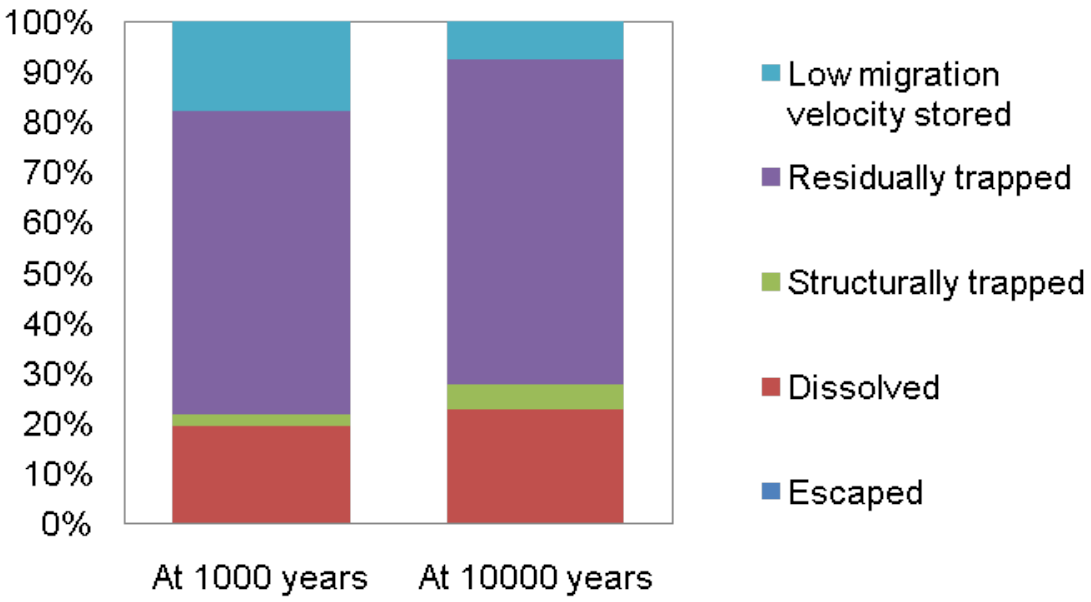


Figure 3.19: Mechanisms trapping CO_2 at 1000 years and 10,000 years.

3.3.3 Model Verification

The base case model was investigated to check its sensitivity to user chosen inputs. In particular, two studies were considered, the sensitivity of results to grid resolution and the boundary condition.

Sensitivity to Grid Resolution

Predicted simulation runtimes of many months meant that grid resolution was reduced from the original geocellular model. To assess the sensitivity of model results to grid resolution we considered how a number of measures were affected when considering a higher resolution model. We compared the original 1.7m cell model with the 450,450 cell version that coarsened the 1.7m cell model by a factor of two in both the x and y horizontal directions, but maintained resolution in the vertical direction. In both cases well locations were the same and rates were determined to maximise storage under the constraints mentioned previously.

We considered the effect upon the following areas:

- Porosity and permeability distribution

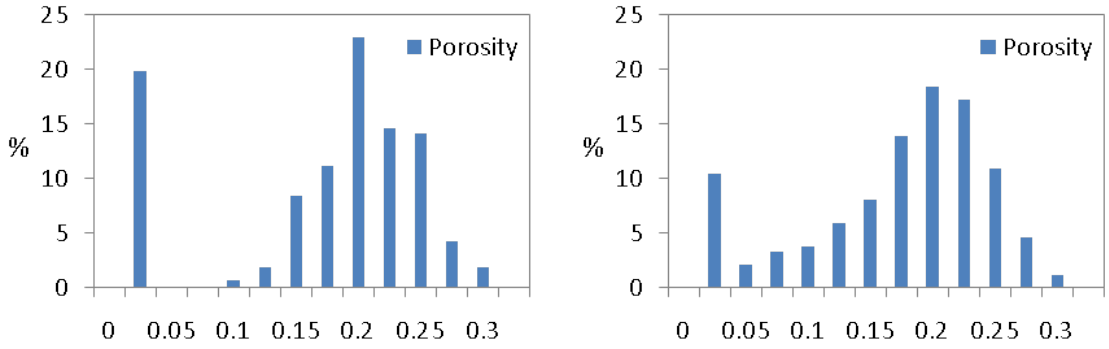


Figure 3.20: Porosity distribution for 1,733,400 (left) and 450,450 (right) cell models.

The general distribution shapes for each stayed the same as shown in Figure 3.20 and Figure 3.21. However the standard deviation of each decreased, from 23mD to 22mD for the permeability and porosity from 0.086 to 0.075. The spike for zero porosity and permeability was also reduced by around half leading to smaller zero permeability shale layers. Figure 3.22 also shows that the channels still remain visually intact.

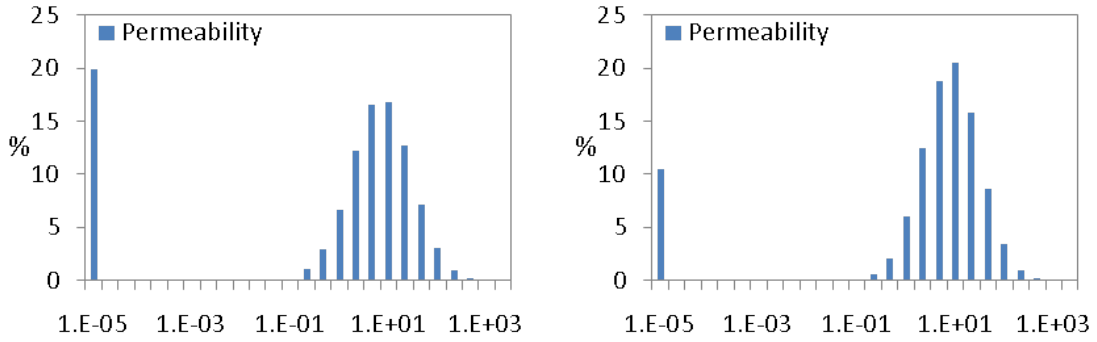


Figure 3.21: Permeability distribution for 1,733,400 (left) and 450,450 (right) cell models

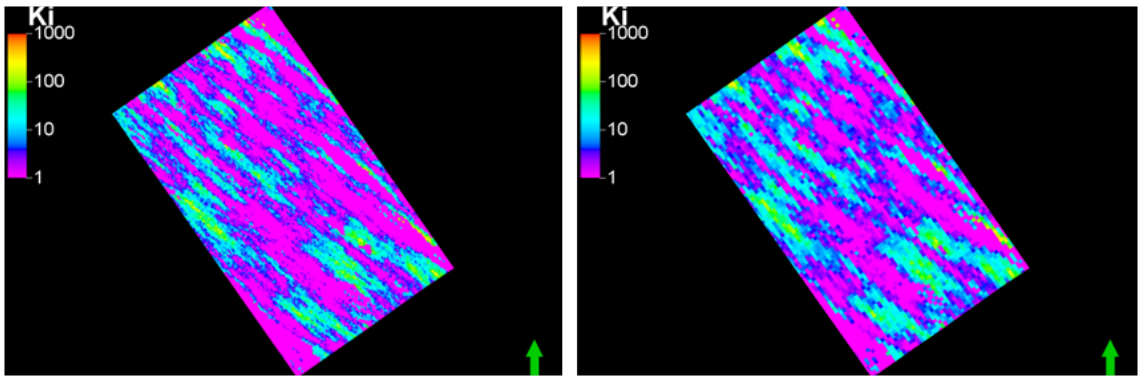


Figure 3.22: Permeability (mD) map for 1,733,400 (left) and 450,450 (right) cell models viewed from above.

- Saturation profiles at 10000 years

In Figure 3.23 the areal spread is captured well by the 450,450 cell model with very similar CO_2 extent to the 1.7m cell model. The cross-sections show slightly greater lateral migration extent within the model with the higher resolution case, which is likely a result of the larger proportion of impermeable shale cells. This may have some effect on the residual trapping and we see in Figure 3.25 that there is an increase in residual trapping in the higher resolution model.

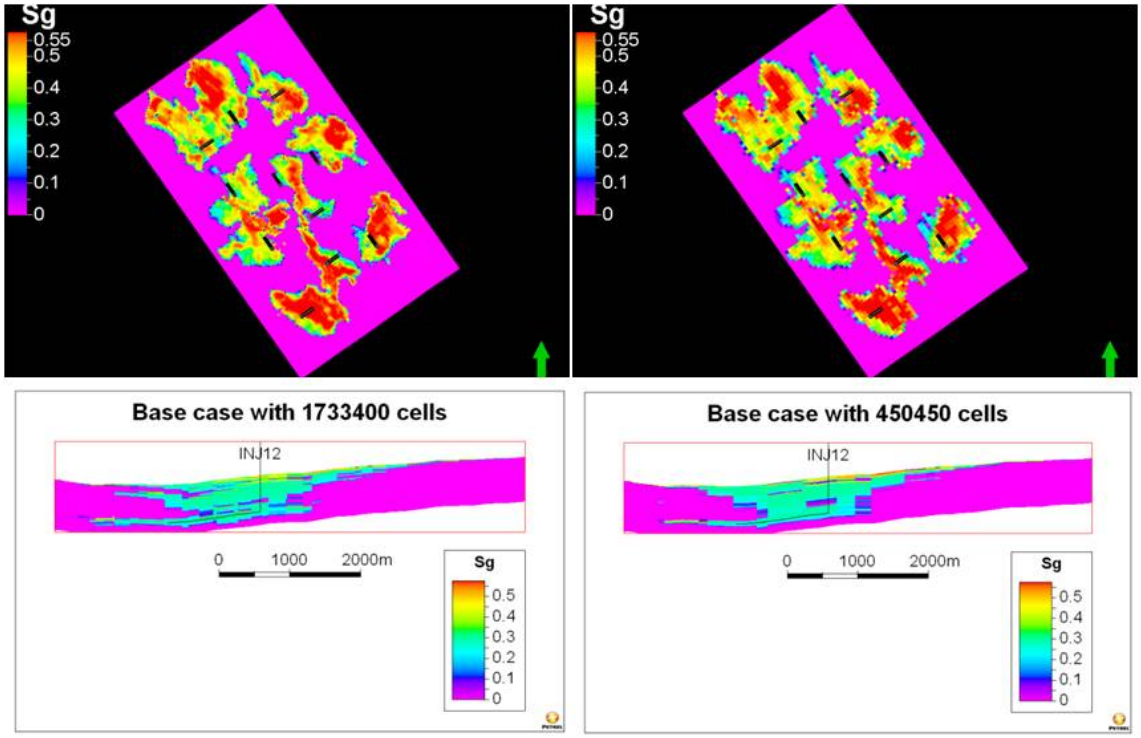


Figure 3.23: Models at top show saturation profiles at 10000 years for 1,733,400 (left) and 450,450 (right) cell models. Top models show top layer viewed from above. The wells are shown in black. Bottom models show saturation distribution around injection well INJ12.

- Total CO_2 storage capacity

The total CO_2 injected into the model changed from 536Mt for the 1,733,400 cell model to 471Mt for the upscaled model. This occurred as more injection was possible under the BHP constraint by which both models were constrained. Figure 3.24 suggests this is because pressure build-up near wells was lower in the 1,733,400 cell model and we see higher localised pressure highs in the 450,450 cell model where injection would be reduced as a result.

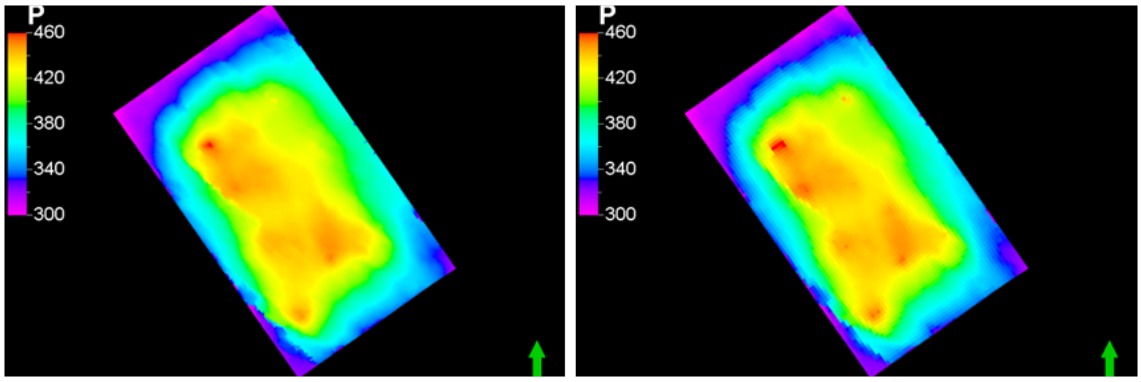


Figure 3.24: Pressure (in bars) profiles on top layer at 40 years for 1,733,400 (left) and 450,450 (right) cell models. Higher localised pressure is visible in the 450,450 cell model.

Although this change in injection is not insignificant it only represents a change in storage efficiency from 3.5% to 3.9%. For our investigations in Section 3.3.4 and Section 3.4, this order of change is smaller than we see for physical sensitivities such as dip and permeability. This change also seems limited to models where the BHP constraint is the limiting factor on storage capacity such as in this base case. For reservoirs where this is not the case we have seen that the migration distances were not changed significantly by Figure 3.23. Further, for resolutions finer than 200m $\times$ 200m, as in the 1733400 call model, it has been seen (UKSAP, 2011a) that there is very little change in storage capacity and migration distances.

Trapping mechanisms in each case are also considered. We have noted above that residual trapping may be increased due to greater lateral movement of CO_2 and an increase is seen in Figure 3.25. This increase is also likely due to the increase in total injection volume. Dissolution does not change significantly although proportionally has decreased a little from the higher resolution model.

The changes we see as a result of a change in grid resolution are not insignificant; however they do not show any signs of changing the way the fundamental dynamics are captured. In particular flow patterns are still captured very well which is important for migration limited storage scenarios. For BHP constrained cases - which we are less interested in - it is possible that injection may be underestimated; however compared to physical sensitivities the change is small. In conclusion the coarser grid resolution is highly unlikely to affect any of the conclusions from our physical sensitivity studies, supporting the trade-off made to achieve feasible runtimes.

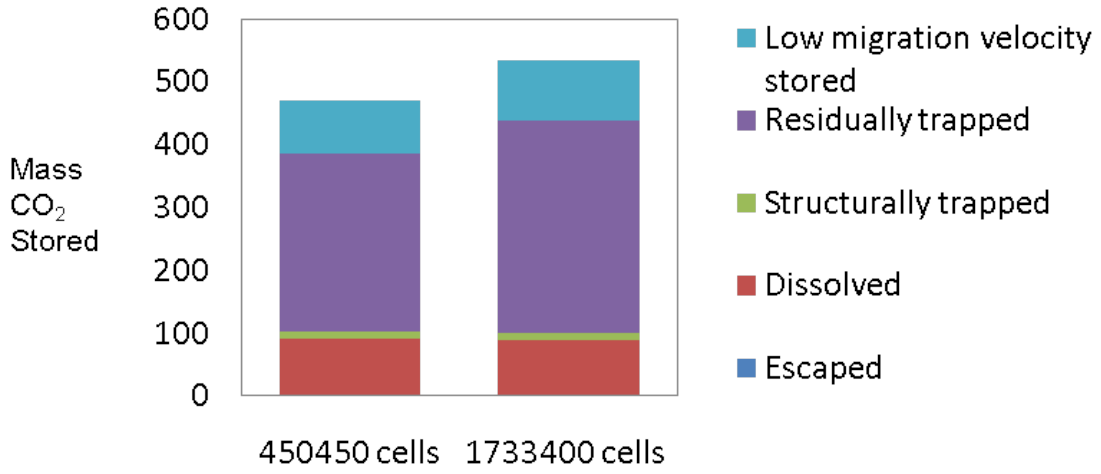


Figure 3.25: Mass (Mt) of CO_2 stored with different grid resolutions at 1000 years.

Sensitivity to Boundary Condition

Reservoir simulations by their nature choose to model a limited volume of space and thus require some simplifying assumptions to represent the behaviour of the volume outside of this and especially the behaviour at the boundary between the two. The boundary condition for this work is described in Section 3.2.2. To support the use of this boundary condition a preliminary study of the sensitivity of our results to over 20 boundary condition scenarios was considered. These sensitivities were constructed as variations of our 6-well injection preliminary base case which injected 360Mt into the Forties geological model. Four of the most interesting scenarios are described as follows:
Scenario 1 Base Case (boundary condition described in Section 3.2.2) boundary pore volumes for four sides starting from the north-west side were $1.0\times10^{11}m^3$, $2.1\times10^{10}m^3$, $8.5\times10^{10}m^3$ and $7.1\times10^{10}m^3$ respectively compared to the $2.0\times10^{10}m^3$ volume of the storage unit.
Scenario 2 Larger connected pore volume - $9.4\times10^{11}m^3$, $1.6\times10^{12}m^3$, $9.4\times10^{11}m^3$ and $1.6\times10^{12}m^3$ for four sides starting from the north-west side.
Scenario 3 The large connected pore volume cells in scenario 1 were refined using grid refinement as shown in Figure 3.26. Therefore flow within this large pore volume was calculated using a larger number of cells. As a result, cells in the connected pore volume had only between 4 and 8 times the pore volume of the cells in the centre of the model.
Scenario 4 Same as scenario 3 but the boundary cells moved in by 400m - 1400m cells depending upon boundary.

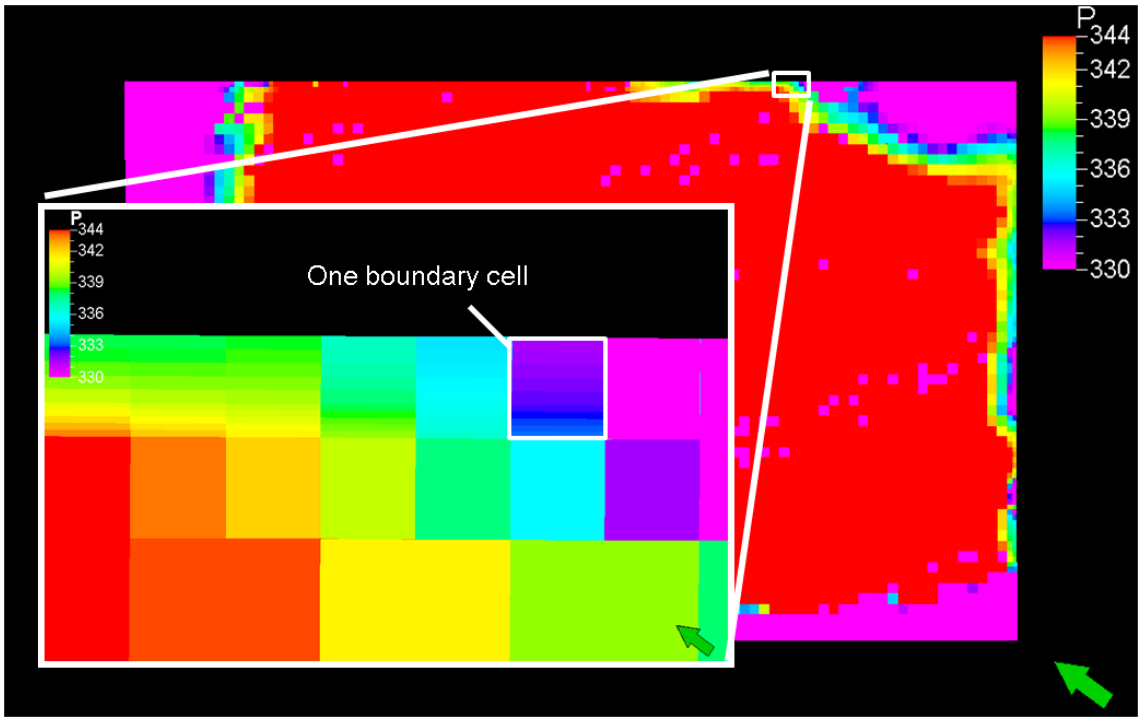


Figure 3.26: Scenario 3 - The cells at the boundary have large pore volumes to represent the volume of aquifer attached to the model. Visually these boundary cells appear with the same area as their neighbours, however their pore volume is larger. To test the effect of the resolution of these boundary cells, such as the one highlighted they were refined. This can be seen by the range of colours inside. This refinement allowed the pressure to be resolved more accurately.

By modelling these scenarios the storage capacity was affected as shown in Figure 3.27. Since the base case capacity is limited by injectivity the changes in capacity seen are due to the change in injection rates.

From the range of boundary conditions considered the greatest change to stored CO_2 was 5% in scenarios 2 and 4. In scenario 2 a far larger pore volume was used to test the sensitivity to pore volume since we had modelled an open aquifer with a restricted pore volume. The larger pore volume caused a 5% increase in capacity since there was a larger volume over which pressure could be dissipated. In scenario 3 we showed that improving the resolution at which the pressure footprint was resolved outside the domain had little effect upon our injected CO_2 volume. In scenario 4, the boundary cells were moved further into the model reducing the distance between the boundary cells and wells by up to 25%. This was also found to change the injected CO_2 volume by 5% thus showing that decreasing resolution nearer to the well and pressure plume has more of an effect on injected CO_2.

From these results we have found that the boundary condition had a limited effect

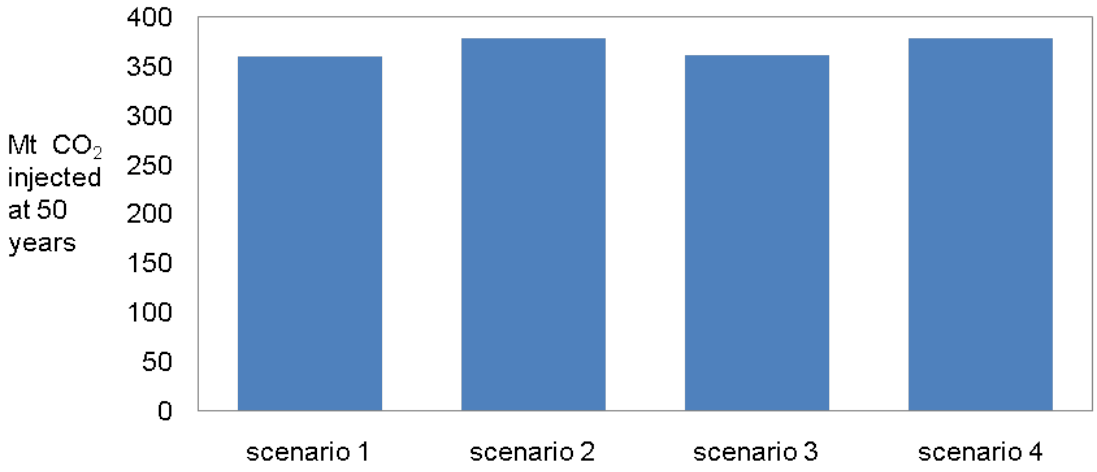


Figure 3.27: Sensitivity of injected CO_2 volume to changes in boundary condition.

upon our injected CO_2 volume and the maximum 5% change in injected volume is considered acceptable under the same reasoning as used with grid sensitivity. Further, as this case was limited by injectivity, we would expect that if the boundary condition was to impact any case it would be this type since the pressure impact of the boundary is most important here. Therefore it seems reasonable to extend the acceptance of the boundary condition to models whose capacity is limited by CO_2 extent rather than injectivity.

Table 3.2: Storage efficiency results for various sensitivities

Average storage unit permeability (mD)	Average storage unit dip	Analytic migration velocity based upon average dip and permeability $\approx 5.5K \sin\theta$ (m/yr)	Storage regime	Storage efficiency		
				Homogenous smooth	Homogeneous with top-surface structure	Heterogeneous with top-surface structure
11	0.27°	0.3	IL/I	5.4%	5.5%	3.5%
145	0.27°	3.8	I	2.6%	1.2%	2%
1000	0.27°	26	MVL	0.2%	0.4%	0.8%
145	1 °	14	MVL(just)	0.9%	0.5%	-
145	3°	42	MVL	0.3%	0.3%	-
11	1°	1.1	I	-	-	3.5%
11	3°	3.2	I	-	-	2.2%

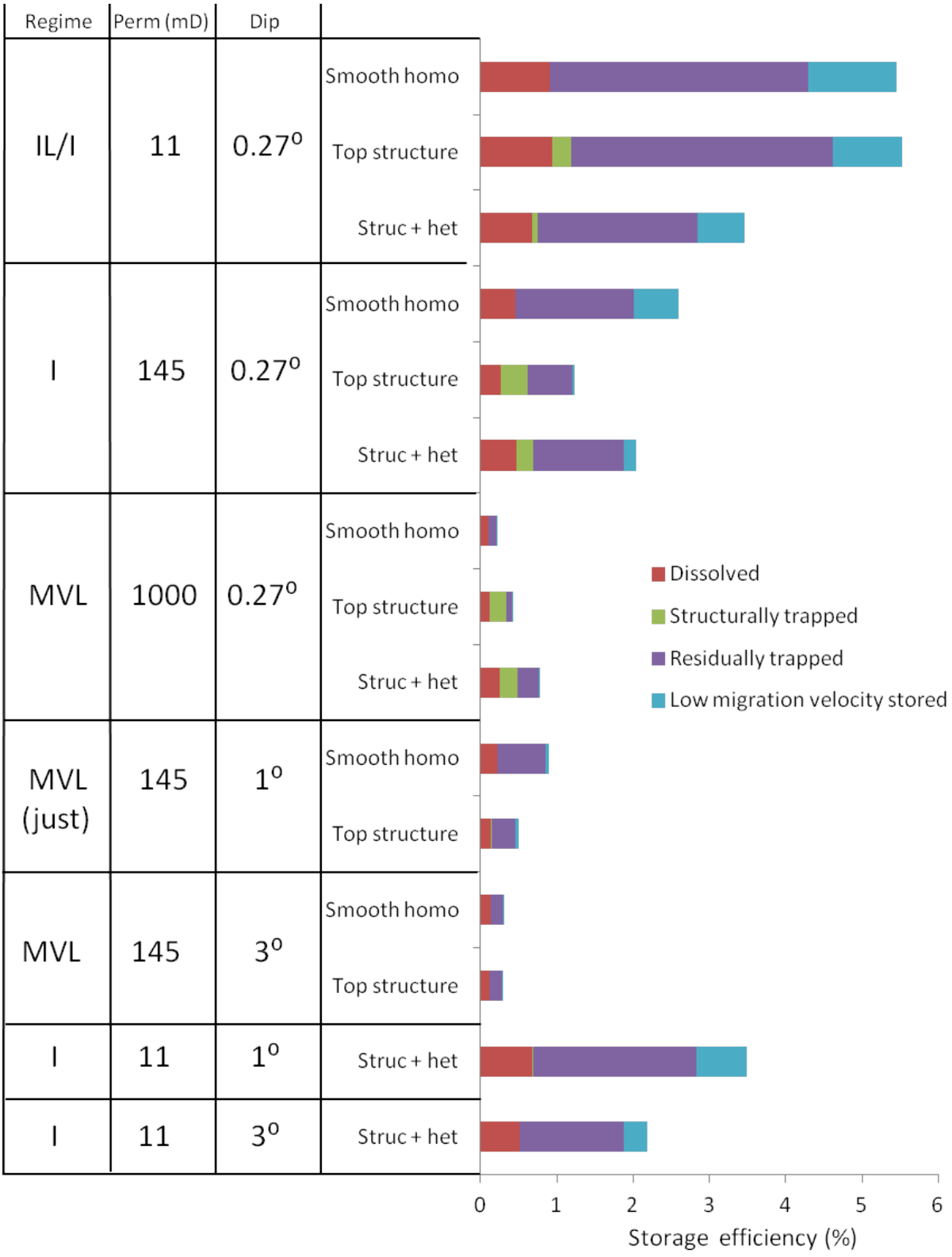


Figure 3.28: Storage efficiency results for various sensitivities

3.3.4 Sensitivity to Reservoir Dip and Permeability

The sensitivity of our capacity results to changes in average reservoir dip and permeability were assessed. This was used to:

- Test the sensitivity results (UKSAP, 2011a) used to form the storage regimes, which showed that dip and permeability had a key influence upon the storage efficiency of a storage unit, with a case that has real top-surface structure and heterogeneity.
- Check the analysis of the resultant three broad storage regimes as described in Section 2.1.2 and shown in Figure 2.2.

All our sensitivity results are shown in a combined form in Figure 3.28 and Table 3.2. In the following analysis selected sensitivities are highlighted.

Base Case Sensitivity to Permeability

We ran sensitivities to the arithmetic average permeability of our base case as described in Section 3.2.5 with results shown in Figure 3.29. The sensitivities considered were 145mD and 1D representing the migration velocity limited and intermediate storage regime cases to be investigated, respectively. Given computational time constraints a <11mD permeability case was not modelled, since the base case was fairly representative of injectivity limited storage regime. This is also a rather low permeability and most storage sites are likely to be chosen to have permeabilities of at least 10 mD to avoid injectivity issues.

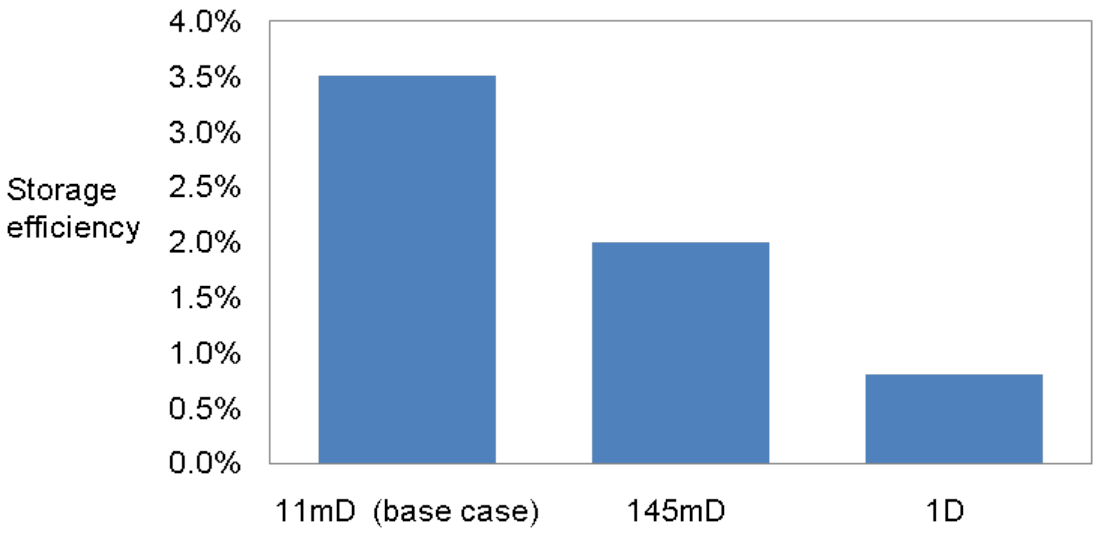


Figure 3.29: Sensitivity of base case storage efficiency to average permeability.

In the 145mD case, representative of the intermediate storage regime, the higher permeability compared to the 11mD case meant storage efficiency was no longer limited by the BHP constraint, confirming the change from the injectivity limited storage regime to intermediate. This allowed for potential injection leading to the CO_2 saturation profile shown in Figure 3.30 where CO_2 equal to 4% of the pore volume was injected; higher than the 3.5% injected into the BHP constraint limited 11mD base case. This injection scenario was able to meet the 99% storage constraint; however it failed the migration velocity constraint. The resulting final injection scenario that satisfied the migration velocity constraint is shown in Figure 3.31 with storage efficiency of 2%. This efficiency was constrained by both the 99% storage constraint and the migration velocity constraint. That the migration velocity constraint has an impact upon this intermediate storage regime result is interesting and we shall consider this in the conclusions at the end of this section.

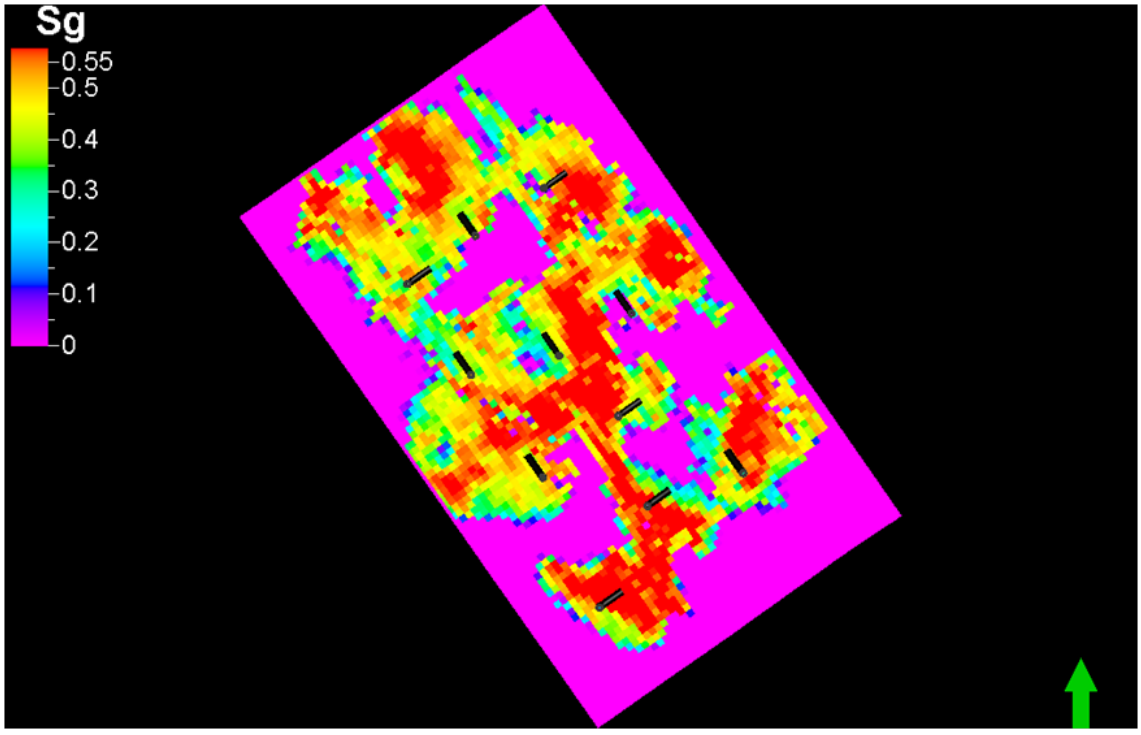


Figure 3.30: Figure 3.14: Top layer saturation profile at 1000 years for 145md permeability sensitivity. The injection scenario shows injected CO_2 equal to 4% of the storage unit pore volume. 0.4% of the injected left the model - meeting the 99% storage constraint; however the migration velocity constraint was failed. Wells shown in black.

This 2% storage efficiency result confirmed that we could still achieve reasonable storage in an intermediate storage regime site and also an expected decrease in capacity with increasing permeability. In the 1 Darcy average permeability case we also saw a further

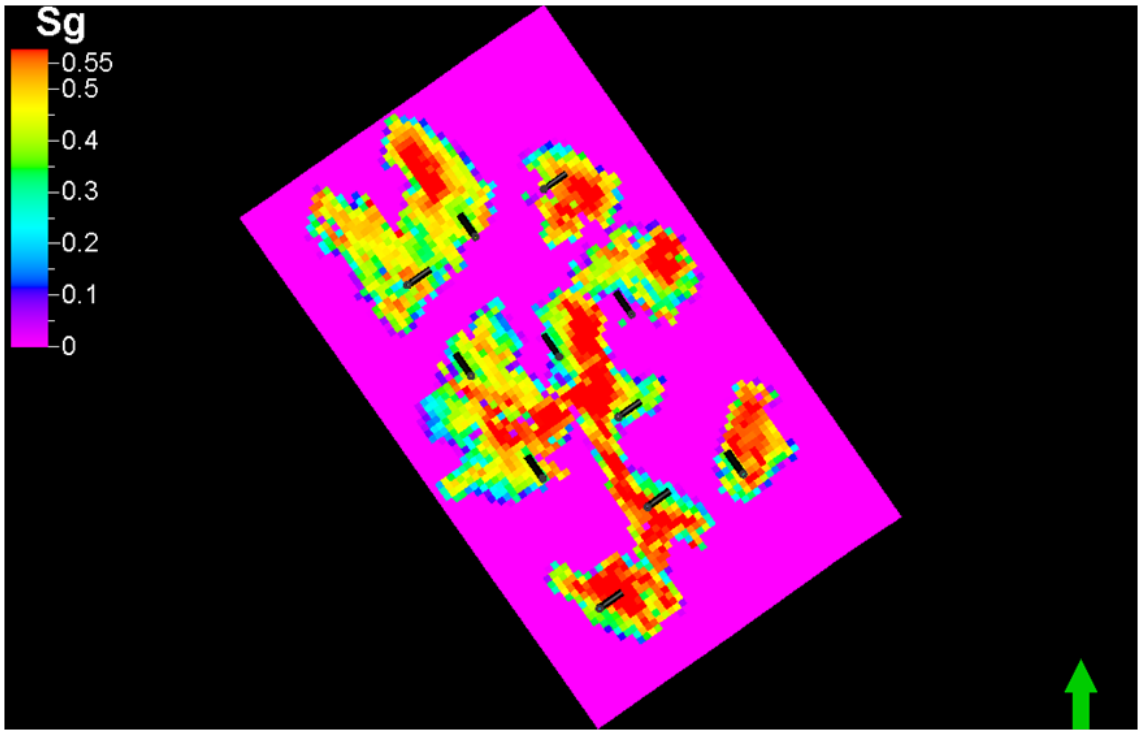


Figure 3.31: Top layer saturation profile at 1000 years for 145md permeability sensitivity. The injection scenario shown injected CO_2 equal to 2% of the storage unit pore volume and met the storage constraints. Wells shown in black.

reduction in storage for a migration velocity limited storage regime site. The storage capacity in the adapted base case was reduced to 0.8% of the pore volume which was significantly limited by the migration velocity constraint, as expected for the migration velocity limited regime.

Base Case Sensitivity to Dip

We ran sensitivities to the reservoir dip of our base case as described in Section 3.2.5. The sensitivities considered were 1° and 3°. Again these dips are larger than the base case that has a value of only 0.27°. Since our base case had 11mD permeability both of these cases still had characteristic velocities representative of the intermediate storage regime as shown in Table 3.2.

The results of these sensitivities are shown in Figure 3.32 and demonstrate a decrease in storage with increasing dip, but only in the 3° case does the migration velocity constraint becomes more important than the BHP constraint. In the 3° dip case the migration velocity constraint reduced the amount stored as otherwise it was possible to inject more CO_2 than the 2.2% injected and still satisfy the 99% storage constraint. The storage efficiencies of 2.2% and 3.5% storage still show that these models had storage

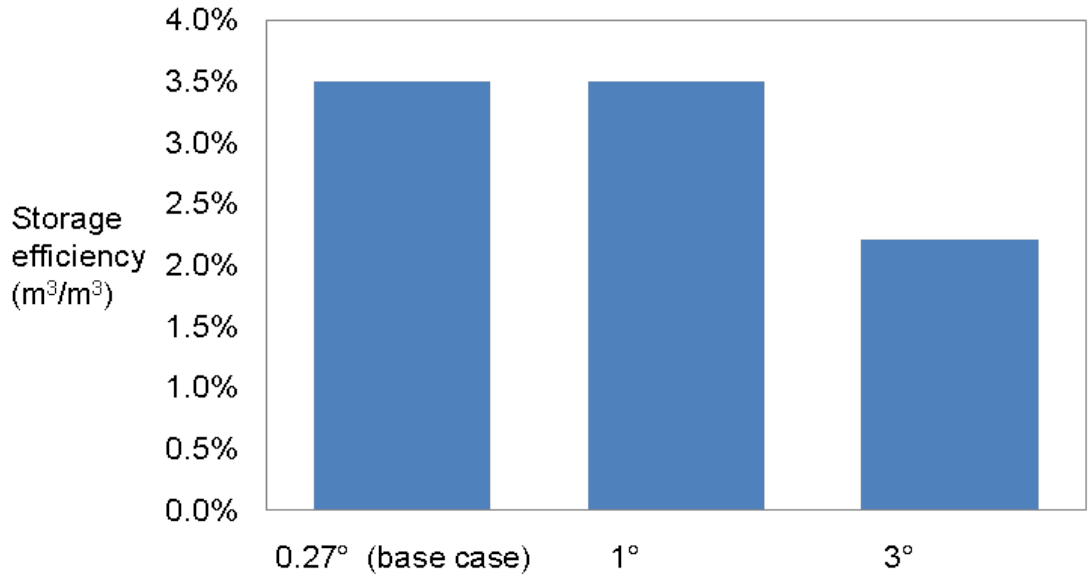


Figure 3.32: Sensitivity of base case storage efficiency to reservoir dip.

efficiency as would be expected by the characteristic velocity analysis categorising these models as intermediate storage regime. However, we again see that the migration velocity constraint can impact the intermediate storage regime as well as the migration velocity limited storage regime storage units here though.

Conclusions and Analysis of the Dip and Permeability Sensitivity and Storage Regime Results

In this section we have shown that the storage regimes shown in Figure 2.2 from Gammer et al. (2011) still apply when structure and heterogeneity are introduced to dip and permeability sensitivities. The storage efficiencies in Section 3.3.4 are broadly consistent with the concept that storage efficiencies in the migration velocity limited and intermediate regimes have come from different distributions with efficiencies below 1% for the migration velocity limited storage regime and above 2% for the intermediate storage regime. However, if we look at Figure 3.33 we can see that the disparity between the two regimes is noticeably smaller for our realistic heterogeneous model with top-surface structure than in the homogeneous smooth models. Section 4 looks more at the effect of top-surface structure and heterogeneity to explain this.

There is one other distinct issue highlighted in these results - that the migration velocity constraint can constrain capacity in the intermediate storage regime. Based upon the analytic up-dip migration calculation used in UKSAP (2011a), and shown in Equation 2.6, we might not expect this, so we consider why this occurred. It is possible

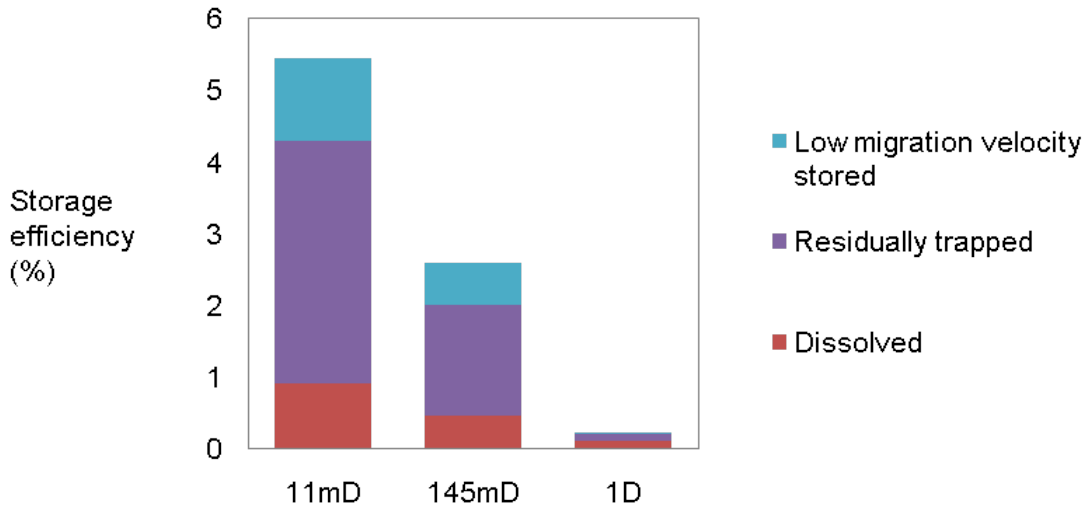


Figure 3.33: Sensitivity of storage efficiency due to changes in permeability in the 0.27° dip, smooth homogeneous model.

this occurs because of high permeability or high dip areas in our heterogeneous base case model, so we consider a smooth homogeneous case to rule this out. The homogenous case considered is the 145md 0.27° dip case and its saturation profile is shown in Figure 3.34.

The result of this is that both the 99% storage constraint and migration velocity constraint constrain capacity. To explain why the migration velocity constraint still has an impact in the intermediate storage regime we consider the analytic analysis of flow velocity a little further than in UKSAP (2011a) and Equation 2.6.

In this analytic analysis we also consider the velocity of spreading of the buoyant CO_2 plume as by Vella and Huppert (2006). This velocity is in addition to the component of flow updip due to gravity that is used to separate the migration velocity limited and intermediate storage regimes in Equation 2.6 - the first term in Equation 3.2. Using this, the velocity of CO_2 migration is estimated as

$$v = \frac{K\lambda_{CO_2}\Delta\rho g}{(1-S_{wc})\phi}\left(\sin\theta + \frac{\partial h}{\partial x}\cos\theta\right) \tag{3.2}$$

where $\Delta\rho = \rho_{water} - \rho_{CO_2}$, h is the connected height of CO_2 in the direction perpendicular to the top-surface and x is the distance along the top-surface, and θ is the dip angle. The second term in this accounts for the buoyant spreading of CO_2, an effect often seen through the resulting gravity tongue. This also provides an explanation of how the intermediate storage regime models can have migration over 10m/year at 1000 years

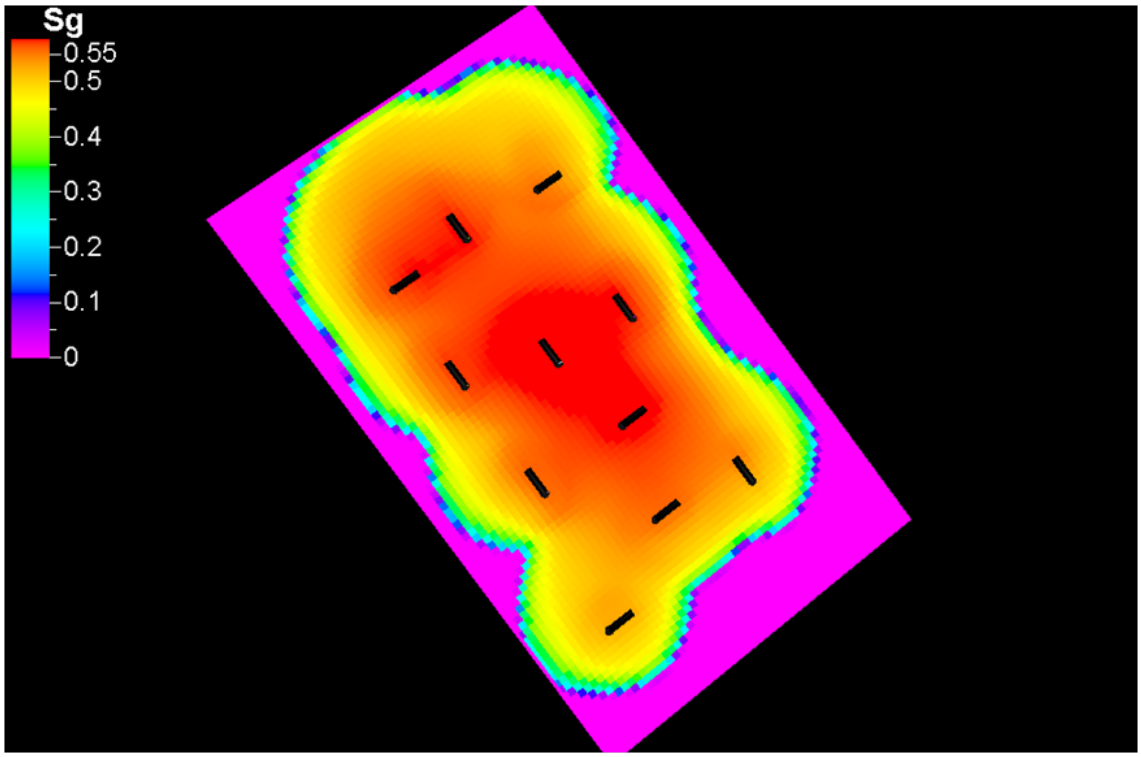


Figure 3.34: Saturation profile at 1000 years for the 0.27° dip, 145md permeability, smooth homogeneous model. The top layer is shown from above.

when the first term alone does not predict this.

To demonstrate that this second term is able to notably increase the size of the migration velocity at 1000 years we consider it in the 0.27° dip, 145md permeability smooth homogeneous case as seen in Figure 3.34. Here sin 0.27 = 0.0047, cos 0.27 = 0.99999 and $\partial h/\partial x \approx 0.002$ estimated using $\Delta h = 4$m and $\Delta x = 2000$m from Figure 3.35. In this case we can see from Equation 3.2 that approximately a third of the velocity is caused by the buoyant spreading term. Using values from Table 3.1, $S_{wc} = 0.423$ and $K_{r,max}$=0.2638 the contribution to the velocity from the first term is 3.8m/yr and the second term is 1.6m/yr. Although the contribution from the second term is smaller in this case it can clearly have sufficient magnitude to cause the migration velocity to breach the 10m/year limit when estimates based upon the first term are below this limit. Further, in cases with higher injection $\partial h/\partial x$ has a tendency to be larger at the same fixed time and thus have a greater relative influence upon migration velocity.

Although the first term may not always predict the velocity exactly there is still a key difference between the two terms though, which means that use of the first term alone is good for dividing models between these the intermediate and migration velocity limited storage regimes. This difference is that the updip gravity term is purely dependent upon

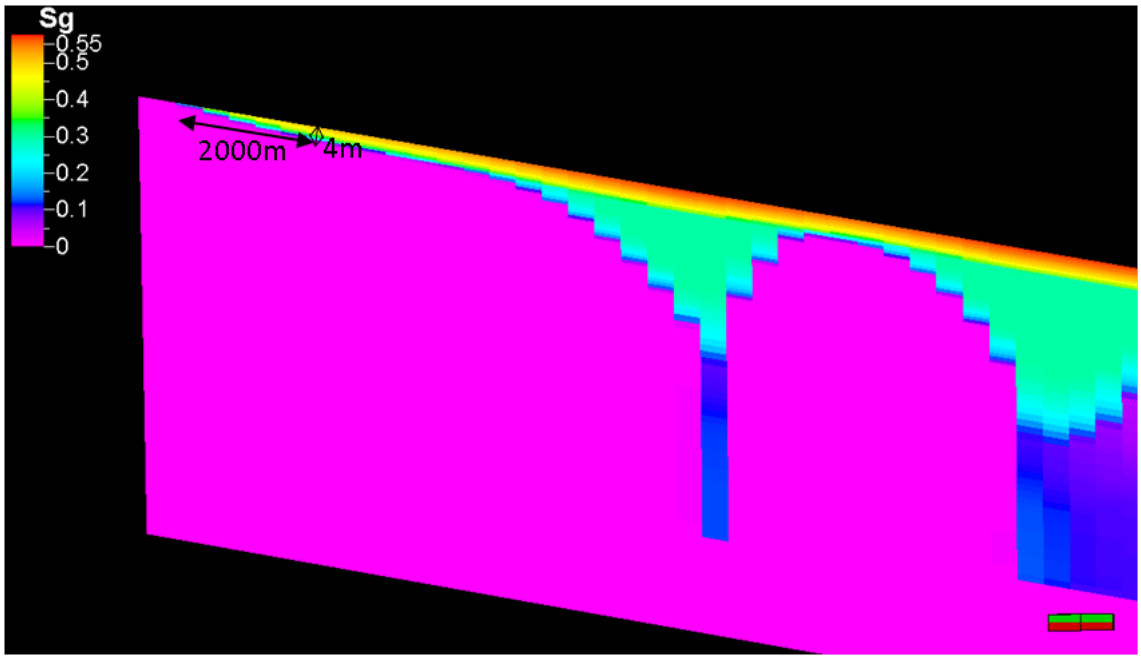


Figure 3.35: Cross-section of saturation profile for the 0.27° dip, 145md permeability, smooth homogeneous model at 1000 years. Estimates of change of the connected height of CO_2 and the distance over which this change occurs are shown. The connected height is estimated by CO_2 above the maximum residual gas saturation. Model exaggerated by a factor of 40 in the vertical direction.

the dip and permeability whereas the other depends upon the amount of CO_2 injected via the connected height of CO_2. This leads to a difference in how the migration velocity constraint acts in the intermediate storage regime and the migration velocity limited storage regime; since in general the second term is more important in the intermediate storage regime and the first term is by the definition of the migration velocity limited storage regime important in this case.

In homogeneous intermediate storage regime cases a volume of mobile CO_2 can be stored without it travelling faster than migration velocity constraint threshold allows. Above this volume the migration velocity constraint is breached due to the magnitude of buoyant spreading term. In homogenous migration velocity limited storage regime cases if any cells with high saturation mobile CO_2 were present they would by definition have too high migration velocities. Thus it is not possible to have any high saturation CO_2 in the migration velocity limited storage regime and the only low velocity CO_2 must be at lower mobility saturations.

Figure 3.36 shows that for the set of smooth homogeneous models with permeability variation we see low migration velocity storage consistent with this understanding. In the 145mD intermediate storage regime case although the migration velocity constraint was

limiting as described above, low migration velocity storage is allowed as can be seen by the high mobility saturations in Figure 3.34 and the 80Mt stored in Figure 3.36. The 1 Darcy case representing the migration velocity limited storage regime also fits our analysis only storing 3Mt of low velocity CO_2 and in Figure 3.37 we see that this is at saturations significantly lower than the highest mobility.

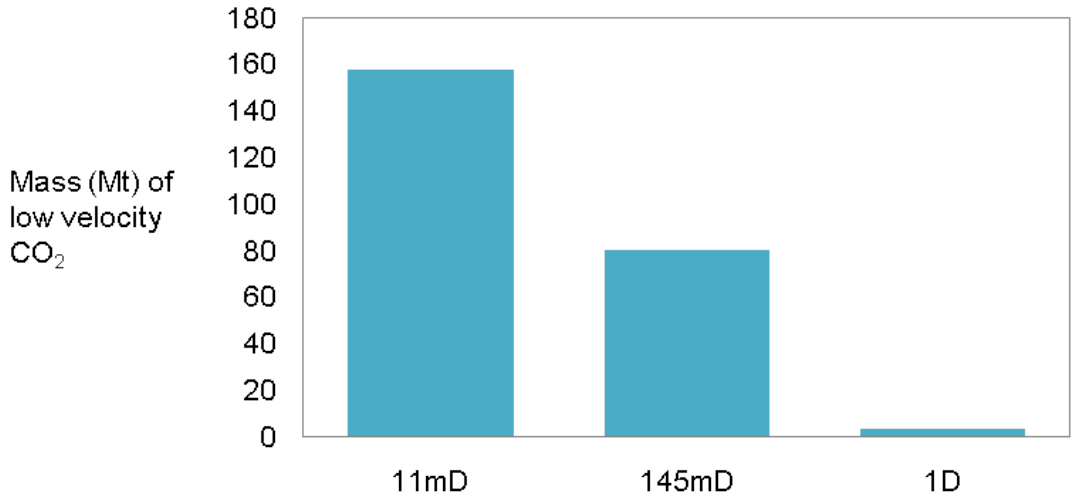


Figure 3.36: Sensitivity of the stored mass (Mt) of 'low velocity CO_2' to permeability in a 0.27° dip, smooth homogeneous scenario. Low velocity CO_2 is defined in Section 3.2.4

To summarise this short analysis, it has been seen that the migration velocity constraint can affect both the intermediate and migration velocity limited storage regimes. In the intermediate storage regime it limits the size of a migrating plume, but in the migration velocity limited storage regime it essentially prevents any highly mobile CO_2 remaining at 1000 years, or alternatively it virtually stops low migration velocity storage. The impact of preventing low migration velocity storage in the migration velocity limited storage regime is that less can be injected, reducing the amount of dissolution and residual trapping and ultimately reducing storage efficiency.

Following the understanding of the migration velocity constraint we can produce a general set of possible capacity constraining scenarios for each storage regime. Table 3.2 shows a summary of the results.

Injectivity Limited Storage Regime

- Limited by BHP combined with 99% storage constraint for location of wells

Intermediate Storage Regime

- Limited by BHP combined with 99% storage constraint for location of wells

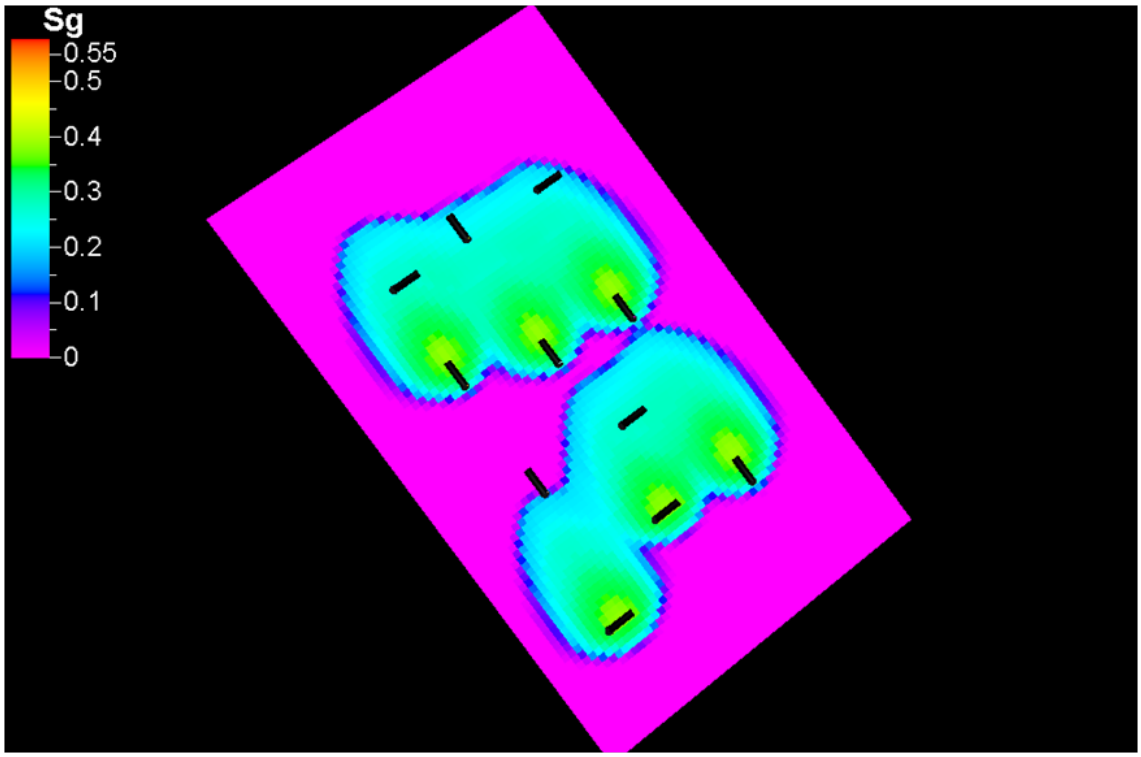


Figure 3.37: Saturation profile in the top layer of a smooth, homogeneous 1 Darcy model at 1000 years. Most gas saturation is seen to be near residual.

- Limited by migration velocity constraint due to size of migrating plume with 99% storage constraint for location of wells
- Limited by 99% storage constraint

Migration Velocity Limited Storage Regime

- Limited by migration velocity constraint preventing highly mobile CO_2 remaining at 1000 years with 99% storage constraint for location of wells

Finally we observe from Equation 3.2 that in the intermediate storage regime the migration velocity constraint for spreading CO_2 is still affected by permeability. Therefore within the intermediate regime once the dip permeability combination is such that the migration velocity is capacity constraining we would expect that as the permeability increases further migration velocity constraint would restrict plume sizes more and thus lower storage efficiency.

3.4 Top-Surface Structure and Heterogeneity Sensitivity Results

In this section we investigate the effect of top-surface structure and heterogeneity upon storage efficiency in dipping open aquifers. We shall use the method described in Section 3.2.5 to evaluate the effect the introduction of top-surface structure and heterogeneity cause to the storage efficiency of smooth homogeneous models in each of the storage regimes.

All our sensitivity results are shown in a combined form in Figure 3.28 and Table 3.2. In the following analysis selected sensitivities are highlighted.

3.4.1 Effect of Top-Surface Structure upon Storage Capacity

The effect of top-surface structure was evaluated in the different storage regimes since these have been seen to be the key determinant of storage efficiency. For the purpose of this analysis we shall consider the 11mD 0.27° cases modelled as our examples of the injectivity limited storage regime although they fall above the 10mD notional boundary set in UKSAP (2011a). These cases do however have the most important feature of the injectivity limitedstorage regime which is that storage is limited by injectivity due to low permeability.

Effect upon Models with Injectivity Limited Storage Capacity

The effect of top-surface structure upon storage capacity in the injectivity limited storage regime is minimal as shown by the change in the first two bars in Figure 3.38. Injectivity still limits storage. We see that some of the CO_2 that had a low migration velocity was stored at the top of the reservoir in the smooth homogeneous case sits within structural closures when top-surface structure is added. Further we can see very little difference between the plumes in Figures 3.39 and 3.40.

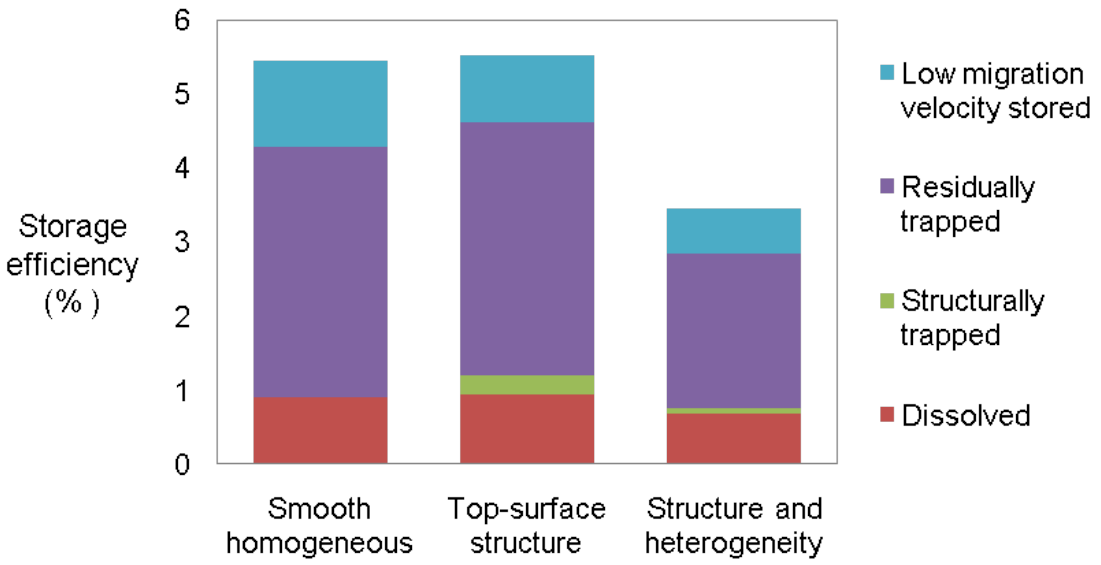


Figure 3.38: Change in storage efficiency due to the introduction of top-surface structure and heterogeneity to the 11mD 0.27° smooth homogeneous case.

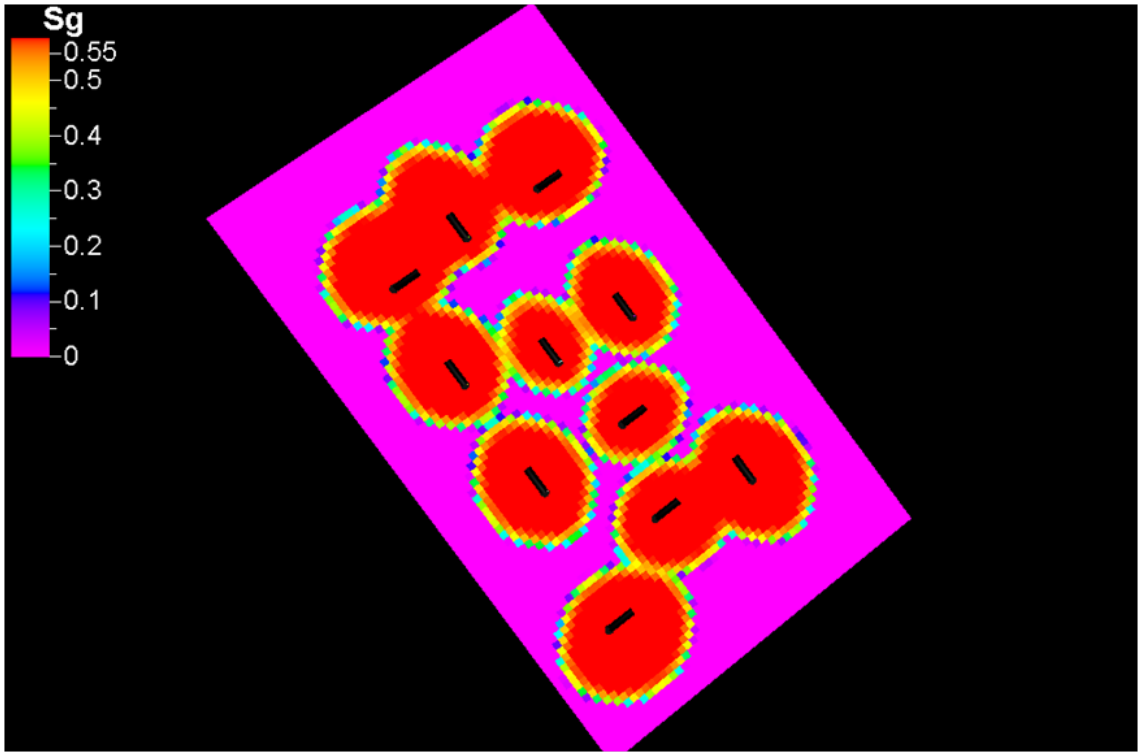


Figure 3.39: Saturation profile showing the top layer of a smooth homogeneous 11mD permeability model with a dip of 0.27° at 1000 years.

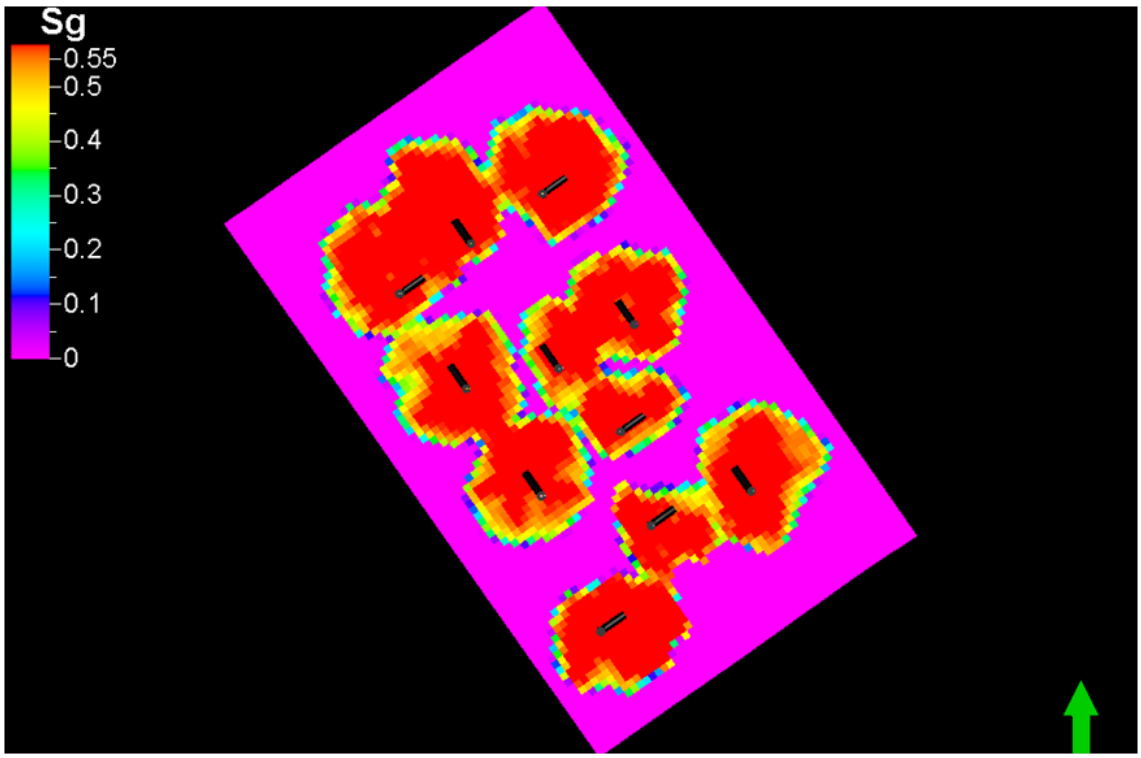


Figure 3.40: Saturation profile showing the top layer of 11mD permeability, 0.27° dip homogeneous model with top-surface structure at 1000 years.

Effect upon Models with Intermediate Storage Capacity

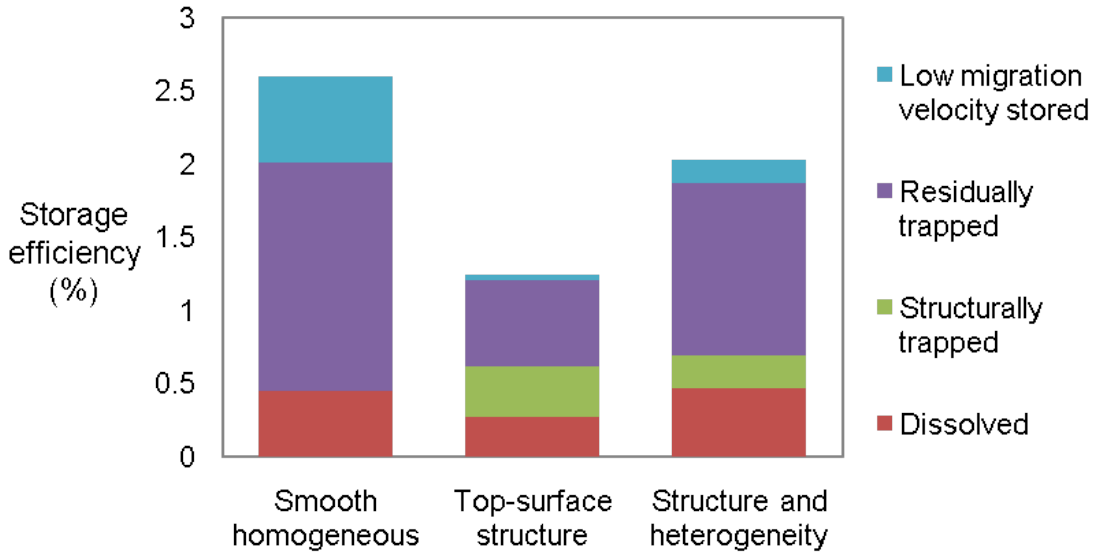


Figure 3.41: Change in storage efficiency due to the introduction of top-surface structure and heterogeneity to the 145mD permeability, 0.27° dip, smooth homogeneous case.

The introduction of top-surface structure into the 145mD intermediate storage regime model caused a drop in storage efficiency from 2.6% to 1.2% as shown in Figure 3.41. This reduction occurred during the optimisation of injection into the model with top-surface structure by the need to reduce injection rates into or even stop wells in regions with locally higher dip to comply with both the 99% storage constraint and the migration velocity constraint. For example, Figure 3.42 shows that it was necessary to shut-in two wells in the north-west (upper left) to meet the migration velocity constraint. In addition channelling led to poorer coverage of the top-surface.

By analysing how the CO_2 is trapped with and without the presence of top-surface structure it is possible to explain this reduction in storage further. Firstly, the introduction of structural trapping due to the introduction of top-surface structure provided 29% of the CO_2 that was injected. This can be seen in Figure 3.42 by the red high saturation patches. This extra trapping mechanism along with the less secure high dip regions introduced two features that had competing effects upon the storage capacity. First, structural trapping increased capacity. Second, high dip regions increased migration velocities, as well as distances, leading to a need to reduce injection to satisfy the storage constraints.

The combined effect of these two impacts is subtle. If the structural closures alone were placed above the smooth model there could be a 48Mt increase in storage. However,

in this realistic example, where the geology has created structural closures there are associated regions that dip away from the structure. Also in other areas full closure is not formed, or even worse, some partial closure or unclosed regions form routes that can either lead to escape or prohibited high velocity migration. The result is that the remaining top-surface area outside the structural closures and the area directly below the structurally stored becomes less efficient at storing than in the smooth model. In fact, the mass of low velocity stored CO_2 in the model fall from 80Mt to 5Mt. Effectively large portions of this area have gained characteristics of the migration velocity limited storage regime. As explained in the conclusions of Section 3.3.4, in the migration velocity limited regime where less CO_2 is low migration velocity stored, less is injected and therefore there is less dissolved or residually trapped CO_2 at 1000 years. This ultimately leads to the lower storage efficiency here.

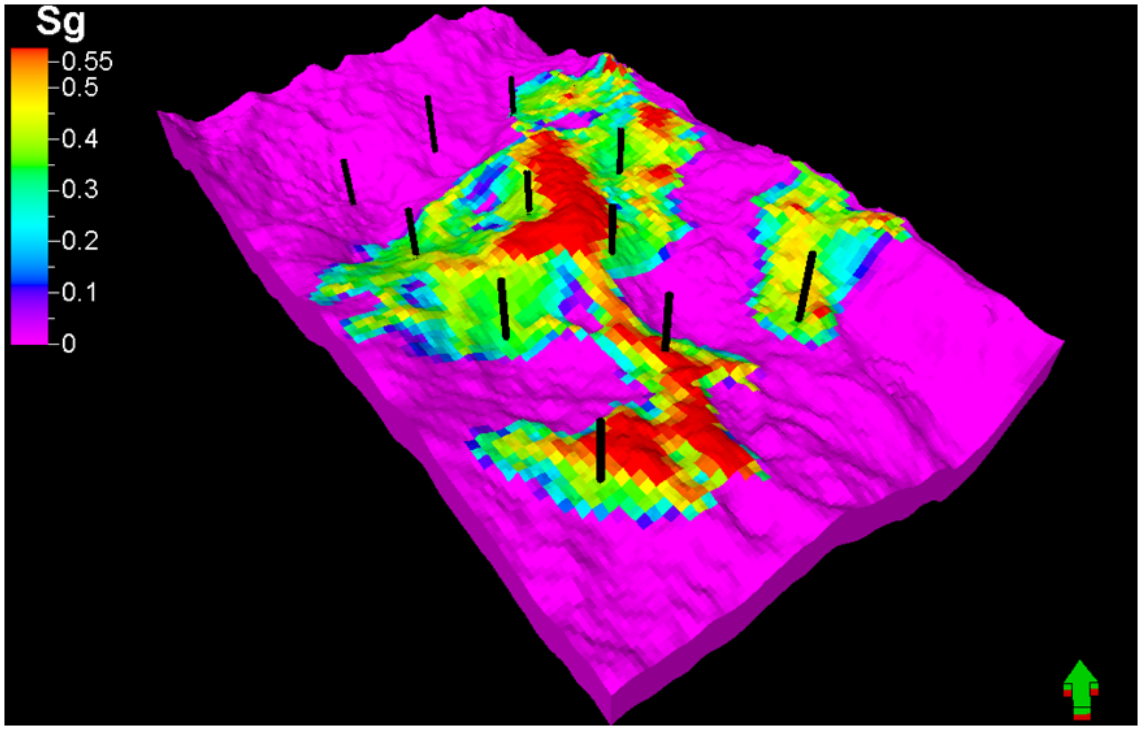


Figure 3.42: Saturation of a homogeneous 145mD, 0.27° dip model with top-surface structure at 1000 years. Model viewed from south and exaggerated by factor 15 in the vertical direction.

Effect upon Migration Velocity Limited Storage Regime Models

We simulated two dip and permeability combinations representative of the migration velocity limited storage regime, the 1D 0.27° case and the 145mD 3° case. A final 145mD 1° simulated scenario also had analytical estimates of its maximum gas saturation velocity

from Equation 2.6 of just over 10m/yr categorizing it as in the migration velocity limited storage regime but giving it characteristics in-between the intermediate and migration velocity limited storage regimes. We also consider this case.

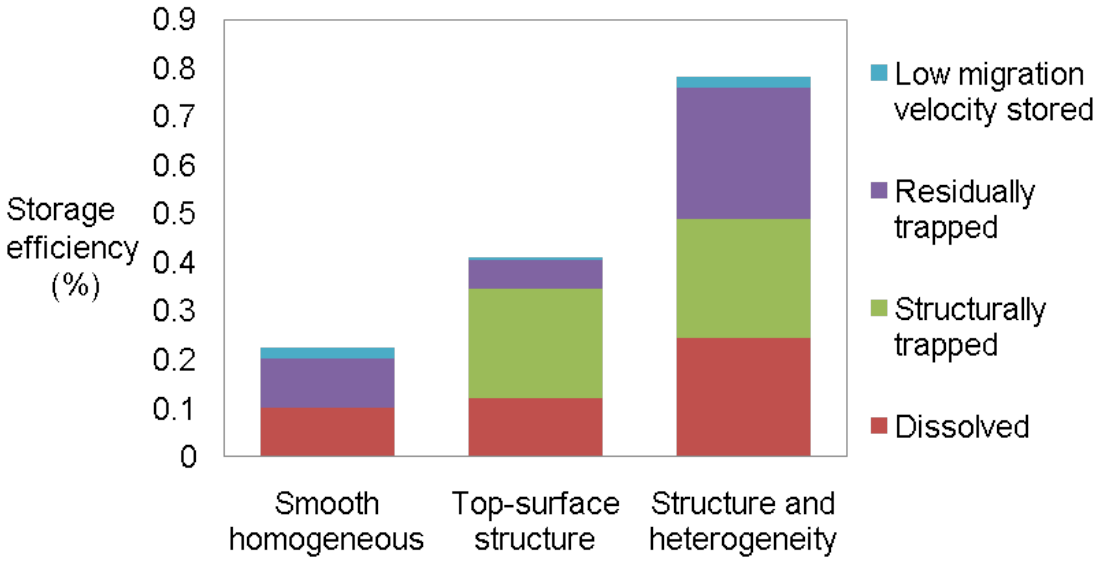


Figure 3.43: Change in storage efficiency due to the introduction of top-surface structure and heterogeneity to the 1 Darcy, 0.27° dip smooth homogeneous case.

First we consider the 1D, 0.27° case. As seen in the conclusions of Section 3.3.4, in the smooth homogeneous model this case had very low storage efficiency because the migration velocity constraint only allowed low migration velocity storage at saturations approaching residual that have very low mobility. Figure 3.43 shows that the introduction of top-surface structure increased the storage efficiency from 0.2% to 0.4%. The increase due to top-surface structure in this case is clear with 55% of the CO_2 stored in structural closures in the top-surface structure scenario; this figure almost directly corresponding to the increase in storage from the smooth case. The other key point is that the effect of high dip areas has been far less. This is because there was virtually no low velocity CO_2 in the smooth homogeneous case and thus the introduction of higher dip regions was unlikely to cause substantial unpermitted migration velocities and a need for reduced injection.

The second case modelled was the 145mD 3° case. The introduction of top-surface structure into the smooth model actually failed to produce any structural closure due to the 3° dip. This meant there was no opportunity to see an increase in storage due to structural trapping, however the effect of different and higher dip regions could be evaluated. The result was that there was no change in the storage efficiency staying at 0.3%

as shown in Table 3.2. Since the smooth case here was in the migration velocity limited storage regime and therefore without significant low migration storage, this supports the idea that the higher dip regions have little effect on storage efficiency if there is not low migration velocity storage in the smooth model.

The final case we consider is the 145mD 1° case, which is just categorized in the migration velocity limited storage regime, however gas saturations only 0.05 below the maximum gas saturation can still flow with velocity less than 10m/yr in the model, so it has some characteristics of the intermediate storage regime. For example at 0.9% the storage efficiency is substantially higher than the other smooth storage 3 models and the mass of low velocity CO_2 stored is 10 times larger than the mass of low velocity CO_2 stored in the 1Darcy and 3° sensitivity cases. At the the same time the efficiency and low migration velocity storage are still lower than the other intermediate storage regime cases. Given this evaluation the result of including top-surface structure seems to more closely represent the style of an intermediate storage regime scenario - see Figure 3.44. The 7Mt of low velocity CO_2 is reduced to 4Mt due to reduced well rates being approximately halved in all injecting wells to keep within the migration velocity constraint. This low level of low migration velocity storage is similar to that in the 145mD 0.27° model with top-surface structure. Also there is a low increase in storage from structural closure as the 1° dip stops most of the closure. The conclusion from this case is that in some cases that are only just across the intermediate/migration velocity limited storage regime boundary modest level of storage due to some fairly high saturation low velocity CO_2 can still occur and that the introduction of extra dip regions reduces storage efficiency in these migration velocity limited storage regime models.

Conclusions on the Effect of Top-Surface Structure

The introduction of top-surface structure introduces both structural closures and regions of high dip. The effects of these regions generally compete to increase or decrease storage efficiency respectively.

The balance of these effects has been assessed by understanding how CO_2 is stored within smooth homogeneous models prior to introducing structure into the models. This analysis of smooth homogeneous models divides them into those which can store CO_2 through low migration velocity storage at high saturations and those that cannot. This division generally divides units between the intermediate and migration velocity limited storage regimes, although one example showed that it is possible to have some modest low migration velocity storage just across the intermediate/migration velocity limited storage regime boundary.

For those smooth models that were in the intermediate storage regime, we saw a

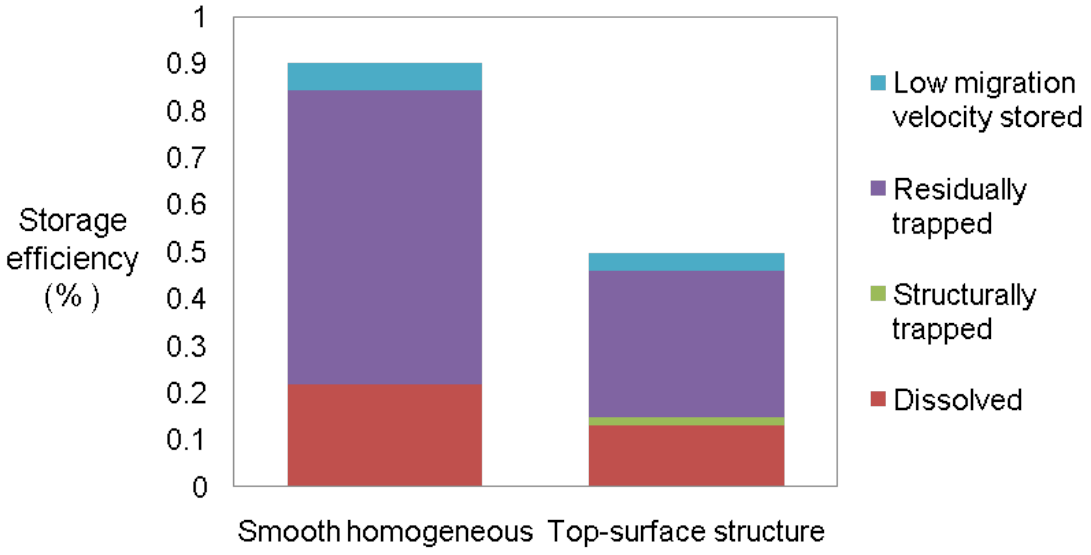


Figure 3.44: Change in storage efficiency due to the introduction of top-surface structure to the 145mD, 1° dip smooth homogeneous case.

decrease in storage as the effect of new higher dip regions reducing storage efficiency was more effective than the addition of structural closures increasing efficiency. For those sites that were in the migration velocity limited storage regime we saw either increases or no change in storage efficiency with the addition of top-surface structure. No change occurred when the top-surface added no structural closure.

These results show that there is only a significant drop in storage efficiency when high dip routes are introduced to intermediate regime models, rather than other regime models. This is because in models in this regime the high dip routes can cause a large reduction in low migration velocity storage.

From this we conclude that high dip routes have a qualitatively different effect on storage when added to intermediate storage regime models than migration velocity limited regime models. This is because the first can lose a lot of low migration velocity storage whereas the second does not.

The identification of the effect of high dip routes is in some way an extension of the migration velocity limited storage regime. As with that storage regime, the high dip routes are characterised by their ability or not to store low velocity CO_2. Therefore the introduction of high dip regions is similar to introducing regions that have the qualitatively lower storage efficiency of the migration velocity limited storage regime. This result further demonstrates the significance of low migration velocity storage upon storage efficiency as shown in the conclusions of Section 3.3.4.

Further, our results show that the addition of localised structural closure alone will increase storage. In cases where there is virtually no low migration velocity storage of CO_2 such as typical migration velocity limited storage regime cases, where the addition of the introduction of high dip regions have little effect upon storage, this may be the dominant effect of the introduction of top-surface structure.

3.4.2 Effect of Heterogeneity upon Storage Capacity

The impact of heterogeneity upon storage efficiency was also evaluated under each of the storage regimes using the same dip and permeability scenarios as in Section 3.4.1.

Effect upon Models with Injectivity Limited Storage Capacity (injectivity limited storage regime)

The effect of heterogeneity upon a storage unit with injectivity limited storage efficiency is evaluated using the 11mD 0.27° scenario with results shown in Figure 3.38. Here we can see that the introduction of heterogeneity significantly reduced the amount injected and resulting storage efficiency from from 5.5% to 3.5%. The capacity in both examples was constrained by the same BHP constraint so we can deduce that the pressure near well built up to this pressure with a lower injection rate than the heterogenous case. To confirm this we can see in Figure 3.45 that in the heterogenous case the pressure at the well has built up as high as the homogeneous case, despite the lower injection. We can also see that this is a result of more localised pressure build-ups. These localised pressures can be seen to occur in regions surrounded by low permeability volumes such as shales, and therefore these low permeability volumes cause lower injection and storage efficiency.

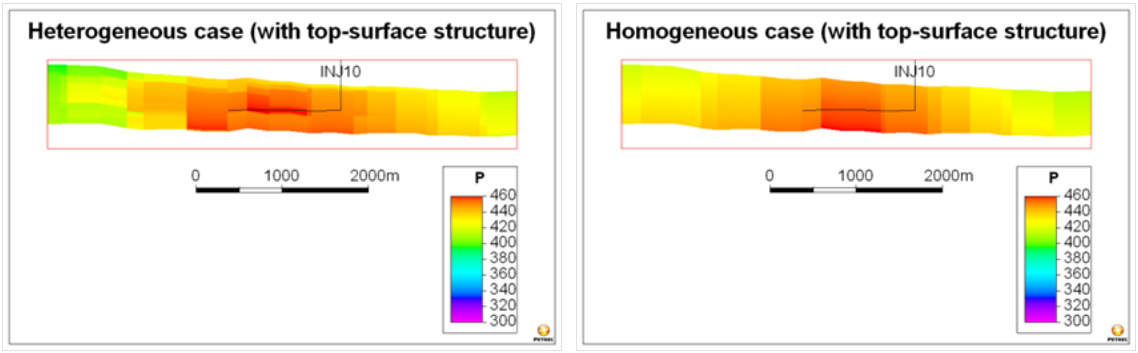


Figure 3.45: Pressure (bars) profile around well INJ10 in heterogeneous (left) and homogeneous (right) cases at 50 years. The intersections show that localised high pressure can build up in the heterogeneous model whereas it spreads further in the homogeneous model.

Effect upon Intermediate and Migration Velocity Limited Storage Regime Models

We consider the effect of heterogeneity upon storage efficiency in models in the intermediate and migration velocity limited storage regimes together since similar results are

found in each. In particular the two cases considered are the 145mD 0.27° intermediate storage regime case and the 1D 0.27° migration velocity limited storage regime case. The storage results for these cases are shown in Figure 3.41 and Figure 3.43 respectively.

In both these figures we see that the introduction of heterogeneity increases storage, from 1.2% to 2.0% and 0.4% to 0.8% respectively. Within this increase dominant rises come from increases in residual trapping and dissolution. The reason for this is that the heterogeneity, such as shale layers, within the model was able to increase the amount of lateral migration of the CO_2 after injection leading to a greater reservoir contact and therefore greater residual trapping and dissolution. This is shown in Figure 3.46 where far greater lateral migration and sweep is seen in the heterogeneous case whereas CO_2 in the homogeneous model takes the most direct route to the surface.

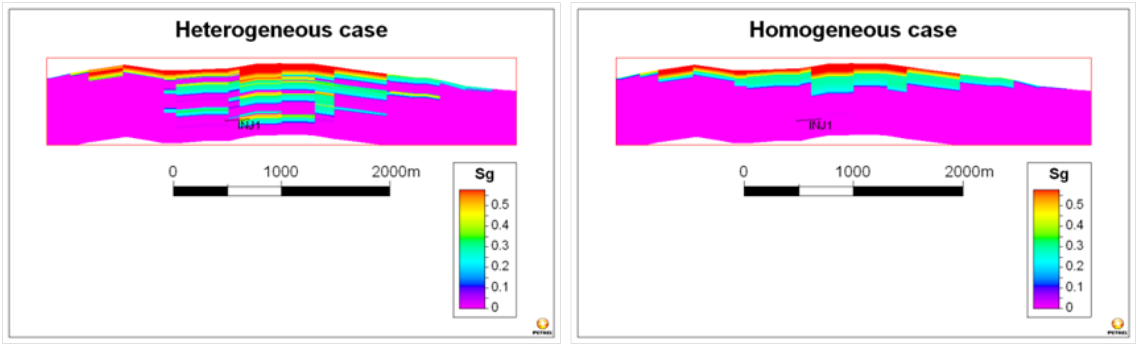


Figure 3.46: Saturation intersections to show wider lateral migration under shales in the heterogeneous model (left) compared to the homogenous model (right) at 1000 years. Both models have 145mD permeability and 0.27° dip.

The other increase that is seen is in the low migration velocity storage; however the extra low migration velocity storage is likely to be due to structural trapping under small shale layers deeper within the reservoir, an example of which is shown in Figure 3.47.

Conclusions on the Effect of Heterogeneity

The introduction of heterogeneity has two major effects upon storage efficiency. In models where injectivity is the limiting factor, such as injectivity limited storage regime and some low permeability intermediate storage regime cases, the addition of heterogeneity reduced the amount that could be injected under a BHP constraint and thus reduced the storage efficiency. In models where either the 99% storage constraint or migration velocity constraint constrained storage efficiency, the introduction of heterogeneity was seen to improve storage efficiency by improving the lateral sweep of CO_2.

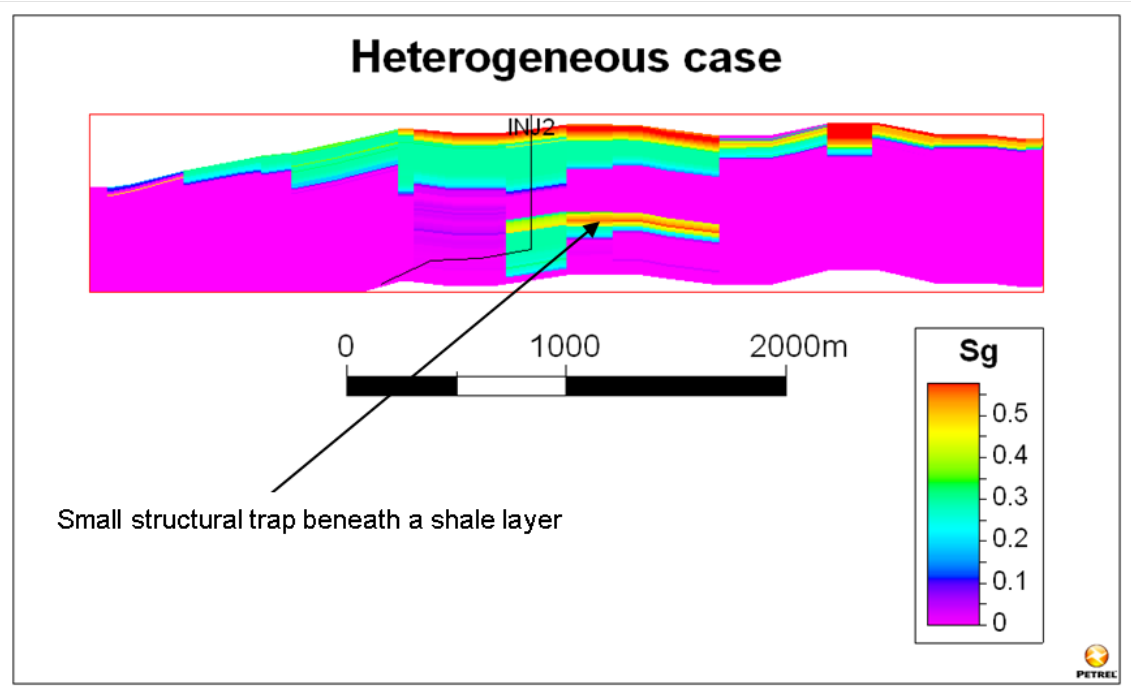


Figure 3.47: Gas saturation intersection around well INJ2 to show structural trapping under shales at 1000 years for the 11mD heterogeneous case.

3.5 Discussion

To assess the implications and significance of the results presented we first consider the limitations of the assumptions and setup used. With these caveats we will then place our results in a broader context for estimating regional storage capacities.

3.5.1 Limitations and Assumptions

Regulatory Assumptions

Some important assumptions influencing these results are the constraints within which storage units had their capacity assessed. These assumptions come from Gammer et al. (2011) and interpret current regulation and guidance. These constraints allow us to make more realistic capacity estimates in keeping with the interpretation of current regulation, for example permitting mobile but very slowly migrating CO_2 at 1000 years in our capacity. However, regulation can change or current regulation could have been interpreted differently and the results of this work could have some sensitivity to this.

We briefly consider what alternative regulations could be used as follows. First, we note that the underlying driver of regulation must be to restrict the mass of CO_2 released

to the atmosphere and stop any form of release that may be dangerous to human health. Therefore in its broadest sense the aim of regulation must be

- To ensure that $x\%$ of injected CO_2 must be stored for z number of years. The proportion x may change with time. Also, rather than a number of years the aim may be permanent. If some volume CO_2 is allowed to escape then a restriction may be applied to the rate of release to avoid human health problems.

However to achieve this aim the actual regulation may be a proxy for this, under the assumption that by satisfying the proxy, the central aim would also be satisfied. Such proxies may be used for practical reasons such as the feasibility of their prediction using reservoir simulation. Possibilities for these proxies may say

1. That $x\%$ of injected CO_2 must be within the storage unit at year z.
2. That $x\%$ of injected CO_2 must be residually/structurally/solubility or mineral trapped at year z.
3. The migration velocity of movement of CO_2 at year z must not exceed w metres/year. This may be limited the velocity of flow of CO_2 at the extent of the plume and/or may need to be monotonically decreasing.

In this work, we had a migration velocity constraint as well as a constraint that 99% of CO_2 is within the storage unit at 1000 years. However, it is not clear that the migration velocity constraint is necessarily the best constraint. In particular the assumption that it, along with the 99% storage constraint, leads to the underlying bullet-pointed aim is uncertain. It does not seem to guarantee security of CO_2 after 1000 years, although this may be the purposeful limit of the regulation. We suggest the second regulation on the list would be more explicit with it's purpose.

If in future there was a change in this regulatory constraint it may affect of our results. The decision over whether or not there should be a change should ideally consider an analysis of the costs, benefits and feasibility of the potential regulation involved.

Assumptions for storage capacity assessment

A number of assumptions were also required for the assessment of storage capacity within the regulatory framework set out. In particular our assessment was based on the storage site scale and scenarios with increased dip used tilted versions of the same top-structure.

The first of these assumptions was evaluation at the scale of a storage unit that may be considered for licensing and provide operations for a company for years to decades, rather

than the entire basin-scale. This provided varying top-surface structure and heterogeneity over a significant 21km × 36km region for assessing the effects of these features. In this work we have assumed that regulation would apply directly to the storage unit scale and therefore assessed the effects of structure and heterogeneity at this scale. At the basin scale the balance of effects of structure and high dip routes could be altered, for example if the effect of high dip routes regions tends to be more influential near boundaries, investigation of this could be considered for further work. In addition we have considered open boundaries over a storage unit scale, when potentially other units could neighbour this unit, changing the nature of the boundary condition. Given the significant scale of a storage unit, it is not clear how often neighbouring storage units would be in operation at the same time and thus if over time neighbouring open units were used, there may be a time interval between injection during which pressure dissipation could occur.

The second was the effect of top-surface structure on storage sites with larger average dip was assessed using tilted versions of the base-case Forties structure. In our examples with 1° and 3° dip this resulted in very little and no structural closure in the models respectively. This example may or may not be representative of structural closure in higher dip reservoirs. To analyse this further new consideration of a variety of structures would be needed.

Finally, we note that we have used a number of deterministic estimates of storage capacity in this work. This has been to identify the effects associated with top-surface structure and heterogeneity. To provide practical storage capacity estimates that take account of uncertainty in a number of parameters, a probabilistic approach should be taken. This approach was taken by the UK Storage Appraisal Project UKSAP (2011b), which this work was closely related to.

3.5.2 Implications of Results

Accepting these assumptions, we now outline the implications of our results to storage capacity estimation.

We begin by looking at the implication of introducing high dip regions to smooth models, then structural closure and then the combination of the two as occurs in a realistic top-surface structure.

First we consider the implication of introducing high dip regions. We have shown in Section 3.4.1 a qualitative difference between the effect of introducing higher dip routes to smooth model cases with strong low migration velocity storage (intermediate storage regime) and cases with weak low migration velocity storage (migration velocity limited storage regime). The implication for storage capacity estimation is that the addition of localised dip that leads to escape or prohibited high migration speeds will:

- Significantly decrease storage efficiency when low migration velocity storage is high in the equivalent smooth model.
- Make significantly less difference to storage efficiency if there was little low migration velocity storage in the smooth model.

Secondly, we consider the implication of introducing structural closure. Our results have shown that the addition of localised structural closure will increase storage almost independently of low migration velocity storage. Therefore we expect that the implication for storage capacity estimation is that structural closures will, unsurprisingly, provide additional storage capacity; although the use of this volume depends upon the CO_2 plumes being able to access the correct regions.

With these evaluations of the effect of high-dip routes and structural closure, the general change in storage efficiencies from top-surface structure will depend upon the geological occurrence of structural closures versus high dip routes that the top-surface structure introduces. However, it is more likely that storage units with high amounts of low migration velocity storage (intermediate storage regime) would have their capacity overestimated by smooth models than storage units with virtually no low migration velocity storage (migration velocity limited storage regime). This idea is demonstrated in Figure 3.48.

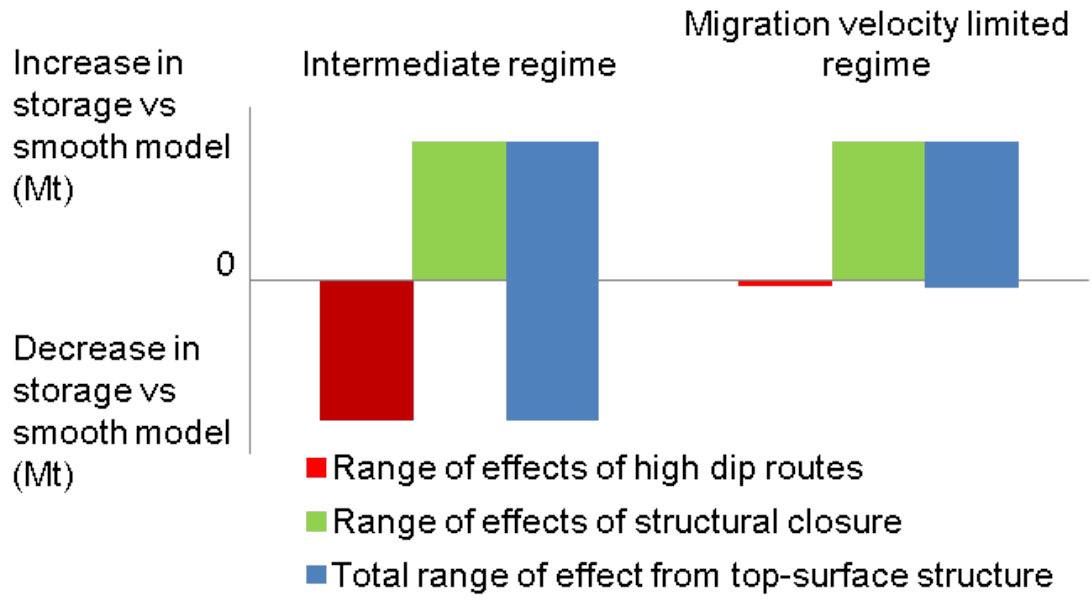


Figure 3.48: Range of potential general effects of the introduction of top-surface structure to intermediate and migration velocity limited storage regime models.

To extend these ideas any further, investigation into the geostatistical occurrence of closure versus high dip routes would be needed. At the national scale this would be useful

to avoid systematically overestimating or underestimating storage with smooth models, especially since we have seen that factor of 2 or more decreases and increases in storage efficiency can occur with the introduction of top-surface structure relative to smooth model figures.

There may also be some risk implications arising from the uncertainty in estimates if the effect of top-surface structure cannot be modelled. If risk is to be avoided more conservative estimates may come from more reliance upon residual trapping, or alternatively estimates that are less influenced by structure may come by considering enhancing residual trapping through the use of brine and CO_2 injection together (Qi et al., 2009).

For heterogeneity similar issues exist with assessing the implications and significance of our conclusions due to the site specific permeability distribution. We have observed that heterogeneity can reduce injection significantly in injectivity limited scenarios and increase sweep in the remaining cases. In both cases the shale layers present in the model played an impact upon these, affecting the spread of the pressure footprint and vertical migration of CO_2 respectively and therefore generalising these results is still unclear. For other models where shales are still present the explanation for reduced injectivity due to localised pressure build-up seems likely to be extendable; however further work could be done on this especially when there are no low permeability layers. The result on sweep is supported by a recent paper from Lengler et al. (2010) who shows that the time taken for breakthrough of CO_2 is increased by heterogeneity. Given the distances we consider are significantly longer than in that study by two orders of magnitude, we expect that heterogeneity improves sweep in the vast majority of cases, by suppressing gravity over-ride and rapid migration along the top of the formation, thus improving storage efficiency.

In summary this work uses a North Sea example to provide new insights into the effect of top-surface structure on storage efficiency and gives grounds for further understanding and analysis in the future. Of key significance is that this understanding is based upon analysis of the trapping mechanisms involved in CO_2 storage and helps to demonstrate their importance in determining capacity.

This understanding clearly demonstrates that top-surface structure can both increase and decrease storage efficiency relative to an equivalent smooth model. Whereas in some previous literature heterogeneity has been touted as a source of decreased security through increased migration, and caprock undulation as increased security (Juanes et al., 2010; Kopp et al., 2009b), it has been seen that top-surface structure provides a mixed picture and that heterogeneity tends to reduce overall CO_2 plume migration.

3.6 Conclusions

Top-surface structure and heterogeneity describe the variation of reservoir dip and permeability, which are the key parameters in determining the storage efficiency of dipping open aquifers. The effects were evaluated under an interpreted set of regulations for capacity estimation using a real North Sea top-surface structure and heterogeneity field and some optimisation of injection rates to estimate storage efficiencies. The results were interpreted in terms of three storage regimes.

In this case it was seen that the introduction of permeability heterogeneity to a homogeneous model

- reduced storage efficiency when the storage in the homogeneous model was limited by injectivity, due to localised pressure build-up;
- increased storage efficiency when injectivity did not constrain storage capacity, by improving the reservoir contact of CO_2.

And the introduction of top-surface structure to smooth storage units

- decreased storage efficiency for smooth units with slower characteristic flow velocities for mobile CO_2;
- increased or maintained efficiency for smooth units with faster characteristic flow velocities for mobile CO_2.

We described how the top-surface structure introduces both structural closures and regions of localised higher dip that either lead to escape or prohibited high migration speeds. The balance of the effects of these features is seen to determine the change in storage efficiency due to top-surface structure.

Further, the reduction in storage capacity due to localised higher dip is seen to be qualitatively larger for one type of storage unit. This is when top-surface structure is introduced to smooth models that have lower dip and permeability - which allow CO_2 to be stored in a mobile and laterally unconfined form at 1000 years - as opposed to those with higher permeability and dip.

In the North Sea model studied this dependency was significant enough that it governed the effect of introducing top surface structure on different models. When the smooth model was able to store mobile and laterally unconfined CO_2 at 1000 years the reduction in storage from the introduction of localised higher dip was greater than the increase in storage from the introduction of structural closure. Conversely when the smooth model was *not* able to store mobile and laterally unconfined CO_2 at 1000 years, the opposite result was found.

More generally we have presented a quantitative framework for assessing storage sites based on different constraints - pressure, migration distance and migration speed and placed different cases into three storage regimes. This has shown that open aquifers of modest permeability and dip can prove to be favourable storage sites with large storage capacities. These aquifers limit the speed with which the CO_2 migrates while the extensive open pore volume can help dissipate pressure, avoiding pressure problems associated with other types of storage site (Gammer et al., 2011). This suggests that with careful selection and design, large open aquifers are promising sites for CO_2 storage.

Chapter 4

Convergence of 1D Three Phase Solutions

4.1 Introduction

In times when the European carbon price is low, CO_2 storage in depleted oil reservoirs may be required to make early commercial projects economically viable. Therefore in Chapters 4 and 5 we shall consider three-phase flow, which models this process. When storing CO_2 in these reservoirs regulation will require that storage is well understood. In particular, it currently requires conformity of actual with modelled behaviour.

In order to make accurate predictions of subsurface CO_2 flow it is critical that the underlying physics are modelled correctly. One area of considerable concern is guaranteeing that simulations in three-phase flow capture physically-correct solutions. In Section 2.3.2 we reviewed work that showed that solutions to the system of equations that model three-phase immiscible water, oil and gas flow problems in one-dimension (1D) are non-unique (Azevedo and Marchesin, 1995; Azevedo et al., 1996). The appearance of transitional wave groups in analytical solutions for three-phase compositional flow that have been verified by physical experimental results (LaForce et al., 2010) is strong evidence that non-uniqueness will persist into these more complex compositional systems, though there are no rigorous mathematical analyses of compositional three-phase flow.

To determine the physical solution to these problems, solutions must satisfy the viscous profile entropy condition. Ideally it would be possible to implement this by the inclusion of the physical diffusive terms and use of a numerical method with no diffusive ($\frac{\partial^2 C}{\partial \xi^2}$) approximation errors. Therefore in this chapter the aim is to minimise diffusive approximation errors. These errors exist when using, for example, the single-point upstream weighting (SPU) scheme explained in Section 4.3.2. The errors of the SPU numerical approximation to Equations 2.13 in the three-component case can be shown by Taylor expanding the SPU approximations to its derivatives. This analysis (LaForce, 2005, Appendix D) shows that SPU actually models Equations 4.1 rather than Equations 2.13, thus producing errors that have a factor of $\frac{\partial^2 C}{\partial \xi^2}$.

$$\begin{pmatrix} \frac{\partial C_1}{\partial \tau} \\ \frac{\partial C_2}{\partial \tau} \end{pmatrix} = \begin{pmatrix} \frac{\partial F_1}{\partial C_1} & \frac{\partial F_1}{\partial C_2} \\ \frac{\partial F_2}{\partial C_1} & \frac{\partial F_2}{\partial C_2} \end{pmatrix} \begin{pmatrix} \frac{\partial C_1}{\partial \xi} \\ \frac{\partial C_2}{\partial \xi} \end{pmatrix} + \frac{1}{2} \begin{pmatrix} \frac{\partial F_1}{\partial C_1}\left[\Delta\xi - \frac{\partial F_1}{\partial C_1}\Delta\tau\right] & \Delta\xi \frac{\partial F_1}{\partial C_2} \\ \Delta\xi \frac{\partial F_2}{\partial C_1} & \frac{\partial F_2}{\partial C_2}\left[\Delta\xi - \frac{\partial F_2}{\partial C_2}\Delta\tau\right] \end{pmatrix} \begin{pmatrix} \frac{\partial^2 C_1}{\partial \xi^2} \\ \frac{\partial^2 C_2}{\partial \xi^2} \end{pmatrix} + \cdots \tag{4.1}$$

To minimise these errors one option is the total-variation diminishing (TVD) method which improves the accuracy of simulations in three-phase flow. Away from shock fronts or extrema, TVD has been shown to produce second order ($\Delta\xi^2$) numerical errors (Harten and Lax, 1984), which have error factors of only $\frac{\partial^3 C}{\partial \xi^3}$. However, TVD is stable because it produces first-order ($\Delta\xi$) numerical errors at smooth extrema (Harten and Lax, 1984). Since this results in diffusive approximation errors we consider the essentially non-oscillatory (ENO) approach proposed by Mallison et al. (2005) for use in studying multiphase flow problems.

Unlike TVD, ENO maintains higher-order accuracy at smooth extrema (Harten et al., 1987) via the use of a moving stencil that adapts so that the chosen grid points are either upstream or downstream of the shock. The third-order ENO scheme formally produces third order numerical errors terms which contain no diffusive ($\frac{\partial^2 C}{\partial \xi^2}$) approximation error factors. For example a selected ENO stencil produces errors like $\frac{\Delta\xi^3}{12}\frac{\partial^4 F}{\partial C^4}\frac{\partial^4 C}{\partial \xi^4}$ [see Appendix G]. Therefore this scheme was proposed for use to minimise diffusive approximation errors.

In this chapter it is shown that ENO is not able to maintain its third order nature throughout solutions that involve shocks but it is still more accurate than first-order methods.

The format of this chapter is as follows. In Section 4.2 the advective transport problem for three-phase flow in 1D is outlined and an analytical benchmark solution for the purely advective problem is presented. In Section 4.3 finite difference schemes are reviewed and the algorithms for 1D ENO and SPU are outlined. In Section 4.4 two simple test problems are solved to establish the rate of convergence of the schemes and then the convergence of both methods towards the proposed analytic solution is demonstrated. Finally, Section 4.5 discusses the implication and conclusions of our results.

4.2 Mathematical Model

In this section we set out the advective transport problem to which we shall investigate solutions. We also look at analytical solutions to this problem that can be used for comparison against numerical solutions later.

Analytical solutions to the transport equations for 1D, three-phase, three-component flow with components partitioning between the phases have been developed by LaForce (2005). LaForce and Johns (2005a) subsequently produced three-phase, three-component solutions for more general relative permeability models. Recently LaForce et al. (2008b) developed solutions for the three-phase four-component problem, first with constant K-values and then LaForce and Orr (2009) with a Peng-Robinson equation of state.

4.2.1 Advective Transport Problem

The 1D compositional transport equations are derived from mass balance and Darcy's law. The following assumptions are made to allow comparison to Method of Characteristics (MOC) solutions as Orr (2007):

1. One-dimensional laminar and isothermal flow
2. Change in pressure over the displacement length has no effect on phase behaviour
3. No dispersion, adsorption or chemical reactions
4. Constant porosity
5. Phase density is not a function of composition or pressure
6. Constant phase viscosity
7. Gravity, and volume change as components change phase, are neglected
8. Capillary pressure effects are neglected.

Analytical solutions are still possible if many of these assumptions are relaxed. Under these assumptions flow is governed by the mass balance equations 2.13 and relations 2.14-2.16. Equation 2.13, combined with constant boundary and initial conditions, is a Riemann problem that models the displacement of a multi-component fluid in a porous medium. In this case where gravity is neglected the fractional flow f_j of the jth phase is given by

$$f_j = \frac{\lambda_j}{\sum_{k=1}^{n_p} \lambda_k} \quad \text{and} \quad \lambda_j = \frac{k_{rj}}{\mu_j} \tag{4.2}$$

where λ_j is the mobility of phase j. In this work C_1 is the CO_2 component, C_2 is the oil component and C_3 is the water component. Similarly S_1 is the gas (or supercritical CO_2), S_2 is the oleic and S_3 is the aqueous phase.

Finally, the thermodynamic partitioning coefficients for the oleic, gas and aqueous phase are assumed to be independent of composition, so that the K-values are constant.

Table 4.1: Example parameters, after Valenti et al. (2004)

Component	i	K_i^1	K_i^2	$C_i^{initial}$	$C_i^{injection}$	Phase	j	μ_j	S_{rj}
CO_2	1	4.5	-	0.1	0.95	Gas	1	0.1	0.05
Oil	2	0.1	-	0.7	0.05	Oleic	2	0.5	0.1/0.2
Water	3	-	-	0.2	0	Aqueous	3	1	0.15

The K-value for the partitioning of component i between the gas and oleic phase is $K_i^1 = c_{i1}/c_{i2}$ and between the oleic and aqueous phase, $K_i^2 = c_{i2}/c_{i3}$.

To verifiably obtain the unique physically correct solution to Eq. 2.13 an we must apply the viscous profile entropy condition, as described in Section 2.3.2 and Equation 2.20. Previous papers on three-phase compositional displacements (LaForce, 2005; LaForce and Johns, 2005a) have not fully addressed issues of non-uniqueness of solutions.

4.2.2 Example Solution

A three-phase, three-component benchmark analytic solution is needed. For comparison the model and boundary conditions are taken from Valenti et al. (2004) for the first step of their three-component water and gas (WAG) injection process. The model consists of the relative permeability and thermodynamic model with the parameters shown in Table 4.1.

The relative permeabilities in the two-phase regions are modelled as

$$\begin{aligned} k_{rj}^{(2)} &= 0 && \text{if } S_j \le S_{rj} \\ &= \alpha(A_1 + A_2 S_j) + (1-\alpha)(B_1 + B_2 S_j^2) && \text{if } S_j > S_{rj} \end{aligned} \tag{4.3}$$

where S_{jr} is the residual saturation of phase j and α is a parameter set to 0.5 for the gas phase and 0 for the liquid phases (Juanes and Patzek, 2002). The two-phase residual oleic saturation varies depending upon the other phase present, as shown in Table 4.1, such that $S_{r2(1)} = 0.1$ is the oleic residual saturation in the presence of gas phase and $S_{r2(3)} = 0.2$ is the oleic residual saturation in the presence of aqueous phase. Due to this we shall also use $k_{r2(1)}^{(2)}$ and $k_{r2(3)}^{(2)}$ as notation to refer to the two-phase oleic phase relative permeabilities in the presence of gas phase and aqueous phase respectively. The constants A_1, A_2, B_1 and B_2 are given by

$$A_1 = \frac{-S_{rj}}{1-S_{rj}} \ , \quad A_2 = \frac{1}{1-S_{rj}} \ , \quad B_1 = \frac{-S_{rj}^2}{1-S_{rj}^2} \ , \ B_2 = \frac{1}{1-S_{rj}^2} \tag{4.4}$$

In the three-phase region, relative permeability is modelled using Baker's relation (Baker, 1988). Using this relation the oleic phase relative permeability is

$$k_{r2}^{(3)} = \frac{(S_3 - S_{r3})k_{r2(3)}^{(2)} + S_1 k_{r2(1)}^{(2)}}{(S_3 - S_{r3}) + S_1} \tag{4.5}$$

where $k_{r2(1)}^{(2)}$ and $k_{r2(3)}^{(2)}$ are evaluated using Equation 4.3. The three-phase relative permeabilities of the gas and aqueous phases are given by their two-phase relative permeabilities, so that

$$k_{rj}^{(3)} = k_{rj}^{(2)}(S_j) \quad , \qquad j = 1, 3 \tag{4.6}$$

The thermodynamic equilibrium model used assumes immiscible water so that the water component is only present in the aqueous phase. Hence the saturation of the aqueous phase is equal to the overall concentration of the water component

$$S_3 = C_3, \tag{4.7}$$

Under this model, only K-values for the partitioning of CO_2 and oil into the oleic and gas phases need be defined. The K-values are used with the Rachford-Rice (Rachford and Rice, 1952) equation

$$\sum_{i=1}^{n_c} \frac{C_i(K_i^1 - 1)}{S_1(K_i^1 - 1) + 1} = 0 \tag{4.8}$$

to determine the phase equilibria in two and three-phase regions of phase space numerically.

The Riemann problem to be solved here has initial condition (also called reservoir oil composition or right state) 10% CO_2, 70% oil and 20% water, and is representative of an oil that naturally contains a small fraction of CO_2 and is in a reservoir that either has been previously waterflooded, or has mobile water present initially as a consequence of aquifer influx. The boundary composition (also called injection gas composition or left state) is 95% CO_2 and 5% oil, which would represent injection of an enriched gas.

Semi-analytic solutions to three-phase, three-component displacements were constructed by LaForce (2011) using the methods described in LaForce and Johns (2005a,b). Solutions were constructed from the initial condition to upstream. The solution is shown on a ternary diagram in Figure 4.1 and on profile against the numerical results in Figure 4.8. The initial composition is within the two-phase water/oil region and the only way to enter the three-phase region is via a shock. The valid shock has velocity 2.38, lands in the three-phase region at a composition of (oil, CO_2, water) = (0.32,0.48,0.20) and has the same velocity as the fast path rarefaction wave. The solution then follows this rarefaction wave upstream to the composition (0.59,0.22,0.19). From this composition there is another shock with velocity 0.22, again with the same velocity as the fast path,

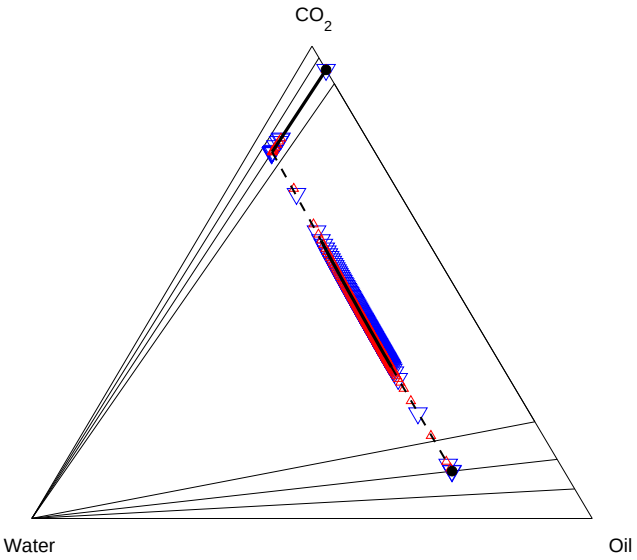


Figure 4.1: The analytic and simulated solutions in composition space for the example three-phase problem. This ternary system has water/CO_2 and water/oil two-phase regions and a large central three-phase region. The SPU simulation with 150 grid blocks is shown as red triangles and the ENO simulation with 150 grid blocks is shown as blue inverted triangles. The analytic solution is in black with solid lines denoting rarefaction curves and dashed lines indicating shocks in composition.

to the composition (0.78,0.04,0.18) in the CO_2/water two-phase region. There is a constant state at this composition before a very slow-moving rarefaction along this two-phase tie-line until the residual water saturation is reached. There is a contact discontinuity with zero velocity from the injection composition to the residual water saturation of 15% since it is not possible to remove the residual water in this model.

The two shocks in composition observed in this solution are both classified as fast shocks using the classification system of Schecter et al. (1996). As there is no transitional wave group in this solution and composition space was found to be strictly hyperbolic (LaForce, 2011) this example is likely to be more numerically stable than many other problems of practical interest and have a unique solution. Therefore it represents a fairly easy test case for the ENO method below.

4.3 Numerical Model

In this section we introduce the numerical methods used to investigate the problem described in Section 4.1 and to solve the equations in Section 4.2.

As discussed in Section 4.1, capturing the correct solution with capillary pressure relies upon limiting diffusive-type numerical error; however, with shocks inherently present in these problems, numerical diffusion may dominate the effect of the capillary pressure term and cause simulated displacements to converge towards an incorrect solution. The aim of our numerical methods is therefore to minimise diffusive-type numerical error.

Different numerical methods, each with their own issues with stability and numerical diffusion, are reviewed. Ultimately the third-order Essentially Non-Oscillatory (ENO) scheme (Harten et al., 1987; Shu and Osher, 1989) is used to minimise numerical errors. Mallison et al. (2005) and Valenti et al. (2004) found this scheme was the most accurate and reliable in their tests of high-order numerical schemes.

4.3.1 General Formulation of Finite Volume/ Finite Difference Schemes for Conservation Laws

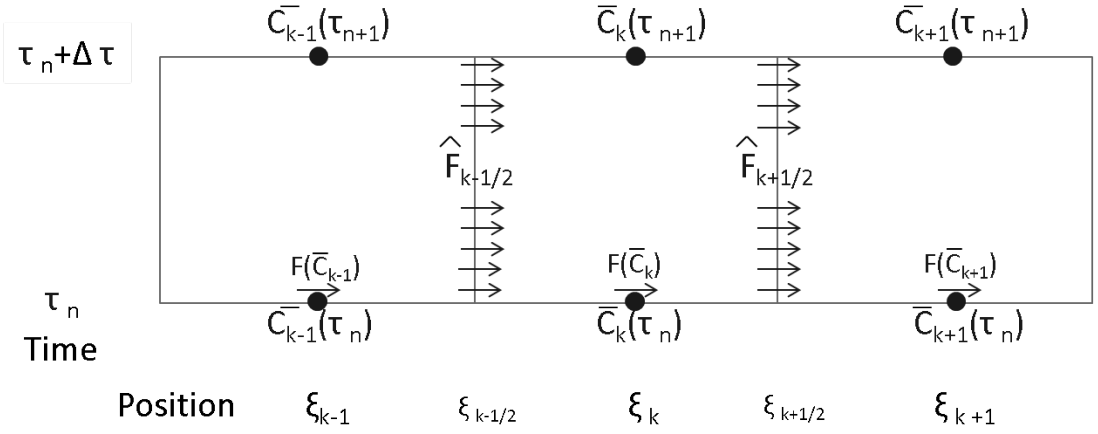


Figure 4.2: A 1D grid where the average composition of each cell is reprented by a point at the cell centre. The vertical axis represents the evolution of the cell average from time τ_n to time τ_{n+1}. The flux $\hat{F}_{k+\frac{1}{2}}$ at the boundary of the cell represent the average flux through the boundary over the timestep.

We first introduce briefly the general formulation of finite volume schemes used for the solution of conservation laws such as Equations 2.13. A more in depth introduction is provided by LeVeque (2002). Finite volume schemes are differentiated from finite difference schemes by their derivation on the basis of the integral form of the conservation

law. However, these methods are closely related to finite difference methods and the schemes introduced can often be interpreted as finite difference approximations. This interpretation is partially made possible by our use of regularly spaced grids.

In this derivation we integrated the compositional Equations 2.13 over a computational grid cell (also known as the finite volume) $\xi_{k-\frac{1}{2}} \leq \xi \leq \xi_{k+\frac{1}{2}}$, $\tau_n \leq \tau \leq \tau_{n+1} \equiv \tau_n + \Delta\tau$ as shown in Figure 4.2, where τ_n is the current timestep, τ_{n+1} is the next, $\Delta\xi$ is the grid spacing $\Delta\tau$ is the timestep size and k is the gridblock number. From this integration we reached the integral form

$$\bar{C}_{k,i}^{n+1} = \bar{C}_{k,i}^{n} - \frac{\Delta\tau}{\Delta\xi}[\hat{F}_{k+\frac{1}{2},i}(C) - \hat{F}_{k-\frac{1}{2},i}(C)] \tag{4.9}$$

where

$$\hat{F}_{k+\frac{1}{2},i}(C) = \frac{1}{\Delta\tau}\int_{\tau_n}^{\tau_{n+1}} F_i(C(\xi_{k+\frac{1}{2}}, \tau))d\tau \tag{4.10}$$

is the average flux through the gridblock boundary $\xi_{k+\frac{1}{2}}$ over a timestep and

$$\bar{C}_{k,i}^{n} = \frac{1}{\Delta\xi}\int_{\xi_{k-\frac{1}{2}}}^{\xi_{k+\frac{1}{2}}} C_i(\xi, \tau_n)d\xi \tag{4.11}$$

is the average composition in the cell at time τ_n.

Equation 4.9 shows us that, given the cell average composition at time τ_n, to find its value at time τ_{n+1} we must estimate $\hat{F}_{k+\frac{1}{2},i}(C)$.

Removing the averages from 4.9 we see the general conservative (Equation 4.12 defines the conservative form) numerical approximation for Eq. 2.13 is

$$C_{k,i}^{n+1} = C_{k,i}^{n} - \frac{\Delta\tau}{\Delta\xi}\left(F_{k+\frac{1}{2},i}^{n} - F_{k-\frac{1}{2},i}^{n}\right) \tag{4.12}$$

where $C_{k,i}^{n}$ represents the volume fraction of component i at the centre of the kth gridblock at timestep n. If we can approximate the flux $F_{k+\frac{1}{2},i}^{n}$ using cell-centred values such as $C_{k,i}^{n}$ then we shall have a finite difference scheme.

4.3.2 Single-Point Upstream Weighting (SPU)

Single Point Upstream weighting (SPU), also known as a first-order upwind method, is a simple finite difference method that can be used to reconstruct the flux at the cell face $F_{k+\frac{1}{2},i}(C)$ in equation 4.12. This uses piecewise constant interpolation of the upwind cell centred flux, thus $F_{k+\frac{1}{2},i}(C)$ is estimated by

$$F_{k+\frac{1}{2},i}^{n}(C) = F_{k,i}^{n} \tag{4.13}$$

Using this estimation, SPU simulates solutions to the 1D equations by updating the composition $C_{k,i}$ of each component i at every grid block k for each timestep n using the following discrete approximation to the conservation equation:

$$C_{k,i}^{n+1} = C_{k,i}^{n} - \frac{\Delta\tau}{\Delta\xi}(F_{k,i}^{n} - F_{k-1,i}^{n}) \tag{4.14}$$

This method uses explicit forward Euler timestepping and produces errors in the solution $C_{k,i}$, proportional to $\Delta\xi$ (LeVeque, 2002, p.143).

4.3.3 Total Variation Diminishing (TVD) Methods

The aim of higher-order numerical methods is to find better estimates for the numerical flux $\hat{F}_{k+\frac{1}{2},i}^{n}$ such that the flux difference approximates the derivative to the p-th order accuracy:

$$\frac{1}{\Delta\xi_k}(\hat{F}_{k+\frac{1}{2},i}^{n} - \hat{F}_{k-\frac{1}{2},i}^{n}) = F'(\xi_k) + O(\Delta\xi^p), \qquad k = 0, 1, ..., n_k \tag{4.15}$$

Traditional higher-order finite difference methods attempt to do this by interpolating the flux at $\xi_{k+\frac{1}{2}}$ using data from some fixed stencil of points. For example, to obtain an interpolation for $\hat{F}_{k+\frac{1}{2},i}$ to second order the information of the three cells $k-1$, k and $k+1$ can be used to build a second-order interpolation polynomial. This works well for globally smooth problems. However fixed stencil interpolation of second or higher order accuracy is necessarily oscillatory near a discontinuity (Godunov, 1959), which often leads to numerical instabilities in nonlinear problems containing discontinuities such as found in multiphase flow in porous media.

One way to have high-order accuracy without oscillations is to use Total-Variation-Diminishing (TVD) methods (Van Leer, 1979; Harten and Lax, 1984; LeVeque, 2002). By carefully designing 'limiters' in these schemes, it can be ensured that the total variation (TV) of a solution, defined as

$$TV(C) = \sum_{k=-\infty}^{\infty} \mid C_k - C_{k-1} \mid \tag{4.16}$$

does not increase over time. This provides smooth solutions for nonlinear scalar 1D problems. One disadvantage of these TVD methods however is that they have been shown to degenerate to first-order at extrema (Osher and Chakravarthy, 1984).

4.3.4 Essentially Non-Oscillatory (ENO) Scheme

ENO as proposed by Harten et al. (1987) was the first successful attempt to obtain a uniformly high-order accurate, yet essentially non-oscillatory interpolation for piecewise smooth functions. This means the magnitude of oscillations decays as $O(\Delta\xi^p)$ where p is the order of the scheme. Its most commonly used form is the third-order scheme such that its estimate of $\hat{F}_{k+\frac{1}{2},i}$ produces the estimate of $C^{n+1}_{k,i}$,

$$C^{n+1}_{k,i} = C^n_{k,i} - \frac{\Delta\tau}{\Delta\xi}[\hat{F}_{k+\frac{1}{2},i}(C) - \hat{F}_{k-\frac{1}{2},i}(C)] + O(\Delta\xi^3) \tag{4.17}$$

An extension to ENO known as the weighted essentially non-oscillatory scheme (WENO) (Liu et al., 1994; Jiang and Shu, 1996) has also been developed, its main idea being to bias the choice of stencil towards the upstream direction to enhance stability and accuracy.

ENO is a high-order accurate finite difference scheme designed for solving conservation laws with piecewise smooth solutions. It interpolates high-order accurate approximations to the flux $F_{k+\frac{1}{2},i}(C)$ at the cell boundaries, but the key feature of ENO is that it bases these interpolations upon points in an adaptive stencil which avoids using points on both sides of a discontinuity.

To calculate the flux at the cell boundary $F_{k+\frac{1}{2},i}(C)$ three stencils are considered: $(k-2,k-1,k)$, $(k-1,k,k+1)$ and $(k,k+1,k+2)$. It is assumed here that left is always the upwind side, though in general ENO may also use the stencil $(k+1,k+2,k+3)$. Using an appropriate measure of smoothness as described by steps 3-5 in the algorithm section below the smoothest stencil is then chosen. This stencil is used to make a polynomial interpolation to the flux at the cell boundary, such that

$$F^n_{k+\frac{1}{2},i}(C) = P^q_{k+\frac{1}{2},i}(\xi_{k+\frac{1}{2}}) \qquad q = L, C \text{ or } R \tag{4.18}$$

where $P^L_{k+\frac{1}{2},i}(\xi)$, $P^C_{k+\frac{1}{2},i}(\xi)$, $P^R_{k+\frac{1}{2},i}(\xi)$ are the polynomial interpolants based on the three respective stencils.

The basis for this ENO algorithm was developed in Harten et al. (1987) and Harten and Osher (1987) with improvements and more easily applicable algorithms in Shu and Osher (1988) and Shu and Osher (1989). These later papers included the third-order multistage Runge-Kutta timestepping algorithm to ensure temporal errors were $O(\Delta\tau^3)$. The whole scheme is well summarised by Shu (1997), although this does not include the modifications used later in this work.

Within Shu (1997) both the solution of the coupled system of equations and the solution of scalar equations are considered. The traditional approach to solving the coupled system of strictly hyperbolic equations has been to decouple the equations by changing to

characteristic variables. These decoupled equations are then solved by the scalar equation approach. However, changing to characteristic variables requires the solution of an eigenvalue problem. This may be impractical because (a) for many compositional problems the eigenvalue problem has not been solved, (b) the numerical or semi-analytical solution of the eigenvalue problem is computationally expensive to calculate and (c) in three-phase problems the eigenvalues may be complex for some compositions. Therefore in this work the system of equations in the conservation law are treated in a componentwise manner, solving for each component independently of the others during each Runge-Kutta timestep, as with a scalar equation. The componentwise reconstruction does not rigorously enforce the limitation of oscillations to $O(\Delta\xi^p)$ and some larger oscillations are possible. as shown by Qiu and Shu (2002). This approach has been successful in high-order central schemes for conservation laws (Levy et al., 1999; Nessyahu and Tadmor, 1990) and was recently used by Mallison et al. (2005).

We shall now summarise the form of ENO used for the solution of scalar equations as in Shu (1997) and therefore drop C's composition subscript i.

ENO Algorithm

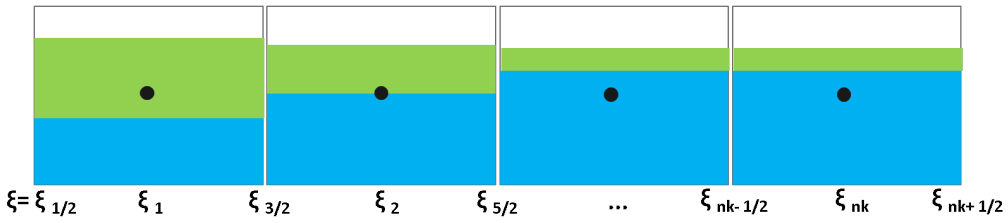


Figure 4.3: A grid with n_k=4 gridblocks where the colours represent the volume fraction of each phase present in each cell.

1. Take a grid, as shown in figure 4.3, with cell boundaries

$$\xi_{\frac{1}{2}} < \xi_{\frac{3}{2}} < ... < \xi_{n_k-\frac{1}{2}} < \xi_{n_k+\frac{1}{2}} \tag{4.19}$$

where $\xi_{\frac{1}{2}}$ represents the start of the 1D reservoir and $\xi_{n_k+\frac{1}{2}}$ the end as shown in Figure 4.3. The cells boundaries are therefore $[\xi_{k-\frac{1}{2}}, \xi_{k+\frac{1}{2}}]$.

2. Calculate the point values of function $F(\xi)$ given the $C(\xi_k)$ using the flash solver described in Section 4.3.6

$$F_k \equiv F(S(C(\xi_k))), \qquad k = 1, 2, ..., n_k \tag{4.20}$$

3. Compute the w-th degree divided differences for $1 \leq w \leq p-1$, which are defined

inductively by

$$d_w[\xi_k, ..., \xi_{k+w}] \equiv \frac{d_{w-1}[\xi_{k+1}, ..., \xi_{k+w}] - d_{w-1}[\xi_k, ..., \xi_{k+w-1}]}{\xi_{k+w} - \xi_k} \tag{4.21}$$

where the 0-th degree divided difference is defined as

$$d_0[\xi_k] \equiv F(\xi_k) \tag{4.22}$$

4. In cell k start with the stencil $B_1(k) = \{\xi_k\}$
5. For $l = 2, ..., p$, assuming $B_{l-1}(k) = \{\xi_r, ..., \xi_{r+l-2}\}$ is known, where r is the left shift, add one of the two neighbouring points, ξ_{k-1} or ξ_{k+l-1} to the stencil, following the ENO procedure:

- If
$$| d_{l-1}[\xi_{r-1}, ..., \xi_{r+l-2}] | \leq | d_{l-1}[\xi_r, ..., \xi_{r+l-1}] | \tag{4.23}$$
add ξ_{r-1} to the stencil to obtain $B_l(k) = \{\xi_{r-1}, ..., \xi_{r+l-2}\}$
- Otherwise, add ξ_{r+l-1} to the stencil to obtain $B_l(k) = \{\xi_r, ..., \xi_{r+l-1}\}$

We end up with the stencil $B_p(k) = \{\xi_{k-r}, ..., \xi_{k-r+p-1}\}$ for cell k.

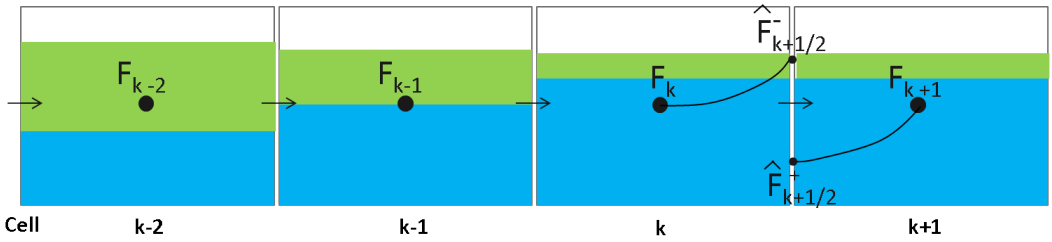


Figure 4.4: A grid with flux calculated at points ξ_k and the interpolations to $\hat{F}_{k+\frac{1}{2}}$.

6. Calculate $\hat{F}^+_{k+\frac{1}{2}}$ and $\hat{F}^-_{k+\frac{1}{2}}$, the approximations to $\hat{F}_{k+\frac{1}{2}}$ shown in Figure 4.4, using a $(p-1)$th degree piecewise polynomial reconstruction of the flux function. As long as we use a fixed width grid this can be simplified by Taylor expansions to the form of Equations 4.25. If our stencils for the cells k and $k+1$ are the following p points respectively:

$$\xi_{k-r(k)}, ..., \xi_{k+p-r(k)-1} \qquad \xi_{k+1-r(k+1)}, ..., \xi_{k+p-r(k+1)} \tag{4.24}$$

then

$$\hat{F}^-_{k+\frac{1}{2}} = \sum_{w=0}^{p-1} c_{r(k),w} F_{k-r(k)+w} \qquad \hat{F}^+_{k+\frac{1}{2}} = \sum_{w=0}^{p-1} c_{r(k+1)-1,w} F_{k+1-r(k+1)+w} \tag{4.25}$$

where the constants c_{rw} for $p = 3$ are given in Table 4.2.

Table 4.2: Constants c_{rw} for $p = 3$

r	$w = 0$	$w = 1$	$w = 2$
-1	11/6	-7/6	1/3
0	1/3	5/6	-1/6
1	-1/6	5/6	1/3
2	1/3	-7/6	11/6

7. The approximations to the flux $\hat{F}_{k+\frac{1}{2}}$ are then combined using one of two methods:

- Either the Lax-Friedrichs flux splitting:

$$\hat{F}_{k+\frac{1}{2}} = \frac{1}{2}[\hat{F}^{-}_{k+\frac{1}{2}} + \hat{F}^{+}_{k+\frac{1}{2}} - \max_{C_k \le C \le C_{k+1}} \mid F'(C) \mid (C^{+}_{k+\frac{1}{2}} - C^{-}_{k+\frac{1}{2}})] \tag{4.26}$$

- or Roe's method, which for stability always uses the upwind flux by computing the Roe speed $\bar{a}_{k+\frac{1}{2}} \equiv \frac{F(C_{k+1}) - F(C_k)}{C_{k+1} - C_k}$ and then
  - if $\bar{a}_{k+\frac{1}{2}} \ge 0$ (i.e. left is upwind) we use $\hat{F}^{-}_{k+\frac{1}{2}}$ for the flux $\hat{F}_{k+\frac{1}{2}}$
  - or if $\bar{a}_{k+\frac{1}{2}} < 0$ then we use $\hat{F}^{+}_{k+\frac{1}{2}}$

One disadvantage of the ENO-Roe approach is that it yields a stationary entropy-violating expansion shock since it is based on the first-order Roe scheme. However this can be resolved with an entropy fix, which proceeds as follows. Let $\hat{F}_{k+\frac{1}{2}}$ be defined as before, then if $F'(C)$ does not change sign between C_k and C_{k+1}; otherwise, let $\hat{F}_{k+\frac{1}{2}}$ be defined by the Lax Friedrichs flux splitting.

8. Up to now we have only considered the spatial discretization, now we account for time discretization using a third-order Runge-Kutta method. If we say that

$$L(C_k) = -\frac{1}{\Delta\xi}(\hat{F}_{k+\frac{1}{2}} - \hat{F}_{k-\frac{1}{2}}) \tag{4.27}$$

where the $\hat{F}_{k+\frac{1}{2}}$ have been calculated by steps 2-7 then C^{n+1}_k is found from C^n_k by iterating through the following lines

$$C^{(1)}_{k,i} = C^n_{k,i} + \Delta t L(C^n_{k,i}) \tag{4.28}$$

$$C^{(2)}_{k,i} = \frac{3}{4}C^n_{k,i} + \frac{1}{4}C^{(1)}_{k,i} + \frac{\Delta t}{4}L(C^{(1)}_{k,i}) \tag{4.29}$$

$$C^{n+1}_{k,i} = \frac{1}{3}C^n_{k,i} + \frac{2}{3}C^{(2)}_{k,i} + \frac{2\Delta t}{3}L(C^{(2)}_{k,i}) \tag{4.30}$$

9. The calculation of C_i^{n+1} completes one timestep, now repeat steps 2-8 until $\tau = \tau_{final}$ ensuring that the CFL $= \frac{\Delta\tau.(\lambda_i)_{max}}{\Delta\xi}$ is between 0 and 1.

4.3.5 Modifications to ENO Algorithm and Implementation Notes

Two changes to the algorithm in Section 4.3.4 are reported in the literature, the modified ENO and the Godunov reconstruction. We use these in some of our analyses. We also give details about the flux splitting and boundary conditions of our implementation.

Modified ENO

In Rogerson and Meiburg (1990) ENO-Roe was used and it was found that solutions did not always converge at the rate expected by truncation error analysis and that it varied as a function of the smooth initial condition. In fact, after reaching a certain resolution, further refinement was seen to result in increased errors. It was found that this loss of accuracy was due to the overuse of linearly unstable stencils in smooth regions. As a result Shu (1990) proposed a modified ENO scheme which adapted step 5 in the ENO algorithm outlined in Section 4.3.4 to:

- Define r_c as the leftmost point on the left linearly stable stencil, which in our case is $r_c = -1$
- If $r > r_c$ then
  - If
$$| \, d[\xi_{r-1}, ..., \xi_{r+l-2}] \, | \leq | \, 2 * d[\xi_r, ..., \xi_{r+l-1}] \, | \tag{4.31}$$
    add ξ_{r-1} to the stencil to obtain $S_l(k) = \{\xi_{r-1}, ..., \xi_{r+l-2}\}$
  - Otherwise, add ξ_{r+l-1} to the stencil to obtain $B_l(k) = \{\xi_r, ..., \xi_{r+l-1}\}$
- If $r \leq r_c$ then
  - If
$$| \, 2 * d[\xi_{r-1}, ..., \xi_{r+l-2}] \, | \leq | \, d[\xi_r, ..., \xi_{r+l-1}] \, | \tag{4.32}$$
    add ξ_{r-1} to the stencil to obtain $T_l(k) = \{\xi_{r-1}, ..., \xi_{r+l-2}\}$
  - Otherwise, add ξ_{r+l-1} to the stencil to obtain $B_l(k) = \{\xi_r, ..., \xi_{r+l-1}\}$

It was found that this modification recovered the high order accuracy of the scheme, while maintaining the essentially non-oscillatory characteristics. In Shu (1990) it is recommended that the factor used to compare the divided differences in equations 4.3.5 and

4.3.5 is between 1 and 2; here 2 is chosen. In a later paper (Wang and Huang, 2002) a factor of 1.5 is recommended.

Godunov Reconstruction

In step 6 of the ENO algorithm presented we interpolate F in space in order to calculate F at the the cell faces. We refer to this as the flux-based-approach (Mallison et al., 2005). An alternative to this is to reconstruct the compositions at the cell faces and then calculate the flux at the cell face based on those compositions. This is Godunov's approach (Godunov, 1959) and we shall refer to this as the Godunov reconstruction.

Flux Splitting

In step 7 of the ENO algorithm there were two choices of flux splitting, Roe's method and the Lax-Friedrichs flux splitting. We considered the use of these two flux splitting methods and also taking

$$\hat{F}_{k+\frac{1}{2}} = \hat{F}^{+}_{k+\frac{1}{2}} \tag{4.33}$$

which we shall call the 'left splitting' approach.

We found the Lax-Friedrichs approach was less flexible than Roe's method as it required the Godunov reconstruction to avoid an inversion that may not be possible for three-phase relative permeabilities ($F^{-1}(\hat{F}^{+}_{k+\frac{1}{2}})$ is not necessarily unique). It also required the calculation of a maximum from a smooth function which was thought computationally expensive and therefore we preferred Roe's method over the Lax-Friedrichs approach.

We implemented Roe's scheme as outlined for the componentwise ENO approach but without the entropy fix, since this led to the same issues as the Lax Friedrichs method. This was then compared against the 'left splitting' approach, which was found to be more accurate in most cases. This approach also corresponds to that taken by Mallison et al. (2005). As a result the left splitting approach was used for most cases, with some use of the Roe's method as noted for cases in Section 4.4.

Boundary Conditions

At the left-hand boundary we set a constant composition boundary condition when using the Godunov reconstruction and a constant flux boundary condition when using the flux-based approach. Ghost cells with the same constant composition/flux were used at the boundaries of our simulation so that we were able to apply the full ENO stencil choosing algorithm all the way along the domain.

4.3.6 Calculation of Two-Phase Saturations

The numerical methods described in Sections 4.3.1-4.3.5 have concentrated on the methods that solve equations of the form in Equations 2.13 with concentrations C_i and fluxes F_i with no discussion of the phase behaviour. When calculating the flux F_i though, such as in step 2 of the ENO algorithm in Section 4.3.4 we must first calculate the phase saturations S_j so that we may calculate the fractional flow f_j of each phase. When components partition between different phases this requires some calculation.

In this work, constant K-values are used to determine saturations and here we consider how the saturations of two partially miscible phases are calculated using these K-values. In some cases there may also be an immiscible aqueous phase present that contains only the water component, which equally is not present in the other two phases. Calculations for the full three-phase case are shown in Section 5.3.3. The equation to find the saturations of the two partially miscible phases are found by rearrangement of the auxiliary relations for C_i and c_{ij} shown in Equations 2.14 and 2.16 respectively along with the K values K_i^1 to give the Rachford-Rice equation

$$\sum_{i=1}^{n_c} \frac{C_i(K_i^1 - 1)}{S_1(K_i^1 - 1) + 1} = 0 \tag{4.34}$$

where $S_2 = 1 - S_1$ or alternatively when a third phase is present but immiscible with saturation S_3 and there are two partially miscible components remaining

$$\sum_{i=1}^{2} \frac{C_i(K_i^1 - 1)}{S_1(K_i^1 - 1) + (1 - S_3)} = 0 \tag{4.35}$$

where $S_2 = 1 - S_1 - S_3$.

It is not possible to solve either of these equations analytically though and to find S_1 a numerical calculation known as a 'flash calculation' must be done. In these two-phase cases this uses a Newton iteration as described in Remson (1971). The iteration defines a function G equal to the left-hand side of 4.34 or 4.35 and repeatedly iterates from a possible S_1^m to S_1^{m+1} using the equation

$$S_1^{m+1} = S_1^m - \frac{G(S_1)}{G'(S_1)} \tag{4.36}$$

until $G(S_1) = 0$ when S_1 is found.

4.4 Results

As explained in Section 4.1 our initial goal in this chapter was to remove first order errors that contain physical error factors of $\frac{\partial^2 C}{\partial \xi^2}$ from our simulations of the three-phase three-component problem. Use of the third order ENO scheme described in Section 4.3.4 was proposed to achieve this.

We built up to modelling the full three-phase three-component problem by modelling simpler problems to allow us to verify our numerical code. In Sections 4.4.2 and 4.4.3 we show results verified by 2-phase immiscible analytic solutions and three-phase three-component analytic solutions. This also enabled us to seek a new numerical benchmark solution for three-phase three-component flow.

Little has been done in the petroleum or broader geoscience literature to verify the order of accuracy of ENO for problems of interest in multiphase porous media flow. However, the method has been used in a broad range of fields (e.g. Dolezal and Wong, 1995; Walsteijn, 1994) and more recently in the petroleum literature by Gerritsen et al. (2005); Jessen et al. (2008); Mallison et al. (2005); Valenti et al. (2004). Therefore we also studied the order of accuracy for ENO and SPU simulations for a series of Riemann problems of increasing complexity in Sections 4.4.1 and 4.4.3.

We shall now show our code verification, accuracy analysis and benchmark results. The key results are that we find that ENO is not third order accurate in problems with shocks and we also obtain a new three-phase three-component high-order numerical solution that is benchmarked against analytic solutions for the first time, correcting a previous mistake in the literature.

4.4.1 Immiscible Two-Phase Order of Accuracy Study

We considered the accuracy of the SPU and ENO methods using some simple problems with general flux functions. We look at two examples to show that ENO loses third order accuracy in the presence of a discontinuity. The first example has a continuous initial condition and the second a discontinuous initial condition. Before looking at the examples we shall briefly review error analysis:

General Method for Analysing Accuracy

In one dimensional finite difference schemes we have an approximation $C^n_{k,numerical}$ to the solution at each grid cell in time. For comparison call $C^n_{k,analytic}$ the analytic solution value. Using these values we can define local and global errors. The *local error* at any

point is defined as

$$\text{Local error} = \mid C^n_{k,numerical} - C^n_{k,analytic} \mid \tag{4.37}$$

Global errors are usually estimated in terms of norms which sum together the errors at all grid points. For example the 1-norm is

$$\| e \|_1 = \Delta\xi \sum_{k=-\infty}^{\infty} \mid C^n_{k,numerical} - C^n_{k,analytic} \mid \tag{4.38}$$

Since we are often considering problems involving discontinuities we shall consider the local error in this work. The rate at which this error decays as the grid spacing is reduced is a measure of the order of accuracy of the method and can be measured by plotting error against grid spacing on a log-log plot. If the error is proportional to $(\Delta\xi)^p$ then these plots will be straight lines with slope p, since error decreases p orders of magnitude for each order reduction in $\Delta\xi$.

Smooth Initial Condition

We study the order of accuracy of ENO and SPU for an example with a single conservation equation

$$\frac{\partial C_1}{\partial \tau} + \frac{\partial (\sin \frac{\pi C_1}{2})}{\partial \xi} = 0. \tag{4.39}$$

This corresponds to substituting $F_1 = \sin(\frac{\pi C_1}{2})$ in Equation 2.13 with $n_c = 2$. The purpose of this flux function is to study accuracy rather than representing reservoir flow.

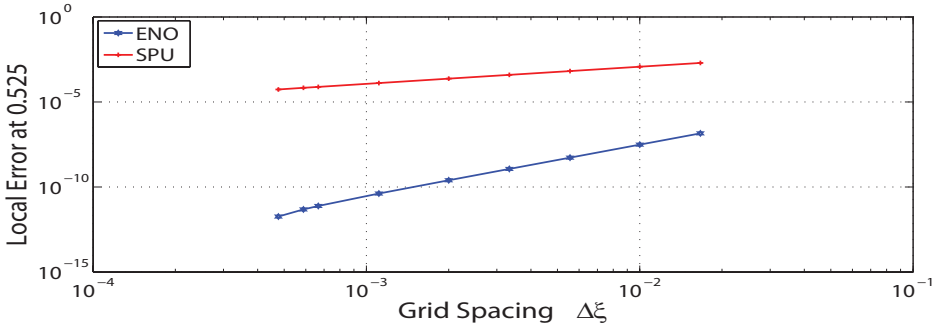


Figure 4.5: Local error at point $\xi = 0.525$ and $\tau = 1$ against grid spacing for the example with $F = \sin \frac{\pi C}{2}$, initial condition $C = \frac{2}{\pi} \cos^{-1} \frac{3\xi}{\pi}$ and boundary condition $C = 1$ so there is no initial discontinuity. The average slope of the curves shows that the local error from ENO in this problem decreases with rate $(\Delta\xi)^{3.17}$ whereas the SPU scheme's error decreases with rate$(\Delta\xi)^{1.01}$

For simplicity, in the first example the boundary condition $C_1 = 1 \mid_{\xi=0}$ and initial

condition

$$C_1 = \frac{2}{\pi}\cos^{-1}\frac{3\xi}{\pi} \qquad 0 < \xi < 1 \tag{4.40}$$

are used, so that the solution to this benchmark problem is continuous, positive and decreasing over the domain. There is no discontinuity at $\xi = 0$ for this choice of initial and boundary condition. Equation 4.39 is simulated using both SPU and ENO for the time $\tau = 0$ to $\tau = 1$ and the local error is evaluated at $\xi = 0.525$ and $\tau = 1$.

Figure 4.5 shows the local error from the simulation for several levels of grid refinement ($\Delta\xi$) on a log-log plot. The slope of the error for the SPU scheme is $p = 1.01$ and for the ENO scheme it is $p = 3.17$. Based on this analysis it can be seen that for the problem without a discontinuity in the initial condition, ENO is approximately third order and SPU is first order.

Discontinuous Initial Condition

The second initial condition considered for benchmarking SPU and ENO accuracy is

$$C_1 = 0 \qquad\qquad 0 < \xi < 1. \tag{4.41}$$

The same boundary condition $C_1 = 1\ |_{\xi=0}$ as the first example is used, so this problem has a discontinuity at $\xi = 0$. Again the simulations are run until $\tau = 1$. In this example the shock does not persist after $\tau = 0$. However as shown on Figure 4.6 the slope of the error line for ENO is $p = 1.00$, which indicates that ENO is only first-order. The slope of the error line for SPU is $p = 0.84$, which indicates that SPU has continued to be around order one for the more complex problem. Though ENO and SPU have the same rate of convergence, the error in the ENO scheme is always around $1/10$ that of the SPU method. These two examples demonstrate that the presence of a discontinuity in the initial condition can be sufficient to reduce the accuracy of ENO to first-order, even in simulation of a single equation with a simple flux function.

This result is disappointing, given our initial goal. Although rarely quoted in the literature, evidence of this result exists in, for example, Engquist and Sjogreen (1998) who showed that in systems of equations non-sharpening characteristics can carry first-order errors away from stable shocks. Though our second example is a single equation rather than a system of equations, it contains a shock that is not self-sharpening. It is likely that the initial discontinuity causes the solution to begin down an incorrect characteristic with first-order error. Without self-sharpening these errors propagate into the smooth region of the solution, where the error is unrecoverable.

In CO_2 storage or EOR there is invariably a discontinuity in fluid saturations at $\xi = 0$ when injection of CO_2 or CO_2/water mixtures is initiated. The conservation law for three-

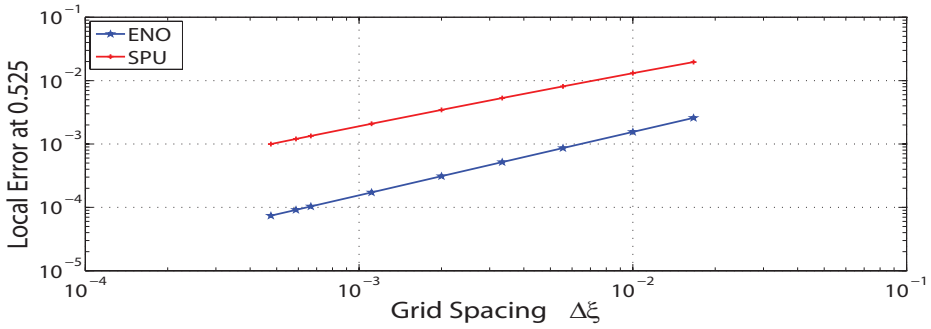


Figure 4.6: Local error at point $\xi = 0.525$ and $\tau = 1$ against grid spacing for the example with $F = \sin\frac{\pi C}{2}$, boundary condition $C = 1$ and initial condition C=0 so that there is an initial discontinuity. The average slope of the curves shows that the local error from ENO in this problem decreases with rate $(\Delta\xi)^{1.00}$ whereas the SPU schemes error decreases with rate $(\Delta\xi)^{0.84}$. There is, however, approximately a factor 10 difference between the size of the errors

phase, three-component flow is a system of two equations and the solution profiles consist of a series of weakly self-sharpening shocks and rarefactions. Thus it is likely that the ENO scheme will be first-order in the three-phase problem. The advantage of using ENO over SPU will be that it is approximately an order of magnitude more accurate, but it is not likely to demonstrate higher order convergence for the Riemann problems of interest.

4.4.2 Immiscible Two-Phase Code Verification

This simulation was very simple and solved a one dimensional version of Equation 2.13 for the immiscible two-phase problem

$$\phi\frac{\partial C_1}{\partial t} + u_t\frac{\partial F_1}{\partial x} = 0 \tag{4.42}$$

where ϕ is porosity, $u_t = \sum_{j=1}^{n_p} u_j$, u_j is the jth phase velocity, x is distance along the porous medium and t is time. The boundary and initial conditions, fluid properties and models used are shown in Table 4.3. Due to immiscibility there was no phase behaviour so $C_1 = S_1$ and $F_1 = f_1$. The Corey relative permeability model defines the k_{rj} in a two phase system as

$$k_{r1} = 0 \qquad \text{if } S_1 \leq S_{1r} \tag{4.43}$$

$$= \left(\frac{S_1 - S_{1r}}{1 - S_{1r} - S_{2r}}\right)^2 \qquad \text{if } S_{1r} > S_1 > 1 - S_{2r} \tag{4.44}$$

$$= 1 \qquad \text{if } S_1 \geq 1 - S_{2r} \tag{4.45}$$

$$k_{r2} = 0 \qquad \text{if } S_2 \leq S_{2r} \tag{4.46}$$

$$= \left(\frac{S_2 - S_{2r}}{1 - S_{2r} - S_{1r}}\right)^2 \qquad \text{if } S_{2r} > S_2 > 1 - S_{1r} \tag{4.47}$$

$$= 1 \qquad \text{if } S_2 \geq 1 - S_{1r} \tag{4.48}$$

where the S_{jr} are the residual saturations. In general the exponents to can be determined by experiment but here they are set to 2.

By comparing our numerical solution to analytic results calculated using the theory of Orr (2007), as shown in Figure 4.7, we confirmed that our basic 2-phase code was working using SPU.

Table 4.3: 2 phase immiscible parameters

	CO_2	Water
Residual saturation	0.15	0.35
Viscosity (Pa.s)	0.00006	0.0005
Initial reservoir compositions	0	1
Injection volume fraction	0.95	0.05
Relative permeability model	Corey with exponents 2	
Numerical solver	SPU	
Injection velocity (m/day)	10	
Injection time (days)	0.5	
Porosity	0.2	

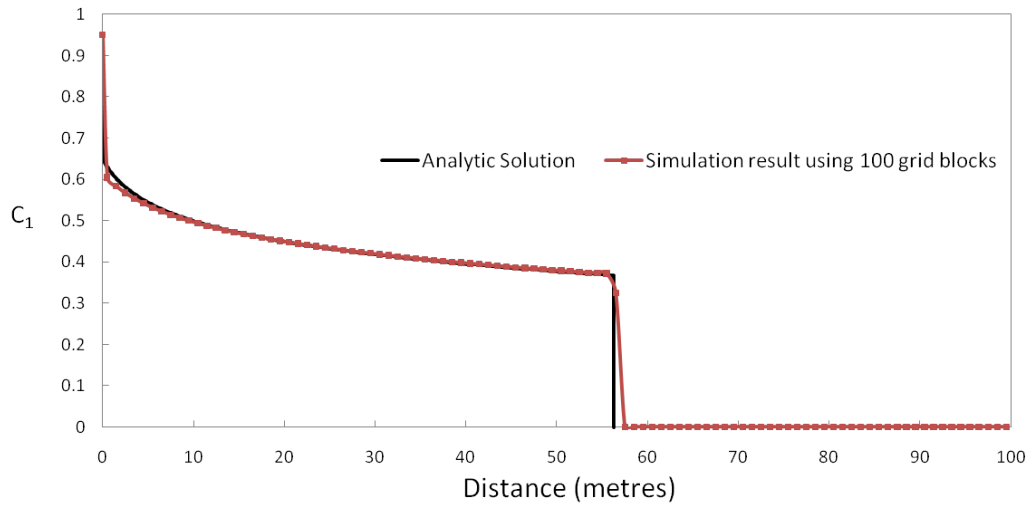


Figure 4.7: Simulated and analytic 1D CO_2 saturation profiles after 0.5 days of injection of 95% CO_2 into a 100% water saturated aquifer. The system was assumed to be 2-phase immiscible.

4.4.3 Three-Phase Three-Component Benchmark Solution

The result of Section 4.4.1 leads us to concentrate upon setting a new high-order numerical benchmark solution for three-phase three-component flow rather than investigating convergence further. We also investigate the accuracy of the numerical methods for this more complex problem.

The three-phase three-component problem and setup to be solved is taken from Valenti et al. (2004). The mathematical model for this problem is set out in Section 4.2.1 with $n_c = 3$. The initial and boundary conditions, fluid properties and relative permeability model are given Table 4.1 in Section 4.2.2 where the analytic solution to the problem is shown.

We use both ENO and SPU to solve the problem. The ENO solutions used the Godunov reconstruction and left splitting explained in Section 4.3.5. Saturations were calculated by using the flash solver described in Section 4.3.6 to solve Equations 4.35.

Previous numerical benchmarks for three-phase, three-component flow by LaForce and Johns (2005a) have always used highly refined SPU simulations for comparison with analytic solutions and Valenti et al. (2004) have benchmarked ENO solutions against highly-refined numerical solution without analytic results. In this work we benchmark ENO solutions against the analytic solution described in the previous section.

The profile of the numerical solution to the benchmark three-phase, three-component problem using SPU and ENO are shown in Figures 4.1, 4.8 and 4.9 along with the analytic solution. The simulations shown are relatively coarsely gridded, but as the number of gridblocks is increased the simulated solutions converge toward the proposed solution.

Figure 4.10 shows the error at $\tau = 1$ at three points along the domain. The average slope of the local error curves for the points $\xi = 1.225$ and $\xi = 2.275$ for SPU is 1.05 and 0.84 and for ENO is 1.03 and 1.08. Therefore at these points ENO and SPU are only converging with a first order rate for this example and from the figure we can see that ENO is around one order of magnitude more accurate than SPU except when the grid is very coarse, as expected.

At $\xi = 0.125$ the ENO solution is not uniformly converging to the analytic solution and the average slope of the error line is $p = 2.68$, which represents nearly third-order convergence and SPU converges with order $p = 2.19$. It is not clear why the ENO and SPU schemes are able to get improved local convergence at this point. It may be related to the fact that $\xi = 0.125$ is upstream of the two weakly self-sharpening shocks in the solution and downstream of the contact discontinuity with velocity zero. Table 4.4 shows that for a set grid size SPU is approximately three times faster than ENO, but given the order of magnitude improvement in accuracy from ENO, ENO is even more efficient.

Finally, the comparison of our solution against analytic solution proved beneficial since the leading front at the end of the first gas cycle in Figure 1 of Valenti et al. (2004) appears to have it's velocity underestimated. After 0.1 pore volumes injected it has progressed approximately 0.2, whereas in our equivalent simulation we can see the leading front progresses approximately 0.25 for each 0.1 pore volumes injected. This velocity error is most likely a result of a difference between the quoted time of the result and that used in their simulation. Since the investigation (LaForce, 2011) into hyperbolicity found this problem to be strictly hyperbolic, this difference cannot be explained by non-uniqueness of solutions.

Table 4.4: The CPU time taken to simulate the benchmark solution posed in Section 4.2.2 using ENO and SPU. The number of timesteps was fixed at 20000.

Number of cells	SPU time (seconds)	ENO time (seconds)
150	2.0	5.0
450	5.7	15.0
1250	16.0	41.2

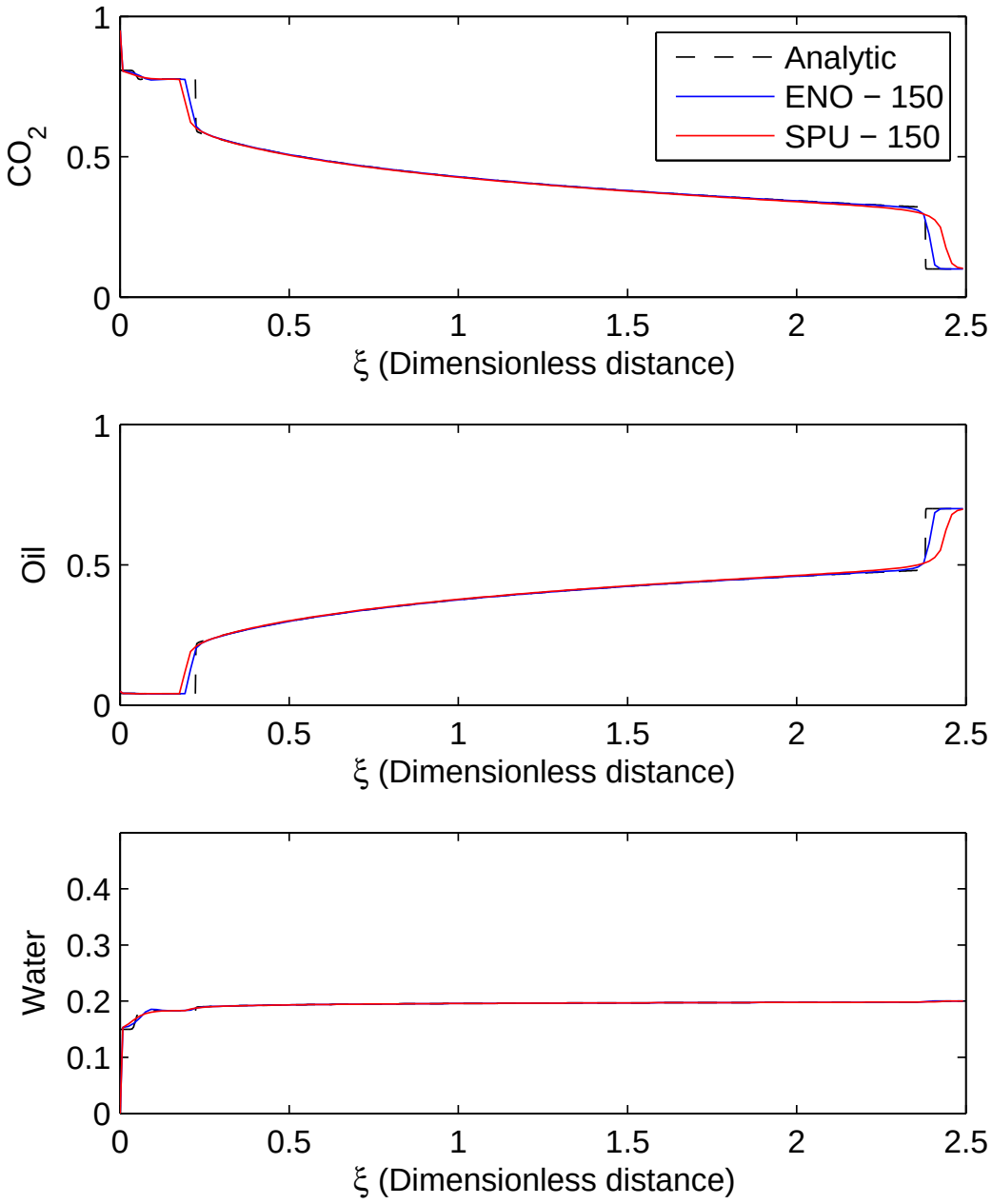


Figure 4.8: Analytic and simulated profiles of the solution to the three-phase, three-component benchmark problem posed in Section 4.2.2. The volume fraction of the CO_2, oil and water components along the 1D reservoir is shown. ENO produces significantly less numerical diffusion than SPU at the shock fronts for the same 150 cell level of grid-refinement. The CPU times taken to reach the solutions were 2 and 5 seconds for SPU and ENO respectively. Analytic solutions provided by LaForce (2011)

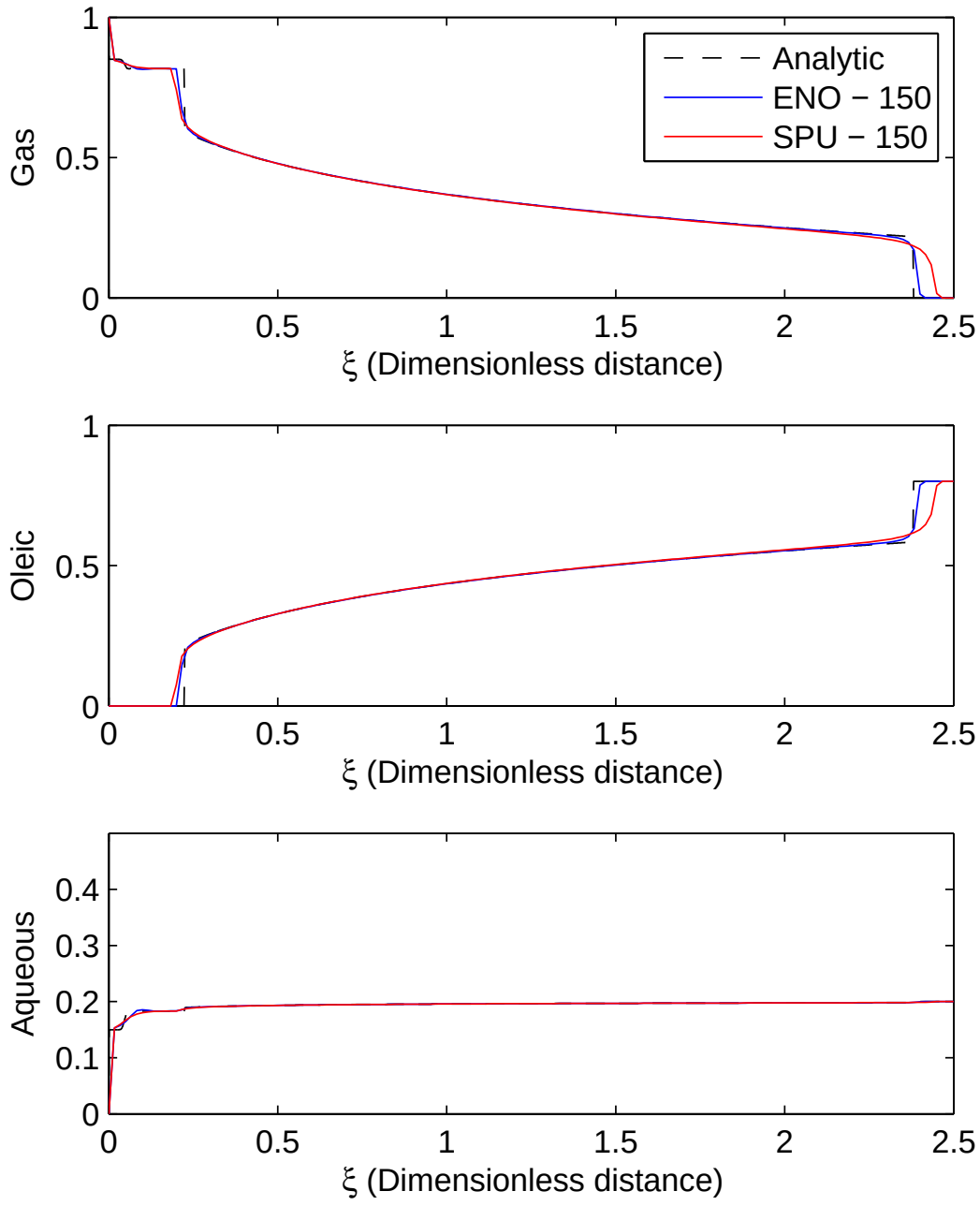


Figure 4.9: Analytic and simulated profiles of the solution to the three-phase, three-component benchmark problem posed in Section 4.2.2. The volume fraction of the gas, oleic and aqueous phases along the 1D reservoir is shown. ENO produces significantly less numerical diffusion than SPU at the shock fronts for the same 150 cell level of grid-refinement. The CPU times taken to reach the solutions were 2 and 5 seconds for SPU and ENO respectively. Analytic solutions provided by LaForce (2011)

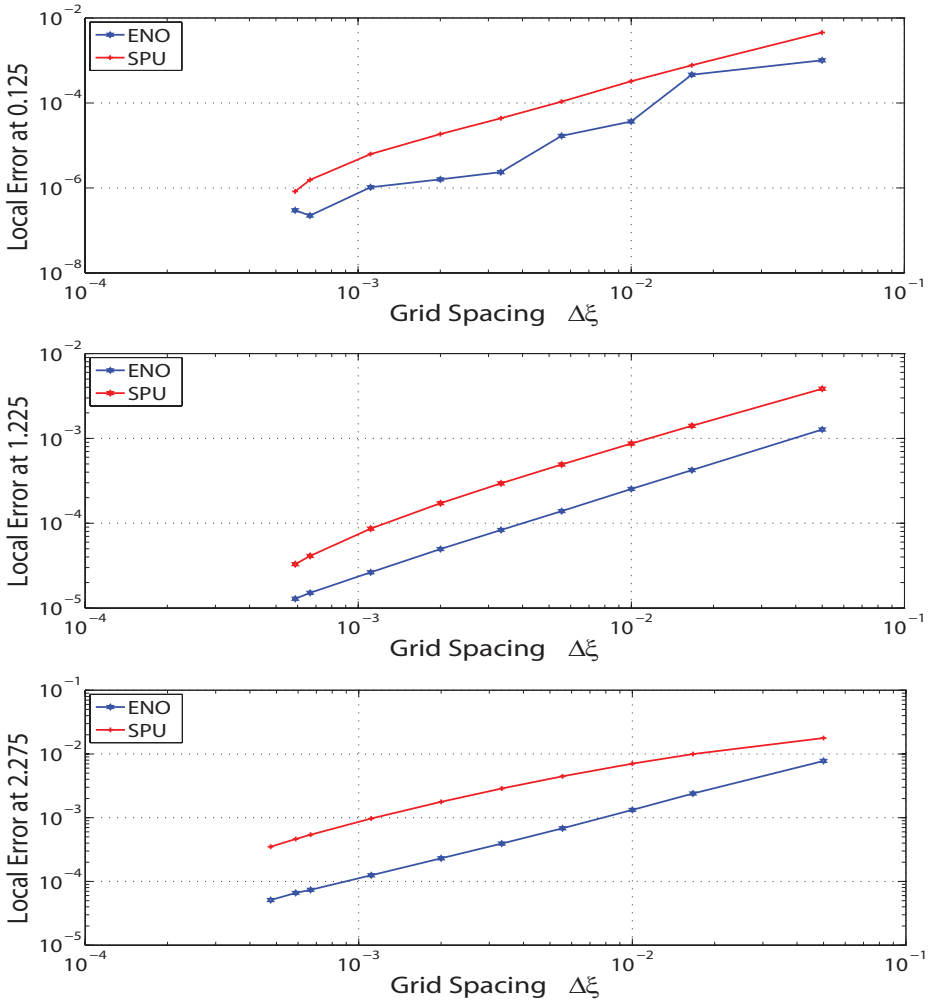


Figure 4.10: Local error at points 0.125, 1.225 and 2.275 against grid spacing $\Delta\xi$ in the three-phase, three-component benchmark problem as posed by Section 4.2.2 and shown in Figures 4.1 and 4.8. The average slope of the local error curves for SPU is 2.19, 1.05 and 0.84 for the points 0.125, 1.225 and 2.275. The average slope of the local error curves for ENO is 2.68, 1.03 and 1.08 for the points 0.125, 1.225 and 2.275. There is a factor of 3 to 20 accuracy improvement in ENO over SPU.

4.5 Discussion - Accuracy of ENO in Presence of Discontinuities

In this work it was found that in solutions with discontinuities present, ENO loses third order accuracy. From further review of the literature this result was not unknown, but is however rarely stated with a tendency for literature to refer to only the 'formal' order of accuracy of the method. This seems to be particularly the case when approaching the problem from a geoscience angle. Firstly, work within the petroleum literature that has taken up the method (Gerritsen et al., 2005; Jessen et al., 2008; Mallison et al., 2005; Valenti et al., 2004) does not mention the loss of accuracy. The references therein tend to direct the reader towards the main ENO literature (Harten et al., 1987; Harten and Osher, 1987; Shu and Osher, 1988, 1989; Shu, 1997), a set of papers which each have over well over 1000 citations. These papers again concentrate upon the formal high order accuracy, although there is an implicit acknowledgment of the loss of high order accuracy since most analysis refers to piecewise smooth functions. Perhaps a point of distraction in these is that ENO schemes can achieve high-order accuracy at extrema, although no convergence proofs of this exist for 3rd order ENO schemes (Shu, 1997) which are highly nonlinear (Harten et al., 1987).

It is in some broader numerical methods texts and in particular more recent texts (LeVeque, 2002; Gustafsson, 2008) where there are useful comments on the accuracy of general high order methods in the presence of shocks. In particular within (LeVeque, 2002, p.191) it is said that "for practical problems with interesting solutions involving shock waves, it appears difficult to formally achieve high-order accuracy in smooth regions with any method". These broader numerical methods texts contain very little, if any, detail about ENO however.

Finally the analysis of papers (Efraimsson and Kreiss, 1999; Engquist and Sjogreen, 1998) with significantly fewer citations than the original ENO papers is able to more explicitly clarify the accuracy of ENO in the presence of shocks. Engquist and Sjogreen (1998) shows that O(1) pointwise errors at a shock may affect the smooth part of a solution such that only first order is achieved even for formally higher order methods. They also show that higher order methods can maintain their order of accuracy in parts of the domain where no characteristics have passed through a shock. In 1D reservoir flow problems where a shock starts the problem, however this only represents the part of the reservoir unaffected by injection. Given this more thorough analysis, it is clear we should not expect to maintain the high order of accuracy in problems with shocks.

4.6 Conclusions

In this chapter the goal was to determine numerically the physical solution to three-phase flow problems by the inclusion of physical diffusive terms and use of an ENO numerical method with no diffusive approximation errors. Three phase flow problems are particularly challenging to solve numerically as at certain saturations the solutions to the equations may be non-unique. However we have demonstrated that ENO produces first-order convergence for the majority of the computational domain and is therefore affected by numerical diffusion approximation errors. Given this result we were not able to produce a rigorous analysis of the convergence of three-phase flow solutions using our proposed methodology. This result provides clarification of an existing result not presented in the geoscience literature and often omitted from highly cited numerical methods literature.

We have benchmarked compositional three-phase, three-component ENO simulations against analytic solutions for the first time. Although this benchmarking process demonstrated that both SPU and ENO methods have first-order convergence, the ENO scheme is generally an order of magnitude more accurate than SPU for a given grid resolution. To achieve this improvement in accuracy ENO requires approximately three-times more CPU time than SPU. Therefore ENO is still approximately three-times more accurate than SPU for a given CPU time and is a preferable numerical method.

Chapter 5

1D Three Phase Solutions in the Presence of Capillary Pressure with Varying Wettability

5.1 Introduction

In Chapters 2 and 4 we raised the issue that the systems of equations that model advective three-phase flow can produce non-unique solutions. To determine the physical solutions to these problems, solutions must satisfy the viscous profile entropy condition. This requires that solutions are found in the zero limit of a physical second-order term. In this chapter we consider the second-order term derived from the inclusion of capillary pressure in the conservation law. Due to numerical diffusion we do not look to rigorously identify zero-limit solutions but instead look for a pair of solutions, which from the use of different wettability capillary pressure models, change/diverge from the purely advective solution with different behaviour. This demonstrates how the nature of solutions can be fundamentally changed by different second-order terms, offering the possibility for different zero-limit convergence. We first consider the system from Chapter 4 with capillary pressure and then a problem with an elliptic region and show that in this case as distinct oleic-wet and aqueous-wet capillary pressures are reduced they converge to the same solution.

The format of the chapter is as follows. In Section 5.2 the advective transport model with capillary pressure and capillary pressure models are outlined. In Section 5.3 we describe both an explicit and operator splitting numerical scheme used to solve this problem as well as a method for the calculation of three-phase saturations. In Section 5.4 we show results for four test models, including results with full partitioning of components between phases, oleic-wet and aqueous-wet capillary pressure. Convergence of the results with different wettability capillary pressures as the capillary pressure size is reduced is then shown. Finally in Section 5.5 we discuss the results and present conclusions.

5.2 Mathematical Model

In this section we set out the advective transport problem with the effect of capillary pressure included. This is an extension of the advective transport problem formulation of Section 4.2 where capillary pressure effects were neglected. The updated equations are described, followed by the capillary pressure models to be used. Finally four test problems are proposed, with partitioning of all components between all three phases in three of the examples.

5.2.1 Advective Transport Model with Capillary Pressure

The 1D compositional transport equations with capillary pressure effects are

$$\frac{\partial C_i}{\partial \tau} + \frac{\partial F_i}{\partial \xi} + \frac{K}{u_t L} \sum_{j=1}^{n_p} \sum_{q \neq j}^{n_p} \frac{\partial}{\partial \xi} \left[c_{ij} f_j \lambda_q \frac{\partial}{\partial \xi} (P_{cjq}) \right] = 0. \qquad i = 1, ..., n_c - 1 \tag{5.1}$$

where u_t is the combined injection velocity of all phases and L is the length of the 1D porous medium. These are derived from the mass balance equations and Darcy's Law, within which the pressure of phase j in Darcy's law is now given by

$$P_j = P_q - P_{cjq} \tag{5.2}$$

where P_{cjq} is the capillary pressure between phase q and phase j.

In addition to Equation 5.1 the thermodynamic partitioning coefficients, K_i^1 and K_i^2, and the auxiliary relations from Section 4.2 still apply. As in Section 4.2.2, where subscripts are used to describe phases, such as S_j and P_{cjq}, subscript 1 represents the gas (or supercritical CO_2) phase, 2 the oleic phase and 3 the aqueous phase.

5.2.2 Capillary Pressure Models

Equations 5.1 require a capillary pressure model for P_{cjq}. Two models are considered, one aqueous-wet and one oleic-wet and are constructed following the saturation dependency suggested in Aziz and Settari (1979); Lenhard and Parker (1988); Sheffield (1968), which combines two-phase capillary pressure results to form three-phase relations as explained in Section 2.3.4. The models are:

Aqueous-wet Capillary Pressure

This capillary pressure model is consistent with a strongly aqueous-wet system with the oleic phase intermediate wetting and gas the non-wetting phase as shown in Figure 5.1.

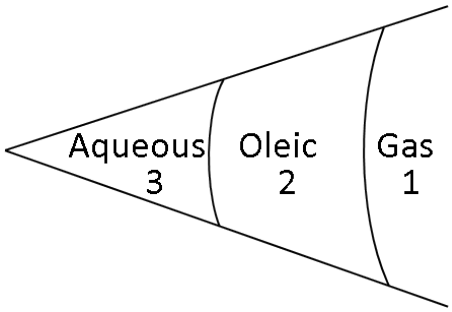


Figure 5.1: Representation of wettability using the crevice of a pore as shown in DiCarlo et al. (2000). The aqueous phase is the wetting phase, oleic phase intermediate-wet and the gas phase non-wetting.

Based upon this setup the oleic-aqueous and oleic-gas capillary pressures are calculated using two-phase capillary pressure functions dependant upon the aqueous phase and combined aqueous and oleic phase saturations respectively.

The two-phase capillary pressure model used in this construction is a Brooks and Corey (1964) type model of the form $P_{cjq} = cS_j^{-\alpha}$. Coefficients proposed by Leverett (1941) are applied to this form to produce appropriately scaled capillary pressures. The resulting three-phase capillary pressure functions are

$$P_{c32} = 0.3(\phi/K)^{\frac{1}{2}}\sigma_{32}(S_3 + 0.05)^{-\frac{1}{2}} \tag{5.3}$$

$$P_{c21} = 0.3(\phi/K)^{\frac{1}{2}}\sigma_{21}(S_3 + S_2 + 0.05)^{-\frac{1}{2}} \tag{5.4}$$

$$P_{c31} = P_{c32} + P_{c21}. \tag{5.5}$$

where σ_{jq} is the interfacial tension between phase j and phase q. Parameter values for the constants in equations 5.3-5.5 are shown in Table 5.1. The σ_{21} and σ_{31} are typical values from Georgiadis et al. (2011) with σ_{21} so that the spreading coefficient is slightly less than zero. The 0.3 value is to scale the entry pressure when $S_3 = 1$ or $S_3 + S_2 = 1$ for P_{c32} and P_{c21} respectively, based upon (Bear, 1988, p.448). L=1m is chosen to be representative of experimental conditions that will not be dominated by end effects. The 0.05 is introduced into the saturation bracket for numerical simplicity to limit asymptotic behaviour as $S_3, S_2 \to 0$ as $S_3 < S_{r3}$ and $S_2 < S_{r2}$ are possible when vaporisation of phases is included in the model. The aqueous-oleic and oleic-gas capillary pressure functions are shown in Figure 5.2.

Table 5.1: Capillary pressure term parameters

ϕ	K	σ_{32}	σ_{21}	σ_{31}	u_t	L
0.2	$2x10^{-13}$ m^2	0.05N/m	0.02N/m	0.06 N/m	0.0001 m/s	1m

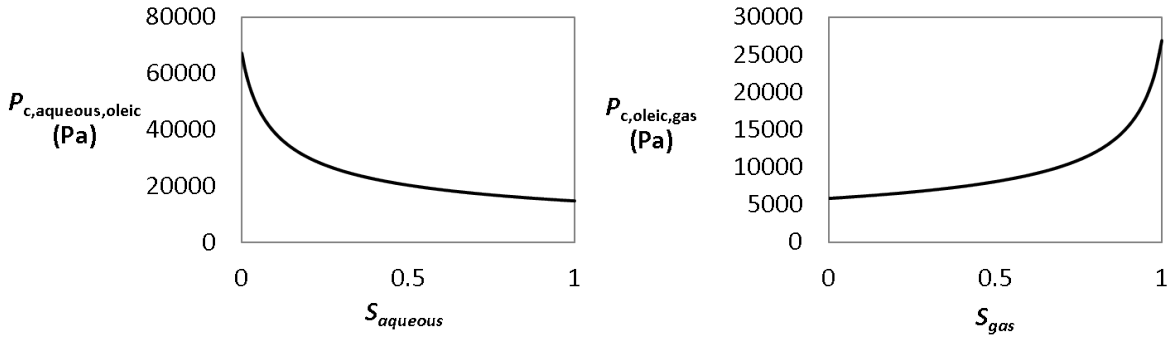


Figure 5.2: The aqueous-oleic and oleic-gas capillary pressure functions in a water-wet porous medium.

Oil-wet Capillary Pressure

This capillary pressure model is equivalent in construction to the previous model, apart from the change in wettability. This setup is based upon a strongly oleic-wet system with the aqueous phase as intermediate wetting and gas the non-wetting phase. This provides a simplified model for numerical purposes, oleic capillary pressure models are often more complex. The resulting three-phase capillary pressure functions are

$$P_{c32} = -0.3(\phi/K)^{\frac{1}{2}}\sigma_{32}(S_2 + 0.05)^{-\frac{1}{2}} \tag{5.6}$$

$$P_{c21} = P_{c31} - P_{c32} \tag{5.7}$$

$$P_{c31} = 0.3(\phi/K)^{\frac{1}{2}}\sigma_{31}(S_3 + S_2 + 0.05)^{-\frac{1}{2}}. \tag{5.8}$$

The parameters from Table 5.1 are used again. The resulting aqueous-oleic and aqueous-gas capillary pressure functions are shown in Figure 5.3.

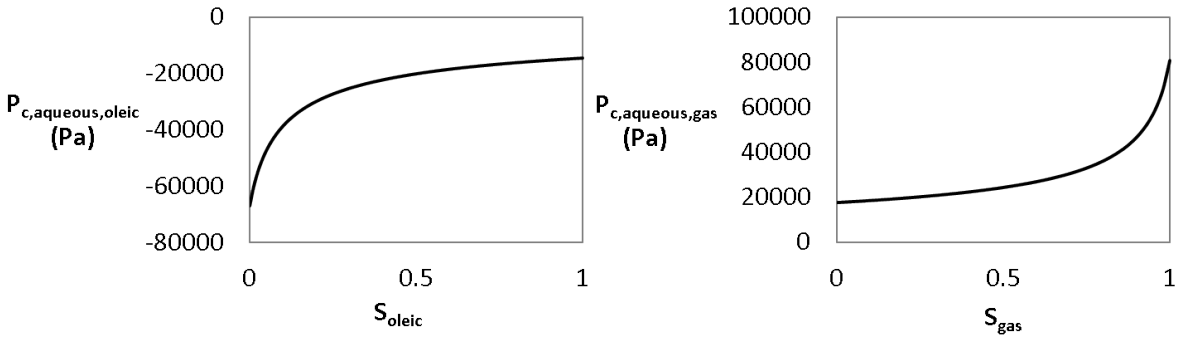


Figure 5.3: The aqueous-oleic and aqueous-gas capillary pressure functions in an oleic-wet porous medium.

5.2.3 Test Models

Four test models are proposed, Models A-D. They progressively build upon the example solution of Section 4.2.2 by sequentially introducing an aqueous-wet capillary pressure, fully compositional model, initial and boundary conditions representative of CO_2 storage and finally an oleic-wet capillary pressure. These allow us to investigate the effect of each feature but in particular we wish to compare the solutions with the oleic-wet and aqueous-wet capillary pressures. The models are:

Model A - Aqueous-wet Capillary Pressure

Table 5.2: Parameters for model A

Component	i	K_i^1	K_i^2	$C_i^{initial}$	$C_i^{injection}$	Phase	j	μ_j (Pa.s)	S_{rj}
CO_2	1	4.5	-	0.1	0.95	Gas	1	0.0001	0.05
Oil	2	0.1	-	0.7	0.05	Oleic	2	0.0005	0.1/0.2
Water	3	-	-	0.2	0	Aqueous	3	0.001	0.15

In Model A a capillary pressure extension to the three-phase three-component solution with immiscible water of Section 4.2.2 is considered. The capillary pressure model used is the aqueous-wet model from Section 5.2.2. Otherwise the rest of the setup including the relative permeability model (Eqs 4.3-4.7) and parameters of Table 5.2 are retained. Although Shearer and Trangenstein (1989) shows that models with Baker relative permeability can be non-strictly hyperbolic, for these parameters the model remains strictly hyperbolic (LaForce, 2011).

Model B - Fully Compositional Model Representative of CO_2, Oil and Water

Table 5.3: Parameters for model B

Component	i	K_i^1	K_i^2	$C_i^{initial}$	$C_i^{injection}$	Phase	j	μ_j (Pa.s)	S_{rj}
CO_2	1	8	3	0.1	0.95	Gas	1	0.0001	0.05
Oil	2	0.01	1000	0.7	0.05	Oleic	2	0.0005	0.1/0.2
Water	3	2	0.01	0.2	0	Aqueous	3	0.001	0.15

This model progresses from Model A by introducing full partitioning of components between all phases. This is shown by the K-values in Table 5.3. The aqueous-wet capillary pressure is maintained. The model also maintains strict hyperbolicity and the analytic solution in Figure 5.9 was constructed (LaForce, 2011) in a similar way to the solution in Section 4.2.2.

Model C - Injection and Boundary Conditions Representative of CO_2 Storage

Table 5.4: Parameters for model C and D

Component	i	K_i^1	K_i^2	$C_i^{initial}$	$C_i^{injection}$	Phase	j	μ_j (Pa.s)	S_{rj}
CO_2	1	8	3	0	1.0	Gas	1	0.0004	0.05
Oil	2	0.01	1000	0.5	0	Oleic	2	0.0005	0.1/0.2
Water	3	2	0.01	0.5	0	Aqueous	3	0.001	0.15

This model differs from model B by changing the initial and boundary conditions as shown in Table 5.4 to be more representative of CO_2 storage. The model is still fully compositional and uses the aqueous-wet capillary pressure model. We also change the gas-phase viscosity to create an elliptic region in the solution so that for the parameters chosen in Model C the purely advective conservation law is a mixed hyperbolic and elliptic system. There is a small region of complex eigenvalues found (LaForce, 2011) near (C_1, C_2, C_3) = (0.498,0.179,0.323).

An analytical solution for this model was constructed (LaForce, 2011) in the same way as for the mixed hyberbolic and elliptic model shown in LaForce and Johns (2005b). The solution is shown in Figure 5.9. Starting at the downstream end, the solution consists of a leading water bank, followed by a shock into the three-phase region and a long rarefaction along a fast path. Then there is a shock to the gas/oil binary system. The water is evaporated across this shock. Finally there is a trailing shock to the injection composition of 100% CO_2 across which the oil component is evaporated. The shock into the three-phase region and the rarefaction path throughout the three-phase region are a transitional wave group. Unlike the solutions seen for compositional three-phase problems in LaForce and Johns (2005b), the solution to this Riemann problem follows the fast path along the boundary of the elliptic region and then continues along the fast path. The small bump in the profile near ξ=0.2 is caused by the solution essentially following the boundary of the elliptic region, which no characteristic paths enter.

Model D - Oleic-wet Capillary Pressure

Finally model D changes from the aqueous-wet capillary pressure model to the oleic-wet capillary pressure model. The model is still fully compositional and maintains the parameters of Table 5.4.

5.3 Numerical Model

In this section we introduce the numerical methods used to solve the set of advection-capillary equations set out in Section 5.2.

First, an extension to the explicit formulation of Section 4.3 was considered, which uses the ENO interpolations in an explicit scheme described in Section 5.3.1. As previously reported (Holm et al., 2010; Jackson and Blunt, 2002) this explicit scheme has restricted stability for capillary pressures of large magnitudes so an operator splitting scheme was also considered. Operator splitting is often used to take advantage of the strengths of different numerical methods by using the different numerical methods to solve each term within an equation. In this case we choose to use a potentially more stable implicit method to advance our solution due to the effect of capillary pressure, while maintaining the ENO explicit method to model advection. We present this second approach in Section 5.3.2.

Within Section 5.2, full partitioning of components between all phases was also introduced, therefore we also present a three-phase flash solver in Section 5.3.3.

5.3.1 Fully Explicit Scheme

First the explicit scheme produced to solve Equation 5.1 is presented. The explicit formulation maintained use of the ENO method described in Section 4.3.4. This method was used to approximate cell-face values in the final discretisation, such as the flux values in the advection term. The new capillary pressure term in Equation 5.1 was discretised forwards in time and centrally in space.

This approach to discretising the capillary pressure term is similar to a common explicit approach ((Strikwerda, 2004, p.160) and (Hundsdorfer, 2003, p.66)) used for discretising the second-order diffusion term in the linear advection-diffusion equation. However, we cannot duplicate the standard method exactly since the second-order capillary pressure derivative term in Equation 5.1 has non-linearity due to spatially varying pre-factors c_{ij}, f_j and k_{rq}. As a result the general forwards in time and central in space approach is applied to form a specific discretisation for this particular second-order equation.

$$C_{k,i}^{n+1} = C_{k,i}^{n} - \frac{\Delta\tau}{\Delta\xi}\left(F_{k+\frac{1}{2},i}^{n} - F_{k-\frac{1}{2},i}^{n}\right) - \frac{K\Delta\tau}{u_t L\Delta\xi}\left[\left(\sum_{j=1}^{n_p}\sum_{q\neq j}^{n_p} c_{ij} f_j \frac{k_{rq}}{\mu_q}\frac{\partial P_{cjq}}{\partial\xi}\right)\Bigg|_{k+\frac{1}{2}}^{n} - \left(\sum_{j=1}^{n_p}\sum_{q\neq j}^{n_p} c_{ij} f_j \frac{k_{rq}}{\mu_q}\frac{\partial P_{cjq}}{\partial\xi}\right)\Bigg|_{k-\frac{1}{2}}^{n}\right] \quad (5.9)$$

$$C_{k,i}^{n+1} = C_{k,i}^{n} - \frac{\Delta\tau}{\Delta\xi}\left(F_{k+\frac{1}{2},i}^{n} - F_{k-\frac{1}{2},i}^{n}\right) - \frac{K\Delta\tau}{u_t L\Delta\xi^2}\sum_{j=1}^{n_p}\sum_{q\neq j}^{n_p}\left[\left(c_{ij} f_j \frac{k_{rq}}{\mu_q}\right)\Bigg|_{k+\frac{1}{2}}^{n}\left[P_{cjq}(S_{k+1}^{n}) - P_{cjq}(S_{k}^{n})\right] - \left(c_{ij} f_j \frac{k_{rq}}{\mu_q}\right)\Bigg|_{k-\frac{1}{2}}^{n}\left[P_{cjq}(S_{k}^{n}) - P_{cjq}(S_{k-1}^{n})\right]\right] \quad (5.10)$$

The final discretisation is shown in Equation 5.10. Equation 5.9 shows the main intermediate step in deriving this discretisation from Equation 5.1. The intermediate step in Equation 5.9 highlights the use of approximations at the cell faces $k + \frac{1}{2}$ and $k - \frac{1}{2}$ to estimate the first derivative in Equation 5.1. Due to the nonlinearity, some of the these cell-face values remain in Equation 5.10 after the second derivative term has been approximated. This maintains the consistency of the scheme as commented in (Strikwerda, 2004, p.163). We chose to estimate these cell-face values using our ENO interpolations. We believe this is the first time cell face values in an explicit scheme for capillary pressure have been approximated using high order interpolations. In a similar scheme (Van Duijn et al., 1995, p.86) estimated these cell-face values using linear interpolation of the saturation values. An explicit scheme by Jackson and Blunt (2002) avoided the need for cell-face values by discretising the terms in equation 5.9 at the upwind points. Berenblyum et al. (2003) and Holm et al. (2010) also solve the equation explicitly as part of IMPES, although it is not clear whether cell-face values are calculated or not.

Implementation

To simulate the compositional advection-capillary gas injection problem we combine the discretisation shown in Equation 5.10 with the algorithm described in Figure 5.4. As in Section 4.3.6 this includes flash solves to calculate phase saturations and Runge-Kutta timestepping to minimise temporal errors. The equations are again dealt with in a componentwise manner, solving for each component independently of the others during each Runge-Kutta timestep. Where the capillary term requires the calculation of a number of

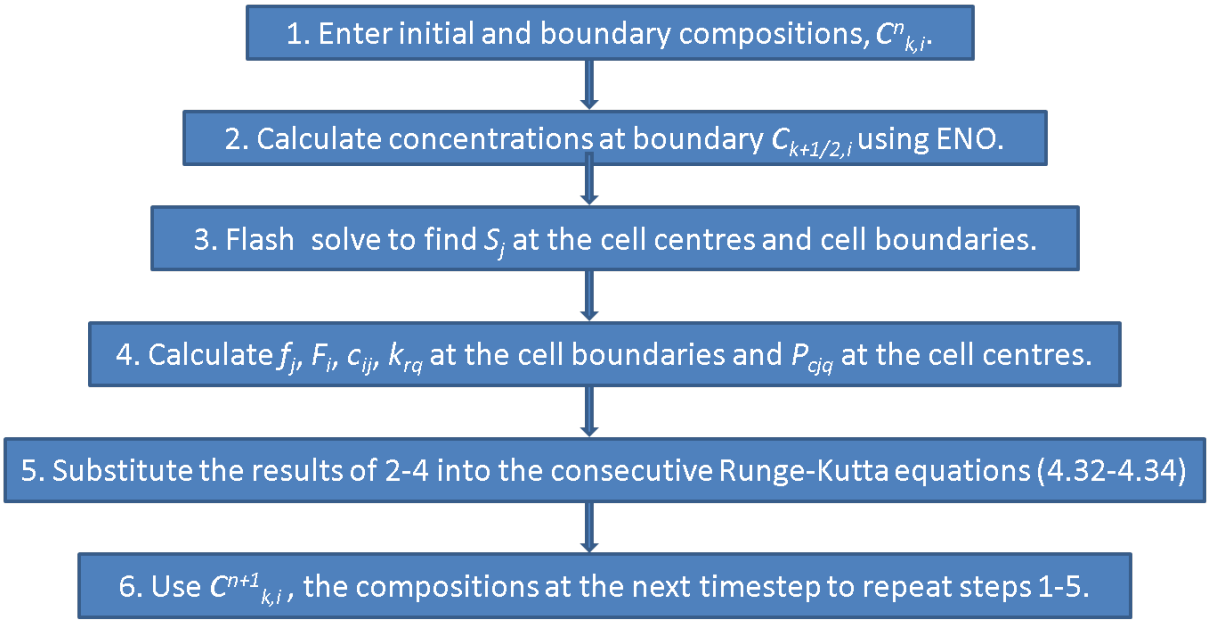


Figure 5.4: Flowchart of numerical method to solve three-phase, three-component transport problem with capillary pressure.

terms at the cell-faces $k + \frac{1}{2}$ and $k - \frac{1}{2}$ as shown in Figure 5.5 these are calculated using values of $C_{k+\frac{1}{2},i}$, which are approximated using third-order ENO interpolations.

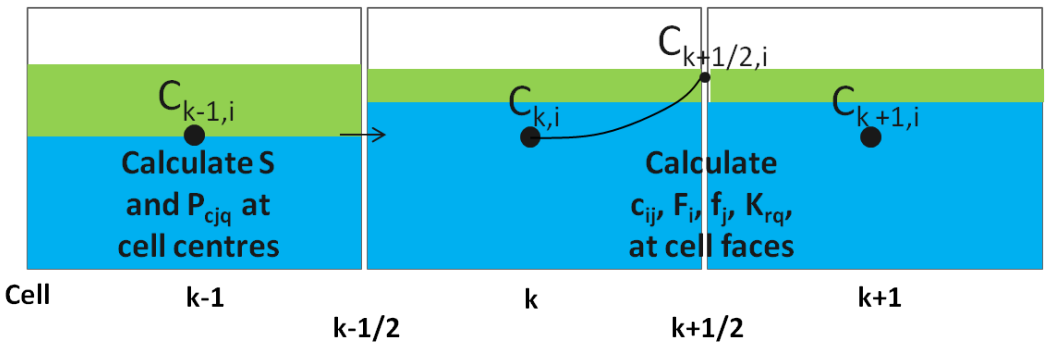


Figure 5.5: Cell centred and call face values used for the discretisation of the capillary pressure term.

The c_{ij} are calculated during the three-phase flash solve described in Section 5.3.3 or if studying a model such as the example solution in Section 4.2.2 where one phase is immiscible then they are calculated from rearranging Equations 2.14 with the K-values

$K_i^1 = c_{i1}/c_{i2}$ to give

$$c_{i1} = \frac{K_i^1 C_i}{S_1(K_i^1 - 1) + (1 - C_3)} \tag{5.11}$$

$$c_{i2} = \frac{C_i}{S_1(K_i^1 - 1) + (1 - C_3)} \tag{5.12}$$

$$c_{33} = 1, c_{13} = c_{23} = 0 \tag{5.13}$$

Accuracy

The accuracy of the numerical approximation in Equation 5.10 to the capillary term in Equation 5.1 is estimated using Taylor expansions of the componentwise discretisation. From this analysis it was found (See Appendix H) that the numerical error e due to the approximation of this term is

$$e = \frac{K}{u_t L} \sum_{j=1}^{n_p} \sum_{q \neq j} \left(\frac{\Delta\xi^2}{8} \frac{\partial^2 \left(c_{ij} f_j \frac{k_{rq}}{\mu_q} \right)}{\partial \xi^2} \frac{\partial^2 P_{cjq}}{\partial \xi^2} + \frac{\Delta\xi^2}{12} \left(c_{ij} f_j \frac{k_{rq}}{\mu_q} \right) \frac{\partial^4 P_{cjq}}{\partial \xi^4} \right.$$
$$\left. + \frac{\Delta\xi^2}{6} \frac{\partial \left(c_{ij} f_j \frac{k_{rq}}{\mu_q} \right)}{\partial \xi} \frac{\partial^3 P_{cjq}}{\partial \xi^3} + \frac{\Delta\xi^2}{24} \frac{\partial^3 \left(c_{ij} f_j \frac{k_{rq}}{\mu_q} \right)}{\partial \xi^3} \frac{\partial P_{cjq}}{\partial \xi} \right) \tag{5.14}$$

which is $\mathrm{O}(\Delta\xi^2)$ and involves terms which all have four derivatives in space. From Section 4.3 we know that errors for the advection term using ENO are formally $\mathrm{O}(\Delta\xi^3)$ with fourth order derivatives in space. Therefore we have no numerical errors that have second order in space derivatives. Since we have no second order in space derivatives involved we hope to be able to capture our second order term, the capillary pressure, clearly. We also hope that given the magnitude of the capillary pressure chosen, the first order errors associated with shocks will not dominate this case as seen in Section 4.4.3. This may not be the case when our initial condition is a shock.

Stability

Finally, we look at the stability of the scheme. Stability analysis for numerical discretisations of coupled advection-diffusion type transport equations with nonlinear second-order terms like our capillary pressure term in Equation 5.1 do not seem to be available in the literature. Therefore we considered stability criteria of discretisations similar to ours for similar scalar equations.

Firstly we considered an equation of the advection-diffusion type but a scalar, linear

version

$$\frac{\partial C}{\partial \tau} + a\frac{\partial C}{\partial \xi} = b\frac{\partial^2 C}{\partial \xi^2} \tag{5.15}$$

where a and b are constant coefficients. For this scalar equation we considered the stability of very similar scheme to ours with upwind differencing for the advection term and central differencing for the second-order term

$$\frac{C_k^{n+1} - C_k^n}{\Delta\tau} + a\frac{C_k^n - C_{k-1}^n}{\Delta\xi} = b\frac{C_{k+1}^n - 2C_k^n + C_{k-1}^n}{\Delta\xi^2} \tag{5.16}$$

In (Strikwerda, 2004, p.160) the stability condition for this scheme is given as

$$2b\frac{\Delta\tau}{\Delta\xi^2} + a\frac{\Delta\tau}{\Delta\xi} \leq 1 \tag{5.17}$$

We also wanted to look at some stability analysis for nonlinear equations. However, we could not find stability analysis available for nonlinear equations including the advective term and so considered analysis for an equation without an advective term. This included a second order term which more closely represents the form of our second order capillary pressure term, the least stable part of our scheme. However, it still also scalar and the second order term was differentiating C rather than P_{cjq}.

$$\frac{\partial C}{\partial \tau} = \frac{\partial}{\partial \xi}\left(b(\tau,\xi)\frac{\partial C}{\partial \xi}\right) \tag{5.18}$$

For this type of equation we considered the same discretisation as we used

$$\frac{C_k^{n+1} - C_k^n}{\Delta\tau} = \frac{b(\tau_n, \xi_{k+\frac{1}{2}})(C_{k+1}^n - C_k^n) - b(\tau_n, \xi_{k-\frac{1}{2}})(C_k^n - C_{k-1}^n)}{\Delta\xi^2} \tag{5.19}$$

With this discretisation Strikwerda (2004) presents the stability criterion

$$b(\tau,\xi)\frac{\Delta\tau}{\Delta\xi^2} \leq \frac{1}{2} \tag{5.20}$$

Although neither of these stability criteria are designed exactly for our case, and both are scalar equations, they provided a useful guideline. From this guideline it was clear we would expect a stricter stability criteria than we saw for the hyperbolic problems with the CFL condition. In practice however we did not estimate the exact value of the criteria since the $b(\tau,\xi)$ in our case, combinations of c_{ij}, f_j and k_{rq} was too complicated to estimate globally. This is not least because we require a flash solve to determine some of these parameters at each step, which couldn't be done globally. Also the second order term in our equation differentiates P_{cjq} rather than C. For this reason we did not seek to

develop a new stability criterion. However, we were able to estimate the stability criterion based upon monitoring stability with different $\frac{\Delta\tau}{\Delta\xi^2}$.

5.3.2 Operator Splitting Scheme

The second scheme produced to solve Equation 5.1 was an operator splitting scheme. Operator splitting has previously been used to solve the immiscible three-phase capillary-advection equations by Abreu et al. (2004). In the simplest operator splitting scheme, rather than solving Equation 5.1 directly during each timestep, the two subproblems Equation 5.21 for explicit advection and 5.22 for implicit capillary pressure

$$\frac{\partial C_i^*}{\partial \tau} + \frac{\partial F_i}{\partial \xi} = 0 \quad \text{for} \quad \tau_n < \tau < \tau_{n+1} \quad \text{with} \quad C_i^{n,*} = C_i^n \tag{5.21}$$

$$\frac{\partial C_i^{**}}{\partial \tau} + \frac{K}{u_t L}\sum_{j=1}^{n_p}\sum_{q\neq j}^{n_p}\frac{\partial}{\partial \xi}\left[c_{ij}f_j\lambda_q\frac{\partial}{\partial \xi}(P_{cjq})\right] = 0 \quad \text{for} \quad \tau_n < \tau < \tau_{n+1} \quad \text{with} \quad C_i^{n,**} = C_i^{n+1,*} \tag{5.22}$$

are solved one after another, starting from C_i^n, and taking $C_i^{n+1} = C_i^{n+1,**}$ to complete a timestep. This scheme produces first order $O(\Delta\tau)$ errors in time due to the operator splitting (Hundsdorfer, 2003, p.325) and so in this work we use the second order symmetrical splitting scheme for $i = 1, ..., n_c$ as follows where

$$\frac{\partial C_i^*}{\partial \tau} + \frac{\partial F_i}{\partial \xi} = 0 \quad \text{for} \quad \tau_n < \tau < \tau_{n+\frac{1}{2}} \quad \text{with} \quad C_i^{n,*} = C_i^n \tag{5.23}$$

$$\frac{\partial C_i^{**}}{\partial \tau} + \frac{K}{u_t L}\sum_{j=1}^{n_p}\sum_{q\neq j}^{n_p}\frac{\partial}{\partial \xi}\left[c_{ij}f_j\lambda_q\frac{\partial}{\partial \xi}(P_{cjq})\right] = 0 \quad \text{for} \quad \tau_n < \tau < \tau_{n+1} \quad \text{with} \quad C_i^{n,**} = C_i^{n+\frac{1}{2},*} \tag{5.24}$$

$$\frac{\partial C_i^{***}}{\partial \tau} + \frac{\partial F_i}{\partial \xi} = 0 \quad \text{for} \quad \tau_{n+\frac{1}{2}} < \tau < \tau_{n+1} \quad \text{with} \quad C_i^{n,***} = C_i^{n+1,**} \tag{5.25}$$

and $C_i^{n+1} = C_i^{n+1,***}$ to complete a timestep. This second order scheme adds negligible computational time for the extra accuracy in our case, since the time-consuming implicit algorithm for solving capillary pressure remains the same.

To solve the advection equations 5.23 and 5.25 the same explicit numerical methods were applied as in Section 4.3. The capillary equation 5.24 is solved with the implicit

method described below.

Implicit Scheme

To model the capillary equation 5.24 the backward-time, central space discretisation scheme is used, resulting in the discretisation

$$C_{k,i}^{n+1} = C_{k,i}^{n} - \frac{K\Delta\tau}{u_t L \Delta\xi^2} \sum_{j=1}^{n_p} \sum_{q\neq j}^{n_p} \left[\left(c_{ij} f_j \frac{k_{rq}}{\mu_q} \right) \Big|_{k+\frac{1}{2}}^{n+1} \left[P_{cjq}(S_{k+1}^{n+1}) - P_{cjq}(S_k^{n+1}) \right] - \left(c_{ij} f_j \frac{k_{rq}}{\mu_q} \right) \Big|_{k-\frac{1}{2}}^{n+1} \left[P_{cjq}(S_k^{n+1}) - P_{cjq}(S_{k-1}^{n+1}) \right] \right] \tag{5.26}$$

This uses the same spatial discretisation as Equation 5.10, similarly leaving terms at $k \pm \frac{1}{2}$ as seen in Figure 5.5.

Since Equations 5.24 and discretisation 5.26 are nonlinear they are not suitable for solution by matrix inversion methods and an iterative method is required to solve Equation 5.26. We use the generalized Newton iteration or nonlinear succesive over-relaxation as described in (Remson, 1971, p.233). Under this method for a general set of finite difference approximations with resulting nonlinear algebraic equations, such as

$$\begin{aligned} G_{1,1}(C_{1,1}, C_{2,1}, ..., C_{n_k,n_c-1}) &= 0 \\ G_{2,1}(C_{1,1}, C_{2,1}, ..., C_{n_k,n_c-1}) &= 0 \\ &\vdots \\ G_{n_k,n_c-1}(C_{1,1}, C_{2,1}, ..., C_{n_k,n_c-1}) &= 0 \end{aligned} \tag{5.27}$$

there n_k is the number of grid cells. The generalized Newton iteration for solving this is

$$\begin{aligned} C_{1,1}^{(m+1)} &= C_{1,1}^{(m)} - \omega \frac{G_{1,1}(C_{1,1}^{m}, C_{2,1}^{m}, ..., C_{n_k n_c-1}^{m})}{\partial G_{1,1}(C_{1,1}^{m}, C_{2,1}^{m}, ..., C_{n_k,n_c-1}^{m})/\partial C_{1,1}} \\ C_{2,1}^{(m+1)} &= C_{2,1}^{(m)} - \omega \frac{G_{2,1}(C_{1,1}^{m+1}, C_{2,1}^{m}, ..., C_{n_k n_c-1}^{m})}{\partial G_{2,1}(C_{1,1}^{m+1}, C_{2,1}^{m}, ..., C_{n_k,n_c-1}^{m})/\partial C_{2,1}} \\ &\vdots \\ C_{n_k,n_c-1}^{(m+1)} &= C_{n_k,n_c-1}^{(m)} - \omega \frac{G_{n_k,n_c-1}(C_{1,1}^{m+1}, C_{2,1}^{m+1}, ..., C_{n_k,n_c-1}^{m})}{\partial G_{n_k,n_c-1}(C_{1,1}^{m+1}, C_{2,1}^{m+1}, ..., C_{n_k,n_c-1}^{m})/\partial C_{n_k,n_c-1}} \end{aligned} \tag{5.28}$$

where m is the iteration number and ω is an acceleration parameter. When the equations 5.27 are satisfied up to the specified tolerance then the solution is converged. ω has to be adjusted to ensure the convergence of the iterative method and is estimated based upon

testing (Remson, 1971).

For our capillary pressure problem the general set of functions 5.27 become Equations 5.29 and the derivatives of this with respect to $C_{i,k}^{n+1}$ are shown in Equations 5.30. In Equations 5.30 we assume $\frac{\partial}{\partial C_{i,k}^{n+1}}(c_{ij}, f_j, k_{rq}) = 0$, which both simplified the algorithm and we found improved its convergence. Combining Equations 5.29 and 5.30 we find that one iteration becomes 5.31. Expanding the derivative of this equation gives equations 5.32. To calculate the $C_{i,k}^{n+1}$ for all i, k we constantly repeat our generalized Newton iteration from our previous best guess $C_{i,k}^{n+1,m}$ to our next guess $C_{i,k}^{n+1,m+1}$ until our $C_{i,k}^{n+1}$ is found when $\mid G_{i,k}^{n+1}(C_{i,k}^{n+1}) \mid < 10^{-10}$.

$$G_{i,k}^{n+1} = \quad C_{i,k}^{n+1} - C_{i,k}^{n} + \frac{K\Delta\tau}{u_t L \Delta\xi^2} \sum_{j=1}^{n_p} \sum_{q \neq j}^{n_p} \left[\left(c_{ij} f_j \frac{k_{rq}}{\mu_q} \right) |_{k+\frac{1}{2}}^{n+1} \left[P_{cjq}(S_{k+1}^{n+1}) - P_{cjq}(S_k^{n+1}) \right] - \left(c_{ij} f_j \frac{k_{rq}}{\mu_q} \right) |_{k-\frac{1}{2}}^{n+1} \left[P_{cjq}(S_k^{n+1}) - P_{cjq}(S_{k-1}^{n+1}) \right] \right] \quad = 0$$

$$i = 1, 2 \quad k = 1, ..., n_k \tag{5.29}$$

$$\frac{\partial G_{i,k}^{n+1}}{\partial C_{i,k}^{n+1}} = 1 - \frac{K\Delta\tau}{u_t L \Delta\xi^2} \sum_{j=1}^{n_p} \sum_{q \neq j}^{n_p} \left[\left(c_{ij} f_j \frac{k_{rq}}{\mu_q} \right) |_{k+\frac{1}{2}}^{n+1} \frac{\partial}{\partial C_{i,k}^{n+1}} \left(P_{cjq}(S_k^{n+1}) \right) + \left(c_{ij} f_j \frac{k_{rq}}{\mu_q} \right) |_{k-\frac{1}{2}}^{n+1} \frac{\partial}{\partial C_{i,k}^{n+1}} \left(P_{cjq}(S_k^{n+1}) \right) \right]$$

$$i = 1, 2 \quad k = 1, ..., n_k \tag{5.30}$$

$$C_{i,k}^{n+1,m+1} = C_{i,k}^{n+1,m} - \omega \frac{C_{i,k}^{n+1,m} - C_{i,k}^{n} + \frac{K\Delta\tau}{u_t L \Delta\xi^2} \sum_{j=1}^{n_p} \sum_{q \neq j}^{n_p} \left[\left(c_{ij} f_j \frac{k_{rq}}{\mu_q} \right) |_{k+\frac{1}{2}}^{n+1} \left[P_{cjq}(S_{k+1}^{n+1}) - P_{cjq}(S_k^{n+1}) \right] - \left(c_{ij} f_j \frac{k_{rq}}{\mu_q} \right) |_{k-\frac{1}{2}}^{n+1} \left[P_{cjq}(S_k^{n+1}) - P_{cjq}(S_{k-1}^{n+1}) \right] \right]}{1 - \frac{K\Delta\tau}{u_t L \Delta\xi^2} \sum_{j=1}^{n_p} \sum_{q \neq j}^{n_p} \left[\left(c_{ij} f_j \frac{k_{rq}}{\mu_q} \right) |_{k+\frac{1}{2}}^{n+1} \frac{\partial}{\partial C_{i,k}^{n+1}} \left(P_{cjq}(S_k^{n+1}) \right) + \left(c_{ij} f_j \frac{k_{rq}}{\mu_q} \right) |_{k-\frac{1}{2}}^{n+1} \frac{\partial}{\partial C_{i,k}^{n+1}} \left(P_{cjq}(S_k^{n+1}) \right) \right]}$$

$$i = 1, 2 \quad k = 1, ..., n_k \tag{5.31}$$

$$C_{i,k}^{n+1,m+1} = C_{i,k}^{n+1,m} -$$

$$\omega \frac{C_{i,k}^{n+1,m} - C_{i,k}^{n} + \frac{K\Delta\tau}{u_t L \Delta\xi^2} \sum_{j=1}^{n_p} \sum_{q \neq j}^{n_p} \left[\left(c_{ij} f_j \frac{k_{rq}}{\mu_q} \right) |_{k+\frac{1}{2}}^{n+1} \left[P_{cjq}(S_{k+1}^{n+1}) - P_{cjq}(S_k^{n+1}) \right] - \left(c_{ij} f_j \frac{k_{rq}}{\mu_q} \right) |_{k-\frac{1}{2}}^{n+1} \left[P_{cjq}(S_k^{n+1}) - P_{cjq}(S_{k-1}^{n+1}) \right] \right]}{1 - \frac{K\Delta\tau}{u_t L \Delta\xi^2} \sum_{j=1}^{n_p} \sum_{q \neq j}^{n_p} \left[\left(c_{ij} f_j \frac{k_{rq}}{\mu_q} \right) |_{k+\frac{1}{2}}^{n+1} \left(\frac{P_{cjq}(S_k^{n+1}(C_{i,k}^{n+1} \pm \Delta C_{i,k}^{n+1})) - P_{cjq}(S_k^{n+1}(C_{i,k}^{n+1}))}{\Delta C_{i,k}^{n+1}} \right) + \left(c_{ij} f_j \frac{k_{rq}}{\mu_q} \right) |_{k-\frac{1}{2}}^{n+1} \left(\frac{P_{cjq}(S_k^{n+1}(C_{i,k}^{n+1} \pm \Delta C_{i,k}^{n+1})) - P_{cjq}(S_k^{n+1}(C_{i,k}^{n+1}))}{\Delta C_{i,k}^{n+1}} \right) \right]}$$

$$i = 1, 2 \quad k = 1, ..., n_k \tag{5.32}$$

The $\pm$ is in case the perturbation takes $C_{i,k}^{n+1}$ outside [0,1].

We now write out the algorithm to use the iterative formula in Equation 5.31.

Algorithm for Implicit Step

1. Our initial condition is $C_{i,k}^n$ for $1 \leq k \leq n_k$ from the previous timestep n. To complete the initial condition we must calculate $S_{j,k}^n$ for all i, k and store it in an $S_{j,k}^n$ vector.

2. Set boundary condition for $C_{i,k}^{n+1}$ in cells $k = 0$ and $n_k + 1$ so that $C_{i,0}^{n+1} = C_{i,1}^{n+1}$ and $C_{i,n_k+1}^{n+1} = C_{i,n_k}^{n+1}$. This ensures no flow due to capillary pressure at the boundary.

3. Set $S_{i,k}^{n+1}$ and $C_{i,k}^{n+1}$ equal to $S_{i,k}^n$ and $C_{i,k}^n$ respectively for all i, k

4. Check if $\mid G_{i,k}^{n+1} \mid \leq 10^{-10}$ for all $1 \leq k \leq n_k$. If yes, we return $S_{j,k}^{n+1}$ and $C_{i,k}^{n+1}$. To calculate these equalities we need to:

   (a) Estimate C_i^{n+1} at $k \pm \frac{1}{2}$. For this we use linear interpolation.

   (b) Calculate S_j^{n+1} at $k \pm \frac{1}{2}$.

   (c) Calculate c_{ij}, f_j, k_{rq} at $k \pm \frac{1}{2}$ for all $0 \leq k \leq n_k$ and $1 \leq j \leq 3$ and $P_{cjq}(S_{j,k}^{n+1})$ for $0 \leq k \leq n_k + 1$ and $1 \leq j \leq 3$.

5. If $\mid G_{i,k}^{n+1} \mid \not\leq 10^{-10}$ for all i,k then do an iteration to $C_{i,k}^{n+1,m+1}$ by stepping through the following steps (a) - (e), for each i, k, looping through i faster. As we update each $C_{i,k}^{n+1,m+1}$ we must use the most up-to-date version of $C_{i,k}^{n+1}$. To do this for the kth gridblock in the mth step we use

$$C_{1,k-1}^{n+1,m+1}, C_{1,k}^{n+1,m}, C_{1,k+1}^{n+1,m}, C_{2,k-1}^{n+1,m+1}, C_{2,k}^{n+1,m}, C_{2,k+1}^{n+1,m} \qquad \text{if } i = 1 \qquad (5.33)$$

$$C_{1,k-1}^{n+1,m+1}, C_{1,k}^{n+1,m+1}, C_{1,k+1}^{n+1,m}, C_{2,k-1}^{n+1,m+1}, C_{2,k}^{n+1,m}, C_{2,k+1}^{n+1,m} \qquad \text{if } i = 2 \qquad (5.34)$$

   to reflect the sequential updating of $C_{1,k}$ prior to $C_{2,k}$. This is achieved by always overwriting $C_{i,k}^{n+1,m}$ when $C_{i,k}^{n+1,m+1}$ is found. For each i, k

   (a) Recalculate C_i^{n+1} at $k \pm \frac{1}{2}$

   (b) Recalculate saturations at $k-1, k, k \pm \frac{1}{2}$

   (c) Recalculate c_{ij}, f_j, k_{rq} at $k \pm \frac{1}{2}$ and $P_{cjq}(S_{j,k}^{n+1})$ at $k-1, k$. For $k = 0$ and $n_k + 1$ set P_{cjq} so that there is no flow due to capillary effects at the boundary such that $P_{cjq}(S_{j,0}^{n+1}) = P_{cjq}(S_{j,1}^{n+1})$ and $P_{cjq}(S_{j,n_k+1}^{n+1}) = P_{cjq}(S_{j,n_k}^{n+1})$.

   (d) Calculate saturations when $C_{i,k}^{m+1} \pm \Delta C$ at k

   (e) $P_{cjq}(S_{j,k}^{n+1})$ at i, k using $S_{j,k}^{n+1}(C_{i,k}^{m+1} \pm \Delta C)$

(f) Use Equation 5.32 to update to $C_{i,k}^{n+1,m+1}$

6. Update saturation S_{j,n_k}^{n+1} and return to step 4.

Accuracy and Stability of Operator Splitting Scheme

The accuracy of the operator splitting scheme depends upon both the numerical methods for advective and capillary flow and errors from the operator splitting itself. As the same spatial discretisations have been used as in Section 5.3.1 the spatial errors remain $\mathrm{O}(\Delta\xi^2)$ for the capillary discretisation and $\mathrm{O}(\Delta\xi^3)$ for the advective approximation using ENO. As a result there are again no numerical errors that have second order in space derivatives.

Temporal errors from the operator splitting algorithm are $\mathrm{O}(\Delta\tau^2)$ (Hundsdorfer, 2003, p.326), from the advective discretisation are $\mathrm{O}(\Delta\tau^3)$ as in Section 4.3.4, but from the implicit capillary discretisation are $\mathrm{O}(\Delta\tau)$ (Strikwerda, 2004). The temporal error for the implicit capillary discretisation could be improved by using Crank-Nicholson timestepping, however this is not our primary aim here.

The stability of operator splitting schemes generally depends upon the stability of the sub-steps (Hundsdorfer, 2003, p.327). Therefore we consider the stability of the advective and capillary schemes. The stability of the advective scheme is given by the CFL condition as set out in Section 4.3.4. The backwards-time central-space discretisation is unconditionally stable when applied to linear scalar systems (Strikwerda, 2004). Based upon this, the stability condition for the whole operator splitting method would be given by the CFL condition, which is notably less restrictive than for the explicit scheme in Section 5.3.1. However, for nonlinear sytems the unconditional stability of an implicit scheme does not extend and the stability must be investigated. In Section 5.4 we find that the solver applied to the implicit discretisation does not converge unconditionally.

5.3.3 Calculation of Three-phase Saturations

In Section 4.3.6 the calculation of saturations of two partially miscible phases was explained which was sufficient for use in three phase systems where one phase was immiscible. In Section 5.2 some models with three partially miscible phases have been introduced and therefore require a three-phase flash solver. To find the three saturations in a three-phase system the following procedure is followed. Steps 1,2 and 3 only need to be done once for a set of K-values as for a three-phase three-component system there are zero degrees of freedom and phase compositions are fixed.

1. Calculate the compositions of two points on the sides of each of the two phase regions. This is achieved by

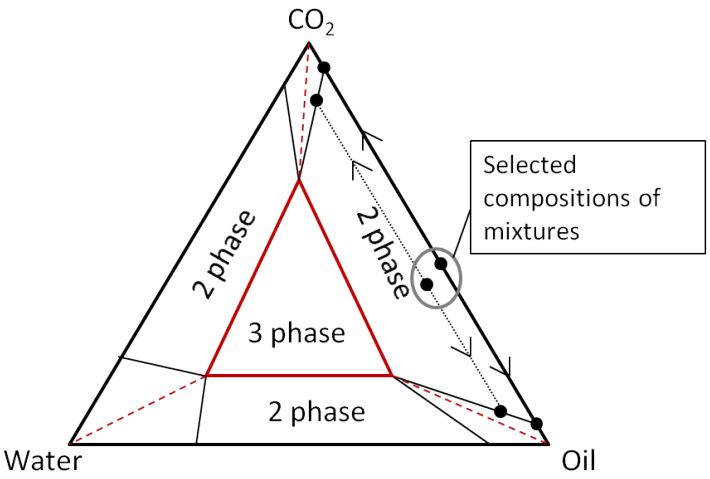


Figure 5.6: General ternary phase diagram. The points demonstrate the selected mixture compositions chosen in step 1 and the compositions of the partitioned phases. Red lines indicate boundaries used in step 4.

(a) Select two compositions within each of the two phase regions as shown in the gas/oil region two phase region in Figure 5.6.

(b) Do a two-phase flash calculation similar to that in section 4.3.6 to solve

$$\sum_{i=1}^{3} \frac{C_i(K_i^1 - 1)}{S_1(K_i^1 - 1) + 1} = 0 \tag{5.35}$$

for S_1 and $S_2 = 1 - S_1$ in the gas/oil two-phase region

$$\sum_{i=1}^{3} \frac{C_i(K_i^2 - 1)}{S_2(K_i^2 - 1) + 1} = 0 \tag{5.36}$$

for S_2 and $S_3 = 1 - S_2$ in the oil/water two-phase region and

$$\sum_{i=1}^{3} \frac{C_i(K_i^3 - 1)}{S_3(K_i^3 - 1) + 1} = 0 \tag{5.37}$$

for S_3 and $S_2 = 1 - S_3$ in the water/gas two-phase region.

(c) calculating the c_{ij} for each of the selected compositions. In the gas/oil two-phase region we use the equations

$$c_{i2} = \frac{C_i}{K_i^1 S_1 + 1 - S_1} \tag{5.38}$$

and

$$c_{i1} = K_i^1 c_{i2} \tag{5.39}$$

In the oil/water two-phase region we use the equations

$$c_{i3} = \frac{C_i}{K_i^2 S_2 + 1 - S_2} \tag{5.40}$$

and

$$c_{i2} = K_i^2 c_{i3} \tag{5.41}$$

In the water/gas two-phase region we use the equations

$$c_{i1} = \frac{C_i}{K_i^3 S_3 + 1 - S_3} \tag{5.42}$$

and

$$c_{i3} = K_i^3 c_{i1} \tag{5.43}$$

The c_{ij} give us the compositions of the two phases which the components partition between, i.e. the points on the two phase boundary as shown in Figure 5.6.

2. Calculate the straight lines through the points on each of the sides of the two-phase boundaries. Then calculate where the lines intersect. The intersection points give the corners of the three-phase region. The corners of the three phase region will give us $c_{11,3p}, c_{21,3p}, c_{31,3p}, c_{12,3p}, c_{22,3p}, c_{32,3p}, c_{13,3p}, c_{23,3p}, c_{33,3p}$ where $c_{ij,3p}$ is the volume fraction of component i in phase j when three phases are present.

3. Calculate the equations of the lines of the three-phase boundaries and the lines linking the corners of the three-phase triangle to the corners of the ternary. These divide up the different two-phase and three-phase regions

4. Given a composition C, determine which region the composition falls into - either the three-phase region, the oil/gas two-phase region, oil/water two-phase region or water/gas two-phase region. In Figure 5.6 these are separated by the red solid and dashed lines calculated in step 3.

5. If inside the three-phase region rearranging Equations 2.14 allows us to calculate

the saturations as

$$S_1 = \frac{\frac{(c_{13,3p}-c_{12,3p})(C_2-c_{23,3p})}{(c_{22,3p}-c_{23,3p})} + C_1 - c_{13,3p}}{c_{11,3p} - c_{13,3p} + \frac{(c_{13,3p}-c_{12,3p})(c_{21,3p}-c_{23,3p})}{(c_{22,3p}-c_{23,3p})}} \tag{5.44}$$

$$S_2 = \frac{C_2 - c_{21,3p}S_1 - c_{23,3p}(1-S_1)}{c_{22,3p} - c_{23,3p}} \tag{5.45}$$

$$S_3 = 1 - S_1 - S_2 \tag{5.46}$$

If inside one of the other regions apply the appropriate two-phase flash calculation as in step 1(b) to find the S_j.

5.4 Results

As outlined in Section 5.1 we modelled a series of solutions to capture the effect of capillary pressure and ultimately search for a pair of solutions to the three-phase transport equations with capillary pressure that demonstrate different divergent behaviour for small capillary pressure.

5.4.1 Numerical Methods Results

The solutions were modelled with both the explicit and operator splitting schemes described in Section 5.3. Stability of the discretisations and convergence of the schemes was seen as follows:

The explicit scheme was, as expected in Section 5.3.1, limited by a timestep size restriction to maintain the stability of the scheme. We tested this stability by running cases with decreasing u_t, corresponding to increasing the relative effect of capillary pressure. It was found that to maintain the stability of the explicit scheme we required a relation of approximately $\frac{(\Delta\xi)^2}{\Delta\tau} > \frac{1\times10^{-7}}{u_t}$

For the operator splitting scheme the overall convergence was determined by the convergence of the generalized Newton iteration used to solve the implicit discretisation 5.26. It was found that the convergence of the iterative scheme generally coincided with the $\Delta\xi$ and $\Delta\tau$ combinations that satisfied the stability criterion for the explicit scheme. When using 500 cells as in Figure 5.7 the results for the explicit and operator splitting schemes were nearly identical with largest differences in composition of the order 10^{-4}, however the operator splitting scheme was significantly slower by up to a factor of 20-30.

The conditions for both stability and convergence were stricter than the CFL condition for the advection problem in each case, however for our purposes they were not overly restrictive. In particular, we were able to run explicit cases with up to 1500 cells in under a minute.

5.4.2 Model A Results

In model A we modelled a capillary pressure extension to the three-phase three-component solution of Section 4.2.2, described in Section 5.2.3. Figure 5.7 shows the results of this model with the solution with and without the inclusion of capillary pressure. The capillary solution is modelled using the operator splitting scheme of Section 5.3.1 with 500 cells and the analytic purely advection solution corresponds to that of Section 4.2.2. We also show the simulated solution with 500 cells to confirm the difference is the effect of capillary pressure rather than numerical diffusion .

The model has an aqueous wet, oleic intermediate capillary pressure, therefore we expect the aqueous phase saturation will have a propensity to imbibe towards lower aqueous phase regions and the oleic phase towards regions with lower combined aqueous and oleic phase saturations. Conceptually this allows each phase to occupy the smallest pores available for the respective wettability. The profiles for C_2-oil and C_3-water support this, as we see capillary pressure causes both the water and oil to be drawn to the left relative to the pure advection solution.

There is also an interesting interaction in the water composition at around $\xi = 0.05$ where imbibition of water to the left is significant at the gas-oil shock producing a dip in water composition where imbibition from the right due to the water saturation change is too slow to fill it. The effect of the gas-oil shock seems less physically intuitive but by considering Equation 5.10 with $c_{33} = 1, c_{31} = c_{32} = 0$ we see that the aqueous phase is - under the standard set of equations - affected by both P_{c31} and P_{c32}. P_{c31} can, depending upon the local saturation gradient and the gradient of the capillary pressure curves, draw aqueous phase towards regions of higher gas saturation.

5.4.3 Model B Results

In model B we allow partitioning of all components between all phases, in particular the water and CO_2 can partition between the aqueous and gas phases. Figure 5.8 shows the numerical solution using the explicit scheme with 1000 cells compared against the analytic solution for the pure advection problem.

The main affect of the partitioning upon the advective solution is that the water is vaporised into the gas phase near $\xi = 0$. When introducing capillary pressure the vaporisation stops the aqueous phase imbibing back into this region. As a result the oil imbibes back into this region instead, due to the lower combined aqueous and oleic phase saturation. This change in the effect of capillary pressure from model A due to the full partitioning of components is quite fundamental with a new oil bank created near the injection well.

5.4.4 Model C and D Results

In models C and D we change the injection and boundary conditions and gas viscosity to give the purely advective solution shown in Figure 5.9 and described in Section 5.2.3. Then model C has the effect of aqueous-wet capillary pressure and model D has the effect of oleic-wet capillary pressure added. These were both modelled with the explicit scheme and 1500 cells and are also shown on Figure 5.9.

It can be seen that the aqueous-wet capillary pressure reduces the size of the water

bank from the purely advective solution and smoothes out the leading shock. In contrast the oleic-wet capillary pressure creates a larger water bank and also creates an oil bank at the trailing shock, where the oleic phase is now wetting but is only slowly vaporised by the gas.

Investigating convergence of solutions with small capilary pressure

Since the analytic solution to this problem contains a transitional wave we have reason to believe that there may exist non-unique solutions to the problem. The solutions in Figure 5.9 diverge in behaviour and we are interested in determining whether, as the magnitude of these capillary effects become smaller, these solutions identify different zero-limit solutions equating to non-unique solutions of the pure advection problem. In particular we note that the effect of capillary pressure on simulated solutions is intrinsically different from those of numerical diffusion, which may otherwise control the limiting behaviour. This is shown in Figure 5.10 where we see that our coarse grid advection simulation smooths all shock similarly in contrast to the capillary pressure results, which smooth some shocks while leaving others sharp. Capillary pressure effects are also fundamentally different from physical dispersion when creating behaviour such as the imbibition driven banks seen. Under normal physical dispersion we would expect smoothing of all shocks.

To determine whether the solutions converge to different advective solutions we increased u_t to 0.005 and 0.002 for the aqueous and oleic capillary pressure functions respectively, therefore reducing the relative effect of capillary pressure. The result of this is shown in Figure 5.11 and we see that all of the characteristics of the proposed purely advective analytic solution return. Therefore in this case we conclude that the solutions converge and that we have not identified non-unique solutions.

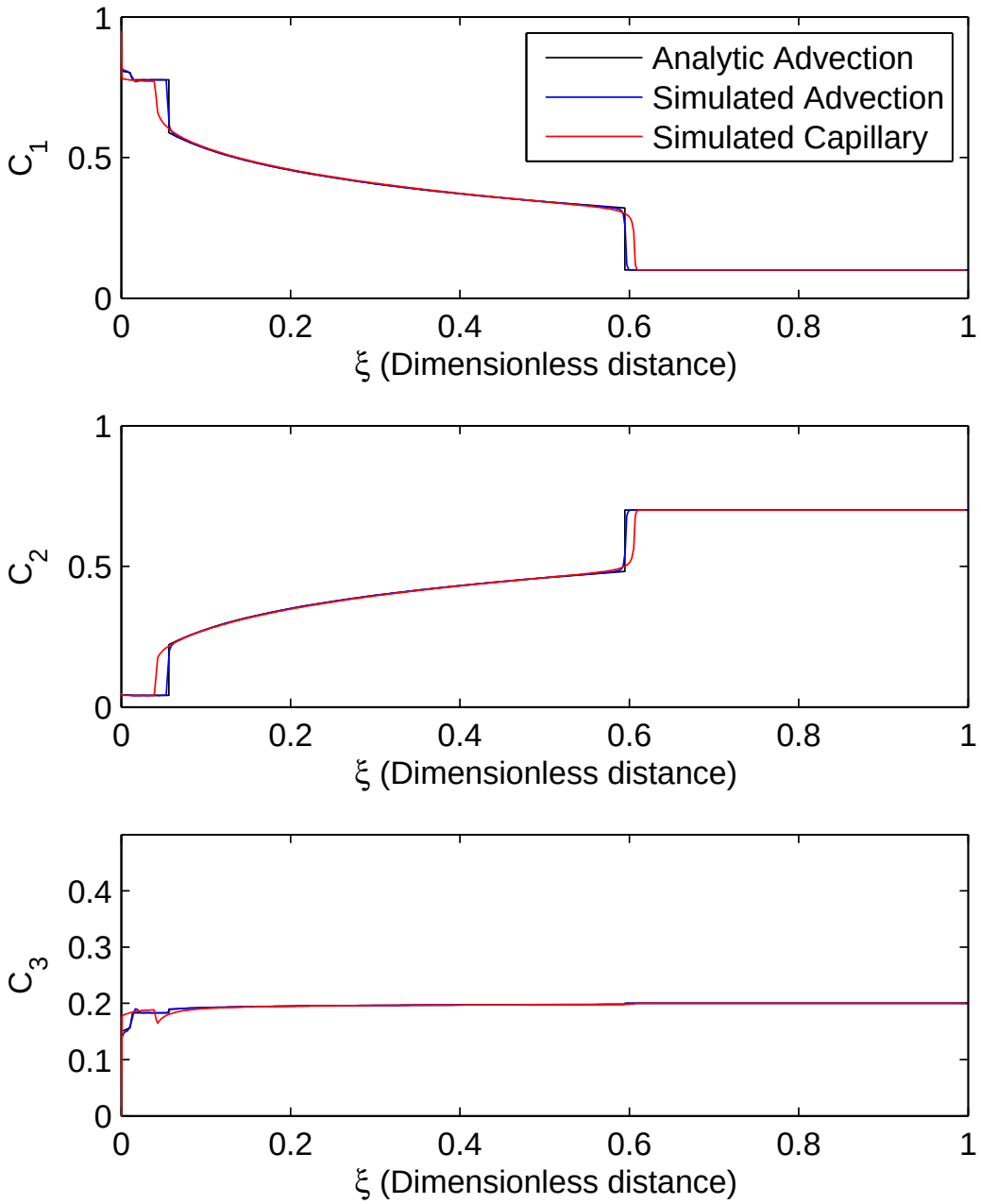


Figure 5.7: The simulated solution profile with capillary pressure (in red) as outlined in Model A against the analytic (in black) and simulated(in blue) purely advective solution profile. Both solutions at $\tau = 0.25$. The simulated solution used the operator splitting scheme with 500 cells and 1250 timesteps. C_1 =CO_2, C_2 =oil, C_3 =water.

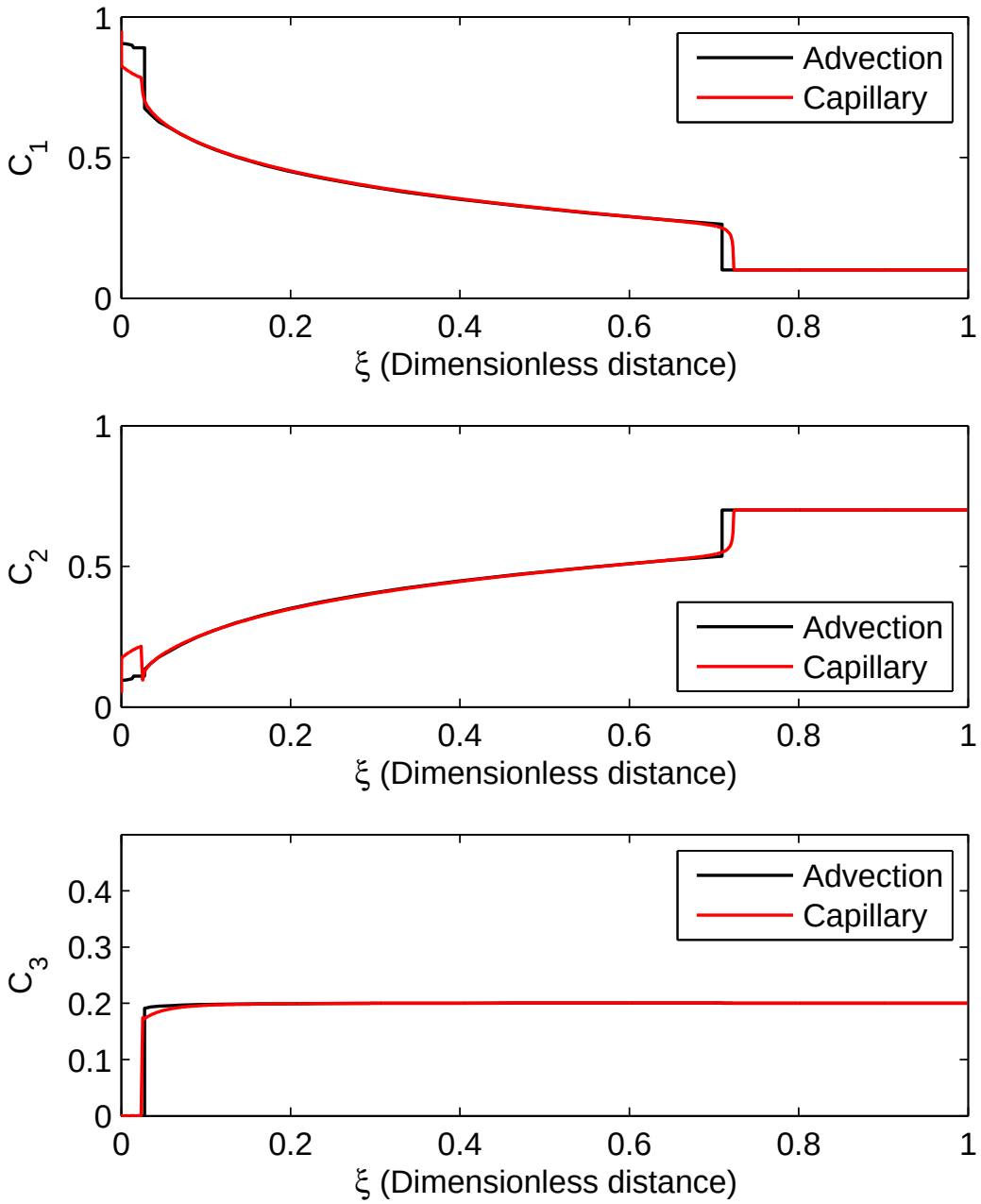


Figure 5.8: The simulated solution profile with capillary pressure (in red) as outlined in Model B against the analytic purely advective solution profile (in black). Both solutions at $\tau = 0.25$. The simulated solution used the explicit scheme with 1000 cells and 2500 timesteps. C_1 =CO_2, C_2 =oil, C_3 =water.

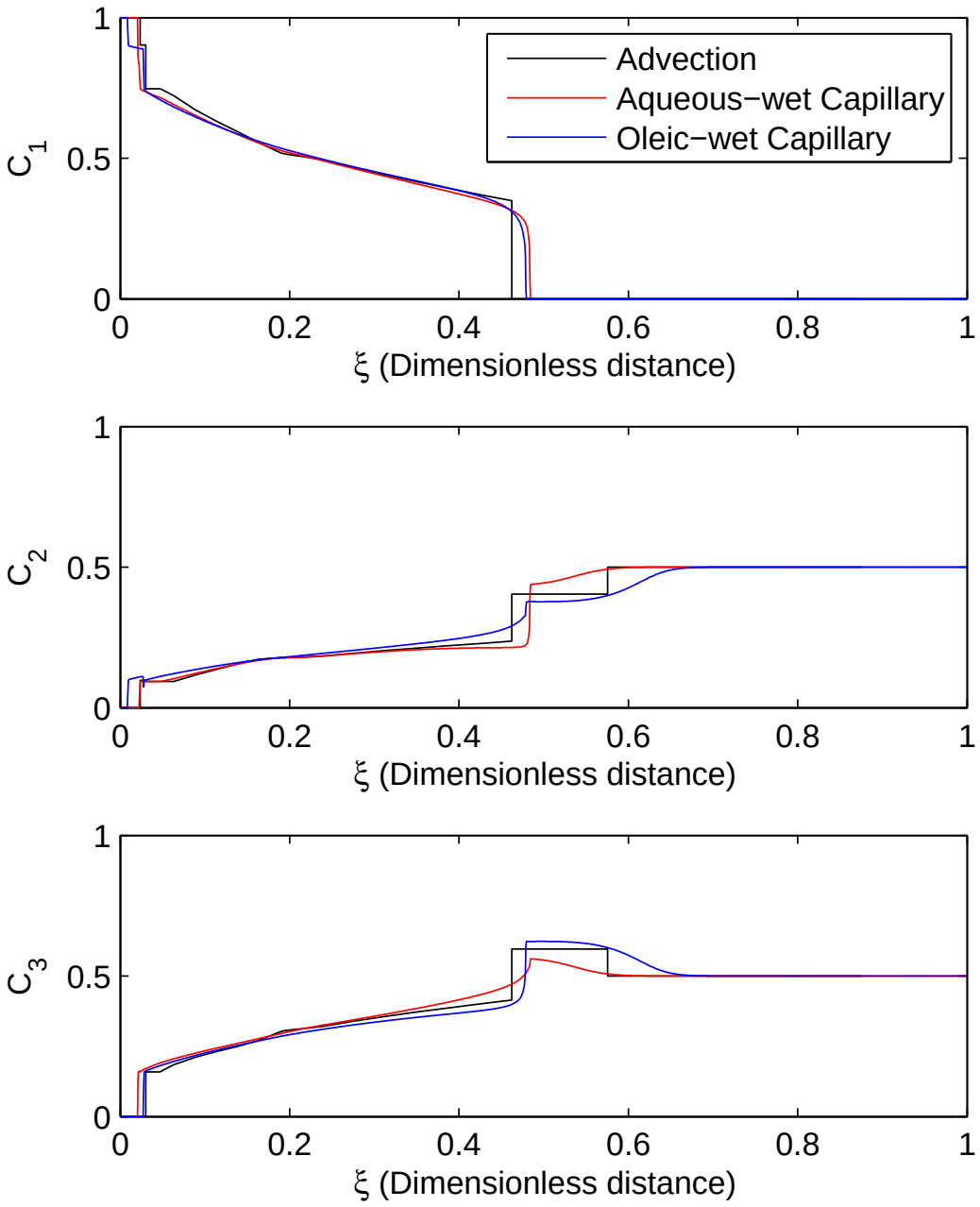


Figure 5.9: The simulated solution profiles with aqueous-wet capillary pressure (in red) as outlined in Model C and oleic-wet capillary pressure (in blue) as outlined in Model D against the analytic purely advective solution profile (in black). Both solutions at $\tau = 0.25$. The simulated solutions used the explicit scheme with 1500 cells and 15000 timesteps. C_1 =CO_2, C_2 =oil, C_3 =water.

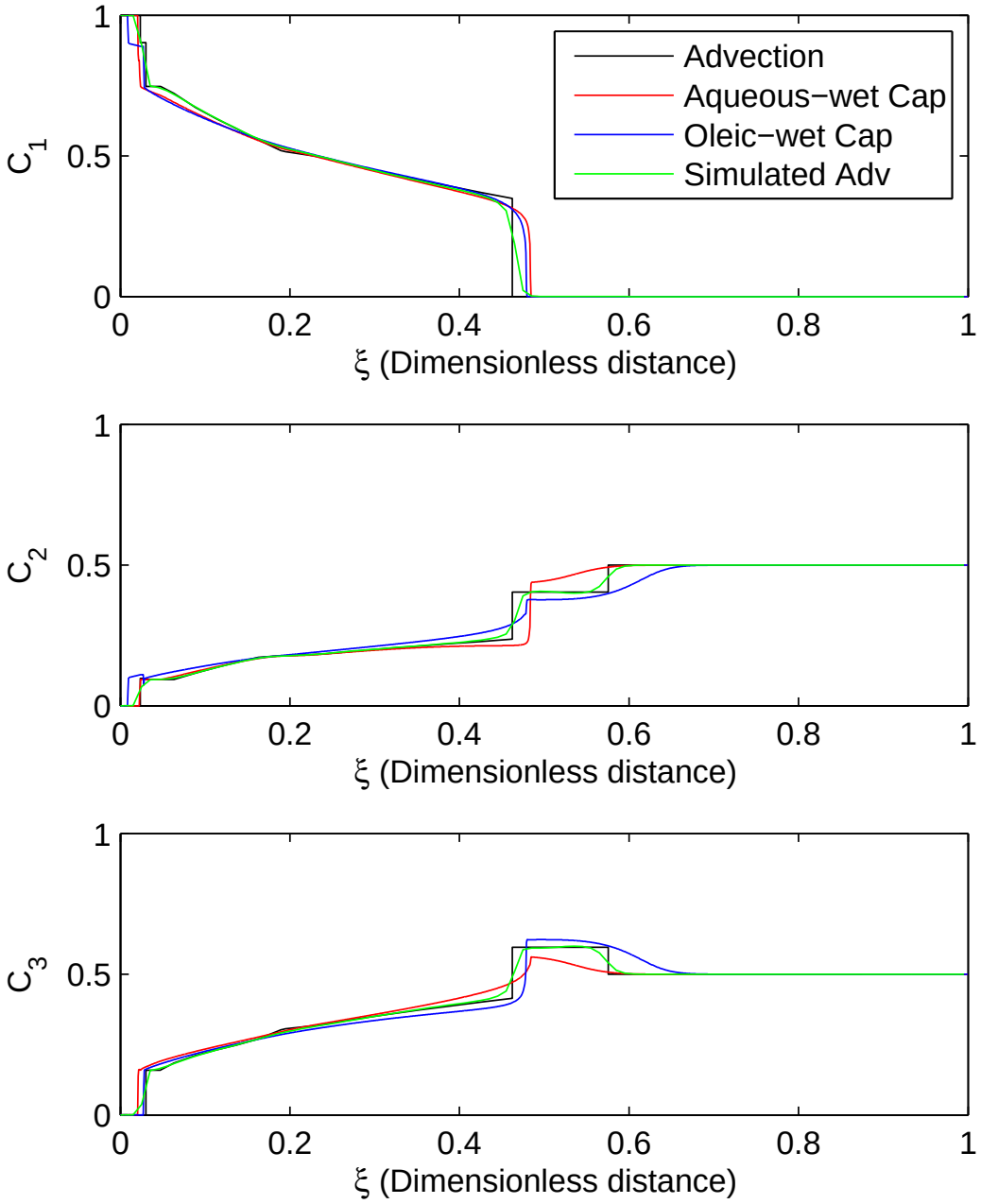


Figure 5.10: The simulated solution profiles with aqueous-wet capillary pressure (in red) as outlined in Model C and oleic-wet capillary pressure (in blue) as outlined in Model D against the analytic purely advective solution profile (in black) and simulated purely advective solution profile (in green). Both solutions at $\tau = 0.25$. The simulated capillary pressure solutions used the explicit scheme with 1500 cells and 15000 timesteps and the simulated advection solution used 100 cells and 1000 timesteps. C_1 =CO_2, C_2 =oil, C_3 =water.

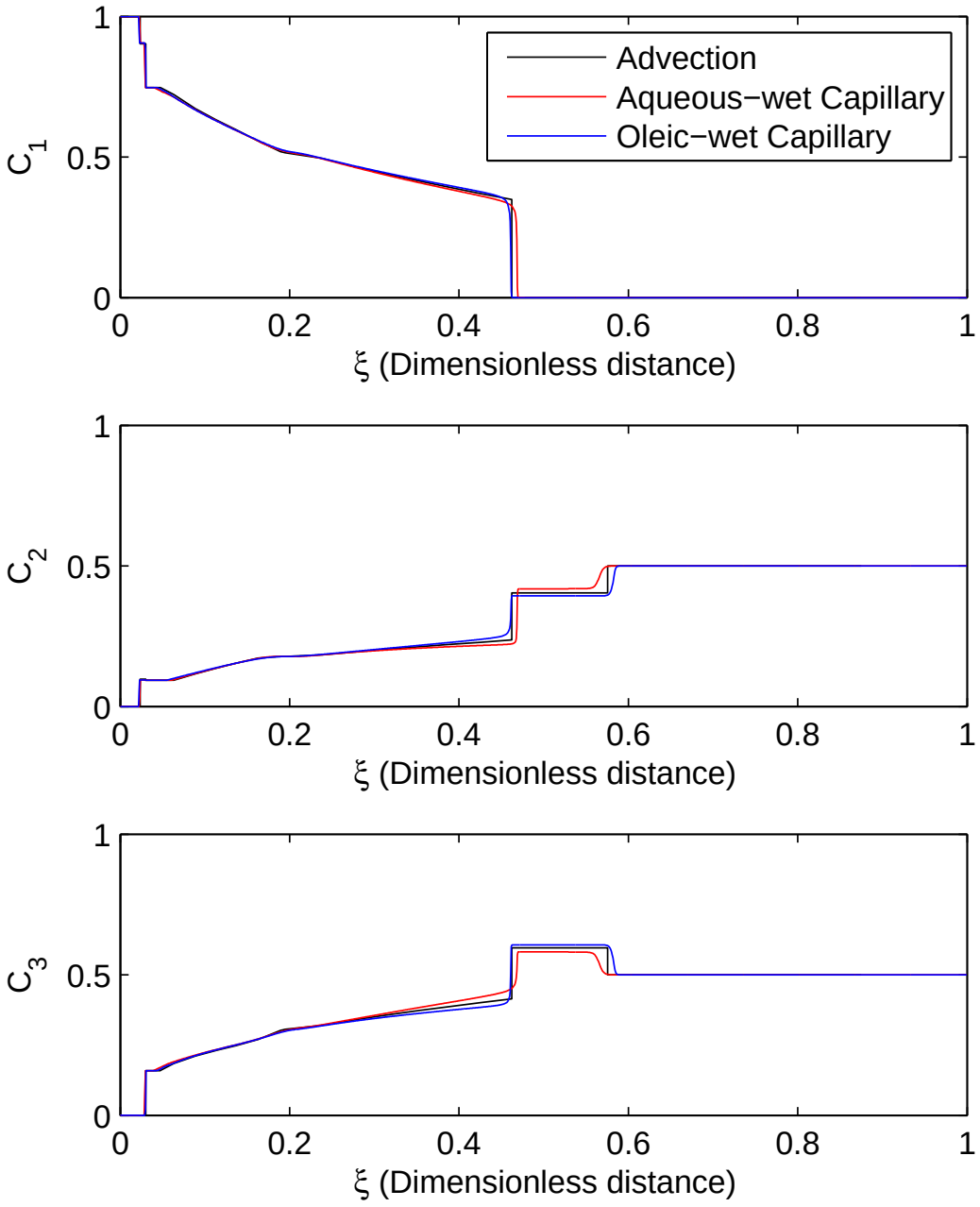


Figure 5.11: The simulated solution profiles with reduced aqueous-wet capillary pressure (in red) given by $u_t = 0.005$ and otherwise as outlined in Model C and reduced oleic-wet capillary pressure (in blue) given by $u_t = 0.002$ and otherwise as outlined in Model D against the analytic purely advective solution profile (in black). Both solutions at $\tau = 0.25$. The simulated solutions used the explicit scheme with 1500 cells and 10000 timesteps. C_1 =CO_2, C_2 =oil, C_3 =water.

5.5 Discussion and Conclusions

In this chapter we have demonstrated a number of numerical methods for studying three-phase three-component flow with capillary pressure. We have shown a new integration of the ENO method into a fully explicit scheme for equations including a diffusive term. In this method ENO calculates all cell-face approximations. We have also described an operator splitting scheme and compared its speed and convergence to the fully explicit scheme. Due to nonlinearity its convergence was found to be comparable to the stability of the explicit scheme, however runtime was slower.

We also described the impact of capillary pressure on a three-phase three-component problem. These solutions demonstrated fundamentally different characteristics to that expected by the presence of other second-order terms, such as dispersion or the presence of numerical diffusion. It was also shown that the introduction of the fully compositional model could alter the effect of capillary pressure due to vaporisation of the wetting phase. The result was that, rather than a bank of wetting-phase developing near the well due to imbibition, a bank of intermediate-wetting phase was created instead.

Finally, we aimed to show a pair of solutions that diverge differently from the purely advective solution of a three-phase problem by introducing the effect of different wettability capillary pressures. It was also investigated whether these solutions converged when the magnitude of capillary pressure was reduced. This was done for a problem where a transitional wave was found in the solution and uniqueness of the purely advective solution not guaranteed.

The result of this investigation was that solution profiles for models including oleic-wet and aqueous-wet capillary pressure were, as expected, seen to significantly differ in nature. Although divergent solutions to the second-order problem were found, when reducing the size of the second-order capillary term the solutions converged towards a proposed purely advective analytic solution. In order to find a set of non-unique solutions for the three-phase flow problem a more comprehensive search may be required. Alternatively it is possible that the capillary pressure functions were sufficiently similar to give them the same result as $P_{cjq} \to 0$.

Chapter 6

Conclusions and Future Work

6.1 Conclusions

A large proportion of Europe's potential storage capacity is to be found in large open aquifers. However, in times when the European carbon price is low, storage in depleted oil reservoirs may be required to make early commercial projects economically viable. In this thesis issues with relevance to CO_2 storage in both saline aquifers and depleted oil reservoirs have been studied. These have been studied using a mixture of 1D and full 3D reservoir models.

In Chapter 3 we presented analysis of the effect of top-surface structure and heterogeneity upon storage capacity in dipping open saline aquifers. The analysis of top-surface structure was the first systematic analysis of this issue. The effects were evaluated under an interpreted set of regulations for capacity estimation using a real North Sea top-surface structure and heterogeneity field. For this analysis it was explained how storage in dipping open aquifers varies strongly depending upon the amount of CO_2 that can be stored in a mobile, slowly migrating and laterally unconfined form at 1000 years. It was noted that this dependency exists because current interpreted regulation sets a cut-off for the flow rate of mobile, laterally unconfined CO_2 at 1000 years. It is not clear whether this regulation achieves its aim, although it may. Other alternative regulations may be, if not better, more explicit in purpose.

We then described how the top-surface structure introduces both structural closures and regions of localised higher dip that either lead to escape or prohibited high migration speeds. The balance of the effects of these features is seen to determine the change in storage efficiency due to top-surface structure. A key result is that the reduction in storage capacity due to localised higher dip is seen to be far more significant when top-surface structure is introduced to those smooth models that allow significant amounts of CO_2 to be stored in a mobile and laterally unconfined form at 1000 years. In the North Sea model studied this dependency of the effect of localised higher dip was significant enough to govern whether top-surface structure increased or decreased capacity. When the smooth model was able to store mobile and laterally unconfined CO_2 at 1000 years,

the reduction in storage from the introduction of localised higher dip was greater than the increase in storage from the introduction of structural closure. When the smooth small was not able to store mobile and laterally unconfined CO_2 at 1000 years the reduction in storage was smaller than the increase in storage from the introduction of structural closures.

Finally, we described the effect of heterogeneity upon storage capacity in open aquifers. The introduction of porosity and permeability heterogeneity to a homogeneous model reduced storage efficiency when the storage in the homogeneous model was limited by injectivity, due to localised pressure build-up. When injectivity did not constrain storage capacity in the homogeneous model the introduction of heterogeneity increased storage efficiency by increasing the reservoir contact of CO_2. This weakened the effect of gravity override.

This work also provided a quantitative framework for assessing storage capacity in open aquifer sites based on different constraints - pressure, migration distance and migration speed. It then divided different cases into three storage regimes. This has shown that open aquifers of modest permeability and dip can prove to be favourable storage sites with large storage capacities. These aquifers limit the speed with which the CO_2 migrates while the extensive open pore volume can help dissipate pressure, avoiding pressure problems associated with other types of storage site. This suggests that with careful selection and design, large open aquifers are promising sites for CO_2 storage.

In Chapters 4 and 5 we considered 1D solutions for three-phase flow problems representative of CO_2 storage in depleted oil reservoirs. A potential issue for modelling this problem is that the advective three-phase transport problem can have non-unique solutions.

In Chapter 4 it was shown that we cannot determine rigorously the physical solution to three-phase flow problems that may have non-unique solutions using the proposed method. The proposed method involved the inclusion of physical dispersive terms in the model and removal of dispersive approximation errors using the ENO numerical method. This was not successful because it is shown that ENO produces first-order convergence for the majority of the computational domain when discontinuities are present in the initial condition as is inevitably the case in gas injection problems. In Chapter 5 we modelled a problem whose purely advective form had features that did not guarantee unique solutions and non-unique solutions were sought. By including oleic-wet and aqueous-wet capillary pressure, solutions significantly different in nature were shown. However, as the size of the second-order capillary term was reduced, the solutions converged.

From this work the uniqueness of solutions to three phase advection problems is still a potential issue. However, this does provide a positive result, in that for our most complex

example there was no sign of convergence to different solutions with different capillary pressures.

Chapters 4 and 5 also contained a range of work applicable to numerical modelling of subsurface flow.

In Chapter 4 we have benchmarked compositional three-phase, three-component ENO simulations against analytic solutions for the first time. Although this benchmarking process demonstrated that both SPU and ENO methods have first-order convergence when shocks are present, the ENO scheme was generally an order of magnitude more accurate for a given grid resolution for approximately three-times the CPU time. Therefore ENO is still a preferable numerical method.

In Chapter 5 a number of numerical methods for studying three-phase three-component flow with capillary pressure were demonstrated. A new version of a fully explicit scheme for equations including a dispersive term was shown. In this method ENO is used to calculate all cell-face approximations. We also described an operator splitting scheme and compared its speed and convergence to the fully explicit scheme. Due to nonlinearity its convergence was found to be comparable to the stability of the explicit scheme, however runtime was slower and the explicit scheme was therefore preferable.

6.2 Future Work

6.2.1 Storage Capacity Estimation Related Work

This study has allowed us to provide a new understanding of the effect of top-surface structure and heterogeneity based upon simulations using a Forties top-surface and heterogeneity. To generalise some of the results, investigation into the statistical occurrence of closure versus high dip routes would be needed. In future this could be done using a geo-statistical approach or by considering a large sample of sites, informed by the results of regional seismic surveys, although the second approach may take a prohibitively long time.

Important new considerations in this work are the new regulatory constraint assumptions and in particular the migration velocity constraint, which plays a significant role in allowing low migration velocity storage in some cases, but also limiting this in others. To understand the implications of this constraint further it would be interesting to compare storage efficiencies under the migration velocity constraint against different sets of constraints. An example motivation is a scenario in Section 3.3.4 (base case sensitivity to permeability) where we see a factor of two difference when the migration velocity constraint was removed. Such a further evaluation of the implications of the storage constraints may help to advise future regulation. Further, we may consider the problems of applying a migration velocity constraint. For example, we may consider the effect of allowing significant low migration velocity storage in a simulation model when an undetected very high perm streak or fracture exists in the real storage unit and therefore leading to significantly more migration than the apparently low velocity CO_2.

Since the results of this study are to determine the effect of top-surface structure in cases where top-surface structure is not modelled, a potential future consideration is at which level accounting for top-surface structure should be omitted or modelled. In the UKSAP (2011b) top-surface structure is currently modelled where 'individual potential structures are known to be large and therefore important in terms of overall UK storage capacity'. At present there is very minimal information, if any, of a scale at which top-surface structure should be considered insignificant, mainly because there had not been an explicit investigation into the effect of top-surface structure until this work. A study to provide more information about suitable levels to consider top-surface structure would be useful. This may be particularly important if future results were to find any systematic over or underestimate of storage due to the omission of top-surface structure at certain levels.

This study investigated in detail the effect of permeability and dip based upon the

results of UKSAP (2011a), which investigated a number of sensitivities of storage efficiency in dipping open aquifers. Further sensitivities that may be of interest for both homogeneous and heterogeneous model may be sensitivity to

- Water injection as a method to increase residual trapping
- Increase or decrease of the migration velocity limit of 10m/yr
- Fracture pressure gradient

In our heterogeneous model further sensitivities for consideration are

- Shale porosity and permeability since some were set arbitrarily small in our model
- The net/gross ratio, which is currently 80% 20% in our model.

An alternative approach to some of the sensitivities looked at previously by using more than one base case may also be useful, to help account for the differing nature of the storage constraints applied by Gammer et al. (2011). Under the current approach the regime the base case is in may affect the sensitivity to some parameters, for example depth would appear more significant if the base case was injection-limited rather than migration limited.

It would also be of interest to investigate the economics and economic sensitivities of the Forties scenarios modelled to see this implication of the results to the costs involved in CO_2 storage. The detail of technical constraints upon the storage capacity estimate could also be increased, moving us further up the further up the techno-economic pyramid of Bradshaw et al. (2007). A key early consideration may be including the technical limit of surface injection pressure, not considered in this study.

6.2.2 1D Three-Phase Solutions Related Work

In this work we have sought to rigorously identify the physical unique solutions to three-phase problems where non-unique solutions may exist. Implementation of the viscous profile entropy condition has proven difficult due to the presence of dispersive numerical errors. However a more thorough study of how zero-limit conditions can be implemented may provide a way to implement the viscous profile entropy condition. Future work may consider how this could be achieved.

We have also sought to identify non-unique solutions to three-phase problems. To determine non-unique solutions to the three-phase problem there is scope for a more comprehensive search. One area for potential is using mixed-wet capillary pressures. Another group of solutions with potential are those considered by Jackson and Blunt

(2002). Based upon relative permeabilities and capillary pressures from a capillary bundle model, they observed some instability when initial states were inside the elliptic region of composition space. We suggest this instability may help yield non-unique solutions to the purely advective problem.

More fundamental to the issue of non-uniqueness is the existence of elliptic regions in composition-space. Much effort has been given to explain these in the past, however it is still not clear why they exist. Work to understand these may improve the understanding of relative permeability models for three-phase flow.

Another potential area of development is the inclusion of some of the numerical methods considered within this thesis in a streamline simulator or conventional finite difference simulator if 3D versions of the schemes are used. The use of ENO can provide improved efficiency of simulations in 1D and this may extend to 3D. The use of some of the methods for modelling capillary pressure could allow an investigation into the effect of a capillary fringe upon CO_2 plume migration.

Bibliography

Abreu, E., Furtado, F., and Pereira, F. (2004). On the numerical simulation of three-phase reservoir transport problems. *Transport Theory and Statistical Physics*, 33(5):503–526.

Araktingi, U. and Orr Jr, F. M. (1990). Viscous fingering, gravity segregation, and reservoir heterogeneity in miscible displacements in vertical cross sections. In *SPE/DOE Enhanced Oil Recovery Symposium*, Tulsa, Oklahoma. SPE-20176.

Azevedo, A. V., de Souza, A., Furtado, F., Marchesin, D., and Plohr, B. (2009). The solution by the wave curve method of three-phase flow in virgin reservoirs. *Transport in Porous Media*, 83:99–125.

Azevedo, A. V. and Marchesin, D. (1995). Multiple viscous solutions for systems of conservation laws. *Transactions of the American Mathematical Society*, 347:3061–3077.

Azevedo, A. V., Marchesin, D., Plohr, B., and Zumbrun, K. (2002). Capillary instability in models for three-phase flow. *Z. Angew. Math. Phys.*, 53(5):713–746. 634941.

Azevedo, A. V., Marchesin, D., Plohr, B. J., and Zumbrun, K. (1996). Nonuniqueness of solutions of Riemann problems. *Zeitschrift fur Angewandte Mathematik und Physik (ZAMP)*, 47:977–998.

Aziz, K. and Settari, A. (1979). *Petroleum reservoir simulation*. Applied Science Publishers (London).

Bachu, S., Bonijoly, D., Bradshaw, J., Burruss, R., Holloway, S., Christensen, N. P., and Mathiassen, O. M. (2007). CO2 storage capacity estimation: Methodology and gaps. *International Journal of Greenhouse Gas Control*, 1(4):430–443. DOI: 10.1016/S1750-5836(07)00086-2.

Baker, L. (1988). Three-phase relative permeability correlations. In *SPE Enhanced Oil Recovery Symposium*, SPE-17369, Tulsa, Oklahoma.

Batycky, R. P., Blunt, M. J., and Thiele, M. R. (1997). A 3D field-scale streamline-based reservoir simulator. *SPE Reservoir Engineering*, 12(4). SPE-36726.

Bear, J. (1988). *Dynamics of fluids in porous media*. Dover Publications.

Bell, J. B., Trangenstein, J. A., and Shubin, G. R. (1986). Conservation laws of mixed type describing three-phase flow in porous media. *SIAM Journal on Applied Mathematics*, 46(6):1000–1017.

Bennion, D. B. and Bachu, S. (2008). Drainage and imbibition relative permeability relationships for supercritical CO2/brine and H2S/brine systems in intergranular sandstone, carbonate, shale, and anhydrite rocks. *SPE Reservoir Evaluation and Engineering*, 11(3):487–496. SPE-99326.

Beraldo, V., Blunt, M. J., and Schiozer, D. (2009). Compressible streamline-based simulation with changes in oil composition. *SPE Reservoir Evaluation and Engineering*, 12(6):963–973. SPE-115983-PA.

Beraldo, V., Blunt, M. J., Schiozer, D., and Qi, R. (2007). Streamline simulation with an API tracking option. In *EUROPEC/EAGE Conference and Exhibition*, SPE-107496, London, U.K.

Berenblyum, R., Shapiro, A., Jessen, K., Stenby, E. H., and Orr, F. (2003). Black oil streamline simulator with capillary effects. In *SPE Annual Technical Conference and Exhibition*, SPE-84037, Denver, Colorado, U.S.A.

Blunt, M. J. (2000). An empirical model for three-phase relative permeability. *SPE Journal*, 5(4). SPE-67950.

Blunt, M. J., Jackson, M. D., Piri, M., and Valvatne, P. H. (2002). Detailed physics, predictive capabilities and macroscopic consequences for pore-network models of multiphase flow. *Advances in Water Resources*, 25(8-12):1069–1089. doi: 10.1016/S0309-1708(02)00049-0.

Bradshaw, B. E., Spencer, L. K., Lahtinen, A., Khider, K., Ryan, D. J., Colwell, J. B., Chirinos, A., Bradshaw, J., Draper, J. J., Hodgkinson, J., and McKillop, M. (2011). An assessment of Queensland's CO2 geological storage prospectivity – the Queensland CO2 geological storage atlas. *Energy Procedia*, 4:4583–4590. doi: 10.1016/j.egypro.2011.02.417.

Bradshaw, J., Bachu, S., Bonijoly, D., Burruss, R., Holloway, S., Christensen, N. P., and Mathiassen, O. M. (2007). CO2 storage capacity estimation: Issues and development of standards. *International Journal of Greenhouse Gas Control*, 1(1):62–68. DOI: 10.1016/S1750-5836(07)00027-8.

Brooks, R. H. and Corey, A. T. (1964). Hydraulic properties of porous media. *Hydrology Papers, Colorado State University, Fort Collins, Colorado*.

Buckley, S. and Leverett, M. (1942). Mechanisms of fluid displacements in sands. *Petroleum Transactions*, 146:107–116.

CarbonStore (2011). www.carbonstore.org.uk. Accessed June 2011.

Carlson, F. (1981). Simulation of relative permeability hysteresis to the nonwetting phase. In *SPE Annual Fall Technical Conference and Exhibition, SPE-10157*, San Antonio, Texas.

Cheng, H., Osako, I., Datta-Gupta, A., and King, M. J. (2006). A rigorous compressible streamline formulation for two- and three-phase black-oil simulation. *SPE Journal*, 11(4):407–417. SPE-96866-PA.

Coats, K., Dempsey, J., and Henderson, J. (1971). The use of vertical equilibrium in two-dimensional simulation of three-dimensional reservoir performance. *SPE Journal*, 11(1):63–71. SPE-2797-PA.

Crane, F., Kendall, H., and Gardner, G. (1963). Some experiments on the flow of miscible fluids of unequal density through porous media. *SPE Journal*, 3(4):277–280. SPE-535-PA.

Crane, M., Bratvedt, F., Bratvedt, K., Childs, P., and Olufsen, R. (2000). A fully compositional streamline simulator. In *SPE Annual Technical Conference and Exhibition*, SPE 63156, Dallas, Texas.

CSLF (2008). Task force for review and identification of standards for CO2 storage capacity estimation. Technical report.

Dahowski, R. T., Li, X., Davidson, C. L., Wei, N., Dooley, J. J., and Gentile, R. H. (2009). A preliminary cost curve assessment of carbon dioxide capture and storage potential in china. *Energy Procedia*, 1(1):2849–2856.

Di Donato, G. and Blunt, M. J. (2004). Streamline-based dual-porosity simulation of reactive transport and flow in fractured reservoirs. *Water Resour. Res.*, 40:W04203.

Di Donato, G., Huang, W., and Blunt, M. J. (2003a). Streamline-based dual porosity simulation of fractured reservoirs. In *SPE Annual Technical Conference and Exhibition*, SPE-84036, Denver, Colorado.

Di Donato, G., Obi, E., and Blunt, M. J. (2003b). Anomalous transport in heterogeneous media demonstrated by streamline-based simulation. *Geophys. Res. Lett.*, 30.

DiCarlo, D., Sahni, A., and Blunt, M. J. (2000). Three-phase relative permeability of water-wet, oil-wet and mixed-wet sandpacks. *SPE Journal*, 5(1). SPE-60767-PA.

Dietz, D. N. (1953). A theoretical approach to the problem of encroaching and by-passing edge water. In *Proc., Koninkl. Ned. Akad. Wetenschap*, volume B56, pages 83–92.

Dindoruk, B., Johns, R., and Orr, F. (1992). *Analytical Theory of Multiphase, Multicomponent Displacement in porous Media.* PhD thesis.

Dolezal, A. and Wong, S. S. M. (1995). Relativistic hydrodynamics and essentially non-oscillatory shock capturing schemes. *Journal of Computational Physics*, 120:266–277.

Dong, H. (2007). *Micro-CT imaging and pore-network extraction.* PhD thesis.

Doughty, C., Pruess, K., Benson, S. M., Hovorka, S. D., Knox, P. R., and Green, C. T. (2001). Capacity investigation of brine-bearing sands of the Frio formation for geologic sequestration of CO2. University of California eScholarship Repository [http://repositories.cdlib.org/cgi/oai2.cgi].

Efraimsson, G. and Kreiss, G. (1999). A remark on numerical errors downstream of slightly viscous shocks. *SIAM Journal on Numerical Analysis*, 36(3):853–863.

Engquist, B. and Sjogreen, B. (1998). The convergence rate of finite difference schemes in the presence of shocks. *SIAM Journal on Numerical Analysis*, 35:2464–2485.

Ennis-King, J. and Paterson, L. (2002). Engineering aspects of geological sequestration of carbon dioxide. In *SPE Asia Pacific Oil and Gas Conference and Exhibition*, SPE-77809, Melbourne, Australia.

Ennis-King, J. and Paterson, L. (2005). Role of convective mixing in the long-term storage of carbon dioxide in deep saline aquifers. *SPE Journal*, 10(3). SPE-84344-PA.

EU (2011). EU CO2 emissions by sector: http://ec.europa.eu/energy/publications. Accessed September 2011.

Evans, D., Graham, C., Armour, A., and Bathurst, P. (2003). *The Millennium Atlas: Petroleum geology of the central and northern North Sea.* The Geological Society of London.

Falls, A. and Schulte, W. (1992a). Features of three-component, three-phase displacement in porous media. *SPE Reservoir Engineering*, 7(4):426–432. SPE-19678.

Falls, A. and Schulte, W. (1992b). Theory of three-component, three-phase displacement in porous media. *SPE Production Engineering*, 7(3):377–384. SPE-19387.

Fayers, F. (1989). Extension of Stone's method 1 and conditions for real characteristics in three-phase flow. *SPE Reservoir Engineering*, 4(4). SPE-16965.

Fayers, F. and Muggeridge, A. (1990). Extensions to Dietz theory and behavior of gravity tongues in slightly tilted reservoirs. *SPE Journal*, 5:487–494. SPE-18438.

Flett, M., Beacher, G., Brantjes, J., Burt, A., Dauth, C., Koelmeyer, F., Lawrence, R., Leigh, S., McKenna, J., Gurton, R., Robinson, W., and Tankersley, T. (2008). Gorgon project: Subsurface evaluation of carbon dioxide disposal under Barrow island. In *SPE Asia Pacific Oil and Gas Conference and Exhibition*, SPE-116372, Perth, Australia.

Flett, M., Gurton, R., and Weir, G. (2007). Heterogeneous saline formations for carbon dioxide disposal: Impact of varying heterogeneity on containment and trapping. *Journal of Petroleum Science and Engineering*, 57(1-2):106–118.

Gammer, D., Green, A., Smith, G., Holloway, S., and Consortium, T. U. (2011). Energy technologies institute's UK CO2 storage appraisal project (UKSAP). In *SPE Offshore Europe Oil and Gas Conference and Exhibition*, SPE-148426, Aberdeen, UK.

Georgiadis, A., Llovell, F., Bismarck, A., Blas, F. J., Galindo, A., Maitland, G. C., Trusler, J. P. M., and Jackson, G. (2011). Interfacial tension measurements and modelling of (carbon dioxide;n-alkane) and (carbon dioxide;water) binary mixtures at elevated pressures and temperatures. *The Journal of Supercritical Fluids*, 55(2):743–754. doi: 10.1016/j.supflu.2010.09.028.

Gerritsen, M., Jessen, K., Mallison, B., and Lambers, J. (2005). A fully adaptive streamline framework for the challenging simulation of gas-injection processes. In *SPE Annual Technical Conference and Exhibition*, SPE-97270, Dallas, Texas.

Gerritsen, M., Lof, H., and Thiele, M. R. (2009). Parallel implementations of streamline simulators. *Computational Geosciences*, 13(1):135–149. 10.1007/s10596-008-9113-y.

Gluyas, J. G. and Hichens, H. M. (2002). *United Kingdom oil and gas fields: commemorative millennium volume*. Geological Society (London) Memoir 20.

Godunov, S. (1959). A difference method for numerical calculation of discontinuous solutions of the equations of hydrodynamics. *Matematicheskii Sbornik*, 47(89)(3):271–306.

Goodman, A., Hakala, A., Bromhal, G., Deel, D., Rodosta, T., Frailey, S., Small, M., Allen, D., Romanov, V., Fazio, J., Huerta, N., McIntyre, D., Kutchko, B., and Guthrie, G. (2011). U.S. DOE methodology for the development of geologic storage potential for carbon dioxide at the national and regional scale. *International Journal of Greenhouse Gas Control*, In Press, Corrected Proof. doi: 10.1016/j.ijggc.2011.03.010.

Gorecki, D., Sorensen, J. A., Bremer, J., Knudsen, D., Smith, S., Steadman, N., and Harju, J. (2009). Development of storage coefficients for determining the effective CO2 storage resource in deep saline aquifers. In *SPE International Conference on CO2 Capture, Storage and Utilization*, SPE-126444, San Diego, California, USA,.

Gustafsson, B. (2008). *High Order Difference Methods for Time Dependent PDE*. Springer Series in Computational Mathematics. Springer.

Guzman, R. (1995). *Mathematics of Three-Phase Flow*. PhD thesis.

Guzman, R. and Fayers, J. F. (1997). Solutions to the three-phase Buckley-Leverett problem. *SPE Journal*, 2. SPE-35156.

Harten, A., Engquist, B., Osher, S., and Chakravarthy, S. R. (1987). Uniformly high order accurate essentially non-oscillatory schemes, iii. *Journal of Computational Physics*, 131:3–47.

Harten, A. and Lax, P. D. (1984). On a class of high resolution total-variation-stable finite-difference schemes. *SIAM Journal on Numerical Analysis*, 21:1–23.

Harten, A. and Osher, S. (1987). Uniformly high-order accurate nonoscillatory schemes. i. *SIAM Journal on Numerical Analysis*, 24(2):279–309.

Hayek, M., Mouche, E., and Mugler, C. (2009). Modeling vertical stratification of CO2 injected into a deep layered aquifer. *Advances in Water Resources*, 32(3):450–462.

Helland, J. O. and Skjaveland, S. M. (2006). Three-phase mixed-wet capillary pressure curves from a bundle of triangular tubes model. *Journal of Petroleum Science and Engineering*, 52(1-4):100–130. doi: 10.1016/j.petrol.2006.03.018.

Hesse, M. A., Orr, F. M., and Tchelepi, H. A. (2008). Gravity currents with residual trapping. *Journal of Fluid Mechanics*, 611(1):35–60.

Holden, H. and Risebro, N. H. (2002). *Front tracking for Hyperbolic Conservation Laws*. Springer.

Holden, L. (1990a). A class of n nonlinear hyperbolic conservation laws. *Journal of Differential Equations*, 84:73.

Holden, L. (1990b). On the strict hyperbolicity of the Buckley-Leverett equations for three-phase flow in a porous medium. *SIAM Journal on Applied Mathematics*, 50(3):667–682.

Holloway, S. (2009). Storage capacity and containment issues for carbon dioxide capture and geological storage on the UK continental shelf. *Proceedings of the Institution of Mechanical Engineers, Part A: Journal of Power and Energy*, 223(3):239–248. 10.1243/09576509JPE650.

Holloway, S., Garg, A., Kapshe, M., Deshpande, A., Pracha, A. S., Khan, S. R., Mahmood, M. A., Singh, T. N., Kirk, K. L., and Gale, J. (2009). An assessment of the CO2 storage potential of the Indian subcontinent. *Energy Procedia*, 1(1):2607–2613.

Holm, R., Kaufmann, R., Dale, E. I., Aanonsen, S., Fladmark, G. E., Espedal, M., and Skauge, A. (2009). Constructing three-phase capillary pressure functions by parameter matching using a modified ensemble Kalman filter. *Communications in Computational Physics*, 6(1):24–48.

Holm, R., van Dijke, M., and Geiger, S. (2010). Three-phase flow modelling using pore-scale capillary pressures and relative permeabilities for mixed-wet media at the continuum-scale. *Transport in Porous Media*, 81(3):423–442.

Hundsdorfer, W. H. (2003). *Numerical solution of time-dependent advection-diffusion-reaction equations*. Springer Series in Computational Mathematics. Springer.

IEA (2008). Energy technology perspectives. Technical report.

IEAGHG (2009). Development of storage coefficients for carbon dioxide storage in deep saline aquifers. Technical report.

Ingebrigtsen, L. and Bradvedt, F. (1999). A streamline based approach to solution of three-phase flow. In *SPE Reservoir Simulation Symposium*, SPE-51904, Houston, Texas.

IPCC (2005). Special report on carbon dioxide capture and storage. Technical report.

IPCC (2007). IPCC fourth assessment report: Climate change 2007. Technical report.

Isaacson, E., Marchesin, D., and Plohr, B. (1990). Transitional waves for conservation laws. *SIAM journal on mathematical analysis*, 21:837.

Isaacson, E., Marchesin, D., Plohr, B., and Temple, B. (1988). The Riemann problem near a hyperbolic singularity: The classification of solutions of quadratic Riemann problems i. *SIAM Journal on Applied Mathematics*, 48(5):1009–1032.

Isaacson, E., Marchesin, D., Plohr, B., and Temple, J. (1992). Multiphase flow models with singular Riemann problems. *Mathematica Applicada e Computacion*, 11:147–166.

Isaacson, E. and Temple, J. (1986). Analysis of a singular hyperbolic system of conservation laws. *Journal of Differential Equations*, pages 250–268.

Jackson, M. D. and Blunt, M. J. (2002). Elliptic regions and stable solutions for three-phase flow in porous media. *Transport in Porous Media*, 48(3):249–269. 10.1023/A:1015726412625.

Jessen, K., Gerritsen, M., and Mallison, B. (2008). High-resolution prediction of enhanced condensate recovery processes. *SPE Journal*, 13(2):257–266. SPE-99619-PA.

Jessen, K., Kovscek, A. R., and Orr, F. M. (2005). Increasing CO2 storage in oil recovery. *Energy Conversion and Management*, 46(2):293–311.

Jessen, K. and Orr, F. (2002). Compositional streamline simulation. In *SPE Annual Technical Conference and Exhibition*, SPE-77379, San Antonio, Texas.

Jessen, K. and Orr, F. (2004). Gravity segregation and compositional streamline simulation. In *SPE/DOE Fourteenth Symposium on Improved Oil Recovery*, SPE-89448, Tulsa, Oklahoma.

Jessen, K., Wang, Y., Ermakov, P., Zhu, J., and Orr, F. (2001). Fast, approximate solutions for 1D multicomponent gas-injection processes. *SPE Journal*, 6(4). SPE-74700-PA.

Jiang, G. and Shu, C. (1996). Efficient implementation of weighted ENO schemes. *Journal of Computational Physics*, 126(1):202–228.

Jin, M., Pickup, G., Mackay, E., Todd, A., Monoghan, A., and Naylor, M. (2010). Static and dynamic estimates of CO2 storage capacity in two saline formations in the UK. In *SPE EUROPEC/EAGE Annual Conference and Exhibition*, SPE-131609, Barcelona, Spain.

Johansen, T., Wang, Y., Orr, F. M., and Dindoruk, B. (2005). Four-component gas/oil displacements in one dimension: Part i: Global triangular structure. *Transport in Porous Media*, 61(1):59–76.

Johns, R. (1992). *Analytical Theory of Multicomponent Gas Drives with Two-Phase Mass Transfer*. PhD thesis.

Juanes, R. (2006). Impact of relative permeability hysteresis on geological CO2 storage. *Water Resources Research*, 42:W12418.

Juanes, R. and MacMinn, C. W. (2008). Upscaling of capillary trapping under gravity override: Application to CO2 sequestration in aquifers. In *SPE/DOE Improved Oil recovery Symposium*, SPE-113496, Tulsa, Oklahoma, U.S.A.

Juanes, R., MacMinn, C. W., and Szulczewski, M. L. (2010). The footprint of the CO2 plume during carbon dioxide storage in saline aquifers: Storage efficiency for capillary trapping at the basin scale. *Transport in Porous Media*, 82:19–30. 10.1007/s11242-009-9420-3.

Juanes, R. and Patzek, T. W. (2002). Three-phase displacement theory: An improved description of relative permeabilites. In *SPE Annual Technical Conference and Exhibition*, SPE 77539, San Antonio, Texas.

Juanes, R. and Patzek, T. W. (2004a). Analytical solution to the Riemann problem of three-phase flow in porous media. *Transport in Porous Media*, 55(1):47–70. 10.1023/B:TIPM.0000007316.43871.1e.

Juanes, R. and Patzek, T. W. (2004b). Relative permeabilities for strictly hyperbolic models of three-phase flow in porous media. *Transport in Porous Media*, 57(2):125–152. 10.1023/B:TIPM.0000038251.10002.5e.

Kalaydjian, F.-M. (1992). Performance and analysis of three-phase capillary pressure curves for drainage and imbibition in porous media. In *67th SPE Annual Technical Conference and Exhibition*, SPE-24878, Washington, DC.

Kopp, A., Class, H., and Helmig, R. (2009a). Investigations on CO2 storage capacity in saline aquifers–part 2: Estimation of storage capacity coefficients. *International Journal of Greenhouse Gas Control*, 3(3):277–287. DOI: 10.1016/j.ijggc.2008.10.001.

Kopp, A., Probst, P., Class, H., Hurter, S., and Helmig, R. (2009b). Estimation of CO2 storage capacity coefficients in geologic formations. *Energy Procedia*, 1(1):2863–2870. DOI: 10.1016/j.egypro.2009.02.060.

Kovscek, A. R. and Wang, Y. (2005). Geologic storage of carbon dioxide and enhanced oil recovery. I. uncertainty quantification employing a streamline based proxy for reservoir

flow simulation. *Energy Conversion and Management*, 46(11-12):1920–1940. DOI: 10.1016/j.enconman.2004.09.008.

Kozlova, A., Bradvedt, F., Bradvedt, K., and Myasnikov, A. (2006). A three-phase compressible dual-porosity model for streamline simulation. In *SPE Annual Technical Conference and Exhibition*, SPE-102549, San Antonio, Texas.

Kumar, A., Noh, G., Sepehrnoori, K., Bryant, S., and Lake, L. (2004). Reservoir simulation of CO2 storage in deep saline aquifers. In *SPE/DOE Fourteenth Symposium on Improved Oil Recovery*, SPE-89343, Tulsa, Oklahoma, U.S.A.

Kuuskraa, V. A., Koperna, G. J., Riestenberg, D., and Esposito, R. (2009). Using reservoir architecture to maximize CO2 storage capacity. *Energy Procedia*, pages 3063–3070.

LaForce, T. (2005). *Mathematics of partially miscible three-phase flow*. PhD thesis.

LaForce, T. (2011). Development of 3-phase analytic solutions and evaluation of eigenvalues to determine the hyperbolicity of problems. Personal communication.

LaForce, T., Cinar, Y., Johns, R., and Orr Jr, F. M. (2010). Experimental confirmation of analytical composition routes in three-phase partially miscible flow. *SPE Journal*, 15(1):160–170. SPE-99505-PA.

LaForce, T., Jessen, K., and Orr, F. (2008a). Four-component gas/water/oil displacements in one dimension: Part I. structure of the conservation law. *Transport in Porous Media*, 71(2):199–216. 10.1007/s11242-007-9120-9.

LaForce, T., Jessen, K., and Orr, F. (2008b). Four-component gas/water/oil displacements in one dimension: Part II, example solutions. *Transport in Porous Media*, 72:83–96.

LaForce, T. and Johns, R. (2005a). Composition routes for three-phase partially miscible flow in ternary systems. *SPE Journal*, 10(2):161–174. SPE-89438-PA.

LaForce, T. and Johns, R. T. (2005b). Analytical solutions for surfactant-enhanced remediation of nonaqueous phase liquids. *Water Resources Research*, 41:W10420.

LaForce, T. and Orr, F. (2009). Four-component gas/water/oil displacements in one dimension: Part III, development of miscibility. *Transport in Porous Media*, 79:225–247.

Land, C. S. (1968). Calculation of imbibition relative permeability for two- and the-phase flow from rock properties. *SPE Journal*, 8(2):149–156. SPE-1942-PA.

Lax, P. D. (1957). Hyperbolic systems of conservation laws II. *Communications on Pure and Applied Mathematics*, 10:537–566.

Lengler, U., De Lucia, M., and KÃijhn, M. (2010). The impact of heterogeneity on the distribution of CO2: Numerical simulation of CO2 storage at Ketzin. *International Journal of Greenhouse Gas Control*, 4(6):1016–1025. doi: 10.1016/j.ijggc.2010.07.004.

Lenhard, R. J. and Parker, J. C. (1988). Experimental validation of the theory of extending two-phase saturation-pressure relations to three-fluid phase systems for monotonic drainage paths. *Water Resour. Res.*, 24(3):373–380.

LeVeque, R. J. (2002). *Finite-Volume Methods for Hyperbolic Problems*. Cambridge University Press.

Leverett, M. (1941). Capillary behaviour in porous solids. *Petroleum Transactions*, 142:152–169.

Levy, D., Puppo, G., and Russo, G. (1999). Central WENO schemes for hyperbolic systems of conservation laws. *Mathematical Modeling and Numerical Analysis*, 33.

Lewis, D., Bentham, M., Cleary, T., Vernon, R., O'Neill, N., Kirk, K., Chadwick, A., Hilditch, D., Michael, K., Allinson, G., Neal, P., and Ho, M. (2009). Assessment of the potential for geological storage of carbon dioxide in Ireland and Northern Ireland. *Energy Procedia*, 1(1):2655–2662.

Li, X., Wei, N., Liu, Y., Fang, Z., Dahowski, R. T., and Davidson, C. L. (2009). CO2 point emission and geological storage capacity in China. *Energy Procedia*, 1(1):2793–2800.

Liu, T.-P. (1974). The Riemann problem for general 2 x 2 conservation laws. *Transactions of the American Mathematical Society*, 199:89–112.

Liu, X.-D., Osher, S., and Chan, T. (1994). Weighted essentially non-oscillatory schemes. *Journal of Computational Physics*, 115(1):200–212. doi: 10.1006/jcph.1994.1187.

Lyle, S., Huppert, H. E., Hallworth, M., Bickle, M., and Chadwick, A. (2005). Axisymmetric gravity currents in a porous medium. *Journal of Fluid Mechanics*, 543(-1):293–302.

MacMinn, C. W., Szulczewski, M. L., and Juanes, R. (2010). CO2 migration in saline aquifers. part 1. capillary trapping under slope and groundwater flow. *Journal of Fluid Mechanics*, 662:329–351.

MacMinn, C. W., Szulczewski, M. L., and Juanes, R. (2011). CO2 migration in saline aquifers: Regimes in migration with dissolution. *Energy Procedia*, 4:3904–3910. doi: 10.1016/j.egypro.2011.02.328.

Maldal, T. and Tappel, I. M. (2004). CO2 underground storage for Snohvit gas field development. *Energy*, 29(9-10):1403–1411. DOI: 10.1016/j.energy.2004.03.074.

Mallison, B., Gerritsen, M., Jessen, K., and Orr, Jr., F. M. (2005). High order upwind schemes for two-phase, multicomponent flow. *SPE Journal*, 10(3):297–311. SPE-79791-PA.

Mallison, B., Gerritsen, M., and Matringe, S. (2006). Improved mappings for streamline-based simulation. *SPE Journal*, 11(3):294–302. SPE-89352.

Mani, V. and Mohanty, K. (1998). Pore-level network modeling of three-phase capillary pressure and relative permeability curves. *SPE Journal*, 3(3):238–248. SPE-50942-PA.

Marchesin, D. and Medeiros, H. B. (1989). A note on the stability of eigenvalue degeneracy in nonlinear conservation laws of multiphase flow. *Contemporary mathematics*, 100.

Maschio, C. and Schiozer, D. (2002). Analysis of the performance of streamline simulation. In *2nd Meeting on Reservoir Simulation*, Buenos Aires, Argentina.

Mathias, S., Gonzalez Martinez de Miguel, G., Thatcher, K., and Zimmerman, R. (2011). Pressure buildup during CO2 injection into a closed brine aquifer. *Transport in Porous Media*, 89(3):383–397.

Matringe, S. and Gerritsen, M. (2004). On accurate tracing of streamlines. In *SPE Annual Technical conference and Exhibition*, SPE-89920, Houston, Texas.

Matringe, S., Gerritsen, M., and Mallison, B. (2005). Optimizing streamline coverage for efficiency and accuracy. In *SPE Reservoir Simulation Symposium*, SPE-93306, The Woodlands, Texas.

Matringe, S., Juanes, R., and Tchelepi, H. (2007). Streamline tracing on general triangular or quadrilateral grids. *SPE Journal*, 12(2):217–233. SPE-96411-PA.

Matringe, S. F., Juanes, R., and Tchelepi, H. A. (2006). Robust streamline tracing for the simulation of porous media flow on general triangular and quadrilateral grids. *Journal of Computational Physics*, 219(2):992–1012. DOI: 10.1016/j.jcp.2006.07.004.

MIT (2011). http://sequestration.mit.edu/index.html.

Mo, S. and Akervoll, I. (2005). Modelling long-term CO2 storage in aquifer with a black-oil reservoir simulator. In *SPE/EPA/DOE Exploration and Production Environmental Conference*, SPE-93951, Galveston, Texas.

Nessyahu, H. and Tadmor, E. (1990). Non-oscillatory central differencing for hyperbolic conservation laws. *Journal of Computational Physics*, 87:408–463.

Nghiem, L., Sammon, P., Grebenstetter, J., and Ohkuma, H. (2004). Modelling CO2 storage in aquifers with a fully-coupled geochemical EOS compositional simulator. In *SPE/DOE Symposium on Improved Oil Recovery*, SPE-89474, Tulsa, Oklahoma.

Nilsen, H. M., Herrera, P. A., Ashraf, M., Ligaarden, I., Iding, M., Hermanrud, C., Lie, K., Nordbotten, J. M., Dahle, H. K., and Keilegavlen, E. (2011). Field-case simulation of CO2 -plume migration using vertical-equilibrium models. *Energy Procedia*, 4(0):3801–3808. doi: 10.1016/j.egypro.2011.02.315.

Nordbotten, J. M., Celia, M., Bachu, S., and Dahle, H. K. (2004). Semianalytical solution for CO2 leakage through an abandoned well. *Environmental Science and Technology*, 39(2):602–611. doi: 10.1021/es035338i.

Nordbotten, J. M., Celia, M. A., and Bachu, S. (2005). Injection and storage of CO2 in deep saline aquifers: Analytical solution for CO2 plume evolution during injection. *Transport in Porous Media*, 58(3):339–360. 10.1007/s11242-004-0670-9.

Nordtvedt, J., Ebeltoft, E., Iversen, J., Sylte, A., Urkedal, H., Vatne, K., and Watson, A. (1997). Determination of three-phase relative permeabilities from displacement experiments. *SPE Formation Evaluation*, 12(4). SPE-36683-PA.

Oak, M., Baker, L., and Thomas, D. (1990). Three-phase relative permeability of Berea sandstone. *SPE Journal of Petroleum Technology*, 42(8):1054–1061. SPE-17370-PA.

Obi, E. I. and Blunt, M. J. (2004). Streamline-based simulation of advective-dispersive solute transport. *Advances in Water Resources*, 27(9):913–924. DOI: 10.1016/j.advwatres.2004.06.003.

Obi, E. I. and Blunt, M. J. (2006). Streamline-based simulation of carbon dioxide storage in a north sea aquifer. *Water Resour. Res.*, 42:W03414.

Ogawa, T., Nakanishi, S., Shidahara, T., Okumura, T., and Hayashi, E. (2011). Saline-aquifer CO2 sequestration in Japan-methodology of storage capacity assessment. *International Journal of Greenhouse Gas Control*, 5(2):318–326.

Oldenburg, C. M., Pruess, K., and Benson, S. M. (2001). Process modeling of CO2 injection into natural gas reservoirs for carbon sequestration and enhanced gas recovery. *Energy and Fuels*, 15(2):293–298. doi: 10.1021/ef000247h.

Oleinik, O. (1959). Uniqueness and stability of the generalized solution of the Cauchy problem for a quasi-linear equation. *UMN*, 14(2(86)):165–170.

Orr, F. (2007). *Theory of Gas Injection Processes*. Tie-Line Publications, Copenhagen, Denmark, 1st edition.

Osher, S. and Chakravarthy, S. R. (1984). High resolution schemes and the entropy condition. *SIAM Journal on Numerical Analysis*, 21(5):955–984.

Ozah, R., Lakshminarasimhan, S., Pope, G., Sepehrnoori, K., and Bryant, S. (2005). Numerical simulation of the storage of pure CO2 and CO2-H2S gas mixtures in deep saline aquifers. In *SPE Annual Technical Conference and Exhibition*, SPE-97255, Dallas, Texas.

Peddibhotla, S., Cubillos, H., Datta-Gupta, A., and Wu, C. (1996). Rapid simulation of multiphase flow through fine-scale geostatistical realizations using a new, 3-D, streamline model: A field example. In *Petroleum Computer Conference*, SPE-36008, Dallas, Texas.

Peddibhotla, S., Datta-Gupta, A., and Xue, G. (1997). Multiphase streamline modelling in three dimensions: Further generalisations and a field application. In *SPE Reservoir Simulation Symposium*, SPE-38003, Dallas, Texas.

Pickup, G. E., Jin, M., Olden, P., Mackay, E., Todd, A. C., Ford, J. R., Lawrence, D., Monaghan, A., Naylor, M., Haszeldine, R. S., and Smith, M. (2011). Geological storage of CO2 : Site appraisal and modelling. *Energy Procedia*, 4:4762–4769. doi: 10.1016/j.egypro.2011.02.440.

Pollock, D. W. (1988). Semianalytical computation of path lines for finite difference models. *Ground Water*, 26(6):743–750.

Preston, C., Monea, M., Jazrawi, W., Brown, K., Whittaker, S., White, D., Law, D., Chalaturnyk, R., and Rostron, B. (2005). IEA GHG Weyburn CO2 monitoring and storage project. *Fuel Processing Technology*, 86(14-15):1547–1568. DOI: 10.1016/j.fuproc.2005.01.019.

Pruess, K. (2005). *A TOUGH2 Fluid Property Module for Mixtures of Water, NaCl, and CO2*. Earth Sciences Division, Lawrence Berkeley National Laboratory, University of California, Berkeleym CA 94720, LBNL-57952.

Pruess, K., Xu, T., Apps, J., and Garcia, J. (2003). Numerical modelling of aquifer disposal of CO2. *SPE Journal*, 8(1):49–60. SPE-83695-PA.

Qi, R., LaForce, T., and Blunt, M. J. (2008a). Design of carbon dioxide storage in oil fields. In *SPE Annual Technical Conference and Exhibition*, SPE-115663, Denver, Colorado.

Qi, R., LaForce, T., and Blunt, M. J. (2008b). A three-phase four-component streamline-based simulator to study carbon dioxide storage. *Computational Geosciences*. 10.1007/s10596-009-9139-9.

Qi, R., LaForce, T. C., and Blunt, M. J. (2009). Design of carbon dioxide storage in aquifers. *International Journal of Greenhouse Gas Control*, 3(2):195–205. DOI: 10.1016/j.ijggc.2008.08.004.

Qiu, J. and Shu, C. (2002). On the construction, comparison, and local characteristic decomposition for high-order central WENO schemes. *Journal of Computational Physics*, 183(1):187–209. DOI: 10.1006/jcph.2002.7191.

Rachford, H. and Rice, J. (1952). Procedure for use of electronic digital computers in calculating flash vaporization hydrocarbon equilibrium. *Petroleum Transactions*, 195:327–328.

Radoslaw, T., Barbara, U. M., and Adam, W. (2009). CO2 storage capacity of deep aquifers and hydrocarbon fields in Poland - EU geocapacity project results. *Energy Procedia*, 1(1):2671–2677. Bob02 Times Cited:1 Cited References Count:11 Energy Procedia.

Remson, I. (1971). *Numerical methods in subsurface hydrology: with an introduction to the finite element method*.

Riddiford, F., Wright, I., Bishop, C., Espie, T., and Tourqui, A. (2005). Monitoring geological storage: The In Salah gas CO2 storage project. In Rubin, E., Keith, D., and Gilboy, C., editors, *Seventh International Conference on Greenhouse Gas Control Technologies*, Vancouver.

Rogerson, A. M. and Meiburg, E. (1990). A numerical study of the convergence properties of ENO schemes. *Journal of Scientific Computing*, 5(2):151–167.

Schaeffer, D. G. (1987). Riemann problems for nonstrictly hyperbolic 2 x 2 systems of conservation laws. *Transactions of the American Mathematical Society*, 304(1):267.

Schecter, S., Marchesin, D., and Plohr, B. J. (1996). Structurally stable Riemann solutions. *Journal of Differential Equations*, 126:303–354.

Seto, C. J., Jessen, K., and Orr, F. (2007). Using analytical solutions in compositional streamline simulation of a field-scale CO2-injection project in a condensate reservoir. *SPE Reservoir Evaluation and Engineering*, 10(4):393–405. SPE-79690-PA.

Shearer, M. (1989). The Riemann problem for 2 x 2 systems of hyperbolic conservation laws with case I quadratic nonlinearities. *Journal of Differential Equations*, 80(2):343.

Shearer, M., Schaeffer, D. G., Marchesin, D., and Paes-Leme, P. L. (1987). Solution of the Riemann problem for a prototype 2 x 2 system of non-strictly hyperbolic conservation laws. *Archive for Rational Mechanics and Analysis*, 97(4):299–320. 10.1007/BF00280409.

Shearer, M. and Trangenstein, J. A. (1989). Loss of real characteristics for models of three-phase flow in a porous medium. *Transport in Porous Media*, 4:499–525.

Sheffield, M. (1968). Three-phase fluid flow including gravitational, viscous and capillary forces. *SPE Journal*, 9(2):255–269. SPE-2012-PA.

Shu, C. (1990). Numerical experiments on the accuracy of ENO and modified ENO schemes. *Journal of Scientific Computing*, 5(2):127–149. 10.1007/BF01065581.

Shu, C. (1997). Essentially non-oscillatory and weighted essentially non-oscillatory schemes for hyperbolic conservation laws. Technical Report ICASE Report No. 97-65, NASA Langley Research Center.

Shu, C. and Osher, S. (1988). Efficient implementation of essentially non-oscillatory shock-capturing schemes. *Journal of Computational Physics*, 77:439–471.

Shu, C. and Osher, S. (1989). Efficient implementation of essentially non-oscillatory shock-capturing schemes, ii. *Journal of Computational Physics*, 83:32–78.

Smalley, P. C., Ross, B., Brown, C. E., Moulds, T. P., and Smith, M. J. (2007). Reservoir technical limits: A framework for maximising recovery from oil fields. In *SPE Annual Technical Conference and Exhibition*, Anaheim, California, U.S.A. SPE 109555.

Stern, N. H. (2007). *The economics of climate change: the Stern review*. Cambridge University Press.

Stone, H. (1970). Probability model for estimating three-phase relative permeability. *SPE Journal of Petroleum Technology*, 22(2):214–218. SPE-2116-PA.

Stone, H. (1973). Estimation of three-phase relative permeability and residual oil data. *Journal of Petroleum Technology*, 12(4):52–61.

Strikwerda, J. C. (2004). *Finite difference schemes and partial differential equations*. SIAM, second edition.

Szulczewski, M. L. and Juanes, R. (2009). A simple but rigorous model for calculating CO2 storage capacity in deep saline aquifers at the basin scale. *Energy Procedia*, 1(1):3307–3314. DOI: 10.1016/j.egypro.2009.02.117.

Taku Ide, S., Jessen, K., and Orr Jr, F. M. (2007). Storage of CO2 in saline aquifers: Effects of gravity, viscous, and capillary forces on amount and timing of trapping. *International Journal of Greenhouse Gas Control*, 1(4):481–491. DOI: 10.1016/S1750-5836(07)00091-6.

Temple, B. (1982). Global solution of the Cauchy problem for a class of 2 x 2 nonstrictly hyperbolic conservation laws. *Advances in Applied Mathematics*, 3(3):335.

Thiele, M. R., Batycky, R., and Blunt, M. J. (1997). A streamline-based 3D field-scale compositional reservoir simulation. In *SPE Annual Technical Conference and Exhibition*, SPE-38889, San Antonio, Texas.

Thiele, M. R., Batycky, R., Iding, M., and Blunt, M. J. (2004). Extension of streamline-based dual porosity flow simulation to realistic geology. In *European Conference on the Mathematics of Oil Recovery*, Cannes, France.

Todd, M. and Longstaff, W. (1972). The development, testing, and application of a numerical simulator for predicting miscible flood performance. *Journal of Petroleum Technology*, 24(7):874–882. SPE-3484-PA.

Torp, T. A. and Gale, J. (2004). Demonstrating storage of CO2 in geological reservoirs: The Sleipner and SACS projects. *Energy*, 29(9-10):1361–1369. DOI: 10.1016/j.energy.2004.03.104.

Trangenstein, J. A. (1989). Three-phase flow with gravity. *Contemporary Mathematics*, 100:147–159.

Ukaegbu, C., Gundogan, O., Mackay, E., Pickup, G., Todd, A., and Gozalpour, F. (2009). Simulation of CO2 storage in a heterogeneous aquifer. *Proceedings of the Institution of Mechanical Engineers Part a-Journal of Power and Energy*, 223(A3):249–267.

UKSAP (2011a). Appendix 3, UK storage appraisal project. Technical report, Energy Technologies Institute.

UKSAP (2011b). UK storage appraisal project. Technical report, Energy Technologies Institute.

USDOE (2010). Carbon sequestration atlas of the United States and Canada. Technical report.

Valenti, G., Jessen, K., Mallison, B., and Gerritsen, M. (2004). High-order upwind schemes for three-phase multicomponent flows, a preliminary investigation. In *SPE Annual technical Conference and Exhibition*, SPE-90594, Houston, Texas.

Van der Meer, L. G. H. and Yavuz, F. (2009). CO2 storage capacity calculations for the Dutch subsurface. *Energy Procedia*, 1(1):2615–2622. doi: 10.1016/j.egypro.2009.02.028.

van Dijke, M. I. J., McDougall, S. R., and Sorbie, K. S. (2001). Three-phase capillary pressure and relative permeability relationships in mixed-wet systems. *Transport in Porous Media*, 44(1):1–32.

Van Duijn, C. J., Molenaar, J., and Neef, M. J. (1995). The effect of capillary forces on immiscible two-phase flow in heterogeneous porous media. *Transport in Porous Media*, 21(1):71–93.

Van Leer, B. (1979). Towards the ultimate conservative difference scheme. V. a second-order sequel to Godunov's method. *Journal of Computational Physics*, 32(1):101–136. doi: 10.1016/0021-9991(79)90145-1.

Vangkilde-Pedersen, T., Anthonsen, K. L., Smith, N., Kirk, K., Neele, F., van der Meer, B., Le Gallo, Y., Bossie-Codreanu, D., Wojcicki, A., Le Nindre, Y. M., Hendriks, C., Dalhoff, F., and Christensen, N. P. (2009). Assessing European capacity for geological storage of carbon dioxide - the EU geocapacity project. *Energy Procedia*, 1(1):2663–2670.

Vella, D. and Huppert, H. (2006). Gravity currents in a porous medium at an inclined plane. *Journal of Fluid Mechanics*, 555:353–362.

Walsteijn, F. H. (1994). Robust numerical methods for 2D turbulence. *Journal of Computational Physics*, 114:129–145.

Wang, Z. and Huang, G. P. (2002). An essentially nonoscillatory high-order Pade-type (ENO-Pade) scheme. *Journal of Computational Physics*, 177(1):37–58. doi: 10.1006/jcph.2002.6998.

Xu, T., Apps, J. A., and Pruess, K. (2003). Reactive geochemical transport simulation to study mineral trapping for CO2 disposal in deep arenaceous formations. *J. Geophys. Res.*, 108.

Yan, W., Michelsen, M., Stenby, E. H., Berenblyum, R., and Shapiro, A. (2004). Three-phase compositional streamline simulation and its applications to WAG. In *SPE/DOE Fourteenth Symposium on Improved Oil Recovery*, SPE-89440, Tulsa, Oklahoma.

Yortsos, Y. C. (1995). A theoretical analysis of vertical flow equilibrium. *Transport in Porous Media*, 18(2):107–129.

Zhu, Z., Gerritsen, M., and Thiele, M. R. (2009). Thermal streamline simulation for hot water flooding. In *SPE Reservoir Simulation Symposium*, SPE-119200, Woodlands, Texas.

Appendix A

Methodology for calculating structural closure and CO_2 migration velocity

A cell A is structurally enclosed if, at the cell centre depth of cell A, there is a closed loop of top layer cells surrounding cell A and all cells within the loop have a depth deeper than cell A. To determine which cells satisfied this condition the algorithm below was applied. This was based upon a set of definitions:
topheight - the cell-centre depth of the cell at the top of a column. It is assigned to all cells within that column.
h - the cell-centre depth of a cell
o - the depth within a column, below which there is a direct horizontal flow path to the boundary without any top-surface in the way.
($fipstruc$=1) - Signifies that a cell is structurally closed or yet to be determined as open.
($fipstruc$=2) - Signifies that a cell is open and waiting to be used to determine whether neighbouring cells are open.
($fipstruc$=3) - Signifies that a cell is open and has currently passed on all its information about open paths to the boundary.

The algorithm requires that the grid has vertical columns. This is usual for most corner point geometries.

Algorithm for calculating structural closure

- Determine the cell centre height h of all cells within the model and for the cells at the top of each column of cells also set *topheight*.
- First it is assumed that all the cells at the boundary of the model are *not* structurally closed. Therefore set all the cells at the boundaries as open - we indicate this by setting $fipstruc = 2$.
- At the boundaries set the depth o equal to *topheight*. Therefore at all boundary

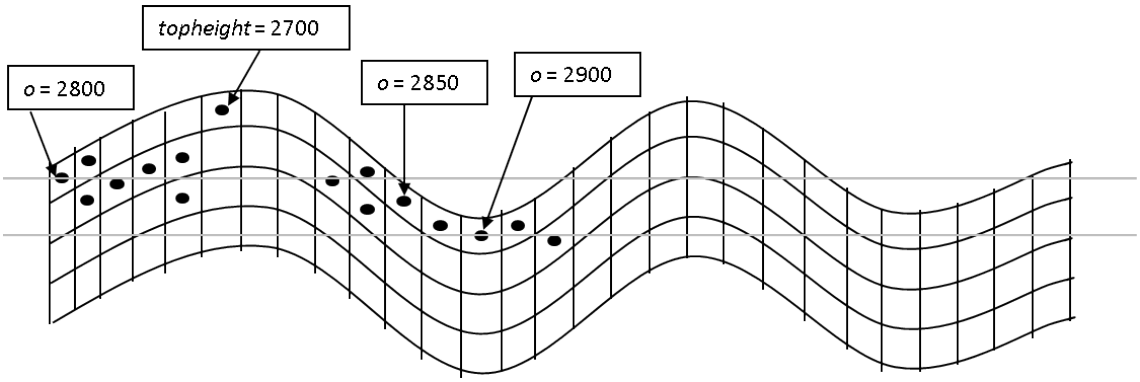


Figure A.1: Vertical cross-section through an example geocellular model.

cells o(boundary cell) = $topheight$(boundary cell). Initially o is not set inside the boundaries. We shall find o and $fipstruc$ for the internal cells next.

- Iterate through all cells in the model and when a cell has $fipstruc$=2 perform the next bullet-pointed step.
- Iterate through all the cells (the cell with $fipstruc$=2) perpendicular neighbours with the following algorithm to determine the $fipstruc$ of each neighbour. Also iterate through all cells in the neighbours column with the same algorithm. Do not iterate through aerially diagonal neighbours.
  - If $fipstruc$(neighbour) = 1 AND h(neighbour) $\geq$ o(selected cell)
    - Make $fipstruc$(neighbour)=2
    - If o(selected cell) $<$ $topheight$(neighbour)
      - Set o(neighbour)= $topheight$(neighbour)
    - If o(selected cell) $\geq$ $topheight$(neighbour)
      - Set o(neighbour)= o(selected cell)
  - If $fipstruc$(neighbour) = 2 or 3 AND o(neighbour) $>$ o(selected cell)
    - Make $fipstruc$(neighbour)=2
    - If o(selected cell) $<$ $topheight$(neighbour)
      - Set o(neighbour)= $topheight$(neighbour)
    - If o(selected cell) $\geq$ $topheight$(neighbour)
      - Set o(neighbour)= o(selected cell)
  - Set selected cell to fipstruc =3

- Repeat iterating through all cells in the model until only cells with $fipstruc$= 3 or 1 remain. At this point all cells are determined as either structurally open or closed.

Appendix B

Methodology for calculating CO_2 migration velocity

Methodology for measuring maximum speed of flow of CO_2

- We extracted the arrays FLOGASI+, FLOGASJ+, SGAS, PORV(rm^3) and GAS_DEN.
- The FLOGAS arrays give the flow between neighbour cells in the gas phase for the positive i,j directions with units sm^3/day.
  - We calculate the maximum horizontal speed of flow in the i and j directions by calculating Flogas×365×1.87272×400/porv×sgas×gas_den for each cell and then finding the maximum magnitude speed in cells with $S_g > 0.3$

Appendix C

Simulation results - Base case injection rates

Table C.1: Base case injection rates

Well	**1**	**2**	**4a**	**5**	**6**	**8a**	**9**	**10**	**11**	**12**	**13**	**All wells**
Mt CO_2 injected 2010 - 2020	16.1	12.1	14.3	19.0	13.2	14.0	14.8	13.9	11.7	12.2	10.9	152.4
Mt CO_2 injected 2020 - 2030	11.7	5.7	4.3	14.9	8.6	6.9	9.3	9.3	7.3	6.4	2.9	87.5
Mt CO_2 injected 2030 - 2040	11.2	5.3	3.4	14.3	7.8	6.4	8.0	8.9	7.2	6.1	2.4	80.9
Mt CO_2 injected 2040 - 2050	10.7	5.0	2.9	13.9	7.5	6.0	7.2	8.5	7.1	5.9	2.0	76.7
Mt CO_2 injected 2050 - 2060	10.2	4.8	2.6	13.6	7.2	5.7	6.4	8.1	6.9	5.7	1.8	73.1
Total injection (Mt)	59.9	32.9	27.5	75.8	44.3	39.0	45.7	48.7	40.2	36.4	20.1	470.5
Average rate (Mt/yr)	1.2	0.7	0.5	1.5	0.9	0.8	0.9	1.0	0.8	0.7	0.4	9.4

Appendix D

Simulation results - Sensitivity study storage data

Table D.1: Setup of optimised models

Simulation Name	Permeability and dip variation	Horizontal Permeability	Dip	Injection rate/ wells	Optimization notes
fine grid 59 (Base case)	Heterogeneous + Structure	11mD average	0.27° average	2Mt/yr per well	Wells positioned to avoid low injectivity regions
fine grid 60 (1733400 cell grid)	Heterogeneous + Structure	11mD average	0.27° average	2Mt/yr per well	Wells positioned to avoid low injectivity regions
fine grid 61b	Heterogeneous + Structure	145mD average	0.27° average	0.5Mt/yr per well	Uniform injection
fine grid 62b	Heterogeneous + Structure	1D average	0.27° average	0.25Mt/yr most wells, 0.1Mt/yr well 10 , well 11&6 shut	Wells closer to leakage routes reduced
fine grid 63c	Heterogeneous + Structure	11mD average	1° average	2Mt per well	Injecting as much as possible
fine grid 64a	Heterogeneous + Structure	11mD average	3° average	0.5Mt/yr per well	Uniform injection

Table D.2: Setup of optimised models

Simulation Name	Permeability and dip variation	Horizontal Permeability	Dip	Injection rate/ wells	Optimization notes
fine grid 100L	Homogeneous + Structure	145mD	0.27°	0.4Mt/yr most well, 0.25Mt/yr 6a and 10, wells 11,5 shut	Reducing well rates and keeping low rates near leakage points
fine grid 101d	Homogeneous + Structure	11mD	0.27°	2 Mt/yr per well	injecting as much as possible, injection limited
fine grid 102K	Homogeneous + Structure	1D	0.27°	0.25Mt/yr well 1,8,12. 0.1Mt/yr well 4,13. wells 2, 11,6, 5, 9 and 10 shut	reducing/stopping well 2 injection and varying injection at wells 1, 4 and 15
fine grid 103M	Homogeneous + Structure	145mD	1°	0.25Mt/yr wells 1,12,8, 2. 0.1Mt/yr wells 10,13. Wells 5,6,11, 4,9 shut	reduced wells 4,9,13, trying slightly more in well 2
fine grid 104j	Homogeneous + Structure	145mD	3°	0.1 Mt/yr wellls 1,2,8,10,9,4, 12. Others shut	turn wells 4 and 12 back on

Table D.3: Setup of optimised models

Simulation Name	Permeability and dip variation	Horizontal Permeability	Dip	Injection rate/ wells	Optimization notes
fine grid 200c	Homogeneous smooth	145mD	0.27°	1Mt/yr wells 2,4,13 . 0.5 Mt/yr other wells	extra injection in centre
fine grid 201a	Homogeneous smooth	11mD	0.27°	2 Mt per well	maximum injection
fine grid 202g	Homogeneous smooth	1D	0.27°	0.1 Mt/yr most wells. Wells 5,6,11, 8,13 shut	using wells that are further apart to avoid plumes connecting and causing faster speeds
fine grid 203e	Homogeneous smooth	145mD	1°	0.4Mt/yr most wells. Wells 5,6,11, 8 13 shut	using wells that are further apart to avoid plumes connecting and causing faster speeds, and reducing rate
fine grid 204f	Homogeneous smooth	145mD	3°	0.1Mt/yr most wells. Wells 5,6,11 shut	avoiding injection near NW boundary

Table D.4: Results from optimised models

Simulation Name	Storage efficiency (rm^3/rm^3)	Net pore volume of model (rm^3)	Total model net pore volume for whole forties (rm^3)	Pore volume within structural closures (rm^3)	rm^3 CO_2 injected (50 years)	sm^3 CO_2 injected (50 years)	Mt CO_2 injected (50 years)
fine grid 59 (Base case)	3.45E-02	2.03E+10	3.04E+11	1.80E+08	7.00E+08	2.51E+11	4.71E+02
fine grid 60 (1733400 cell grid)	3.93E-02	2.03E+10	3.04E+11	1.95E+08	7.96E+08	2.86E+11	5.36E+02
fine grid 61b	2.03E-02	2.03E+10	3.04E+11	1.80E+08	4.12E+08	1.47E+11	2.75E+02
fine grid 62b	7.81E-03	2.03E+10	3.04E+11	1.80E+08	1.58E+08	5.61E+10	1.05E+02
fine grid 63c	3.48E-02	1.83E+10	2.72E+11	1.10E+07	6.39E+08	2.28E+11	4.27E+02
fine grid 64a	2.19E-02	1.86E+10	2.70E+11	0.00E+00	4.06E+08	1.42E+11	2.66E+02
fine grid 100l	1.24E-02	2.03E+10	3.44E+11	1.72E+08	2.52E+08	8.94E+10	1.67E+02
fine grid 101d	5.53E-02	2.03E+10	3.44E+11	1.72E+08	1.12E+09	4.05E+11	7.59E+02
fine grid 102k	4.10E-03	2.03E+10	3.44E+11	1.72E+08	8.31E+07	2.94E+10	5.50E+01
fine grid 103m	4.96E-03	1.83E+10	3.09E+11	1.08E+07	9.09E+07	3.21E+10	6.00E+01
fine grid 104j	2.89E-03	1.85E+10	3.08E+11	0.00E+00	5.36E+07	1.87E+10	3.50E+01
fine grid 200c	2.60E-02	2.02E+10	3.59E+11	0.00E+00	5.26E+08	1.87E+11	3.50E+02
fine grid 201a	5.45E-02	2.02E+10	3.59E+11	0.00E+00	1.10E+09	3.96E+11	7.42E+02
fine grid 202g	2.26E-03	2.02E+10	3.59E+11	0.00E+00	4.56E+07	1.60E+10	3.00E+01
fine grid 203e	9.01E-03	2.02E+10	3.59E+11	0.00E+00	1.82E+08	6.41E+10	1.20E+02
fine grid 204f	3.03E-03	2.02E+10	3.59E+11	0.00E+00	6.14E+07	2.14E+10	4.00E+01

Table D.5: Results from optimised models

Simulation Name	Free CO_2 within structural traps (sm^3 @ 1000yrs)	Residually trapped CO_2 outside structural traps (sm^3 @ 1000yrs)	CO_2 dissolved (sm^3 @ 1000 years)	Low velocity CO_2 (sm^3 @1000 years)	CO_2 escaped into boundaries (sm^3 @ 1000yrs)
fine grid 59 (Base case)	5.88E+09	1.52E+11	4.90E+10	4.46E+10	8.67E+06
fine grid 60 (1733400 cell grid)	6.33E+09	1.80E+11	4.77E+10	5.21E+10	5.54E+06
fine grid 61b	1.67E+10	8.49E+10	3.36E+10	1.16E+10	2.18E+07
fine grid 62b	1.75E+10	1.94E+10	1.76E+10	1.62E+09	4.75E+06
fine grid 63c	7.51E+08	1.40E+11	4.45E+10	4.24E+10	1.01E+07
fine grid 64a	0.00E+00	8.80E+10	3.34E+10	2.06E+10	6.15E+04
fine grid 100l	2.54E+10	4.21E+10	1.89E+10	2.61E+09	3.83E+08
fine grid 101d	1.86E+10	2.51E+11	6.88E+10	6.65E+10	2.41E+03
fine grid 102k	1.61E+10	4.38E+09	8.55E+09	3.04E+08	1.12E+07
fine grid 103m	1.11E+09	2.01E+10	8.49E+09	2.30E+09	2.08E+07
fine grid 104j	0.00E+00	1.07E+10	7.79E+09	2.42E+08	0.00E+00
fine grid 200c	0.00E+00	1.12E+11	3.25E+10	4.28E+10	9.16E+07
fine grid 201a	0.00E+00	2.46E+11	6.62E+10	8.41E+10	7.95E+02
fine grid 202g	0.00E+00	7.05E+09	7.23E+09	1.74E+09	0.00E+00
fine grid 203e	0.00E+00	4.46E+10	1.55E+10	4.00E+09	0.00E+00
fine grid 204f	0.00E+00	1.15E+10	9.40E+09	3.37E+08	1.66E+08

Table D.6: Results from optimised models

Simulation Name	Free CO_2 within structural traps (Mt @ 1000yrs)	Residually trapped CO_2 outside structural traps (Mt @ 1000yrs)	CO_2 dissolved (Mt @ 1000 years)	Low velocity CO_2 (Mt @ 1000 years)	CO_2 escaped into boundaries (Mt @ 1000yrs)
fine grid 59 (Base case)	1.10E+01	2.84E+02	9.18E+01	8.36E+01	1.62E-02
fine grid 60 (1733400 cell grid)	1.19E+01	3.37E+02	8.93E+01	9.75E+01	1.04E-02
fine grid 61b	3.13E+01	1.59E+02	6.30E+01	2.17E+01	4.07E-02
fine grid 62b	3.28E+01	3.63E+01	3.29E+01	3.04E+00	8.90E-03
fine grid 63c	1.41E+00	2.63E+02	8.33E+01	7.93E+01	1.89E-02
fine grid 64a	0.00E+00	1.65E+02	6.26E+01	3.86E+01	1.15E-04
fine grid 100L	4.76E+01	7.88E+01	3.54E+01	4.89E+00	7.17E-01
fine grid 101d	3.49E+01	4.70E+02	1.29E+02	1.24E+02	4.51E-06
fine grid 102k	3.02E+01	8.21E+00	1.60E+01	5.70E-01	2.10E-02
fine grid 103m	2.09E+00	3.77E+01	1.59E+01	4.31E+00	3.90E-02
fine grid 104j	0.00E+00	2.00E+01	1.46E+01	4.53E-01	0.00E+00
fine grid 200c	0.00E+00	2.09E+02	6.09E+01	8.01E+01	1.72E-01
fine grid 201a	0.00E+00	4.60E+02	1.24E+02	1.58E+02	1.49E-06
fine grid 202g	0.00E+00	1.32E+01	1.35E+01	3.26E+00	0.00E+00
fine grid 203e	0.00E+00	8.35E+01	2.91E+01	7.49E+00	0.00E+00
fine grid 204f	0.00E+00	2.15E+01	1.76E+01	6.31E-01	3.12E-01

Table D.7: Results from optimised models

Simulation Name	% CO_2 free and structurally trapped (1000yrs)	% CO_2 Residually trapped outside structural traps (1000 years)	% CO_2 dissolved (1000 years)	% Low velocity CO_2 (1000 years)	% escaped (1000 years)	Max speed of CO_2 at 1000 years (m/year)
fine grid 59 (Base case)	2.34E-02	6.04E-01	1.95E-01	1.78E-01	3.45E-05	10.99 (only 3 cells over 10)
fine grid 60 (1733400 cell grid)	2.21E-02	6.29E-01	1.67E-01	1.82E-01	1.94E-05	22.1 (over in 26 cells, allow up to 40 on larger grid)
fine grid 61b	1.14E-01	5.78E-01	2.29E-01	7.89E-02	1.48E-04	22.7 (10 cells above 10)
fine grid 62b	3.12E-01	3.45E-01	3.13E-01	2.90E-02	8.47E-05	25.5 (over in 10 cells)
fine grid 63c	3.29E-03	6.16E-01	1.95E-01	1.86E-01	4.43E-05	3.76E+00
fine grid 64a	0.00E+00	6.20E-01	2.35E-01	1.45E-01	4.33E-07	8.86E+00
fine grid 100L	2.85E-01	4.70E-01	2.12E-01	2.92E-02	4.28E-03	12.3 (10 cells above 10)
fine grid 101d	4.60E-02	6.20E-01	1.70E-01	1.64E-01	5.94E-09	4.05E+00
fine grid 102k	5.49E-01	1.49E-01	2.91E-01	1.04E-02	3.82E-04	13.5 (5 cells over)
fine grid 103m	3.47E-02	6.28E-01	2.65E-01	7.17E-02	6.49E-04	18.3 (9 over in j direction)
fine grid 104j	0.00E+00	5.70E-01	4.17E-01	1.29E-02	0.00E+00	13.7 (3 cells over 10)
fine grid 200c	0.00E+00	5.97E-01	1.74E-01	2.29E-01	4.90E-04	5.50E+00
fine grid 201a	0.00E+00	6.20E-01	1.67E-01	2.12E-01	2.01E-09	1.96E+00
fine grid 202g	0.00E+00	4.40E-01	4.51E-01	1.09E-01	0.00E+00	1.76E+00
fine grid 203e	0.00E+00	6.96E-01	2.42E-01	6.24E-02	0.00E+00	10.3 (over 10 in 2cells)
fine grid 204f	0.00E+00	5.37E-01	4.40E-01	1.58E-02	7.79E-03	13.0 (6cells over)

Table D.8: Results from optimised models

Simulation Name	Free CO_2 within structural traps (sm3 @ 10000yrs)	Residually trapped CO_2 outside structural traps (sm3 @ 10000yrs)	CO_2 dissolved (sm3 @ 10000 years)	Low velocity CO_2 (sm3 @10000 years)	CO_2 escaped into boundaries (sm3 @ 10000yrs)
fine grid 59 (Base case)	1.18E+10	1.63E+11	5.80E+10	1.87E+10	1.77E+07
fine grid 60 (1733400 cell grid)	1.46E+10	1.92E+11	5.93E+10	1.99E+10	2.02E+08

Table D.9: Results from optimised models

Simulation Name	CO_2 within structural traps (Mt @ 10000yrs)	Residually trapped CO_2 outside structural traps (Mt @ 10000yrs)	CO_2 dissolved (Mt @ 10000 years)	Low velocity CO_2 (Mt @ 10000 years)	CO_2 escaped into boundaries (Mt @ 10000yrs)
fine grid 59 (Base case)	2.21E+01	3.05E+02	1.09E+02	3.50E+01	3.31E-02
fine grid 60 (1733400 cell grid)	2.73E+01	3.60E+02	1.11E+02	3.74E+01	3.78E-01

Table D.10: Results from optimised models

Simulation Name	% CO_2 free and structurally trapped (10000yrs)	% CO_2 Residually trapped outside structural traps (10000 years)	% CO_2 dissolved (10000 years)	% Low velocity CO_2 (10000 years)	% escaped (10000 years)	Max speed of CO_2 at 10000 years (m/year)
fine grid 59 (Base case)	4.69E-02	6.48E-01	2.31E-01	7.43E-02	7.03E-05	1.92E+00
fine grid 60 (1733400 cell grid)	5.08E-02	6.72E-01	2.07E-01	6.97E-02	7.05E-04	3.35E+00

Appendix E

Simulation results - Simulation runs used for capacity optimisation

Table E.1: Setup of models tested during optimisation

Simulation Name	Dip and permeability variation	Horizontal Permeability	Dip (degrees)
fine grid 59	Heterogeneous + structure	11mD average	0.27° average
fine grid 60 (1733400 cells)	Heterogeneous + structure	11mD average	0.27° average
fine grid 61a	Heterogeneous + structure	145mD average	0.27° average
fine grid 61b	Heterogeneous + structure	145mD average	0.27° average
fine grid 61c	Heterogeneous + structure	145mD average	0.27° average
fine grid 61d	Heterogeneous + structure	145mD average	0.27° average
fine grid 61e	Heterogeneous + structure	145mD average	0.27° average
fine grid 61f	Heterogeneous + structure	145mD average	0.27° average
fine grid 62a	Heterogeneous + structure	1D average	0.27° average
fine grid 62b	Heterogeneous + structure	1D average	0.27° average
fine grid 62c	Heterogeneous + structure	1D average	0.27° average
fine grid 62e	Heterogeneous + structure	1D average	0.27° average
fine grid 62f	Heterogeneous + structure	1D average	0.27° average
fine grid 62g	Heterogeneous + structure	1D average	0.27° average
fine grid 63c	Heterogeneous + structure	11mD average	1° average
fine grid 64a	Heterogeneous + structure	11mD average	3° average
fine grid 64b	Heterogeneous + structure	11mD average	3° average
fine grid 64c	Heterogeneous + structure	11mD average	3° average
fine grid 64f	Heterogeneous + structure	11mD average	3° average

Table E.2: Setup of models tested during optimisation

Simulation Name	Dip and permeability variation	Horizontal Permeability	Dip (degrees)
fine grid 100a	Homogeneous + structure	145mD	0.27° average
fine grid 100b	Homogeneous + structure	145mD	0.27° average
fine grid 100c	Homogeneous + structure	145mD	0.27° average
fine grid 100d	Homogeneous + structure	145mD	0.27° average
fine grid 100e	Homogeneous + structure	145mD	0.27° average
fine grid 100g	Homogeneous + structure	145mD	0.27° average
fine grid 100i	Homogeneous + structure	145mD	0.27° average
fine grid 100j	Homogeneous + structure	145mD	0.27° average
fine grid 100k	Homogeneous + structure	145mD	0.27° average
fine grid 100L	Homogeneous + structure	145mD	0.27° average
fine grid 100M	Homogeneous + structure	145mD	0.27° average
fine grid 101a	Homogeneous + structure	11mD	0.27° average
fine grid 101d	Homogeneous + structure	11mD	0.27° average
fine grid 102a	Homogeneous + structure	1D	0.27° average
fine grid 102b	Homogeneous + structure	1D	0.27° average
fine grid 102e	Homogeneous + structure	1D	0.27° average
fine grid 102f	Homogeneous + structure	1D	0.27° average
fine grid 102g	Homogeneous + structure	1D	0.27° average
fine grid 102h	Homogeneous + structure	1D	0.27° average
fine grid 102I	Homogeneous + structure	1D	0.27° average
fine grid 102J	Homogeneous + structure	1D	0.27° average
fine grid 102K	Homogeneous + structure	1D	0.27° average
fine grid 102L	Homogeneous + structure	1D	0.27° average
fine grid 103a	Homogeneous + structure	145mD	1° average
fine grid 103b	Homogeneous + structure	145mD	1° average
fine grid 103c	Homogeneous + structure	145mD	1° average
fine grid 103d	Homogeneous + structure	145mD	1° average
fine grid 103e	Homogeneous + structure	145mD	1° average
fine grid 103f	Homogeneous + structure	145mD	1° average
fine grid 103j	Homogeneous + structure	145mD	1° average
fine grid 103k	Homogeneous + structure	145mD	1° average
fine grid 103L	Homogeneous + structure	145mD	1° average
fine grid 103M	Homogeneous + structure	145mD	1° average
fine grid 104b	Homogeneous + structure	145mD	3° average
fine grid 104c	Homogeneous + structure	145mD	3° average
fine grid 104d	Homogeneous + structure	145mD	3° average
fine grid 104e	Homogeneous + structure	145mD	3° average
fine grid 104f	Homogeneous + structure	145mD	3° average
fine grid 104g	Homogeneous + structure	145mD	3° average
fine grid 104h	Homogeneous + structure	145mD	3° average
fine grid 104i	Homogeneous + structure	145mD	3° average

Table E.3: Setup of models tested during optimisation

Simulation Name	Dip and permeability variation	Horizontal Permeability	Dip (degrees)
fine grid 200a	Homogeneous smooth	145mD	0.27°
fine grid 200c	Homogeneous smooth	145mD	0.27°
fine grid 201a	Homogeneous smooth	11mD	0.27°
fine grid 202a	Homogeneous smooth	1D	0.27°
fine grid 202b	Homogeneous smooth	1D	0.27°
fine grid 202c	Homogeneous smooth	1D	0.27°
fine grid 202d	Homogeneous smooth	1D	0.27°
fine grid 202e	Homogeneous smooth	1D	0.27°
fine grid 202g	Homogeneous smooth	1D	0.27°
fine grid 203a	Homogeneous smooth	145mD	1°
fine grid 203b	Homogeneous smooth	145mD	1°
fine grid 203c	Homogeneous smooth	145mD	1°
fine grid 203d	Homogeneous smooth	145mD	1°
fine grid 203e	Homogeneous smooth	145mD	1°
fine grid 204a	Homogeneous smooth	145mD	3°
fine grid 204b	Homogeneous smooth	145mD	3°
fine grid 204d	Homogeneous smooth	145mD	3°
fine grid 204e	Homogeneous smooth	145mD	3°
fine grid 204f	Homogeneous smooth	145mD	3°

Table E.4: Notes on models tested during optimisation

Simulation Name	Injection rate/ wells	Optimisation notes
fine grid 59	Attempted 2Mt/yr	All wells positioned to avoid low injectivity regions
fine grid 60	Attempted 2Mt/yr	
fine grid 61a	0.25 Mt per well	Uniform injection at different rates
fine grid 61b	0.5 Mt per well	Uniform injection at different rates
fine grid 61c	1 Mt per well	Uniform injection at different rates
fine grid 61d	0.5 Mt per well, 6a and 10 0.25Mt 11 shut	Wells closer to leakage routes reduced
fine grid 61e	1Mt well 2, 4 13 0.5 Mt per well, 6a and 10 0.25Mt 11 shut	Attempting to inject more around structurally secure areas
fine grid 61f	0.75 Mt per well, 6a and 10 0.25Mt 11,5 shut	Trying to maximise rate in majority of wells, up from 0.5 Mt
fine grid 62a	0.1 Mt per well	Uniform low injection
fine grid 62b	0.25 Mt per well, well 11&6 off, 0.1Mt/yr well 10	Wells closer to leakage routes reduced
fine grid 62c	0.5 Mt per well 1,2,4,13 0.25Mt per well 5,8,9,12 0.1Mt well 10 well 11&6 off	increasing injection in more secure regions
fine grid 62e	0.25 Mt per well, well 11,6 and 5 off, 0.1Mt/yr well 10	just turning well 5 off after 62b
fine grid 62f	0.25 well 2,4,13 0.1 Mt per well well 5,6,11,10,9 off	cautious case
fine grid 62g	0.1 Mt per well well 5,6,11,10,9 off	cautious case
fine grid 63c	2 Mt per well	injecting as much as possible, injection limited
fine grid 64a	0.5 Mt per well	Uniform injection at different rates
fine grid 64b	0.25 Mt per well	Uniform injection at different rates
fine grid 64c	0.1 Mt per well	Uniform injection at different rates
fine grid 64f	0.75 Mt per well	Uniform injection at different rates

Table E.5: Notes on models tested during optimisation

Simulation Name	Injection rate/ wells	Optimisation notes
Fine grid 100a	0.5 Mt per well, 10 6a and 11 0.25Mt	wells closer to leakage routes reduced
fine grid 100b	1 Mt per well	uniform injection
fine grid 100c	0.25 Mt per well	uniform injection
fine grid 100d	0.5 Mt per well, 6a and 10 0.25Mt 11 shut	wells closer to leakage routes reduced
fine grid 100e	1Mt well 2 0.5 Mt per well, 6a and 10 0.25Mt 11 shut	variety of higher central injection strategies
fine grid 100g	1Mt well 2, 13 0.5 Mt per well, 6a and 10 0.25Mt 11 shut	variety of higher central injection strategies
fine grid 100i	1Mt well 2, 4 13 0.5 Mt per well, 6a and 10 0.25Mt 11,5 shut	variety of higher central injection strategies
fine grid 100j	0.4 Mt per well, 6a and 10 and 5 0.25Mt 11 shut	reducing well rates and keeping low rates near leakage points
fine grid 100k	0.5 Mt per well, 6a and 10 0.25Mt 11,5 shut	reducing well rates and keeping low rates near leakage points
fine grid 100L	0.4 Mt per well, 6a and 10 0.25Mt 11,5 shut	reducing well rates and keeping low rates near leakage points
fine grid 100M	0.3 Mt per well, 6a and 10 0.25Mt 11,5 shut	reducing well rates and keeping low rates near leakage points
fine grid 101a	1.5 Mt per well	injecting as much as possible, injection limited
fine grid 101d	2 Mt per well	injecting as much as possible, injection limited
fine grid 102a	0.1 Mt per well	2/3 leaked from NW boundary , 1/3 from NE boundary
fine grid 102b	0.25 Mt per well, well 11&6 off, 0.1Mt/yr well 10	3/4 leaked from NW boundary, 1/4 from NE boundary
fine grid 102e	0.25 Mt per well, well 11,6, 5, 9 and 10 off well 2, 4,13 0.1Mt	CO_2 from well 2 still moving, stopping this should make case acceptable
fine grid 102f	0.25 Mt per well, well 11,6, 5, 9 and 10 off well 2 - 0.1 Mt	CO_2 from well 2 still moving
fine grid 102g	0.25 Mt per well, well 11,6 and 5 off, 0.1Mt/yr well 10	this is the case in 62, CO_2 from well 2 still moving
fine grid 102h	0.1 Mt per well 5,6,11, 8,13 off	this is the case in 202, CO_2 from well 2 still moving
fine grid 102I	well 4,13,1,8,12 0.25 Mt well 2, 11,6, 5, 9 and 10 off	reducing/stopping well 2 injection and varying injection at wells 1, 4 and 13
fine grid 102J	well 13, 1,8,12 0.25 Mt well 2, 11,6, 5, 9 and 10 off well 4 0.1Mt	reducing/stopping well 2 injection and varying injection at wells 1, 4 and 14
fine grid 102K	well 1,8,12 0.25 Mt well 2, 11,6, 5, 9 and 10 off well 4,13 0.1Mt	reducing/stopping well 2 injection and varying injection at wells 1, 4 and 15
fine grid 102L	well 8,12 0.25 Mt well 2, 11,6, 5, 9 and 10 off well 1,4,13 0.1Mt	reducing/stopping well 2 injection and varying injection at wells 1, 4 and 16

Table E.6: Notes on models tested during optimisation

Simulation Name	Injection rate/ wells	Optimisation notes
fine grid 103a	1 Mt per well 5,6,11 off	no NW leakage
fine grid 103b	0.5 Mt per well	significant NW boundary release, too much out of side
fine grid 103c	0.25 Mt per well	significant NW boundary release, almost too much out of side
fine grid 103d	0.1 Mt per well	significant NW boundary release
fine grid 103e	0.5Mt 2,13,12,8 1 - 0.25Mt 10 0.1Mt 5,6,11, 4,9 off	5,6,11 off in all since even the 0.1Mt showed leak with these on
fine grid 103f	0.5Mt 2,12,13,8 4,9,1 - 0.25Mt 10 0.1Mt 5,6,11, off	5,6,11 off in all since even the 0.1Mt showed leak with these on
fine grid 103j	0.5Mt 12,8 1,2 - 0.25Mt 10 13 0.1Mt 5,6,11, 4,9 off	reduce wells 2, 4, 9 and 13
fine grid 103k	0.5Mt 12,8 1 - 0.25Mt 10 13, 2 0.1Mt 5,6,11, 4,9 off	reduce wells 2, 4, 9 and 13
fine grid 103L	1,12,8 - 0.25Mt 10 13, 2 0.1Mt 5,6,11, 4,9 off	reduce wells 2, 4, 9 and 13
fine grid 103M	1,12,8, 2 - 0.25Mt 10, 13 0.1Mt 5,6,11, 4,9 off	trying slightly more in well 2
fine grid 104b	0.25 Mt per well	uniform injection
fine grid 104c	0.1 Mt per well	uniform injection
fine grid 104d	0.5 Mt per well Only wells 1,2,8,10,13 open	injection with larger well spacing to reduce flow speeds
fine grid 104e	0.25 Mt per well Only wells 1,2,8,10,13 open	injection with larger well spacing to reduce flow speeds
fine grid 104f	0.1 Mt per well Only wells 1,2,8,10,13 open	injection with larger well spacing to reduce flow speeds
fine grid 104g	0.4 Mt per well Only wells 1,2,8,10,13 open	injection with larger well spacing to reduce flow speeds
fine grid 104h	0.1 Mt per well Only wells 1,2,8,10,9 open	we turn 13 off and 9 on since the CO_2 from 2 connects with CO_2 from 13
fine grid 104i	0.2 Mt per well Only wells 1,2,8,10,9 open	we turn 13 off and 9 on since the CO_2 from 2 connects with CO_2 from 14

Table E.7: Notes on models tested during optimisation

Simulation Name	Injection rate/ wells	Optimisation notes
fine grid 200a	0.5Mt per well	uniform injection
fine grid 200c	1 Mt per well 2,4,13 0.5 Mt per well	extra injection in centre
fine grid 201a	2 Mt per well	maximum injection
fine grid 202a	0.1 Mt per well	uniform injection
fine grid 202b	0.25 Mt per well	uniform injection
fine grid 202c	0.1 Mt per well 5,6,11 off	reducing wells near NW boundary
fine grid 202d	0.25 Mt per well, 5,6,11 off	reducing wells near NW boundary
fine grid 202e	0.1 Mt per well 5,6,11 off 2,4,13 0.25Mt	reducing wells near NW boundary, keeping some extra central injection
fine grid 202g	0.1 Mt per well 5,6,11, 8,13 off	using wells that are further apart to avoid plumes connecting and causing faster speeds
fine grid 203a	0.5Mt all wells	uniform injection
fine grid 203b	0.5Mt most 5,6,11, off	reducing wells near NW boundary
fine grid 203c	0.5Mt most 5,6,11, 8 13 off	using wells that are further apart to avoid plumes connecting and causing faster speeds
fine grid 203d	0.4Mt most 5,6,11, off	reducing wells near NW boundary and reducing rate
fine grid 203e	0.4Mt most 5,6,11, 8 13 off	using wells that are further apart to avoid plumes connecting and causing faster speeds, and reducing rate
fine grid 204a	0.1 Mt per well Only wells 1,2,8,10,13 open	avoiding injection near NW boundary
fine grid 204b	0.2 Mt per well Only wells 1,2,8,10,13 open	avoiding injection near NW boundary
fine grid 204d	0.2Mt most 5,6,11, 8 13 off	keeping plumes separated and avoiding injection near NW boundary
fine grid 204e	0.1Mt most 5,6,11, 8 13 off	keeping plumes separated and avoiding injection near NW boundary
fine grid 204f	0.1Mt most 5,6,11 off	avoiding injection near NW boundary

Table E.8: Results of models tested during optimisation

Simulation Name	Storage efficiency (rm^3/rm^3)	% escaped (1000 years)	Max speed of CO_2 at 1000 years (m/year)
fine grid 59	3.45E-02	3.45E-05	10.99 (only 3 cells over 10)
fine grid 60	3.93E-02	1.94E-05	22.1 (over in 26 cells, allow up to 40 on larger grid)
fine grid 61a	1.02E-02	1.13E-09	14.5(4 cells above 10)
fine grid 61b	2.03E-02	1.48E-04	22.7 (10 cells above 10)
fine grid 61c	4.02E-02	4.22E-03	27.8 (43 cells over 10)
fine grid 61d	1.67E-02	4.65E-07	22.8 (9 cells over 10)
fine grid 61e	2.21E-02	1.49E-06	30.9 (24 cells over 10)
fine grid 61f	2.12E-02	2.70E-05	27.8 (13 cells over 10)
fine grid 62a	4.10E-03	1.81E-03	2.78E+01
fine grid 62b	7.81E-03	8.47E-05	25.5 (over in 10 cells)
fine grid 62c	1.15E-02	2.23E-06	22.8 (over in 24)
fine grid 62e	6.89E-03	8.10E-11	16.8 (8 cells over 10)
fine grid 62f	3.91E-03	0.00E+00	
fine grid 62g	2.24E-03	0.00E+00	
fine grid 63c	3.48E-02	4.43E-05	3.76E+00
fine grid 64a	2.19E-02	4.33E-07	8.86E+00
fine grid 64b			6.27E+00
fine grid 64c			3.76E+00
fine grid 64f	2.80E-02	1.55E-06	1.70E+01

Table E.9: Results of models tested during optimisation

Simulation Name	Storage efficiency (rm^3/rm^3)	% escaped (1000 years)	Max speed of CO_2 at 1000 years (m/year)
Fine grid 100a	1.76E-02	1.23E-02	14.6 (37 cells above 10)
fine grid 100b	4.03E-02	5.58E-02	
fine grid 100c	1.02E-02	1.43E-02	1.41E+01
fine grid 100d	1.67E-02	5.13E-03	14.3 (33 cells over 10)
fine grid 100e	1.85E-02	4.58E-03	18.6 (too many over 10)
fine grid 100g	2.03E-02	4.06E-03	18.5 (too many over 10)
fine grid 100i	2.03E-02	2.76E-03	18.3 (too many over 10)
fine grid 100j	1.33E-02	3.96E-03	12.2 (13 cells 10)
fine grid 100k	1.48E-02	3.87E-03	14.2 (21 over 10 in j direction)
fine grid 100L	1.24E-02	4.28E-03	12.3 (10 cells above 10)
fine grid 100M	9.80E-03	5.48E-03	10.7 (2 over 10)
fine grid 101a	5.15E-02	0.00E+00	3.75E+00
fine grid 101d	5.53E-02	5.94E-09	4.05E+00
fine grid 102a	4.10E-03	3.69E-02	11.0 (over in 2)
fine grid 102b	7.81E-03	2.22E-02	82.8 (over in 100)
fine grid 102e	3.91E-03	3.70E-04	23.7 (22 over 10, away from edges)
fine grid 102f	5.03E-03	3.44E-04	40.6 (over in 43)
fine grid 102g			8.29E+01
fine grid 102h	2.24E-03	2.10E-02	8.19E+00
fine grid 102I			38 (over in 22)
fine grid 102J	4.10E-03	3.82E-04	13.5 (5 cells over)
fine grid 102K	3.54E-03	4.02E-04	13.5 (4 cells over)
fine grid 102L	2.98E-03	4.70E-04	
fine grid 103a	3.26E-02	5.11E-02	
fine grid 103b	2.25E-02	4.97E-02	
fine grid 103c	1.13E-02	2.49E-02	1.63E+01
fine grid 103d	4.55E-03	1.03E-02	1.12E+01
fine grid 103e	9.69E-03	5.20E-04	16.4 (many over)
fine grid 103f	1.17E-02	4.38E-04	17.0 (many over)
fine grid 103j	7.02E-03	0.00E+00	14.4 (38 above 10)
fine grid 103k	6.40E-03	0.00E+00	18.5 (17 above 10)
fine grid 103L	4.34E-03	7.73E-04	18.3 (2 above 10 in i direction)
fine grid 103M	4.96E-03	6.49E-04	18.3 (9 over in j direction)
fine grid 104b	1.13E-02	9.36E-02	
fine grid 104c	4.54E-03	4.08E-02	
fine grid 104d	1.03E-02	1.11E-02	
fine grid 104e	5.16E-03	1.38E-03	3.43E+01
fine grid 104f	2.07E-03	0.00E+00	13.8 (11 cells over 10m/year)
fine grid 104g	8.24E-03	6.97E-03	3.50E+01
fine grid 104h	2.07E-03	0.00E+00	5.03E+00
fine grid 104i	4.13E-03	2.28E-04	14.4 (14 cells over)

Table E.10: Results of models tested during optimisation

Simulation Name	Storage efficiency (rm^3/rm^3)	% escaped (1000 years)	Max speed of CO_2 at 1000 years (m/year)
fine grid 200a	2.05E-02	4.43E-04	5.98E+00
fine grid 200c	2.60E-02	4.90E-04	5.50E+00
fine grid 201a	5.45E-02	2.01E-09	1.96E+00
fine grid 202a			13.7 (over 10 in loads of cells)
fine grid 202b	0.00E+00		20.2 (over 10 in loads of cells)
fine grid 202c	3.01E-03		11.7 (over 10 in loads of cells)
fine grid 202d			21.9 (over 10 in loads of cells)
fine grid 202e	0.00E+00		15.1 (over 10 in loads of cells)
fine grid 202g	2.26E-03	0.00E+00	1.76E+00
fine grid 203a	2.05E-02	5.71E-02	
fine grid 203b	1.50E-02	9.81E-05	1.71E+01
fine grid 203c	1.13E-02	1.19E-08	11.1 (over in 24)
fine grid 203d	1.20E-02	0.00E+00	1.47E+01
fine grid 203e	9.01E-03	0.00E+00	10.3 (over 10 in 2cells)
fine grid 204a	1.90E-03	0.00E+00	4.41E+00
fine grid 204b	3.79E-03	0.00E+00	2.04E+01
fine grid 204d	4.55E-03	1.39E-02	2.22E+01
fine grid 204e	2.28E-03	2.81E-03	3.73E+00
fine grid 204f	3.03E-03	7.79E-03	13.0 (6cells over)

Appendix F

ECLIPSE input file for the base case

RUNSPEC
TITLE
LARGE OPEN DIPPING AQUIFER MODEL HORIZONTAL WELL

DIMENS
107 180 90 /

TABDIMS
2 1 25 500 2 55 /

REGDIMS
6 3 /

–NOSIM

WELLDIMS
15 20 15/

VFPIDIMS
10 20 1 /

OIL – Water present
GAS – CO2 present
DISGAS
VAPOIL

SATOPTS
HYSTER /

UNIFOUT

METRIC

START
1 'JAN' 2010 /

MESSAGES
2* 100000 100000 4* 1000000 1000000 2* /

–PARALLEL
–2 DISTRIBUTED /

EXTRAPMS
4 /

NSTACK
20 /

FMTOUT

GRID

NOECHO

GRIDFILE
0 1 /

INIT

INCLUDE
'../INCLUDES/GRID-fine/Base_case_fine_GRID.inc' /

INCLUDE
'../INCLUDES/GRID-fine/Perm.inc' /

```
INCLUDE
'../INCLUDES/GRID-fine/Porosity.inc' /

COPY
PERMX PERMY /
PERMX PERMZ /
/

—-EQUALS
—- 'PORO' 0.24 /
—- 'PERMY' 150 /
—- 'PERMX' 15 /
—- 'PERMZ' 1.5 / kv:kh of 0.01
—- 'NTG' 1 /
—-/


BOX
– I1 I2 J1 J2 K1 K2
1 107 180 180 1 90 /
MULTPV
9630*900 /


BOX
– I1 I2 J1 J2 K1 K2
1 107 1 1 1 90 /
MULTPV
9630*1080 /

BOX
– I1 I2 J1 J2 K1 K2
107 107 1 180 1 90 /
MULTPV
16200*135 /
```

BOX
– I1 I2 J1 J2 K1 K2
1 1 1 180 1 90 /
MULTPV
16200*450 /

ENDBOX

COARSEN
– I1 I2 J1 J2 K1 K2 NX NY NZ
3 106 2 179 1 90 52 89 90 /
1 2 2 179 1 90 2 89 90 /
107 107 2 179 1 90 1 89 90 /
3 106 1 1 1 90 52 1 90 /
3 106 180 180 1 90 52 1 90 /
/

–grid sensitivity
–COARSEN
–3 106 92 179 1 90 8 8 5 /
–55 106 2 91 1 90 4 9 5 /
–/

PROPS

– Relative permeaiblity and capillary pressure

– Dataset taken from SPE Paper 99326
– Supercritical CO2 and H2S - Brine Drainage and imbibition relative permeability relationships for
– intergranular sandstone and carbonate formations - Bennion and Bachu

– In a black oil representation model - WATER IS MODELLED AS OIL
– This Dataset includes the correction

– Water saturation functions
SOF2
– Sw Krw
– —— ——
0.0000 0.0000 – Data line not originally published but included for Eclipse compatibility
0.4230 0
0.4520 0.0059
0.4810 0.019
0.5100 0.038
0.5380 0.0622
0.5670 0.0912
0.5960 0.1248
0.6250 0.1628
0.6540 0.205
0.6830 0.2512
0.7110 0.3014
0.7400 0.3553
0.7690 0.413
0.7980 0.4743
0.8270 0.5392
0.8560 0.6076
0.8850 0.6794
0.9130 0.7546
0.9420 0.8332
0.9710 0.915
1.0000 1
/

– imbibition data
0.0000 0.0000 – Data line not originally published but included for Eclipse compatibility
0.4230 0
0.4370 0.001
0.4510 0.0036
0.4650 0.0079

0.4790 0.0141
0.4930 0.022
0.5070 0.0317
0.5210 0.0432
0.5350 0.0566
0.5490 0.0719
0.5630 0.089
0.5770 0.108
0.5910 0.1288
0.6050 0.1516
0.6190 0.1763
0.6330 0.2029
0.6470 0.2314
0.6610 0.2618
0.6750 0.2941
0.6890 0.3284
0.7030 0.3646
1.0000 1
/

– Gas saturation functions
SGFN
– Sg Krg Drain Pcog (bars)
– —— —— ———-
0.000 0 0.1432
0.029 0.0002 0.1732
0.058 0.0006 0.1916
0.087 0.0015 0.2013
0.115 0.0031 0.2104
0.144 0.0055 0.2141
0.173 0.009 0.2141
0.202 0.0138 0.2141
0.231 0.0199 0.222
0.260 0.0276 0.23
0.289 0.037 0.2349
0.317 0.0484 0.235

0.346 0.0619 0.2629
0.375 0.0776 0.2659
0.404 0.0957 0.2918
0.433 0.1163 0.3004
0.462 0.1398 0.33
0.490 0.166 0.3576
0.519 0.1954 0.4132
0.548 0.2279 0.466
0.577 0.2638 0.5775
1.000 1.0000 0.5776 – Data line not originally published but included for Eclipse compatibility
/

– imbibition data (no imbibition capillary pressure data available)
0.000 0.0000 0
0.297 0.0000 0
0.311 0.0001 0
0.325 0.0003 0
0.339 0.0005 0
0.353 0.0009 0
0.367 0.0017 0
0.381 0.0029 0
0.395 0.0048 0
0.409 0.0077 0
0.423 0.0119 0
0.437 0.0176 0
0.451 0.0253 0
0.465 0.0354 0
0.479 0.0483 0
0.493 0.0645 0
0.507 0.0846 0
0.521 0.1091 0
0.535 0.1386 0
0.549 0.1737 0
0.563 0.2152 0
0.577 0.2638 0
1.000 1.0000 0 – Data line not originally published but included for Eclipse compatibility

/

– Carlson model for rel perms only
EHYSTR
1* 1 2* KR /

ROCK
318.68 4.89E-5 /

– PVT PROPERTIES

–ECLIPSE 100 PVT Data for simulation of CO2 Sequestration
————————————————————-
–
–METRIC UNITS USED
–
–Temperature 105 degC
–Salinity 100000 ppm
–
–Psc = 101325 Pa
–Tsc = 15 degC
–
DENSITY
–Water (kg/m3) N/A CO2 (kg/m3)
1067.272805 1000.000000 1.872720
/
PVTO
– Rs (sm3/sm3) P (bars) Bo(rm3/sm3) Vo (cp)
0.000000 1.000000 1.041708 0.334555
2.000000 1.041365 0.334588
5.000000 1.041232 0.334690
10.000000 1.041009 0.334860
15.000000 1.040787 0.335030
20.000000 1.040565 0.335200

25.000000 1.040343 0.335369
30.000000 1.040120 0.335539
35.000000 1.039898 0.335709
40.000000 1.039676 0.335878
45.000000 1.039454 0.336048
50.000000 1.039231 0.336217
55.000000 1.039009 0.336386
60.000000 1.038787 0.336555
65.000000 1.038565 0.336725
70.000000 1.038342 0.336894
75.000000 1.038120 0.337063
80.000000 1.037898 0.337232
85.000000 1.037676 0.337401
90.000000 1.037453 0.337570
95.000000 1.037231 0.337738
100.000000 1.037009 0.337907
110.000000 1.036564 0.338244
120.000000 1.036120 0.338582
130.000000 1.035675 0.338918
140.000000 1.035231 0.339255
150.000000 1.034786 0.339591
160.000000 1.034342 0.339928
170.000000 1.033897 0.340264
180.000000 1.033453 0.340600
190.000000 1.033008 0.340935
200.000000 1.032564 0.341271
220.000000 1.031675 0.341941
240.000000 1.030786 0.342611
260.000000 1.029897 0.343280
280.000000 1.029008 0.343949
300.000000 1.028119 0.344617
320.000000 1.027230 0.345284
340.000000 1.026341 0.345951
360.000000 1.025452 0.346618
380.000000 1.024563 0.347284
400.000000 1.023674 0.347950
420.000000 1.022785 0.348615

440.000000 1.021896 0.349280
460.000000 1.021007 0.349945
480.000000 1.020118 0.350610
500.000000 1.019229 0.351274
520.000000 1.018340 0.351939
540.000000 1.017451 0.352603
560.000000 1.016562 0.353267
580.000000 1.015673 0.353931
600.000000 1.014784 0.354595 /
0.154134 2.000000 1.041604 0.334588 /
0.692162 5.000000 1.042307 0.334690 /
1.552965 10.000000 1.043422 0.334860 /
2.376258 15.000000 1.044478 0.335030 /
3.166608 20.000000 1.045484 0.335200 /
3.926954 25.000000 1.046443 0.335369 /
4.661676 30.000000 1.047362 0.335539 /
5.368659 35.000000 1.048238 0.335709 /
6.048669 40.000000 1.049072 0.335878
45.000000 1.048850 0.336048
50.000000 1.048627 0.336217
55.000000 1.048405 0.336386
60.000000 1.048183 0.336555
65.000000 1.047961 0.336725
70.000000 1.047738 0.336894
75.000000 1.047516 0.337063
80.000000 1.047294 0.337232
85.000000 1.047072 0.337401
90.000000 1.046849 0.337570
95.000000 1.046627 0.337738
100.000000 1.046405 0.337907
110.000000 1.045960 0.338244
120.000000 1.045516 0.338582
130.000000 1.045071 0.338918
140.000000 1.044627 0.339255
150.000000 1.044182 0.339591
160.000000 1.043738 0.339928
170.000000 1.043293 0.340264

180.000000 1.042849 0.340600
190.000000 1.042404 0.340935
200.000000 1.041960 0.341271
220.000000 1.041071 0.341941
240.000000 1.040182 0.342611
260.000000 1.039293 0.343280
280.000000 1.038404 0.343949
300.000000 1.037515 0.344617
320.000000 1.036626 0.345284
340.000000 1.035737 0.345951
360.000000 1.034848 0.346618
380.000000 1.033959 0.347284
400.000000 1.033070 0.347950
420.000000 1.032181 0.348615
440.000000 1.031292 0.349280
460.000000 1.030403 0.349945
480.000000 1.029514 0.350610
500.000000 1.028625 0.351274
520.000000 1.027736 0.351939
540.000000 1.026847 0.352603
560.000000 1.025958 0.353267
580.000000 1.025069 0.353931
600.000000 1.024180 0.354595 /
6.704547 45.000000 1.049868 0.336048 /
7.336441 50.000000 1.050628 0.336217 /
7.944318 55.000000 1.051350 0.336386 /
8.529447 60.000000 1.052037 0.336555 /
9.091770 65.000000 1.052688 0.336725 /
9.632495 70.000000 1.053306 0.336894 /
10.151458 75.000000 1.053889 0.337063 /
10.650364 80.000000 1.054442 0.337232 /
11.129154 85.000000 1.054964 0.337401 /
11.588408 90.000000 1.055455 0.337570
95.000000 1.055233 0.337738
100.000000 1.055010 0.337907
110.000000 1.054566 0.338244
120.000000 1.054121 0.338582

130.000000 1.053677 0.338918
140.000000 1.053232 0.339255
150.000000 1.052788 0.339591
160.000000 1.052343 0.339928
170.000000 1.051899 0.340264
180.000000 1.051454 0.340600
190.000000 1.051010 0.340935
200.000000 1.050565 0.341271
220.000000 1.049676 0.341941
240.000000 1.048787 0.342611
260.000000 1.047898 0.343280
280.000000 1.047009 0.343949
300.000000 1.046120 0.344617
320.000000 1.045231 0.345284
340.000000 1.044342 0.345951
360.000000 1.043453 0.346618
380.000000 1.042564 0.347284
400.000000 1.041675 0.347950
420.000000 1.040786 0.348615
440.000000 1.039897 0.349280
460.000000 1.039008 0.349945
480.000000 1.038119 0.350610
500.000000 1.037230 0.351274
520.000000 1.036341 0.351939
540.000000 1.035452 0.352603
560.000000 1.034564 0.353267
580.000000 1.033675 0.353931
600.000000 1.032786 0.354595 /
12.027675 95.000000 1.055915 0.337738 /
12.448393 100.000000 1.056346 0.337907 /
13.237801 110.000000 1.057128 0.338244 /
13.959436 120.000000 1.057805 0.338582 /
14.621829 130.000000 1.058389 0.338918 /
15.227992 140.000000 1.058886 0.339255 /
15.786507 150.000000 1.059309 0.339591 /
16.302778 160.000000 1.059667 0.339928 /
16.782267 170.000000 1.059967 0.340264 /

17.231719 180.000000 1.060221 0.340600
190.000000 1.059776 0.340935
200.000000 1.059332 0.341271
220.000000 1.058443 0.341941
240.000000 1.057554 0.342611
260.000000 1.056665 0.343280
280.000000 1.055776 0.343949
300.000000 1.054887 0.344617
320.000000 1.053998 0.345284
340.000000 1.053109 0.345951
360.000000 1.052220 0.346618
380.000000 1.051331 0.347284
400.000000 1.050442 0.347950
420.000000 1.049553 0.348615
440.000000 1.048664 0.349280
460.000000 1.047775 0.349945
480.000000 1.046886 0.350610
500.000000 1.045997 0.351274
520.000000 1.045108 0.351939
540.000000 1.044219 0.352603
560.000000 1.043330 0.353267
580.000000 1.042441 0.353931
600.000000 1.041552 0.354595 /
17.653883 190.000000 1.060432 0.340935 /
18.053770 200.000000 1.060609 0.341271 /
18.789098 220.000000 1.060862 0.341941 /
19.449499 240.000000 1.060999 0.342611 /
20.048387 260.000000 1.061040 0.343280 /
20.592052 280.000000 1.060996 0.343949 /
21.086005 300.000000 1.060874 0.344617 /
21.538611 320.000000 1.060688 0.345284 /
21.956594 340.000000 1.060448 0.345951 /
22.333832 360.000000 1.060145 0.346618
380.000000 1.059256 0.347284
400.000000 1.058367 0.347950
420.000000 1.057478 0.348615
440.000000 1.056589 0.349280

460.000000 1.055700 0.349945
480.000000 1.054812 0.350610
500.000000 1.053923 0.351274
520.000000 1.053034 0.351939
540.000000 1.052145 0.352603
560.000000 1.051256 0.353267
580.000000 1.050367 0.353931
600.000000 1.049478 0.354595 /
22.686151 380.000000 1.059804 0.347284 /
23.011919 400.000000 1.059421 0.347950 /
23.305899 420.000000 1.058989 0.348615 /
23.585825 440.000000 1.058534 0.349280 /
23.838724 460.000000 1.058038 0.349945 /
24.052269 480.000000 1.057481 0.350610 /
24.180873 500.000000 1.056792 0.351274 /
24.331511 520.000000 1.056137 0.351939 /
24.505364 540.000000 1.055518 0.352603 /
24.703743 560.000000 1.054937 0.353267
580.000000 1.054048 0.353931
600.000000 1.053159 0.354595 /
24.928106 580.000000 1.054397 0.353931 /
25.180072 600.000000 1.053899 0.354595
605.000000 1.053894 0.354595
610.000000 1.053888 0.354595 /
/
PVTG
–P (bars) Rv (sm3/sm3) Bg (rm3/sm3) Vg (cp)
– 1.000000 Infinity Infinity 0.018817
– 0.000000000 1.3347854 0.018817 /
2.000000 0.000886097 0.9987568 0.018832
0.000000000 0.6636296 0.018832 /
5.000000 0.000208569 0.2960032 0.018878
0.000000000 0.2645568 0.018878 /
10.000000 0.000093623 0.1376408 0.018960
0.000000000 0.1306689 0.018960 /
15.000000 0.000061503 0.0891211 0.019050
0.000000000 0.0861031 0.019050 /

20.000000 0.000046439 0.0655242 0.019148
0.000000000 0.0638348 0.019148 /
25.000000 0.000037717 0.0515551 0.019255
0.000000000 0.0504702 0.019255 /
30.000000 0.000032029 0.0422885 0.019372
0.000000000 0.0415304 0.019372 /
35.000000 0.000028056 0.0357141 0.019499
0.000000000 0.0351520 0.019499 /
40.000000 0.000025137 0.0308081 0.019636
0.000000000 0.0303730 0.019636 /
45.000000 0.000022907 0.0269970 0.019785
0.000000000 0.0266491 0.019785 /
50.000000 0.000021157 0.0239528 0.019947
0.000000000 0.0236674 0.019947 /
55.000000 0.000019757 0.0214673 0.020121
0.000000000 0.0212283 0.020121 /
60.000000 0.000018618 0.0193976 0.020310
0.000000000 0.0191940 0.020310 /
65.000000 0.000017681 0.0176492 0.020514
0.000000000 0.0174731 0.020514 /
70.000000 0.000016903 0.0161513 0.020734
0.000000000 0.0159972 0.020734 /
75.000000 0.000016253 0.0148552 0.020971
0.000000000 0.0147189 0.020971 /
80.000000 0.000015708 0.0137209 0.021227
0.000000000 0.0135992 0.021227 /
85.000000 0.000015251 0.0127211 0.021504
0.000000000 0.0126115 0.021504 /
90.000000 0.000014867 0.0118336 0.021802
0.000000000 0.0117341 0.021802 /
95.000000 0.000014549 0.0110422 0.022122
0.000000000 0.0109514 0.022122 /
100.000000 0.000014285 0.0103317 0.022466
0.000000000 0.0102482 0.022466 /
110.000000 0.000013897 0.0091087 0.023238
0.000000000 0.0090371 0.023238 /
120.000000 0.000013665 0.0081002 0.024122

0.000000000 0.0080376 0.024122 /
130.000000 0.000013557 0.0072569 0.025140
0.000000000 0.0072013 0.025140 /
140.000000 0.000013551 0.0065497 0.026289
0.000000000 0.0064995 0.026289 /
150.000000 0.000013629 0.0059529 0.027583
0.000000000 0.0059071 0.027583 /
160.000000 0.000013771 0.0054499 0.029005
0.000000000 0.0054074 0.029005 /
170.000000 0.000013959 0.0050266 0.030551
0.000000000 0.0049870 0.030551 /
180.000000 0.000014179 0.0046704 0.032190
0.000000000 0.0046330 0.032190 /
190.000000 0.000014414 0.0043717 0.033902
0.000000000 0.0043360 0.033902 /
200.000000 0.000014653 0.0041202 0.035651
0.000000000 0.0040861 0.035651 /
220.000000 0.000015109 0.0037300 0.039166
0.000000000 0.0036982 0.039166 /
240.000000 0.000015511 0.0034475 0.042582
0.000000000 0.0034173 0.042582 /
260.000000 0.000015854 0.0032359 0.045843
0.000000000 0.0032070 0.045843 /
280.000000 0.000016142 0.0030725 0.048926
0.000000000 0.0030445 0.048926 /
300.000000 0.000016384 0.0029428 0.051832
0.000000000 0.0029156 0.051832 /
320.000000 0.000016590 0.0028368 0.054586
0.000000000 0.0028102 0.054586 /
340.000000 0.000016766 0.0027481 0.057208
0.000000000 0.0027221 0.057208 /
360.000000 0.000016919 0.0026735 0.059685
0.000000000 0.0026479 0.059685 /
380.000000 0.000017053 0.0026087 0.062068
0.000000000 0.0025836 0.062068 /
400.000000 0.000017172 0.0025521 0.064356
0.000000000 0.0025273 0.064356 /

420.000000 0.000017279 0.0025025 0.066539
0.000000000 0.0024781 0.066539 /
440.000000 0.000017374 0.0024578 0.068668
0.000000000 0.0024337 0.068668 /
460.000000 0.000017462 0.0024179 0.070712
0.000000000 0.0023941 0.070712 /
480.000000 0.000017547 0.0023827 0.072674
0.000000000 0.0023591 0.072674 /
500.000000 0.000017639 0.0023535 0.074506
0.000000000 0.0023301 0.074506 /
520.000000 0.000017720 0.0023250 0.076338
0.000000000 0.0023018 0.076338 /
540.000000 0.000017790 0.0022972 0.078170
0.000000000 0.0022741 0.078170 /
560.000000 0.000017848 0.0022700 0.080002
0.000000000 0.0022471 0.080002 /
580.000000 0.000017893 0.0022434 0.081835
0.000000000 0.0022208 0.081835 /
600.000000 0.000017925 0.0022175 0.083667
0.000000000 0.0021950 0.083667 /
/

REGIONS

EQUALS
'SATNUM' 1 /
'IMBNUM' 2 /
/

INCLUDE
'../INCLUDES/GRID-fine/fipnum3.inc' /

INCLUDE
'../INCLUDES/GRID-fine/fipstruc_upscaled_no_diagonal.inc' /

SOLUTION

–RPTRST
– Controls output of .UNRST file
– BASIC=4 => Restart file is written every 3. year
– BASIC=2 FREQ=1 FIP=3 FLOWS KRG KRO DEN /

EQUIL
– DATUM P OWC PC(OWC) GOC PC(GOC)
2800 318.68 10000 0 1 0 1 1 0 /

RSVD
2000 0
4000 0 /

RVVD
2000 0
4000 0 /

SUMMARY

TCPU
ELAPSED
NEWTON
NLINEARS
MLINEARS
MSUMLINS
MSUMNEWT
TIMESTEP
TCPUTS
TCPUDAY
STEPTYPE
TELAPLIN
RUNSUM
SEPARATE

FPR
FGPR
FGPT
FGIR
FGIT

FOIP
FGIP
FGIPR
FGIPG
FGIPL
FVIR
FVIT

WOPR
/
WOPT
/
WBHP
/
WBP
/
WBP5
/
WBP9
/
WGPR
/
WGPT
/

WGIR
/
WGIT
/

```
RPR
1 2 3 4 5 6
/
RGIP
1 2 3 4 5 6
/
RGIPL
1 2 3 4 5 6
/
RGIPG
1 2 3 4 5 6
/
```

```
SCHEDULE

ECHO

TUNING
0.0001 365 0.1 0.15 3 0.3 0.5 1.25 /
/
2* 50 1* 15 /

RPTRST
– Controls output of .UNRST file
BASIC=2 FREQ=1 FLOWS SGAS PRESSURE KRG DEN/

– Controls output at each timestep
RPTSCHED
FIP=3 WELLS=2 WELSPECS /

WELSPECS
'INJ1' CO2 1 180 2850 'GAS' /
'INJ2' CO2 1 180 2840 'GAS' /
'INJ4A' CO2 1 180 2833 'GAS' /
'INJ5' CO2 1 180 2932 'GAS' /
'INJ6A' CO2 1 180 2819 'GAS' /
'INJ8A' CO2 1 180 2824 'GAS' /
```

'INJ9' CO2 1 180 2790 'GAS' /
'INJ10' CO2 1 180 2820 'GAS' /
'INJ11' CO2 1 180 2799 'GAS' /
'INJ12' CO2 1 180 2900 'GAS' /
'INJ13' CO2 1 180 2810 'GAS' /
/

COMPDAT
'INJ1' 21 152 76 76 'OPEN' 1* 1* 0.2 3* 'X' /
'INJ1' 22 152 76 76 'OPEN' 1* 1* 0.2 3* 'X' /
'INJ1' 23 152 76 76 'OPEN' 1* 1* 0.2 3* 'X' /
'INJ1' 24 152 76 76 'OPEN' 1* 1* 0.2 3* 'X' /
'INJ1' 25 152 76 76 'OPEN' 1* 1* 0.2 3* 'X' /
'INJ1' 26 152 76 76 'OPEN' 1* 1* 0.2 3* 'X' /
'INJ1' 27 152 76 76 'OPEN' 1* 1* 0.2 3* 'X' /
'INJ1' 28 152 76 76 'OPEN' 1* 1* 0.2 3* 'X' /
'INJ1' 29 152 76 76 'OPEN' 1* 1* 0.2 3* 'X' /
'INJ1' 30 152 76 76 'OPEN' 1* 1* 0.2 3* 'X' /
'INJ2' 49 136 76 76 'OPEN' 1* 1* 0.2 3* 'X' /
'INJ2' 50 136 76 76 'OPEN' 1* 1* 0.2 3* 'X' /
'INJ2' 51 136 76 76 'OPEN' 1* 1* 0.2 3* 'X' /
'INJ2' 52 136 76 76 'OPEN' 1* 1* 0.2 3* 'X' /
'INJ2' 53 136 76 76 'OPEN' 1* 1* 0.2 3* 'X' /
'INJ2' 54 136 76 76 'OPEN' 1* 1* 0.2 3* 'X' /
'INJ2' 55 136 76 76 'OPEN' 1* 1* 0.2 3* 'X' /
'INJ2' 56 136 76 76 'OPEN' 1* 1* 0.2 3* 'X' /
'INJ2' 57 136 76 76 'OPEN' 1* 1* 0.2 3* 'X' /
'INJ2' 58 136 76 76 'OPEN' 1* 1* 0.2 3* 'X' /
'INJ4A' 53 78 75 75 'OPEN' 1* 1* 0.2 3* 'Y' /
'INJ4A' 53 79 75 75 'OPEN' 1* 1* 0.2 3* 'Y' /
'INJ4A' 53 80 75 75 'OPEN' 1* 1* 0.2 3* 'Y' /
'INJ4A' 53 81 75 75 'OPEN' 1* 1* 0.2 3* 'Y' /
'INJ4A' 53 82 75 75 'OPEN' 1* 1* 0.2 3* 'Y' /
'INJ4A' 53 83 75 75 'OPEN' 1* 1* 0.2 3* 'Y' /
'INJ4A' 53 84 75 75 'OPEN' 1* 1* 0.2 3* 'Y' /
'INJ4A' 53 85 75 75 'OPEN' 1* 1* 0.2 3* 'Y' /
'INJ4A' 53 86 75 75 'OPEN' 1* 1* 0.2 3* 'Y' /

'INJ4A' 53 87 75 75 'OPEN' 1* 1* 0.2 3* 'Y' /
'INJ5' 29 45 75 75 'OPEN' 1* 1* 0.2 3* 'X' /
'INJ5' 30 45 75 75 'OPEN' 1* 1* 0.2 3* 'X' /
'INJ5' 31 45 75 75 'OPEN' 1* 1* 0.2 3* 'X' /
'INJ5' 32 45 75 75 'OPEN' 1* 1* 0.2 3* 'X' /
'INJ5' 33 45 75 75 'OPEN' 1* 1* 0.2 3* 'X' /
'INJ5' 34 45 75 75 'OPEN' 1* 1* 0.2 3* 'X' /
'INJ5' 35 45 75 75 'OPEN' 1* 1* 0.2 3* 'X' /
'INJ5' 36 45 75 75 'OPEN' 1* 1* 0.2 3* 'X' /
'INJ5' 37 45 75 75 'OPEN' 1* 1* 0.2 3* 'X' /
'INJ5' 38 45 75 75 'OPEN' 1* 1* 0.2 3* 'X' /
'INJ6A' 77 44 78 78 'OPEN' 1* 1* 0.2 3* 'X' /
'INJ6A' 78 44 78 78 'OPEN' 1* 1* 0.2 3* 'X' /
'INJ6A' 79 44 78 78 'OPEN' 1* 1* 0.2 3* 'X' /
'INJ6A' 80 44 78 78 'OPEN' 1* 1* 0.2 3* 'X' /
'INJ6A' 81 44 78 78 'OPEN' 1* 1* 0.2 3* 'X' /
'INJ6A' 82 44 78 78 'OPEN' 1* 1* 0.2 3* 'X' /
'INJ6A' 83 44 78 78 'OPEN' 1* 1* 0.2 3* 'X' /
'INJ6A' 84 44 78 78 'OPEN' 1* 1* 0.2 3* 'X' /
'INJ6A' 85 44 78 78 'OPEN' 1* 1* 0.2 3* 'X' /
'INJ6A' 86 44 78 78 'OPEN' 1* 1* 0.2 3* 'X' /
'INJ8A' 30 104 68 68 'OPEN' 1* 1* 0.2 3* 'Y' /
'INJ8A' 30 105 68 68 'OPEN' 1* 1* 0.2 3* 'Y' /
'INJ8A' 30 106 68 68 'OPEN' 1* 1* 0.2 3* 'Y' /
'INJ8A' 30 107 68 68 'OPEN' 1* 1* 0.2 3* 'Y' /
'INJ8A' 30 108 68 68 'OPEN' 1* 1* 0.2 3* 'Y' /
'INJ8A' 30 109 68 68 'OPEN' 1* 1* 0.2 3* 'Y' /
'INJ8A' 30 110 68 68 'OPEN' 1* 1* 0.2 3* 'Y' /
'INJ8A' 30 111 68 68 'OPEN' 1* 1* 0.2 3* 'Y' /
'INJ8A' 30 112 68 68 'OPEN' 1* 1* 0.2 3* 'Y' /
'INJ8A' 30 113 68 68 'OPEN' 1* 1* 0.2 3* 'Y' /
'INJ9' 78 80 68 68 'OPEN' 1* 1* 0.2 3* 'Y' /
'INJ9' 78 81 68 68 'OPEN' 1* 1* 0.2 3* 'Y' /
'INJ9' 78 82 68 68 'OPEN' 1* 1* 0.2 3* 'Y' /
'INJ9' 78 83 68 68 'OPEN' 1* 1* 0.2 3* 'Y' /
'INJ9' 78 84 68 68 'OPEN' 1* 1* 0.2 3* 'Y' /
'INJ9' 78 85 68 68 'OPEN' 1* 1* 0.2 3* 'Y' /

'INJ9' 78 86 68 68 'OPEN' 1* 1* 0.2 3* 'Y' /
'INJ9' 78 87 68 68 'OPEN' 1* 1* 0.2 3* 'Y' /
'INJ9' 78 88 68 68 'OPEN' 1* 1* 0.2 3* 'Y' /
'INJ9' 78 89 68 68 'OPEN' 1* 1* 0.2 3* 'Y' /
'INJ10' 77 136 59 59 'OPEN' 1* 1* 0.2 3* 'Y' /
'INJ10' 77 137 59 59 'OPEN' 1* 1* 0.2 3* 'Y' /
'INJ10' 77 138 59 59 'OPEN' 1* 1* 0.2 3* 'Y' /
'INJ10' 77 139 59 59 'OPEN' 1* 1* 0.2 3* 'Y' /
'INJ10' 77 140 59 59 'OPEN' 1* 1* 0.2 3* 'Y' /
'INJ10' 77 141 59 59 'OPEN' 1* 1* 0.2 3* 'Y' /
'INJ10' 77 142 59 59 'OPEN' 1* 1* 0.2 3* 'Y' /
'INJ10' 77 143 59 59 'OPEN' 1* 1* 0.2 3* 'Y' /
'INJ10' 77 144 59 59 'OPEN' 1* 1* 0.2 3* 'Y' /
'INJ10' 77 145 59 59 'OPEN' 1* 1* 0.2 3* 'Y' /
'INJ11' 54 36 56 56 'OPEN' 1* 1* 0.2 3* 'Y' /
'INJ11' 54 37 56 56 'OPEN' 1* 1* 0.2 3* 'Y' /
'INJ11' 54 38 56 56 'OPEN' 1* 1* 0.2 3* 'Y' /
'INJ11' 54 39 56 56 'OPEN' 1* 1* 0.2 3* 'Y' /
'INJ11' 54 40 56 56 'OPEN' 1* 1* 0.2 3* 'Y' /
'INJ11' 54 41 56 56 'OPEN' 1* 1* 0.2 3* 'Y' /
'INJ11' 54 42 56 56 'OPEN' 1* 1* 0.2 3* 'Y' /
'INJ11' 54 43 56 56 'OPEN' 1* 1* 0.2 3* 'Y' /
'INJ11' 54 44 56 56 'OPEN' 1* 1* 0.2 3* 'Y' /
'INJ11' 54 45 56 56 'OPEN' 1* 1* 0.2 3* 'Y' /
'INJ12' 30 68 73 73 'OPEN' 1* 1* 0.2 3* 'Y' /
'INJ12' 30 69 73 73 'OPEN' 1* 1* 0.2 3* 'Y' /
'INJ12' 30 70 73 73 'OPEN' 1* 1* 0.2 3* 'Y' /
'INJ12' 30 71 73 73 'OPEN' 1* 1* 0.2 3* 'Y' /
'INJ12' 30 72 73 73 'OPEN' 1* 1* 0.2 3* 'Y' /
'INJ12' 30 73 73 73 'OPEN' 1* 1* 0.2 3* 'Y' /
'INJ12' 30 74 73 73 'OPEN' 1* 1* 0.2 3* 'Y' /
'INJ12' 30 75 73 73 'OPEN' 1* 1* 0.2 3* 'Y' /
'INJ12' 30 76 73 73 'OPEN' 1* 1* 0.2 3* 'Y' /
'INJ12' 30 77 73 73 'OPEN' 1* 1* 0.2 3* 'Y' /
'INJ13' 57 110 75 75 'OPEN' 1* 1* 0.2 3* 'X' /
'INJ13' 58 110 75 75 'OPEN' 1* 1* 0.2 3* 'X' /
'INJ13' 59 110 75 75 'OPEN' 1* 1* 0.2 3* 'X' /

'INJ13' 60 110 75 75 'OPEN' 1* 1* 0.2 3* 'X' /
'INJ13' 61 110 75 75 'OPEN' 1* 1* 0.2 3* 'X' /
'INJ13' 62 110 75 75 'OPEN' 1* 1* 0.2 3* 'X' /
'INJ13' 63 110 75 75 'OPEN' 1* 1* 0.2 3* 'X' /
'INJ13' 64 110 75 75 'OPEN' 1* 1* 0.2 3* 'X' /
'INJ13' 65 110 75 75 'OPEN' 1* 1* 0.2 3* 'X' /
'INJ13' 66 110 75 75 'OPEN' 1* 1* 0.2 3* 'X' /
/

WCONINJE
'INJ1' 'GAS' 'OPEN' 'BHP' 2.925e6 1* 464.2 / – 1000 1/
'INJ2' 'GAS' 'OPEN' 'BHP' 2.925e6 1* 462.5 / –1000 1/
'INJ4A' 'GAS' 'OPEN' 'BHP' 2.925e6 1* 461.4 / –1000 1/
'INJ5' 'GAS' 'OPEN' 'BHP' 2.925e6 1* 477.5 / –1000 1/
'INJ6A' 'GAS' 'OPEN' 'BHP' 2.925e6 1* 459.1 / –1000 1/
'INJ8A' 'GAS' 'OPEN' 'BHP' 2.925e6 1* 459.9 / –1000 1/
'INJ9' 'GAS' 'OPEN' 'BHP' 2.925e6 1* 454.4 / –1000 1/
'INJ10' 'GAS' 'OPEN' 'BHP' 2.925e6 1* 459.3 / –1000 1/
'INJ11' 'GAS' 'OPEN' 'BHP' 2.925e6 1* 455.9 / –1000 1/
'INJ12' 'GAS' 'OPEN' 'BHP' 2.925e6 1* 472.3 / –1000 1/
'INJ13' 'GAS' 'OPEN' 'BHP' 2.925e6 1* 457.7 / –1000 1/
/

TUNING
0.1 36500 0.1 0.15 3 0.3 0.5 1.25 /
/
2* 25 1* 15 /

–TSTEP
–2*0.5 –1yr
–/

TSTEP
5*3652.5 –50yrs
/

WCONINJE

'INJ1' 'GAS' 'SHUT' 'BHP' 2.925e6 1* 362 /
'INJ2' 'GAS' 'SHUT' 'BHP' 2.925e6 1* 362 /
'INJ4A' 'GAS' 'SHUT' 'BHP' 2.925e6 1* 362 /
'INJ5' 'GAS' 'SHUT' 'BHP' 2.925e6 1* 362 /
'INJ6A' 'GAS' 'SHUT' 'BHP' 2.925e6 1* 362 /
'INJ8A' 'GAS' 'SHUT' 'BHP' 2.925e6 1* 362 /
'INJ9' 'GAS' 'SHUT' 'BHP' 2.925e6 1* 362 /
'INJ10' 'GAS' 'SHUT' 'BHP' 2.925e6 1* 362 /
'INJ11' 'GAS' 'SHUT' 'BHP' 2.925e6 1* 362 /
'INJ12' 'GAS' 'SHUT' 'BHP' 2.925e6 1* 362 /
'INJ13' 'GAS' 'SHUT' 'BHP' 2.925e6 1* 362 /
/

TSTEP
2*9131.25 –50yrs
/

TSTEP
4*109575 –1200yrs
/

TSTEP
3*1059225 –8700yrs
/

END

Appendix G

ENO truncation error

If we assume we use ENO stencils with r=0 from Table 4.2 to approximate both $\hat{F}_{k+\frac{1}{2},i}(C)$ and $\hat{F}_{k-\frac{1}{2},i}(C)$ from Equation 4.17 for a single component then

$$\hat{F}_{k+\frac{1}{2}} = \frac{1}{3}F_k + \frac{5}{6}F_{k+1} - \frac{1}{6}F_{k+2} \tag{G.1}$$

$$\hat{F}_{k-\frac{1}{2}} = \frac{1}{3}F_{k-1} + \frac{5}{6}F_k - \frac{1}{6}F_{k+1} \tag{G.2}$$

and

$$\hat{F}_{k+\frac{1}{2}} - \hat{F}_{k-\frac{1}{2}} = -\frac{1}{3}F_{k-1} - \frac{1}{2}F_k + F_{k+1} - \frac{1}{6}F_{k+2} \tag{G.3}$$

Using a Taylor expansion

$$F_{k+1} = F(\xi - \Delta\xi) = F(\xi) - \Delta\xi F'(\xi) + \frac{1}{2}(\Delta\xi)^2 F''(\xi) - \frac{4}{3}(\Delta\xi)^3 F''' + \frac{2}{3}(\Delta\xi)^4 F'''' \tag{G.4}$$

$$F_k = F(\xi) \tag{G.5}$$

$$F_{k+1} = F(\xi + \Delta\xi) = F(\xi) + \Delta\xi F'(\xi) + \frac{1}{2}(\Delta\xi)^2 F''(\xi) + \frac{4}{3}(\Delta\xi)^3 F''' + \frac{2}{3}(\Delta\xi)^4 F'''' \tag{G.6}$$

$$F_{k+2} = F(\xi + 2\Delta\xi) = F(\xi) + 2\Delta\xi F'(\xi) + 2(\Delta\xi)^2 F''(\xi) + \frac{1}{6}(\Delta\xi)^3 F''' + \frac{1}{24}(\Delta\xi)^4 F'''' \tag{G.7}$$

Substituting these into Equation G.3 we find that

$$\hat{F}_{k+\frac{1}{2}} - \hat{F}_{k-\frac{1}{2}} = \frac{\partial F}{\partial \xi} - \frac{(\Delta\xi)^3}{12}\frac{\partial^4 F}{\partial \xi^4} \tag{G.8}$$

Therefore the truncation error from Equation 4.17 using this stencil from the ENO approximation is $\frac{\Delta\xi^3}{12}\frac{\partial^4 F}{\partial C^4}\frac{\partial^4 C}{\partial \xi^4}$.

Appendix H

Explicit scheme capillary truncation error

We approximate the capillary terms in Equation 5.1 by

$$\frac{1}{\Delta\xi^2}\left[\left(c_{ij}f_j\frac{k_{rq}}{\mu_q}\right)\Big|_{k+\frac{1}{2}}^{n}\left[P_{cjq}(S_{k+1}^n)-P_{cjq}(S_k^n)\right]-\left(c_{ij}f_j\frac{k_{rq}}{\mu_q}\right)\Big|_{k-\frac{1}{2}}^{n}\left[P_{cjq}(S_k^n)-P_{cjq}(S_{k-1}^n)\right]\right] \tag{H.1}$$

For this analysis let $a = c_{ij}f_j\frac{k_{rq}}{\mu_q}$ and $p = P_{cjq}$ so that our approximation becomes

$$\frac{1}{\Delta\xi^2}\left[a|_{k+\frac{1}{2}}^{n}\left[p_{k+1}-p_k\right]-a|_{k-\frac{1}{2}}^{n}\left[p_k-p_{k-1}\right]\right] \tag{H.2}$$

By substituting Taylor approximations for both a and p and multiplying out we find this approximation becomes

$$a\frac{\partial^2 p}{\partial\xi^2}+\frac{\partial a}{\partial\xi}\frac{\partial p}{\partial\xi}+\frac{\Delta\xi^2}{8}\frac{\partial^2 a}{\partial\xi^2}\frac{\partial^2 p}{\partial\xi^2}+\Delta\xi^2\frac{a}{12}\frac{\partial^4 p}{\partial\xi^4}+\frac{\Delta\xi^2}{6}\frac{\partial a}{\partial\xi}\frac{\partial^3 p}{\partial\xi^3}+\frac{\Delta\xi^2}{24}\frac{\partial^3 a}{\partial\xi^3}\frac{\partial p}{\partial\xi} \tag{H.3}$$

which substituting a and p back in gives us errors of

$$\begin{aligned}&\frac{\Delta\xi^2}{8}\frac{\partial^2\left(c_{ij}f_j\frac{k_{rq}}{\mu_q}\right)}{\partial\xi^2}\frac{\partial^2 P_{cjq}}{\partial\xi^2}+\frac{\Delta\xi^2}{12}\left(c_{ij}f_j\frac{k_{rq}}{\mu_q}\right)\frac{\partial^4 P_{cjq}}{\partial\xi^4}\\&+\frac{\Delta\xi^2}{6}\frac{\partial\left(c_{ij}f_j\frac{k_{rq}}{\mu_q}\right)}{\partial\xi}\frac{\partial^3 P_{cjq}}{\partial\xi^3}+\frac{\Delta\xi^2}{24}\frac{\partial^3\left(c_{ij}f_j\frac{k_{rq}}{\mu_q}\right)}{\partial\xi^3}\frac{\partial P_{cjq}}{\partial\xi}\end{aligned} \tag{H.4}$$